

University of Missouri, St. Louis

IRL @ UMSL

Dissertations

UMSL Graduate Works

11-14-2023

Binding Interactions of Biologically Relevant Molecules Studied Using Surface-Modified and Nanostructured Surfaces

Palak Sondhi

University of Missouri–St. Louis

Follow this and additional works at: <https://irl.umsl.edu/dissertation>

 Part of the [Analytical Chemistry Commons](#), [Biochemistry Commons](#), [Materials Chemistry Commons](#), [Nanotechnology Commons](#), and the [Physical Chemistry Commons](#)

Recommended Citation

Sondhi, Palak, "Binding Interactions of Biologically Relevant Molecules Studied Using Surface-Modified and Nanostructured Surfaces" (2023). *Dissertations*. 1384.

<https://irl.umsl.edu/dissertation/1384>

This Dissertation is brought to you for free and open access by the UMSL Graduate Works at IRL @ UMSL. It has been accepted for inclusion in Dissertations by an authorized administrator of IRL @ UMSL. For more information, please contact marvinh@umsl.edu.

Binding Interactions of Biologically Relevant Molecules Studied
Using Surface-Modified and Nanostructured Surfaces

By

Palak Sondhi

M.Tech. Advanced Methods of Chemical Analysis-Graduate,

Indian Institute of Technology Roorkee, India, 2018

A Dissertation

Submitted to the Graduate School at the

University of Missouri-St. Louis

In partial fulfillment of the requirements for the degree

Doctor of Philosophy in Chemistry with an emphasis in Biochemistry

December 2023

Advisory Committee

Chair and Advisor, Keith J. Stine, Ph.D.

Alexei V. Demchenko, Ph.D.

Chung F. Wong, Ph.D.

Michael R. Nichols, Ph.D.

ABSTRACT

Binding Interactions of Biologically Relevant Molecules Studied Using Surface-Modified and Nanostructured Surfaces

December 2023

Palak Sondhi, M.S. Chemistry-Graduate, University of Missouri-StLouis, MO,
USA

Chair and Advisor: Professor Keith J. Stine

This research focuses on the field of surface nanobioscience, wherein different nanosurfaces that will be used as working electrodes in the electrochemical cell are manufactured and surface modified to understand the critical binding interactions between biologically significant molecules like proteins, carbohydrates, small drug molecules, and glycoproteins. This research is essential if we are to determine whether a synthetic molecule can serve as a therapeutic candidate or diagnose a disease in its early stages. In order to fully understand the binding interactions, the study begins with defining some of the fundamental concepts, principles, and analytical tools for biosensing.

Afterwards, we addressed a crucial issue in material chemistry: integrating a large surface area with easy molecular movement in the same material. The problem was successfully resolved by developing a hierarchical nanoporous gold (hb-NPG) electrode using the fundamental principles of electrochemistry. An important biomarker for osteoporosis called fetuin A was monitored using square wave voltammetry technique by employing surface-modified hb-NPG as working

electrode. The project was advanced by creating a monolith, which has a wide range of industrial applications. The material was created by using the approach of templating and dealloying and was characterized using Brunauer-Emmett-Teller analysis, thermogravimetric analysis, and scanning electron microscopy techniques.

The surface modification process was extended to include other materials like indium tin oxide and Au coated quartz crystal in addition to NPG and hb-NPG. It was critical to comprehend the affinities of synthetically produced compounds with membrane proteins implicated in the transmission of the disease to investigate their potential as therapeutic candidates against a particular disease. Lipopolysaccharide antagonists (such as AM12 and compounds with a lactone structure) and curcumin analogs are examples of synthetic compounds used in this investigation. Lipid binding protein (LBP), Cluster of differentiation 14 (CD14), and Myeloid Differentiation factor 2 (MD-2) are the key proteins in sepsis, and in this study, we examine how well they attach to the LPS antagonists. Receptor Binding Domain (RBD) and Angiotensin Converting Enzyme 2(ACE2) are another set of proteins that are investigated that are important in covid and explored for their binding affinity towards curcumin analogs.

We created platforms with immobilized proteins to test these drugs' binding affinities for membrane proteins. To observe the outcome of the interaction, various sensing techniques including Quartz Crystal Microbalance, Electron Impedance Spectroscopy, and fluorescence have been employed. The solubility and stability of curcumin analogs were also explored before exploring their binding potential. As seen using UV-vis spectrophotometry, the presence of sugar units in the side chain boosted their hydrophilicity and stability.

Dedication

TO MY FAMILY

ACKNOWLEDGEMENTS

I have a strong sense of purpose and passion for science, especially the fascinating discipline of chemistry, where I can contribute by finding solutions to some challenging issues. Before starting, I was aware that completing a PhD would need a great deal of perseverance, commitment, diligence, and an unwavering spirit of never giving up. It was fortuitous that Dr. Stine accepted me in his group as our perspectives and goals align very well. My most profound appreciation goes to Dr. Keith J. Stine, my Ph.D. advisor. He has been a great support system and inspiration for me. His dedication to mentorship, his support of my attendance at numerous conferences, and his encouragement of my intellectual independence in research projects have all greatly contributed to my fruitful research experience. Even the most complex topics have become easier to understand thanks to the stimulating and engaging nature of our research discussions. His passion for the subject matter is evident, and it has encouraged me to explore and learn beyond the confines of the research lab. Additionally, I would like to give a big shout out to my committee members, Dr. Alexei V. Demchenko, Dr. Michael R. Nichols, and Dr. Chung F. Wong. They provided a fresh path for my problem-solving strategy with their keen insightful analysis and original viewpoints on how to address some of the research issues in my project. Their thought-provoking inquiries have helped me comprehend the topics better as a researcher.

I really believe that a calm lab atmosphere and cooperative lab mates are key ingredients for successful research endeavors. When I first started working in the lab, I was a little anxious about the unfamiliar environment, but Dr. Jay Bhattarai,

Dr. Dharmendra Neupane, and Dr. Bishal Nepal made me feel welcome and at ease. I owe a lot to them because their research expertise and relentless work ethic have greatly influenced me during my early graduate years. Their extensive chemistry understanding, subject matter knowledge, and scientific zeal helped me a lot. My go-to person in the lab was Dr. Neupane, who patiently taught me a range of analytical techniques and collaborated closely with me on the production of the hb-NPG I present in this thesis.

My present lab mates are my best supporters and excellent research partners. Dhanbir Lingden came to the department a semester after I started working. We have grown as researchers by supporting one another and taking advice from our more seasoned peers. We successfully ran our lab and watched Covid together. After Covid, Taiwo Adeniji and Naila Haroon came to the lab. Their upbeat demeanor revitalizes the area around them, and I am motivated by their eagerness to learn more. I would like to thank all the graduate, undergraduate, and high school students who have collaborated with me to advance the initiatives, whether directly or indirectly.

The consistent encouragement and words of affirmation from my parents (Sanjay Sondhi and Sunanda Sondhi) have helped me get where I am. I've always looked up to my father as a role model since he gave me the skills to be a successful researcher with a positive outlook on life. I've always had faith in my mother's prayers, and they've given me a boost along the way. I find it extremely admirable that she places such a high value on her children's education. My siblings (Vani Sondhi and Paramdeep Sondhi) are my biggest cheerleaders. Last but not least, I could not have

completed it on my own without my husband's (Ayush Kashyap) support and my new parents (Arun Kashyap and Mamta Kashyap) love during this journey. I really believe that a strong and supportive husband is the foundation of every successful wife.

TABLE OF CONTENT

ABSTRACT	2
DEDICATION	4
ACKNOWLEDGEMENTS	5
TABLE OF CONTENTS	8
LIST OF ABBREVIATIONS	14
LIST OF FIGURES	16
LIST OF TABLES	26
CHAPTER I: INTRODUCTION	27
1.1 Overview	27
1.2 Nanobiotechnology-Importance and Scope	28
1.3 Biosensors	30
1.4 Surface modification	32
1.5 Transduction elements	37
1.6 Sensing techniques- General overview and principle	39
1.6a) Electrochemical Impedance Spectroscopy (EIS)	39
1.6b) Square Wave Voltammetry (SWV)	43
1.6c) Fluorescence spectroscopy	45
1.7 Impact of the study on healthcare system	46
1.7a) Osteoporosis	46
1.7b) Sepsis	49
1.7c) Covid-19	58
CHAPTER II: MATERIALS AND METHODS	74
2.1 Materials	74
2.2 Instrumentation	76

2.3 Fabrication of electrodes	78
2.3a) Nanoporous gold coated gold wires	78
2.3b) Hierarchical bimodal nanoporous gold coated gold wires	78
2.3c) Hierarchical bimodal nanoporous monolith	79
2.4 Self-assembled monolayer preparation and analysis	80
2.5 Activation and surface modification of ITO glass	80
2.6 Activation and surface modification of Au-QCM sensor	81
2.7 Preparation of protein solutions	82
2.8 Solution depletion technique to study protein loading onto fabricated electrodes	83
2.9 Investigation of the electron transfer in 6-ferrocenyl-1-hexanethiol SAMs on NPG and hb-NPG	84
2.10 Electrochemical detection of glucose and the effect of interferents	85
2.11 Stability analysis of curcumin analog solutions	85
2.12 Solubility analysis of curcumin analog solutions	86
2.13 Preparation and immobilization of lectin-enzyme conjugate	87
2.14 Michaelis-Menten kinetics of the SNA-ALP conjugates on electrodes	87
2.15 Electrochemical enzyme-linked kinetic lectin assay	88
2.16 Characterization of surface-modified sensors	89
2.16a) Imaging the microstructure and morphology of the material (SEM/EDS)	89
2.16b) Thermal (TGA)	89
2.16c) Mechanical (AFM)	89
2.16d) Optical (contact angle measurement)	90
2.16e) Surface chemical characterization (XPS)	90
2.17 Evaluation of binding affinities	91

CHAPTER III: METHODS TO GENERATE HIERARCHICAL BIMODAL NANOPOROUS GOLD ELECTRODE AND ITS APPLICATION (RESULTS AND DISCUSSION)	97
3A. FABRICATION OF HIERARCHICAL BIMODAL NANOPOROUS GOLD FOR STUDYING GLYCOPROTEIN-LECTIN INTERACTION BY AN ELECTROCHEMICAL BIOSENSOR	97
3.1 Characterization of nanoporous gold and hierarchical bimodal nanoporous gold electrode prepared by varying the ratio of the Au-Ag alloy	97
3.2 Surface area measurement and roughness factor analysis	103
3.3 Determination of surface coverage of lipoic acid molecules on NPG and hb-NPG using thermogravimetric analysis and reductive desorption	106
3.4 Adsorption of proteins with varying structures onto NPG and hb-NPG	108
3.5 Quantitative analysis of the SAMs of ferrocene 1-hexanethiol	113
3.6 Electrochemical detection of Glucose	116
Conclusion and future perspectives	121
3B. ENGINEERING HIERARCHICALLY NANOPOROUS GOLD MONOLITH USING TEMPLATING APPROACH	124
3.7 The hierarchical bimodal pore structure characterization of hb-NPG monolith	124
3.8 BET analysis	127
3.9 TGA analysis	128
Conclusion and future perspectives	130
3C. COMPARATIVE STUDY OF ELECTROCHEMICAL RECOGNITION OF GLYCOPROTEIN BIOMARKERS USING LECTIN MODIFIED NPG AND HB-NPG	131
3.10 Analysis of the surface morphology of the fabricated electrodes	131
3.11 Lectin-enzyme conjugate activity detected by square-wave voltammetry	132
3.12 Evaluation of the Michaelis-Menten constant K_m for NPG and hb-NPG electrodes	134

3.13 Kinetic enzyme-linked lectinsorbent assay on NPG and hb-NPG electrodes	137
3.14 Effect of BSA on ELLA	140
Conclusion and future perspectives	141
CHAPTER IV: EVALUATING THE BINDING AFFINTY OF LPS ANTAGONISTS AND CURCUMIN ANALOGS TO PROTEIN RECEPTORS INVOLVED IN SEPSIS	144
4A. QUARTZ CRYSTAL MICROBALANCE AS A SENSITIVE TECHNIQUE FOR REAL-TIME ANALYSIS OF THE BINDING AFFINITYOF LPS ANTAGONISTS TO PROTEIN RECEPTORS	144
4.1 Characterization of surface modified QCM sensors using contact angle measurement	145
4.2 Characterization of surface modified QCM sensors using AFM	146
4.3 Characterization of surface modified QCM sensors using XPS	148
4.4 Binding affinities of LPS antagonists with CD14 and LBP	151
Conclusion and future perspectives	154
4B. EXPLORING THE POTENTIAL ROLE OF GLYCO-CURCUMIN ANALOGS AS MD-2 INHIBITORS IN THE INHIBITION OF RESPONSE TOWARDS LPS	156
4.5 Curcumin and Curcuminoids Chemical Stability Analysis by UV-Visible Absorption Spectra	158
4.6 Solubility analysis of curcumin and curcuminoids	161
4.7 The binding affinities of Curcuminoids to MD-2 receptor	163
Conclusion and future perspectives	169

CHAPTER V: EVALUATING THE BINDING AFFINITY OF CURCUMIN ANALOGS TOWARDS PROTEIN RECEPTORS INVOLVED IN COVID-19	173
5. INVESTIGATION OF THE POTENTIAL INHIBITORY EFFECT OF GLYCOCURCUMINOIDS AGAINST THE BINDING OF SPIKE PROTEIN AND MEMBRANE RECEPTOR ACE2: POTENTIAL NEW TREATMENT OPTION FOR SARS-COV-2	173
5.1 Topography and elemental composition of the surface-modified working electrode using SEM-EDS analysis	174
5.2 Gold nanoparticle's colloidal solution- characterization using UV-vis spectroscopy	177
5.3 Step-wise modification of the working electrode using electrochemical impedance spectroscopy (EIS)	178
5.4 Optimization of analysis parameters	180
5.5 Electrochemical impedance response of the modified electrode (with ACE2 and RBD) towards varying concentrations of glyco-curcuminoids	181
5.6 Understanding how ACE-2, RBD, and glyco-curcuminoids work in conjunction to cause binding	188
Conclusion and future perspective	190
CHAPTER VI: PRELIMINARY WORK	195
6.1 GUVs to study the interaction of LPS analogs with cell membrane	195
6.1a) Giant Unilamellar Vesicles (GUVs) electroformation procedure: Assembling the chamber	196
6.1b) Electroformation	197
6.1c) Harvesting GUVs and preparing the imaging chamber	197
6.1d) LPS analogs of varying chain lengths incubation with GUVs	197
6.2 Formation of supported lipid bilayer	205

6.3 Evaluating the Effectiveness of β -Cyclodextrin as a Surface Modification to Nanoporous Gold in the Electrochemical Detection of Acetaminophen	207
References	212

LIST OF ABBREVIATIONS

AFM	Atomic Force Microscopy
11-MUA	11-Mercaptoundecanoic acid
APMBA	Aminophenylmethylboronic acid
AUC	Area Under the Curve
AuNPs	Gold nanoparticles
BET	Brunauer-Emmett-Teller
BJH	Barrett-Joyner-Halenda
BSA	Bovine serum albumin
SNA	Sambucus Nigra Lectin
HRP	Horseradish peroxidase
EDC	1-Ethyl-3-(3-dimethylaminopropyl) carbodiimide hydrochloride
EDX	Energy dispersive X-ray spectroscopy
ELLA	Enzyme linked lectinsorbent assay
NHS	N-hydroxysuccinimide
LPS	Lipopolysaccharide
SWV	Square Wave Voltammetry
P-APP	Para-aminophenyl phosphate

Kd	Dissociation Constant
LA	Lipoic acid
SEM	Scanning Electron Microscopy
AFM	Atomic Force Microscopy
QCM	Quartz Crystal Microbalance
EIS	Electrochemical Impedance Spectroscopy
RT	Room Temperature
R _{ct}	Charge Transfer Resistance
SAM	Self-assembled monolayer
SBET	BET specific surface area
GUVs	Giant Unilamellar Vesicles
Hb-NPG	Hierarchical Bimodal Nanoporous Gold
LBP	Lipopolysaccharide Binding Protein
CD14	Cluster of differentiation 14
ACE2	Angiotensin Converting Enzyme 2
RBD	Receptor Binding Domain
TGA	Thermogravimetric analysis
UV-Vis	Ultraviolet-visible
XPS	X-ray photoelectron spectroscopy

LIST OF FIGURES

Figure 1. SAMs as components of nanoscience and nanotechnology.	33
Figure 2. EDC-NHS coupling chemistry mechanism.	35
Figure 3. The immobilization of L-Arg in the PDA coating.	36
Figure 4. Randles equivalent electrical circuit over a broad frequency range.	41
Figure 5. Schematic showing the square-wave voltammetry potential shape. A single SW cycle and the procedure for measuring the current in SWV are shown in the inset. Square-wave voltammogram showing the transport of electrons between a working electrode and a water-soluble redox analyte (forward, backward, and net current components)	44
Figure 6. Lipopolysaccharide (LPS) transport pathway in <i>Escherichia coli</i> .	50
Figure 7. Schematic showing mammalian endotoxin sensing and signaling	52
Figure 8. The LPS antagonistic action of compound AM-12 with good cell viability.	53
Figure 9. Aryl side chain modification (A), modification of the diketo functionality(B), modification of the double bond (C), modification of the active methylene functionality (D), metal complexes of curcumin (E), and appended curcumin mimics/structural analogs of curcumin (F) are examples of structural modifications that can be made to curcumin.	57
Figure 10. The SARS-CoV-2 structure is displayed along with the viral S protein's attachment to the host's ACE2 receptor	59

<p>Figure 3.1 SEM images of a) 10:90 (Au: Ag) alloy prepared by applying -1.0 V (vs. Ag/AgCl, KCl saturated) for 10 min on gold wire, b) morphology after electrochemical dealloying, c) pore-coarsening seen after annealing, d) Larger pores seen after chemical dealloying in concentrated nitric acid, e) and f) are showing the ligament width and interligament distance in upper and lower hierarchy respectively. Thickness of the hierarchical structure deposited on gold wire is shown in (g), (h) Histograms showing the ligament width and interligament distance in upper and lower hierarchy respectively.</p>	99
<p>Figure 3.2 A) Color SEM of the A1) Au₁₀:Ag₉₀ alloy, A2) electrochemically dealloyed structure, A3) annealed structure, and a4) hierarchical nanoporous structure after the final step of chemical dealloying B) EDX spectrum showing the elemental composition of the B1) alloy, B2) electrochemically dealloyed structure, and B3) hierarchical bimodal nanoporous gold structure.</p>	101
<p>Figure 3.3 Cyclic voltammograms showing a) the comparison of electrochemically active surface area for the porous structure formed from different Au: Ag atomic percentages of the alloy. The varying composition of the starting alloy was Au₁₀:Ag₉₀, Au₂₀:Ag₈₀, Au₂₅:Ag₇₅ and Au₃₀:Ag₇₀ b) Au₁₀:Ag₉₀ alloy, chemically dealloyed structure formed after immersing in nitric acid, and finally the enhancement of peak current when electrochemical and chemical dealloying is used in combination (c) the oxidation and reduction peaks after electrochemical dealloying are shown in red where the peak at 1) denotes the oxidation of Au. The oxidation and reduction peaks after annealing are shown in blue where the peak at 1) is associated with the oxidation of Ag₂O to AgO. The peak at 2) in both cases is due to the reduction to Ag₂O layers.</p>	104
<p>Figure 3.4 A) TGA thermograms of lipoic acid loading on NPG and hb-NPG from room temperature to 600 °C at a ramping rate of 20 °C min⁻¹. B) Reductive desorption of lipoic acid immobilized on NPG and hb-NPG carried out in 0.5 M NaOH solution, performed between 0 and -1.5 V at a scan rate of 20 mV s⁻¹.</p>	108

<p>Figure 3.5 Real-time protein loading study using UV-vis spectrophotometer showing the change in absorbance and the average number of immobilized BSA, Fetuin and HRP molecules on NPG and hb-NPG electrodes. BSA, Fetuin, and HRP loading on NPG is shown in (a), (c), and (e) respectively. The loading of same proteins on hb-NPG is shown in (b), (d), and (f) respectively. Each graph depicted is an average of three measurements. Data depicted as an average (N=3).</p>	112
--	-----

Figure 3.6 Cyclic voltammograms of SAMs of 6-ferrocenyl-1-hexanethiol with unmodified bare gold wire, chemically dealloyed electrode, and hb-NPG(solution composition reported) (NaClO ₄ , 0.1M; scan rate = 50 mV s ⁻¹). Increasing the concentration of the electrolyte to 0.5M has little variation on the shape of the curve.	114
Figure 3.7 CVs of (i) bare gold, (ii) NPG and (iii) hb-NPG recorded in N ₂ saturated NaOH solution with 10 mM glucose.	118
Figure 3.8 The chronoamperometric curve of (i) NPG and (ii) hb-NPG towards glucose with successive addition in 0.1M NaOH at the working potential of 0.02 V and 0.57 V, respectively. The calibration curve of the NPG and hb-NPG glucose sensor is shown below each of the figures.	119
Figure 3.9 The current response of the fabricated hb-NPG glucose sensor in the presence of common interferents	121
Figure 3.10 SEM images of a) gold-silver monolith after being annealed at 600°C showing pore coarsening b) pores of upper hierarchy, c) pores of lower hierarchy after chemical dealloying, and d) EDS data after chemical dealloying in concentrated nitric acid.	126
Figure 3.11 Pore size distribution in hierarchical bimodal nanoporous gold monolith, representing a) upper hierarchical pore size distribution and b) lower hierarchical pore size distribution.	127
Figure 3.12 BET isotherm (N ₂ gas) of a) annealed and b) hbNPG. BJH pore size distribution is shown for c) annealed and d) hbNPG.	128
Figure 3.13 Thermogravimetric curve of hb-NPG (blue) and hb-NPG with lipoic acid (red)	130

<p>Figure 3.14 SEM images (top-view) of two different types of electrodes (a) nanoporous gold prepared (at 150 kX magnification) using 30:70 (Au:Ag) alloy deposition by providing -1.0 V (vs. Ag/AgCl, KCl saturated) for 10 min on gold wire and subsequently immersing in concentrated nitric acid for chemical dealloying to generate a porous architecture and, (b) hierarchical bimodal nanoporous gold (at 80 kX magnification) prepared using a multistep alloying-partial dealloying-annealing- chemical dealloying strategy to generate dual sized pores.</p>	132
<p>Figure 3.15 Square-wave voltammograms of SNA-ALP conjugate immobilized on lipoic acid modified a) NPG and b) Hb-NPG. SWV were recorded with 1 mM p-APP in glycine buffer (pH 9, 100 mM) after 5 min incubation with the substrate p-APP. To conduct SWV (vs. the Ag AgCl reference electrode), the following parameters were used: 50 mV for the pulse height, 0.2 sec for the pulse width, 2 mV for the step height, and 5.0 mV sec⁻¹ for the scan rate.</p>	133
<p>Figure 3.16 SWV for lipoic acid SAMs that have SNA-alkaline phosphatase conjugate immobilized on (a) NPG and (c) hb-NPG. After two minutes of incubation, SWV was tested for p-APP concentrations in a pH 9.0 glycine buffer (100 mM). SWV was measured using an Ag AgCl reference electrode, a pulse height of 50 mV, a pulse width of 0.2 seconds, a step height of 2 mV, and a scan rate of 5.0 mV sec⁻¹.</p>	136
<p>Figure 3.17 Voltammograms recorded after binding of SNA – ALP conjugate to varying concentrations of fetuin immobilized on (a) NPG and (c) hb-NPG by covalent conjugation to lipoic acid SAMs. Different concentrations of fetuin were incubated for 2 hours (in PBS, pH 7.4, 10 mM with 1 mM) with SNA-ALP conjugate immobilized on lipoic acid modified electrodes. To perform SWV, a pH 9.0 glycine buffer (100 mM) with a pulse height of 50 mV, a pulse width of 0.2 sec, a step height of 2 mV, and a scan rate of 5.0 mV sec⁻¹ were used.</p>	138

<p>Figure 3.18 (a) NPG and (b) hb-NPG kinetic ELLA response. The difference in SWV peak difference current before and after incubation was plotted to obtain the response plot. Different concentrations of asialofetuin were incubated for 2 hours (in PBS, pH 7.4, 10 mM with 1 mM) with SNA-ALP conjugate immobilized on lipoic acid modified electrodes. To perform SWV, a pH 9.0 glycine buffer (100 mM) with a pulse height of 50 mV, a pulse width of 0.2 sec, a step height of 2 mV, and a scan rate of 5.0 mV sec⁻¹ were used. The error bars show the standard deviation across three measurements.</p>	139
<p>Figure 3.19 Effect of BSA on hb-NPG kinetic ELLA assay. SWV measurements were carried out a) before and b) after the addition of BSA (5 mg mL⁻¹) in the incubation solution containing fetuin 2 μM dissolved in PBS, pH 7.4, 10 mM. SWV was carried out in pH 9.0 glycine buffer (100 mM) with pulse heights of 50 mV, pulse widths of 0.2 sec, step heights of 2 mV, and scan rates of 5.0 mV sec⁻¹.</p>	140
<p>Figure 4.1 Surface contact angles of the unmodified a) QCM sensor, b) 11-MUA modified, c) EDC/NHS treated, and d) protein immobilized QCM sensor.</p>	146
<p>Figure 4.2 AFM micrographs of a) unmodified QCM sensor, b) 11-MUA modified, c) CD14 immobilized, and d) LBP modified QCM sensor.</p>	148
<p>Figure 4.3 XPS analysis of QCM sensor after each stage of surface modification. XPS spectra for a) C1s, b) O1s, c) N1s, d) Au4f, and e) S2p</p>	151

Figure 4.4 QCM data illustrating fundamental frequency variation derived from LPS antagonist deposition onto a protein-immobilized Au-coated quartz crystal. The QCM profiles made using (a) CD14 and (c) LBP together with C10 lactone are displayed. Ligand binding curves showing the frequency variation with concentration of the antagonist are shown in (b) and (d) to evaluate the binding affinity of C10 with CD14 and LBP respectively.	152
Figure 4.5 QCM data illustrating fundamental frequency variation derived from AM12 onto a protein-immobilized Au-coated quartz crystal. The QCM profiles made using (a) CD14 and (c) LBP together with AM12 are displayed. Ligand binding curves showing the frequency variation with concentration of the antagonist are shown in (b) and (d) to evaluate the binding affinity of AM12 with CD14 and LBP respectively.	153
Figure 4.6 QCM sensorgram showing the fundamental frequency variation vs time when varying concentrations of BSA was added on the modified Au-coated quartz crystal.	154
Scheme 1	157
Figure 4.7 UV- visible absorption spectra of curcumin and glycocurcuminoids in PBS buffer (pH 7.4) a) deacetylated-galactosylated methylated curcumin b) deacetylated- glucosyl methylated curcumin c) deacetylated-glycosyl benzylated curcumin d) deacetylated-galactosylated benzylated curcumin e) deacetylated-galactosyl monocarbonyl curcumin f) curcumin	159
Figure 4.8 UV-visible absorption spectra showing the impact of varying pH on the stability of deacetylated glucosyl benzylated curcumin.	160
Figure 4.9 UV-visible spectra of the supernatant collected after 24h from the saturated solutions of curcumin and curcuminoid formulations prepared in PBS buffer (pH 7.4)	161

<p>Figure 4.10 (a) UV-visible absorption spectrum of varying concentrations of deacetylated glucosyl benzylated curcumin and (b) Calibration plot of deacetylated glucosyl benzylated curcumin showing a linear plot with slope as 0.0164. Similar calibration plots were made with other analogs to evaluate the slope which was used to calculate and molar extinction coefficient for solubility calculations.</p>	<p>163</p>
<p>Figure 4.11 MD-2 interacts with deacetylated glucosyl benzylated curcumin in solution (excitation at 370 nm and emission at 490 nm, slit width at 20). The fluorescence emission of only glucosyl benzylated curcumin analog in PBS buffer is shown in (a). When MD-2 (50 nM) is added to a curcumin solution (25 μM), the curcumin fluorescence emission (b) increases. The value of K_d of $0.34 \pm 0.39 \mu$M is found from the data fit shown in (c)</p>	<p>166</p>
<p>Figure 4.12 Ligand binding plots with MD-2 for (a) deacetylated glucosyl methylated curcumin (b) deacetylated galactosyl monocarbonyl curcumin (c) deacetylated galactosyl methylated curcumin (d) deacetylated galactosyl benzylated curcumin.</p>	<p>169</p>
<p>Scheme 2. The surface modification steps performed on ITO glass.</p>	<p>174</p>
<p>Figure 5.1. SEM images of (a) clean ITO glass at the magnification of 5kX, (b) APTES modified ITO coated glass (magnification 10kX), (c) AuNPs/APTES/ITO modified surface (at 2kX magnification), and (d) PDA (30 min polymerization)/AuNPs/APTES/ITO (at 80kX magnification). EDS analysis for APTES modified ITO glass is shown in e) and f) is showing the EDS spectrum of AuNPs/APTES/ITO modified surface.</p>	<p>176</p>
<p>Figure 5.2 UV-Visible absorption spectrum of AuNPs, collected in milli-Q water, showing a strong absorbance peak observed at 525 nm.</p>	<p>177</p>

<p>Figure 5.3 Nyquist plots for (a) clean bare ITO (b) APTES/ITO (c) AuNPs/APTES/ITO and (d) PDA/AuNPs/APTES/ITO, acquired in a PBS solution containing 5 mM $[\text{Fe}(\text{CN})_6]^{3-}/[\text{Fe}(\text{CN})_6]^{4-}$ in the frequency range from 1 Hz to 100 kHz at an AC voltage of 10 mV and a scan rate of 50 mV/s.</p>	179
<p>Figure 5.4. Nyquist plots of different concentrations (1.56 μM, 3.12 μM, 6.25 μM, 12.5 μM, and 25 μM) of curcumin analogs on the ACE2 (0.1 μM) modified ITO surface in the frequency range from 1 Hz to 100 kHz at an AC voltage of 10 mV and a scan rate of 50 mV/s. (a) glucosylated benzylated curcumin, (b) glucosylated methylated curcumin, (c) galactosylated monocarbonyl curcumin, (d) galactosylated-methylated curcumin, and (e) galactosylated-benzylated curcumin</p>	182
<p>Figure 5.5. Nyquist plots of different concentrations (1.56 μM, 3.12 μM, 6.25 μM, 12.5 μM, and 25 μM) of curcumin analogs on the RBD (0.1 μM) modified ITO surface in the frequency range from 1 Hz to 100 kHz at an AC voltage of 10 mV and a scan rate of 50 mV/s. (a) glucosylated benzylated curcumin, (b) glucosylated methylated curcumin, (c) galactosylated monocarbonyl curcumin, (d) galactosylated-methylated curcumin, and (e) galactosylated-benzylated curcumin.</p>	183
<p>Figure 5.6. Ligand binding plots of glycocurcuminoids with ACE2 (a1 to e1) and RBD (a2 to e2) where, (a) galactosylated-methylated curcumin, (b) galactosylated-benzylated curcumin, (c) glucosylated methylated curcumin, (d) glucosylated benzylated curcumin, and (e) galactosylated monocarbonyl curcumin</p>	186
<p>Figure 5.7. Blank test of glycocurcuminoids on the modified ITO (without RBD or ACE2) where, (a) galactosylated-methylated curcumin, (b) galactosylated- benzylated curcumin, (c) glucosylated methylated curcumin, (d) glucosylated benzylated curcumin, and (e) galactosylated monocarbonyl curcumin</p>	187

Figure 5.8 Nyquist plots of different concentrations (1.56 μM , 3.12 μM , 6.25 μM , 12.5 μM , and 25 μM) of curcumin analogs with RBD (0.1 μM) on the ACE2 (0.1 μM) modified ITO surface in the frequency range from 1 Hz to 100 kHz at an AC voltage of 10 mV and a scan rate of 50 mV/s. (a) glucosylated benzylated curcumin, (b) glucosylated methylated curcumin, (c) galactosylated monocarbonyl curcumin, (d) galactosylated-methylated curcumin, and (e) galactosylated-benzylated curcumin.	190
Figure 6.1 Interaction of (A) LPS antagonists of varying chain lengths (a) C4, (b) C6, (c) C8, (d) C10, (e) C12, (B) LPS, and (C) AM12 with GUVs.	204
Figure 6.2. a) DLS analysis of lipid vesicles with filters of varying pore size b) AFM image after vesicle fusion c) QCM-D analysis of vesicle fusion	206
Figure 6.3 a) freshly cleaved mica surface b) 1,2-Dipalmitoyl-sn-glycero-3- phosphoethanolamine (DPPE) monolayer formation c) after incubation with LPS	207
Figure 6.4 Structure of thiolated β -cyclodextrin and its attachment on the electrode's surface	208
Figure 6.5 Comparison of typical cyclic voltammetry scans of 100 μM acetaminophen on bare and modified NPG	210
Figure 6.6 Cyclic voltammetry scans at selected acetaminophen concentrations on modified NPG electrode	210
Figure 6.7 Comparison of peak current and concentration trend in (a) unmodified and (b) modified NPG	211

List of the Tables

Table 1. Distribution of ligament width and inter-ligament distance of varying alloy compositions. The evaluation was done after completion of the multistep synthesis involving electrochemical dealloying, annealing, and chemical dealloying.	102
Table 2. Distribution of ligament width and inter-ligament distance for the hierarchical bimodal structure where alloy composition was Au ₁₀ :Ag ₉₀ . The evaluation was done after completion of the multistep synthesis involving electrochemical dealloying, annealing, and chemical dealloying.	103
Table 3. Calculation of the roughness factor (R_f) and electrochemically active surface area (ECSA) of the final structure formed from varying Au:Ag alloy composition. The charge under the reduction peak seen in CV was evaluated for all the different compositions. The 10:90 composition formed the hb-NPG structure with the highest roughness factor.	105
Table 4. TGA and reductive desorption data showing surface coverage for Lipoic acidSAMs on NPG and hb-NPG. The data presented is compared with previously reported values.	108
Table 5. Number of immobilized protein molecules on NPG and hb-NPG. Data depicted as average (3 measurements)	113
Table 6. Voltammetric parameters and surface coverage (per geometric area) values. Data depicted as average (3 measurements) \pm std dev.	116
Table 4.1 Degradation (%) of curcumin and curcuminoid during a period of 2h in PBS buffer (pH 7.4)	160
Table 4.2 Solubility of curcumin and curcuminoid in PBS buffer (pH 7.4)	162
Table 4.3 Comparing the dissociation constants for glycocurcuminoids used in this work	168
Table 5.1 Binding affinity data of glycocurcuminoids with membrane proteins-ACE2 and RBD	189

Chapter I INTRODUCTION

1.1 Overview

Our investigations' main objective was to create electrodes with surface modifications for measuring protein-protein, protein-drug, and lectin-glycoprotein binding interactions. Various electrode materials, including hb-NPG, ITO, and Au-based QCM sensor, were used in our analysis. The binding affinities have been examined using a variety of electroanalytical techniques. Sensors designed in the study can monitor even the smallest change in analyte levels and assess if the binding is strong enough. The platforms have enormous potential for disease diagnosis and determining a good drug candidate.

The key principles used in the research are introduced in Chapter I. It has been discussed how the field of nanobiotechnology will develop in the future. The components of biosensors and their expanding influence on the healthcare system have also been described. To comprehend the study discussed in the next chapters, it is essential to understand how to modify the surfaces of nanomaterials and use them to detect analytes utilizing electrochemical methods. Chapter II goes into detail about the materials and methods used in this study. In Chapter III, the fabrication of hb-NPG and its application in studying the glycoprotein-lectin interaction utilizing SWV are discussed along with the results. The findings and discussion of the binding affinities of AM12 and other LPS antagonists with sepsis-related protein receptors are covered in Chapter IV. In Chapter V, the potential inhibitory action of curcumin analogs against the binding of RBD and ACE2 is presented, and in Chapter VI, a compilation of all the other brief experiments

conducted while pursuing the main objectives of the research is presented.

1.2 Nanobiotechnology-Importance and scope

Integrating different scientific disciplines so that their shortcomings are overcome by one another suggests promising outcomes. Biotechnology has achieved significant advancements during the past few decades. In recent years, nanobiotechnology—which combines biotechnology and nanomaterials—has advanced significantly.¹ Researchers can create less labor-intensive, more economical, and effective procedures by combining nanotechnology and biotechnology methodologies.² Lynn W. Jelinski, a biophysicist at Cornell University in the United States, coined the phrase "nanobiotechnology" initially. A promising field called nanobiotechnology brings together nanofabrication and biosystems for the mutual benefit of both.³ When it comes to nanobiotechnology, biology offers models and biologically constructed components as sources of inspiration, while nanotechnology offers instruments and technological platforms for the investigation and modification of biological systems. As a result of nanobiotechnology, new classes of micro- and nanofabricated devices and machines that are motivated by bio-structured machines have been developed.⁴⁻⁶ Nanobiotechnology has grown in prominence in the fields of gene therapy, tissue engineering, medication delivery, cancer immunotherapy, and wound healing.⁷ To fill the gap between the two fields of science, there is a constant need for novel materials and methods. To expand the uses of nanobiotechnology in health, numerous innovative and promising technologies, and procedures for the creation of nanomaterials are being developed through chemical modification, biological

reduction, and scaffolding. Biosensor development has been aided by nanobiotechnology in various ways. In fabricated devices, the fusion of biomaterials and nanomaterials can produce unseen functions. To create new devices, a variety of biomaterials have been used, including metalloproteins, antibodies, enzymes, DNA, RNA, ribozymes, and aptamers.⁸ The development of biosensing devices has benefited from the expansion of the use of biomaterials made possible by the advent of nanotechnology. Nanotechnology offers nanopatterns, nanostructures, and nanoscale electrodes. The electrode platform can be created using nanopatterns.⁹ Also, nanotechnology produces synthesized nanomaterials including topological insulators, quantum dots (QDs), graphene, gold nanoparticles (AuNPs), silver nanoparticles, and carbon nanotubes (CNTs).¹⁰⁻
¹¹ Biomaterials can be mixed with the produced nanomaterial to improve their electrical characteristics or add new functionality. Nanobiotechnology has enormous potential for disease diagnosis, treatment, and prevention; however, more thorough research is required to address potential clinical trial challenges, regulatory issues, and toxicity in order to advance medical science and healthcare in the future.¹²

Modern analytical chemistry relies heavily on nanobiosensors, but they are also an important area of multidisciplinary study that connects the fundamentals of basic science with those of bio/nanotechnology and electronics.¹³ It is crucial to understand how the five main components of the biosensor function before learning about the basics of the nanobiosensor.¹⁴

1.3 Biosensors

A biosensor is a device that detects the presence of an analyte in a biological or chemical reaction and produces signals corresponding to the concentration of the analyte.¹⁵ Leland C. Clark Jr. developed the first "true" biosensor in 1956 for the purpose of detecting oxygen. He is regarded as the "father of biosensors," and the oxygen electrode he created, the "Clark electrode," is named after him. In 1962, Leland Clark performed a demonstration of an amperometric enzyme electrode for the detection of glucose using the fabricated biosensor.¹⁶ Every biosensor possesses a set of both static and dynamic characteristics. Selectivity, repeatability, stability, sensitivity, and linearity are a few characteristics that affect how well a biosensor performs.¹⁵

Biosensors typically consist of three major parts comprising of a signal processing system, a physicochemical detector or transducer, and a biological sensing component.¹⁷ In order to interact with the target analyte and produce a signal, biological sensing components are used. Materials like tissues, bacteria, organelles, cell receptors, enzymes, antibodies, and nucleic acids are frequently used as sensing elements. The transducer converts the signal produced by the interaction of the sensing element and the target analyte into a quantifiable and detectable electrical signal. Therefore, the signal processing system amplifies the electrical signal before sending it to a data processor, which creates a signal that can be measured.¹⁸⁻¹⁹ In recent years, the field of biosensor development has experienced spectacular expansion, with new applications appearing in a variety of areas. These encompass disease detection, food safety, defense, and environmental

monitoring.

The focus of our study will be the discipline of medical science, where applications for biosensors are expanding quickly. Applications like cancer diagnosis and monitoring, cardiovascular disease monitoring, and diabetes management have profited from the development of biosensors.²⁰ In the field of medicine, biosensors can be used to track the growth of cancer, identify microorganisms, and monitor blood glucose levels in diabetics. Emerging biosensor technology may play a key role in the early detection of fatal diseases and the efficient administration of treatment.²¹ Biosensors can identify the presence of an abnormality in its early stages and provide information on whether treatment is successful in lowering or eliminating such problems by monitoring levels of certain proteins expressed and/or secreted by cells.²⁰

Several sensitive biosensors for the detection of various biomarkers in complicated biological fluids have been developed and implemented in the medical area using ligand-receptor interactions (LRIs), which are the basis for all biological processes occurring in live cells. Drug- target interactions, one of the LRIs, are crucial to comprehending the biological mechanisms that help in the future development of novel and improved therapeutic compounds. We can determine whether it is necessary to modify currently available medications or to generate new ones using biosensors based on these interactions.²² Numerous cell adhesion, signaling, and regulatory activities are triggered by ligand interactions with membrane proteins. Membrane proteins are significant therapeutic targets because of their wide range of functions.²³ A crucial part of the cell membrane,

carbohydrates are specifically recognized by molecules like proteins.²⁴ The interactions between carbohydrates and proteins are crucial for biological processes such as cell adhesion, cell trafficking, cell communication, and immunological responses.²⁵ The elucidation of intercellular signaling pathways would be aided by a greater comprehension of carbohydrate-protein interactions, perhaps resulting in the development of new diagnostic and therapeutic tools.²⁶⁻²⁷ Due to the importance of detecting carbohydrate-protein interactions, new, effective biosensing techniques are needed for quick and accurate recognition testing.

1.4 Surface modification

The abundance and significance of numerous detecting processes that take place at interfaces have heightened attention in the design of chemically modified interfaces in recent years.²⁸ Self-assembled monolayers (SAMs) are used as an interface layer between a metal surface and a solution²⁹ or vapor.³⁰ SAMs made from organosulfur compounds chemisorbed at metals have gained popularity in recent years because of their potential applications in a wide range of technical fields, in addition to the fact that they make excellent interface models.³¹ Metals like gold, copper, and silver are used as substrates for the SAMs preparation based on organosulfur species as they strongly coordinate onto these metals. Due to its resistance to the majority of contaminant adsorption and oxide production, gold is primarily used as a substrate to build monolayers.³² SAM technology produces the best outcomes of all the reported immobilization techniques.³³ SAMs can provide a very convenient and flexible technique for the covalent immobilization of biomolecules on gold surfaces for the construction of biosensors because of their

stability, orientation, and capacity to functionalize the terminal groups on the molecules.³⁴⁻³⁵ Because it contains sulfur, LA has drawn a lot of interest in the field of gold surface functionalization for a variety of reasons, including the expectation that its longer alkyl chain will produce a more disordered SAM than a straightforward mercaptoalkyl tether and that disulphide attachment to gold surfaces will increase stability. To connect lipids, carbohydrates, proteins, and oligonucleotides to gold surfaces, LA has been used as a linker.³⁶

The advantages of SAMs are their orderly compact arrangement, high substrate coverage, and few defects. Forming an Au-thiol self-assembled monolayer (SAM) with a bi-functional linker molecule that has a thiol group at one end and a chemically reactive group at the other end (functionalization) for covalent bonding of biomolecular probes is the "gold standard" for biomolecule immobilization.³⁷⁻³⁸ An ideal, SAM of alkanethiolates supported on a gold surface with a (111) texture is shown in Figure 1.

The SAM's structure and characteristics are emphasized.

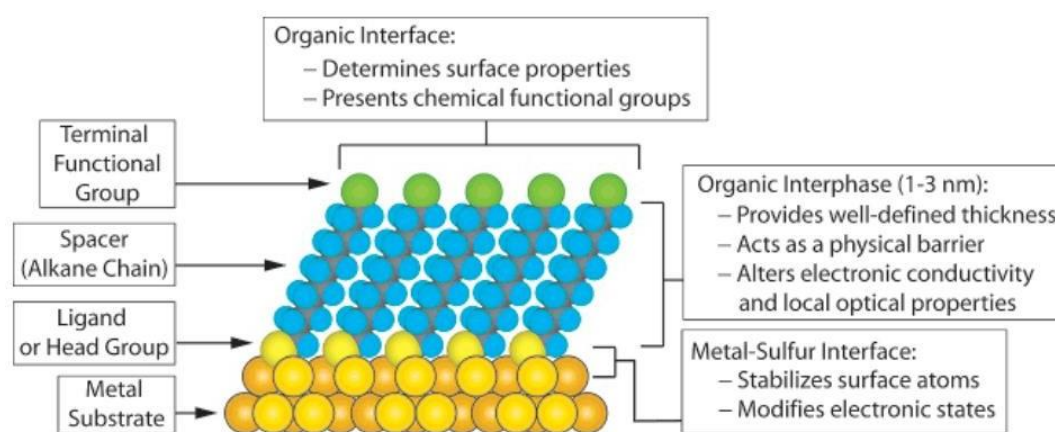


Figure 1. SAMs as components of nanoscience and nanotechnology. Reproduced from reference 37.

Biological molecules' amino (carboxyl) groups can be connected to the carboxyl (amino) groups at the end of a SAM using a coupling agent, which creates ideal circumstances for immobilization.³⁹ In the development of biosensors, self-assembled monolayers (SAMs) and 1-Ethyl-3-(3-dimethylaminopropyl)carbodiimide/N-hydroxysuccinimide (EDC/NHS) have frequently been utilized to form covalent amide bonds between solid substrate and bio-recognition components.⁴⁰⁻⁴¹ Three stages are normally required for the covalent immobilization of bio-recognition components on a solid surface: attaching SAMs to an inert surface, subsequent surface activation by EDC/NHS to create an active layer, and covalent attachment of biomolecules such as proteins, carbohydrates, antibodies, etc.⁴² In the coupling chemistry of EDC-NHS, EDC combines with a carboxylic acid group on the SAM (depicted by the spheres bearing the number 1) to produce an amine-reactive intermediate called O-acyl isourea. This intermediate could interact with an amine on a biomolecule (depicted by the spheres bearing the number 2), resulting in a conjugate of the two molecules connected by a strong amide bond. The amine-reactive intermediate is stabilized by the addition of sulfo-NHS by becoming an amine-reactive sulfo-NHS ester, improving the effectiveness of EDC-mediated coupling processes (Figure 2).⁴³ The EDC/NHS reaction will significantly affect the stable modification of the bio-recognition elements required to obtain good reproducibility when developing biosensors, but the conditions during these immobilization processes involving the reaction time, the concentration ratio of reagents, and the composition in the buffer solution should be optimized for the adsorption of SAMs.⁴⁴⁻⁴⁵

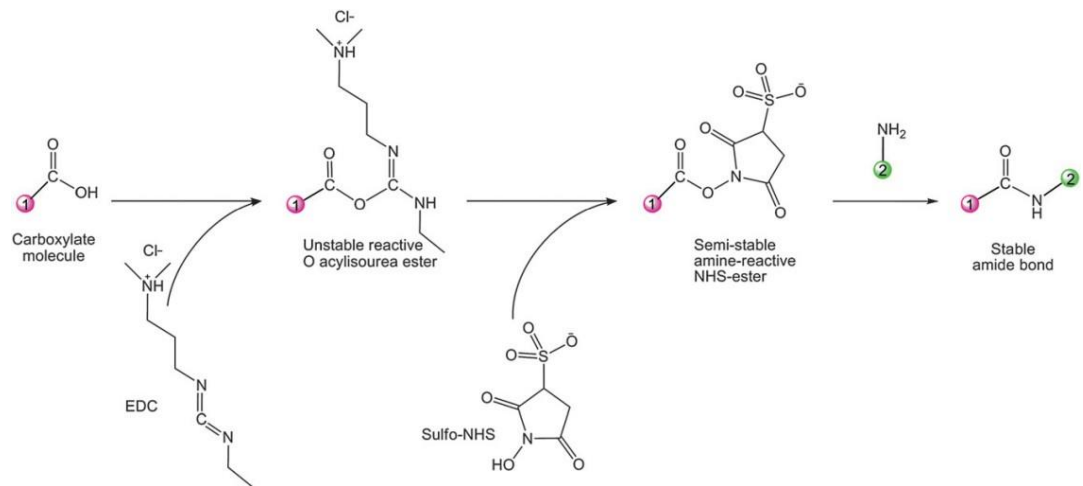


Figure 2. EDC-NHS coupling chemistry mechanism. Reproduced from reference 43.

Thin films made of bio-inspired polymers are frequently used as reactive coatings to immobilize biomolecules on a variety of surfaces. For instance, the synthetic polymer polydopamine (PDA) was created as a thin film by the spontaneous oxidative polymerization of dopamine.⁴⁶⁻⁴⁸ Due to its adaptability to numerous substrates, good biocompatibility, and chemical reactivity, PDA has garnered considerable interest for biological and biomedical applications since its development.⁴⁹⁻⁵¹ Because of its active quinone group, which may covalently conjugate to nucleophilic amine in biomolecules via Schiff's base formation or Michael addition, it has been widely employed as a universal reactive coating for protein/DNA attachment. In neutral solution, these reactions happen on their own without the requirement for an extra reagent or activation step. Additionally, PDA's active quinone group is stable, making it a particularly practical technique to prepare many surfaces for protein attachment (Figure 3).⁵²⁻⁵³

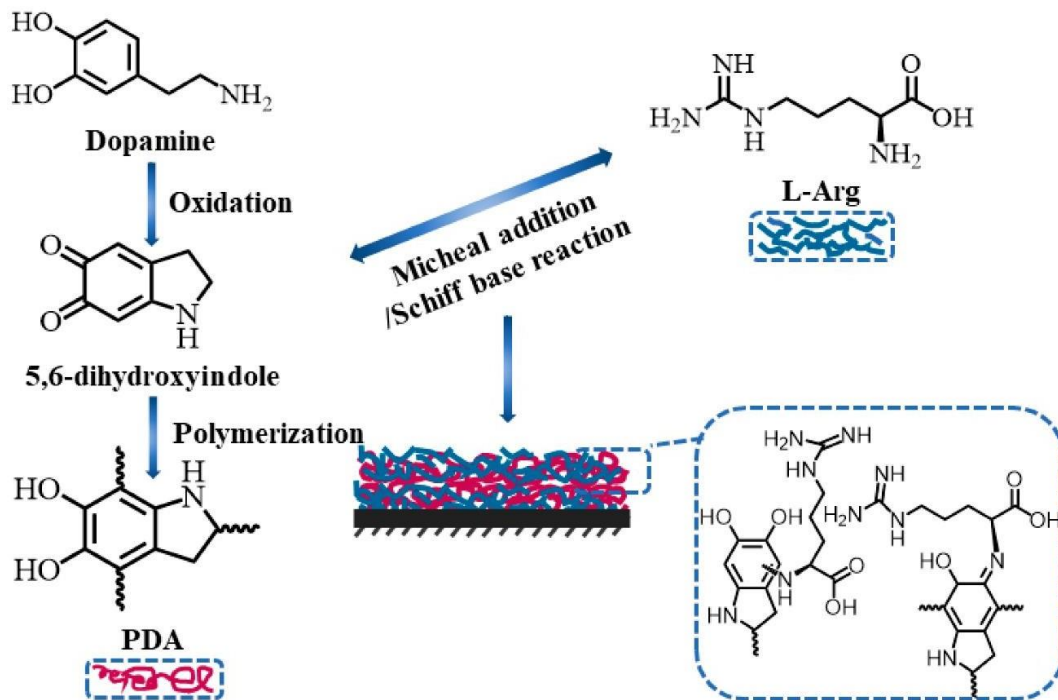


Figure 3. The immobilization of L-Arg in the PDA coating. Reproduced from reference 53.

1.5 Transduction elements

Biosensor transduction element is influenced by the material utilized, sensor device characteristics, and the actual signal conversion process. The materials used in transducers can be categorized as inorganic, organic, conductor, biological molecule, insulator, and semiconductor. The capabilities of the active sensing material dominate the definition of the transducer's parameters, but the device's design also has a significant impact on the specifications.⁵⁴ Different transduction units used in the study are porous gold substrate, Au-QCM sensor, and ITO coated glass.

Gold electrodes are among the most common electrochemical biosensor substrate materials because they can easily be functionalized with thiolated biomolecules. The increased surface area and sensitivity of NPG electrodes, however, make them more responsive than planar gold electrodes.⁵⁵⁻⁵⁶ As a mesh barrier against electrode fouling agents while allowing tiny analytes of interest to access the sensor, NPG electrodes also display anti-biofouling capabilities.⁵⁷⁻⁵⁸ NPG electrodes have been utilized to create immuno, enzymatic, small molecule, and DNA sensors, illustrating the range of biosensor applications for these materials.⁵⁹

The QCM is potentially the most used mass-based biosensor transduction component. Due to their sensitive mass detection capabilities and the ability to observe binding events in real time, QCM-based biosensors are an alternative to standard analytical techniques. On both sides of quartz crystal sensors, there is a thin

layer of a metal that acts as an electrode.⁶⁰⁻⁶¹ The sensor is coupled to an oscillator circuit, which causes the quartz crystal to vibrate at a specific frequency. A broad transverse wave is created, and it moves parallel to the quartz surface. The surface of the crystal is often covered with a particular receptor material that interacts with the target analyte to raise the rigid mass of the crystal. As a result, the crystal's fundamental resonance frequency changes, and this sensor signal can be utilized to precisely calculate the adsorbed mass on the crystal surface.⁶²

Considering the geometrical and physical characteristics of quartz crystal, the Sauerbrey equation, which is shown in equation (1), has been utilized to convert frequency to mass. This equation demonstrates the linear relationship between the quartz crystal's resonance frequency and the additional mass of the solid layer that is applied to the surface.⁶³

$$\Delta F = -\frac{2f^2}{A\sqrt{\rho\mu}}\Delta m \quad (1)$$

Here, f , μ , ρ , Δm , and A represents the crystal's fundamental resonance frequency, shear modulus (=2.947 1011 g/cm. s²), quartz density ($\rho = 2.648$ g/cm³), surface mass loading, and gold disk area, respectively. The mass increase per unit of area (ng cm⁻²) is represented by the unit $\Delta m/A$ and the frequency variation is represented as ΔF .⁶³

ITO coated onto glass is the most popular ceramic electrode among sensor matrices because of its superior electrical conductivity, wide operating window (0.4 –1.9 V), high substrate adhesion capability, low capacitive current, consistent electrochemical and physical characteristics, and optical clarity.⁶⁴⁻⁶⁵ In order to anchor biomolecules, ITO has been increasingly employed in biosensors using silanization which involves forming a covalently bound SAM layer on a hydroxyl surface using silane molecules such as 3-aminopropyltriethoxysilane (APTES) to anchor biomolecules.⁶⁴ ITO is a material that holds promise for biosensing technology.

1.6 Sensing techniques-General overview and principle

1.6 a) ***Electrochemical Impedance Spectroscopy (EIS)***: This technique which is frequently used in corrosion studies, semiconductor science, energy conversion and storage technologies, chemical sensing and biosensing, noninvasive diagnostics, etc., provides kinetic and mechanistic data of diverse electrochemical systems. EIS is based on the perturbation of an electrochemical system that is in equilibrium or in a steady state by applying a sinusoidal signal (ac current or voltage) over a broad frequency range and observing the sinusoidal response of the system (current or voltage, respectively) to the applied perturbation.⁶⁶ EIS provides the capacity to investigate inherent material characteristics or particular processes that might affect an electrochemical system's conductance, resistance, or capacitance. The difference between impedance and resistance is that the resistance in DC circuits directly follows Ohm's Law. The impedance response is measured using a modest signal stimulation. The current response to a sinusoidal potential is a sinusoid at the

applied frequency, whereas the electrochemical cell response is pseudo-linear in that a phase-shift is acquired.⁶⁷⁻⁶⁸ As a result, equation (2) illustrates the excitation signal as a function of time:

$$E_t = E_0 \sin(\omega t) \quad (2)$$

where E_0 is the signal's amplitude, E_t is the potential at time t , and ω is its radial frequency. Equation (3) is used to determine the relationship between the applied frequency (f) and the radial frequency (ω):⁶⁷

$$\omega = 2 \cdot \pi \cdot f \quad (3)$$

Equation (4) states that in a linear system, the signal is amplitude- and phase-shifted (ϕ) from I_0 .

$$I_t = I_0 \sin(\omega t + \phi) \quad (4)$$

Thus, equation (5) may be used to determine the impedance of the entire system:

$$Z = E/I = Z_0 \exp(i\phi) = Z_0 (\cos \phi + i \sin \phi) \quad (5)$$

Here, Z , E , I , ω , and ϕ stand for impedance, potential, current, frequency, and phase shift between E and I , respectively. The impedance is expressed in terms of a magnitude, Z_0 , and a phase shift, ϕ .⁶⁷ EIS is available in both faradic and non-faradic forms. In our investigation, faradaic EIS, which produces impedance when redox reactions occur, was applied. In order to concentrate on the R_{ct} fluctuations between the solution and the electrode interface, EIS measurements were carried out in Faradaic mode utilizing electrochemical redox probes (electron mediators). We employed ferro/ferricyanide as our usual redox probe.⁶⁹

Electrical circuits with electrical components (resistors, capacitors, and inductors) are used to mimic and compute electrochemical processes connected to the

electrolyte/interface and redox reactions. To comprehend and assess the many elements of the EIS system, an electric circuit was created and put into use.⁷⁰ The Randles equivalent circuits simplify the Warburg resistance (Z_w), charge transfer resistance (R_{ct}), resistance of the solution (R_s), and double layer capacitance at the electrode surface (C_{dl}). At electrode-electrolyte contact, a diffusion process produces Warburg resistance.⁷⁰ EIS is illustrated using Nyquist plots, where the real component of the impedance (Z_{real}) is plotted on the X-axis and the imaginary component of the impedance (Z_{imag}) is plotted on the Y-axis. The Z_{imag} is negative, whereas each point on the Nyquist plot represents an impedance value at a certain frequency. Low frequency impedance is conducted on the right side of the plot along the X-axis, whereas higher frequency impedances are formed on the left. ⁷¹⁻⁷² Randles equivalent electrical circuit over a broad frequency range is shown in Figure 4.

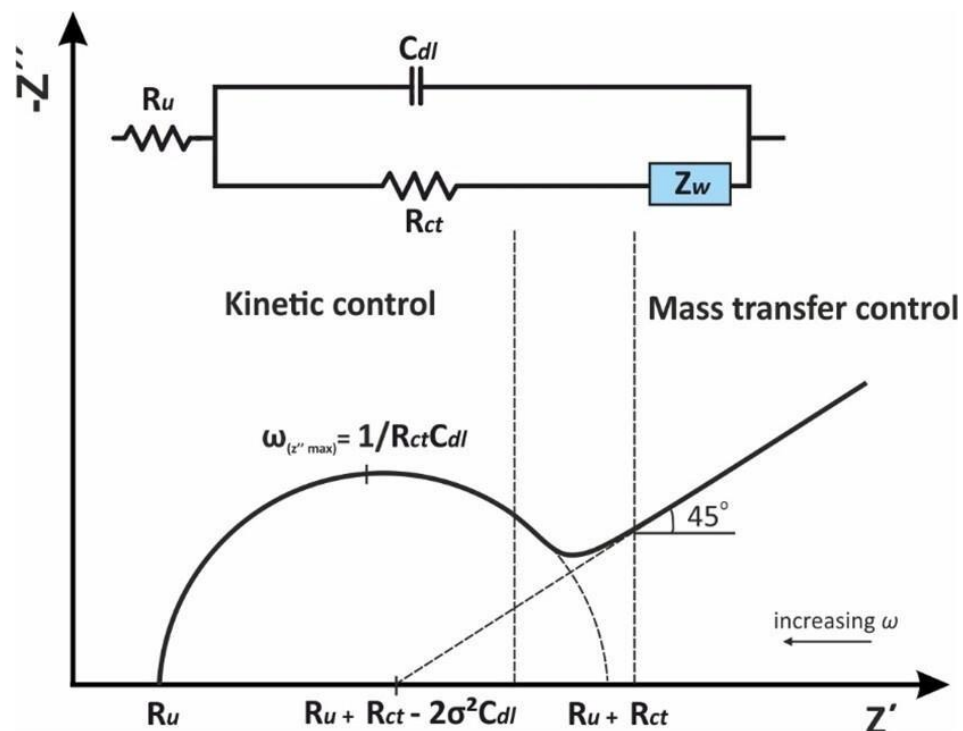


Figure 4. Randles equivalent electrical circuit over a broad frequency range.

Reproduced from reference 66.

The components of the equivalent circuit are determined by fitting the parameters of the equivalent circuit to best match the data in the Nyquist plot. To analyze surface features from fitting the electrical circuit simulation, the EIS curve, which is the most crucial datum, must first be produced.⁷⁰ The electrode matrix (i.e., composition of the working electrode) and the electrochemical reactions occurring either at the surface of the working electrode or in the bulk solution determine the shape of a Nyquist plot. A Bode plot, which is highly popular in the engineering world in contrast to the Nyquist plot and consists of two independent logarithmic plots: magnitude vs. frequency and phase vs. frequency, is another approach to present the impedance measurements.⁷⁰ EIS is a crucial approach for comprehending the interfacial characteristics connected to specific bio-recognition events, such as the antigen-antibody capture that takes place at the sensor surface. The kinetic binding of the receptor and analyte at the sensors surface produces a difference in the electrical signal in EIS-biosensors.⁷³ The amount of bound molecules is then reflected by a change in the electron transfer/charge transfer resistance. As a result, the EIS biosensors allow for the direct determination of biomolecular recognition actions.⁷⁴ The use of EIS biosensors has expanded dramatically because of its easy manipulation, quick reaction, ability to be miniaturized, and readiness for lab-on-a-chip integration with affordable and real-time monitoring to detect very low concentrations.⁷⁵⁻⁷⁶

1.6 b) **Square Wave Voltammetry (SWV)**: To eliminate capacitive effects from the response and reduce detection limits, pulsed voltammetric techniques are a frequent strategy to increase detection sensitivity in electroanalysis.⁷⁷ Due to its ability to perform analyses more quickly than other pulse techniques like differential pulse voltammetry or normal pulse voltammetry, SWV, which was first developed by Kalousek and Barker,⁷⁸ is especially popular. The most typical application of SWV is to improve electroanalytical current signals of a target redox analyte.⁷⁹ SWV produces a voltammetric linear sweep by superimposing a square wave potential pulse waveform on a stair step (Figure 5a). SWV's standard current sampling method minimizes non-Faradaic contributions (such as charging currents) by considering the current response during the second half of the potential pulse.⁸⁰ The forward and reverse current samples are extracted from the forward and reverse pulses, and the difference between them is used to represent the current- voltage curve (Figure 5b). This further minimizes any charging current that may still be present and amplifies the peak current to produce square wave voltammetric data with great sensitivity.⁸¹⁻⁸²

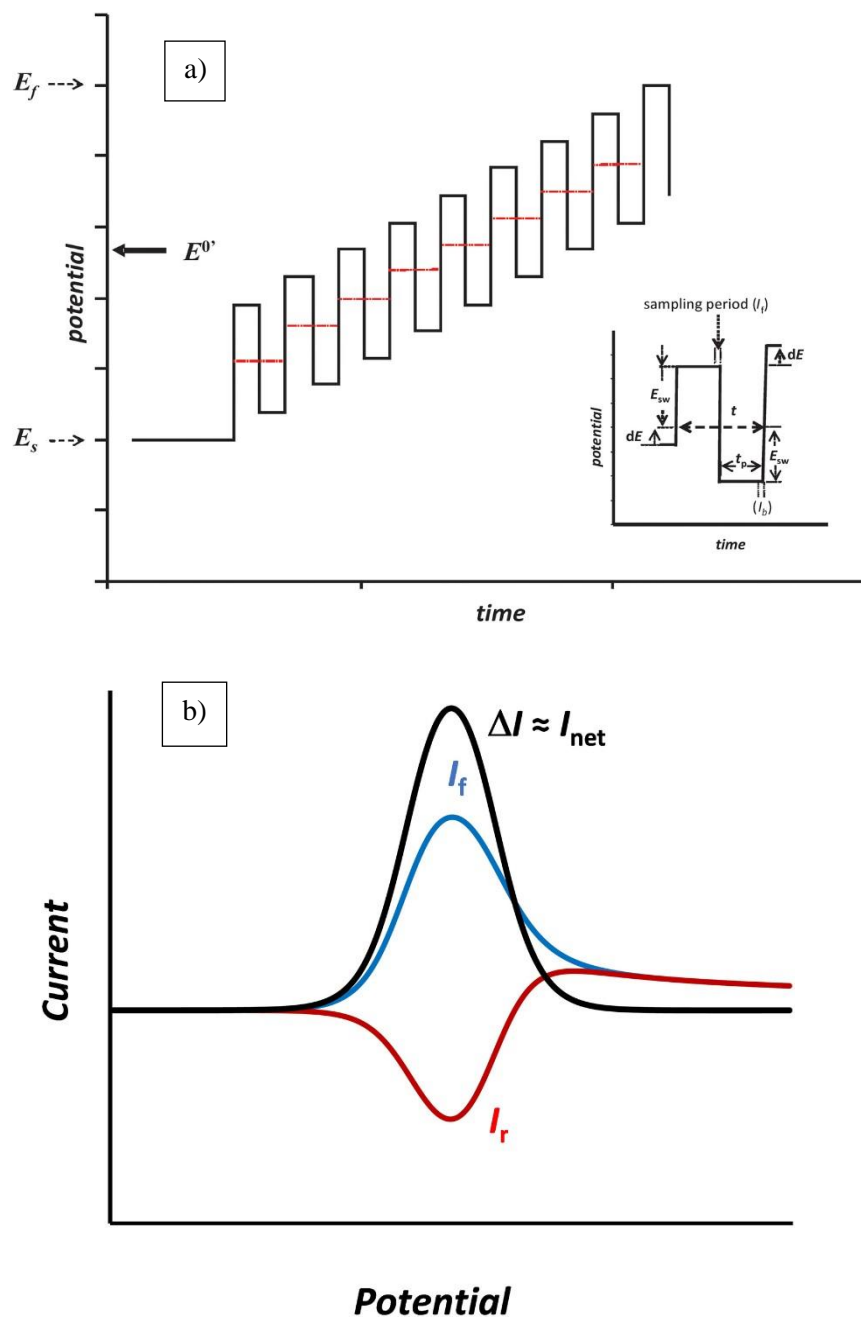


Figure 5. Schematic showing the square-wave voltammetry potential shape. A single SW cycle and the procedure for measuring the current in SWV are shown in the inset. Square-wave voltammogram showing the transport of electrons between a working electrode and a water- soluble redox analyte (forward, backward, and net current components). Reproduced from reference 82.

SWV is a great option for sensitive analyte determination because of its potent discrimination capabilities against both background and charging currents. SWV has found applications in the study of mechanisms despite being developed and utilized largely for electroanalytical purposes.⁸³⁻⁸⁴ Furthermore, access to the thermodynamic and kinetic characteristics of diverse electrode reactions is made possible by the technique's robust theoretical foundation. Numerous kinetic methods based on the analysis of the net-peak height, its half-peakwidth or peak potential, as well as the relative positioning of the forward and backward voltammetric components have been developed because of the abundance of data obtained from the differential and experimentally measured forward and backward voltammetric components.⁸⁵⁻⁸⁶

1.6 c) ***Fluorescence spectroscopy***: One of the most practical and effective methods for the efficient and trustworthy investigation of protein-ligand interactions is fluorescence spectroscopy.⁸⁷ Electronic transitions in molecules with conjugated bonds are the source of fluorescence. A fluorophore that has been stimulated by a photon may produce fluorescence as it transitions back from an excited singlet electronic state to the ground singlet electronic state. If the energy of the light quantum is equal to the difference in energy levels between the two states, an exciting light beam can cause the transition between two electronic states.⁸⁸ The optical density and quantum yield are both related to the observed fluorescence intensity I_f , which is a wavelength-dependent variable. It is given as equation 6.

$$I_f = I_0 \varphi(1 - 10^{-\varepsilon c l}) \sim 2.303 I_0 \varphi \varepsilon c l \quad (6)$$

where I_0 is the intensity of the excitation light, ε is the molar extinction coefficient at the excitation wavelength, and c is the molar concentration, and l is the optical path length.⁸⁸

The stoichiometry and energetics (affinity and thermodynamics) of binding can be calculated using equilibrium titration methods if a change in the fluorescence properties (such as intensity or anisotropy) occurs along with the binding of two species. Such methods have been widely applied to investigate a variety of protein-ligand interactions in solutions.⁸⁹ In general, whenever a molecule changes in its intrinsic fluorescence (for example, tryptophan in a protein) upon being titrated with a nonfluorescent molecule, the change in fluorescence signal (intensity or anisotropy) is measured as a function of total ligand concentration to calculate the binding affinity between the two.⁹⁰⁻⁹¹

1.7 Impact of the study on healthcare system

1.7 a) ***Osteoporosis***: Glycoproteins, whether soluble or membrane-bound, hold a special place in all our biological systems since they are involved in so many crucial functions. Diseases alter the structure of eukaryotic cells' glycan-adorned cell surfaces. Changes in the glycosylation pattern can be used as a biomarker to determine the presence of a disease.⁹² Proliferation, differentiation, adhesion, and metastasis are examples of cellular activities that are affected by changes in either the type or level of glycosylation. It is vital to identify an altered glycosylation pattern on the glycoprotein since it can provide significant insight into the course of the disease and function as a possible biomarker to help with early identification.⁹³⁻

The development of osteophytes, synovial inflammation, cartilage loss, and bone mineral density rise are all symptoms of osteoarthritis (OA), a common cause of morbidity in the elderly population.⁹⁵ Extracellular levels of inorganic phosphate and calcium, as well as levels of mineralization inhibitors that may be expressed systemically or locally, all have an impact on the mineralization of tissues. Serum glycoprotein fetuin-A, also known as α 2-HS, is crucial for the stability and elimination of precursor phases in amorphous minerals.⁹⁶ Fetuin-A serves as a lipid transporter in addition to binding calcium phosphate, which may affect calcification, inflammation, and apoptosis.⁹⁷ Fetuin-A, a 59 kDa protein that is a member of the cystatin family, is mostly made in the liver. Serum fetuin A levels are shown to have an inverse relationship with OA severity in those with knee OA, making it a crucial biomarker for tracking the disease's progression.⁹⁸

Numerous indicators linked to various illnesses can be found through the investigation of protein glycosylation in biological systems. This encourages study into the effectiveness of lectins in figuring out how much a sample is glycosylated. The relevant group of proteins, called lectins, have an affinity for particular carbohydrate structures, and they bind to them.⁹⁹ The specificity and affinity of the lectin-carbohydrate complex are determined by the lectin, whose binding behavior can be highly sensitive to the structure of the carbohydrate or to the orientation of the anomeric substituent (vs anomer or both). In the interaction of lectins with carbohydrates, hydrogen bonds, van der Waals (steric interactions), and hydrophobic forces are mostly present.¹⁰⁰ Creating array-based methods for

screening glycoforms is gaining increasing interest from researchers exploring glycomics. The measurement of protein glycosylation variations in blood samples is now possible thanks to recent advancements in lectin-based antibody microarray and lectin-ELISA techniques.¹⁰¹⁻¹⁰² ELISA is the industry standard for immunoassays, whereas enzyme-linked lectin sorbent assays (ELLA), which use lectins as the glycans' recognition element, are rarely used. Lectins are the preferred recognition components in glycoanalysis while carbohydrate-specific antibodies are less frequently used due to the decreased affinity of the resultant antibodies. Although ELLA are significant techniques for the analysis of glycoforms, they have not been utilized as frequently as ELISA. This is partially due to the weaker carbohydrate-lectin affinities, the complexity of the carbohydrate distribution in biological systems, the lack of a standardized and user-friendly technique, and the high background in traditional ELLA due to the nonspecific adsorption of other proteins that are frequently glycosylated and thereby bind to the lectin.¹⁰³

To solve the issue, our lab has recently devised a rapid and dependable process using electrochemical alloying and dealloying methods to produce hierarchical bimodal nanoporous gold electrodes (hb-NPG) with structural hierarchy. Large specific surface areas for functionalization based on smaller pores and quick transport channels for faster reaction based on considerably larger pores are both present in the design of the hb-NPG. The surface architecture of hb-NPG demonstrated significant potential for the creation of biosensors and enhanced analytical performance by changing the scaling relations between volume and surface area.¹⁰⁴⁻¹⁰⁵

In the present study, SWV-based kinetic ELLA on NPG and hb-NPG are compared as two distinct substrates with different topological features. We also demonstrate that glycoproteins immobilized on NPG and hb-NPG react differently to the binding of a lectin-enzyme conjugate (SNA, Sambucus Nigra bound to alkaline phosphatase), as demonstrated by SWV detection of oxidation of the product p-aminophenol formed when alkaline phosphatase acts on the substrate p-aminophenyl phosphate (p-APP). It has been discovered that sialic acid coupled to galactose or N-acetylgalactosamine can bind to SNA. NeuAc α 2 \rightarrow 6Gal α 1 \rightarrow 4Glc specifically binds to SNA in contrast to monomeric sialic acids.¹⁰⁶ The inclusion of terminal Neu5Ac-Gal/GalNAc sequences is required for high affinity binding of SNA; in particular, N-acetylneuraminic acid linked by 2,6-linkages to galactose or N-acetylgalactosamine bind with remarkable affinity. The current study demonstrates how, compared to the traditional NPG electrode design, hb-NPG offers better sensitivity and specificity towards the electroanalytical detection of glycoprotein-lectin interactions.¹⁰⁷

1.7 b) **Sepsis:** Sepsis is a potentially fatal illness characterized by bacterial infection and a substantial rise in systemic inflammation.¹⁰⁸ A crucial element for bacterial cell integrity, survival, and protection against environmental stress is lipopolysaccharide (LPS). Almost all Gram- negative bacteria retain a significant amount of LPS, which is a potent inducer of inflammatory responses. The immune system and disease susceptibility are directly impacted by LPS because it is continually present in the environment.¹⁰⁹⁻¹¹⁰ It can trigger the host defense system, causing pro-inflammatory processes to be activated, by interacting with proteins

that are either embedded in the membrane or floating freely in the blood. The immune system becomes too engaged when LPS levels are too high, which causes an exaggerated inflammatory response, serious organ damage, and sepsis damage.¹¹¹ With an estimated increase of 11.5%, the cost of treating microbiological sepsis during hospital stays in the United States is among the highest, totalling more than \$20 billion yearly.¹¹²

LPS is composed of three structural components: O-antigen, hydrophilic polysaccharides, and lipophilic lipid A (Figure 6). One of these is the Lipid A region, which has a polyacylated glucosamine disaccharide and is mostly responsible for the toxic activity.¹¹³⁻¹¹⁴

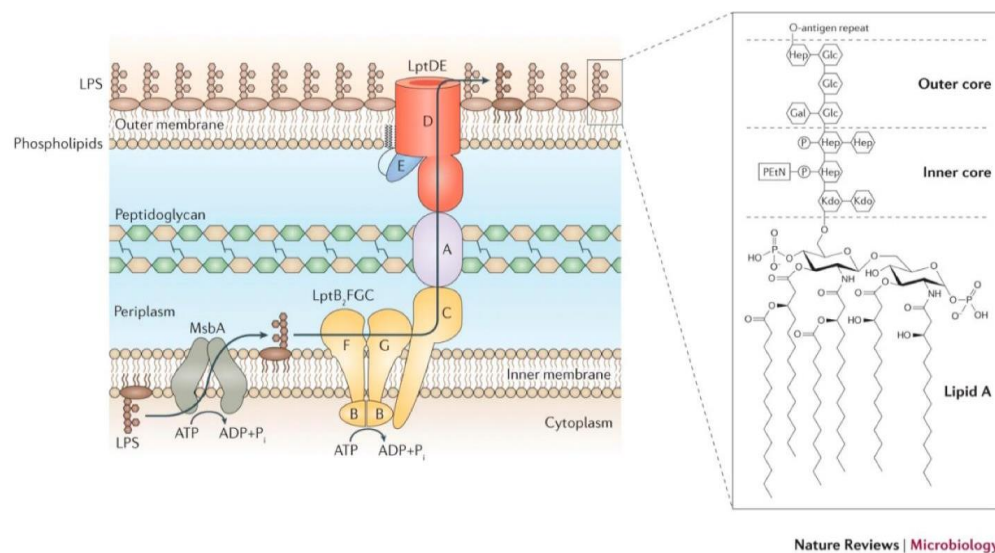


Figure 6. Lipopolysaccharide (LPS) transport pathway in *Escherichia coli*.

Reproduced from reference 114.

To understand the sequential chemical and structural basis of LPS recognition, numerous investigations have been conducted. Lipopolysaccharide aggregates are regularly released by gram-negative bacteria as outer membrane vesicles. For the LPS monomer to be freed from the LPS micelles, LBP and CD14 must work together.¹¹⁵⁻¹¹⁶ To exert its effects, LPS interacts with the plasma LPS-binding protein (LBP), which has a strong affinity for both the Lipid A region of the endotoxin and the glycosylphosphatidyl inositol-anchored LPS receptor CD14 on mononuclear phagocytes. Once the LPS-LBP complex binds with CD14, the Toll-Like Receptor 4 (TLR4) and its co-receptor MD-2 become implicated in complex formation.¹¹⁴ The integral membrane protein TLR4 transmits the LPS signal inside of the cell, and it also initiates the signaling pathways that lead to the production of proinflammatory molecules like the cytokine tumor necrosis factor- α (TNF α) (Figure 7).¹¹⁷⁻¹¹⁸

glucopyranoside core, hydrophobic ether substituents, and an amino acid. It is stable, active, nontoxic, and comparatively simple to use.¹⁰⁸

The 2,3-di-O-alkylated methyl glucoside linked to Fmoc-protected serine via a 6-O-succinoyl bridge is one of the main structural components of AM-12. Significant LPS antagonistic action without toxicity is shown by compound AM-12 (Figure 8). Preliminary research on the relationship between structure and activity revealed vital structural traits that are responsible for the potent antagonist activity and minimal toxicity of these drugs. Extremely lipophilic Fmoc and alkyl (tetradecyl) groups, as well as a free carboxylic acid group, are some of these features.¹¹²

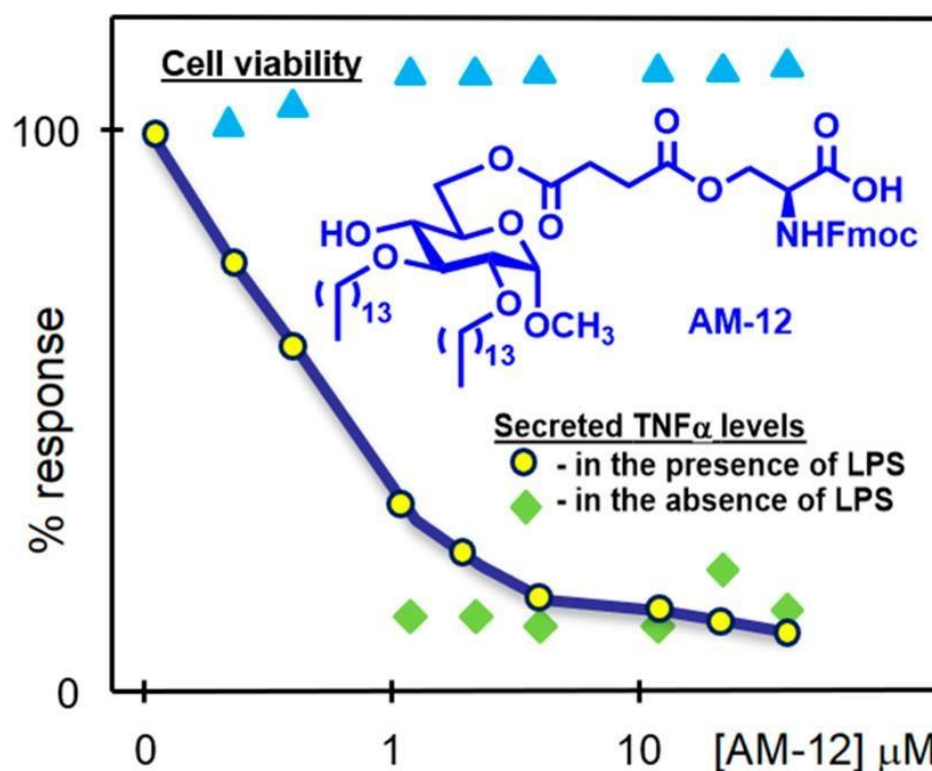


Figure 8. The LPS antagonistic action of compound AM-12 with good cell viability. Reproduced from reference 112.

The possible antibacterial activities of six-membered lactones (δ -lactones) have lately come under investigation. A preliminary analysis of new possible δ -lactone

compounds as antibacterial drug candidates has been done. Regarding the action on bacterial lipopolysaccharide(LPS) in the model strains of Escherichia coli K12 (LPS of different lengths in its structure) and R2-R4 (LPS of different lengths in its structure), special emphasis was placed on the selection of the structure of lactones with the highest biological activity.¹²¹⁻¹²² The components of the bacterial membrane that carry LPS underwent polarity rearrangement as a result of their interaction with lactones.¹²³

A co-receptor for TLR4, MD-2 has recently been discovered to be a target for LPS antagonists and small compounds that can bind to its hydrophobic pocket. The cellular TLR4 signaling pathway induced by LPS can be inhibited by blocking the signaling TLR4 coreceptor, MD-2.¹²⁴ In the past, it has been observed that a number of organic, bioactive herbal components and phytochemicals have therapeutic benefits on sepsis. Patients with sepsis may supplement their diets with phytochemicals that have similar anti-inflammatory effects in an effort to prevent problems from sepsis.¹²⁵

Many studies have documented the therapeutic advantages of plant-derived bioactive chemicals in a range of biological events, including reducing necrotic cell death, modifying cellular antioxidant defense systems, restoring redox equilibrium, and decreasing inflammation.¹²⁶ Several MD-2 inhibitors have been reported so far which includes chalcone derivative, xanthohumol competitively binding with MD-2.¹²⁷ The LPS-induced TLR4 activity has also been demonstrated to be inhibited by natural substances that include 3-(4-hydroxyphenyl) acrylaldehyde in their core structure by blocking MD-2 receptor.¹²⁸ Another bioactive dietary polyphenol

known as curcumin has been utilized for thousands of years in Asian households and is well-known for its cardiovascular, anti-inflammatory, anticancer, and antioxidant properties.¹²⁹ According to molecular docking studies, curcumin, a planar hydrophobic molecule, can fit into the cavity of MD-2, a key protein target for innate immune response suppression. Curcumin may be positioned in the hydrophobic cavity of MD-2 through stable hydrogen bonding interactions with the residues R90 and Y102 of MD-2, according to simulated studies of molecular dynamics (MD). Additionally, experimental evidence supports the idea that these residues play a role in the recognition of curcumin's protein-binding.¹³⁰ Curcumin binds at submicromolar affinity to MD-2 thereby, inhibiting its linkage to LPS.¹³¹ Although curcumin has received a lot of interest recently, its poor stability and low solubility have hampered its potential for use in medicine. Curcumin's poor bioavailability, which restricts the concentration that may be reached in the biological system, is explained by the fact that it degrades quickly in physiological buffer, in the presence of light, and under reducing conditions, according to pharmacokinetic studies.¹³² To mitigate the above limitations researchers are looking into synthesizing new curcumin analogs with good efficacy and reduced toxicity.¹³³ As a symmetrical β -diketone that contains numerous functional groups, curcumin provides a lot of room for structural changes. Numerous research teams have tried to change the structural motif of curcumin by concentrating on the, α,β -unsaturated carbonyls acting as Michael acceptors for nucleophilic additions, altering the side chains of aryl compounds, changing the functionality of active methylene, and producing metal complexes of curcumin.¹³⁴ A bioconjugate of

Luteinizing Hormone Releasing Hormone (LHRH) and curcumin has been prepared by Aggarwal and coworkers by aryl side chain modification, wherein the water soluble conjugate has shown to inhibit cell proliferation.¹³⁵ Ferrari et al. created derivatives of curcumin by glycosylating aromatic rings to increase its solubility in water, kinetic stability, and hence bioavailability. Curcumin derivatives' cytotoxicity toward cisplatin-sensitive and -resistant human ovarian cancer cell lines has been found to be reduced by the binding of glucose to curcumin.¹³⁶ Tetrahydrocurcumin, a double bond reduced derivative of curcumin produced by Wu et al., has been found to inhibit the signaling of phosphatidylinositol 3-kinase/protein kinase B and mitogen-activated protein kinase.¹³⁷ Under mild basic conditions, the diketone moiety can be quickly changed to enolic form, and it is the β -diketone moiety that may be the cause of the rapid metabolic breakdown of curcumin in vivo. As a result, numerous groups are working to create monocarbonyl curcuminoids that nevertheless have biological action.¹³⁸ The methylene group is another active site that causes rapid metabolism of curcumin and removes it from the body. Hence, adding groups on the methylene site has attracted a lot of attention. Figure 9 below is depicting the structural possibilities

for modification of curcumin.¹³³

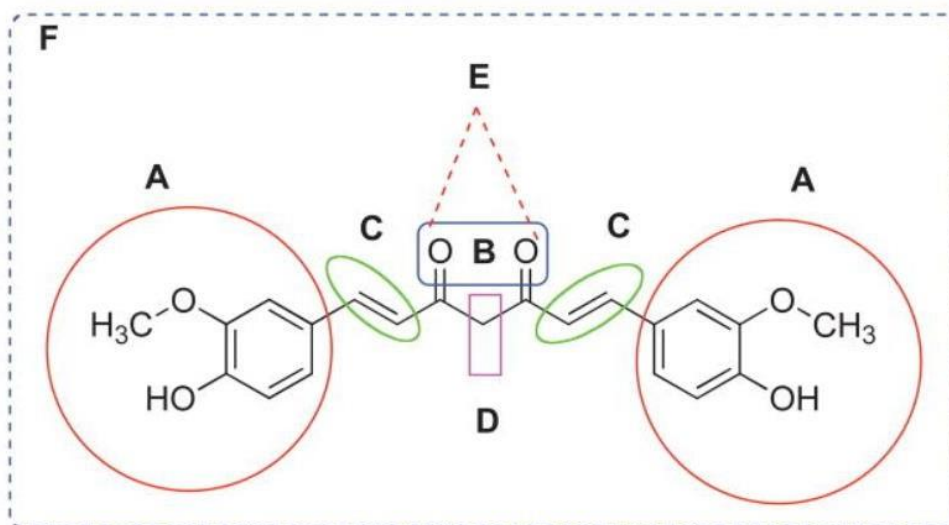


Figure 9. Aryl side chain modification (A), modification of the diketo functionality (B), modification of the double bond (C), modification of the active methylene functionality (D), metal complexes of curcumin (E), and appended curcumin mimics/structural analogs of curcumin (F) are examples of structural modifications that can be made to curcumin. Reproduced from reference 133.

The study of compounds that can block the interaction between protein receptors and LPS may offer new treatment alternatives to treat sepsis. In the current study, we created a surface- modified QCM sensor to measure the binding affinities of certain novel LPS antagonists with protein receptors, such as LBP and CD14, in an effort to look into compounds that block LPS signaling without inducing the inflammatory cascade. Also, we screened the binding efficiency of glyco-curcumin derivatives to the pocket of MD-2 protein. The binding constant was evaluated using fluorescence data. Further, we assessed the stability and solubility of these curcuminoids under physiological conditions.

1.7 c) ***Covid-19***: Acute respiratory tract infections are the most prevalent infections affecting individuals, regardless of age or gender. These illnesses are frequently caused by a wide variety of bacteria and viruses, including *Streptococcus pneumoniae*, *Haemophilus influenzae*, *Moraxella catarrhalis*, Influenza A or B ("the flu"), respiratory syncytial virus (RSV), parainfluenza, adenoviruses, coronaviruses, and others. The most serious infections, however, are frequently associated with coronaviruses, influenza A or B, and RSV, which have been implicated in numerous epidemics and pandemics and have the capacity to spread as well as cause medical catastrophes.¹³⁹ The fast spreading Coronavirus disease-19 (COVID-19), which the World Health Organization labeled a pandemic on March 11, 2020, has recently attracted the interest of the public health community on a global scale. SARS coronavirus-2, the most recent coronavirus species to infect humans, is categorized as a novel beta CoV strain. The virus' genomes resembled SARS-CoV by more than 80%, but unlike SARS, it possesses a novel, risky, and deadly viral infection mechanism, pathophysiology, death rate, and other dangers.¹⁴⁰

The receptor binding stage of viral invasion is crucial. SARS-CoV-2, like SARS-CoV, is able to recognize the host receptor angiotensin converting enzyme 2 (ACE2) through its spike protein. The C-terminal domain of the S protein, often referred to as the receptor-binding domain (RBD), recognizes ACE2 and is essential for establishing the host range.¹⁴¹ The SARS-COV-2 virus's Spike (S1) protein binds readily to host cell membrane receptors like ACE2 and transmembrane serine protease 2 (TMPRSS-2) protein, which facilitates virus

replication (Figure 10). This infection spreads from person to person via aerosolization and rapidly affects the lungs.¹⁴²

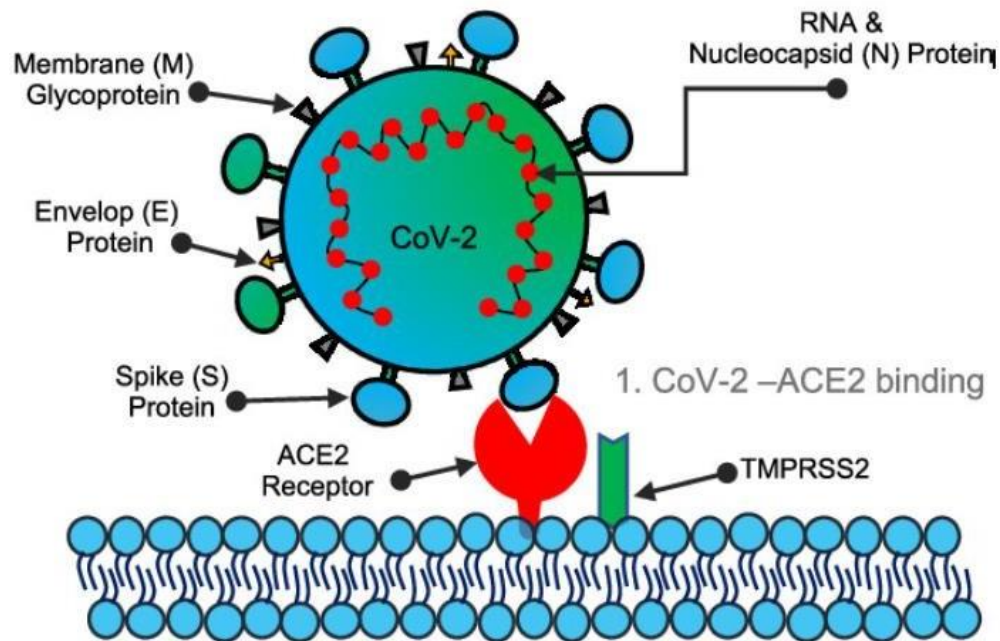


Figure 10. The SARS-CoV-2 structure is displayed along with the viral S protein's attachment to the host's ACE2 receptor. Reproduced from reference 142.

The binding interface is adjacent to the areas of significant glycosylation on the ACE2 receptor and spike proteins, respectively. The importance of glycosylation in binding has been highlighted, even though the interactions between amino acids at the ACE2-spike binding interface have received most of the attention. The extracellular domain of the ACE2 receptor contains multiple O-glycosylation sites (such as T730) and seven N-glycosylation sites (N53, N90, N103, N322, N432, N546, and N690). The only ACE2 glycosylation site whose effects on spike binding

and viral contagiousness have been properly investigated is N90. Previous SARS-CoV research has shown that glycosylation at the N90 position may impair virus binding and infectivity.¹⁴³

From the viral envelop, the spike glycoprotein appears as a clove-shaped homo-trimer. Each monomer consists of two segments, S1 and S2. The contact of the S1 domains from the three trimers results in the formation of the ectodomain of a viral spike, whereas the association of the trimer's S2 domains results in the formation of the spike stalk, transmembrane, and microscopic intracellular domains. The host cell surface receptor is recognized by the S1's receptor-binding domain (RBD), a subdomain. Another S2 cleavage site becomes accessible during virus entry when the RBD binds to the peptidase domain of the ACE2 receptor. The cleavage by host proteases facilitates the fusion of the viral membrane with the host membrane. The RBD is composed of a core domain and an addition called the receptor-binding motif (RBM). A few simple adjustments at the RBM in the instance of SARS-CoV and SARS-CoV2 can drastically alter the binding affinity of RBD to the ACE2. SARS-CoV2 S1 domain binding to human ACE2 has an equilibrium dissociation constant (KD) of 94.6 ± 6.5 nM, whereas SARS-RBD has a KD of 408.7 ± 11.1 nM, according to real-time surface plasmon resonance (SPR) tests.¹⁴⁴⁻¹⁴⁶

According to literature, several medicinal plant extracts and phytochemicals have broad-spectrum antiviral activity since the majority of those antiviral plants contain flavones, polyphenols, and alkaloids. The rapid spread of new, highly contagious viruses, the reappearance of diseases that are challenging to cure due to treatment

resistance, and the simultaneous accessibility of cutting-edge scientific tools have all given rise to an increased interest in the antiviral activity of medicinal plants. According to recent studies, a variety of plants' natural compounds and metabolites have a surprising capacity to block specific SARS-CoV-2 proteins. Phytochemicals are top prospects for the development of antiviral drugs due to their widespread use, affordability, and minimal risk of adverse effects.¹⁴⁷⁻¹⁴⁸ In numerous clinical trials, the phytochemicals quercetin, isoquercetin, and curcumin that are used to treat COVID-19 are being studied. It's interesting to note that a phase 2 clinical trial for a spray formulation of curcumin- based anti-SARS-CoV-2 therapy has been successfully completed. Notably, phytochemicals have a lower bioavailability, are less toxic, and have less adverse effects, hence the best effective dosage is higher.¹⁴⁹

Curcumin has several disadvantages despite having potential as an antiviral. Only 1% of the injected curcumin is absorbed by the body; the remainder is essentially undetectable in the target tissues. At physiological pH, curcumin is also unstable and degrades into several ineffective metabolites. The exceedingly encouraging in vitro results with curcumin have been impeded clinically by these limitations.¹⁵⁰⁻¹⁵¹ Our research is investigating the usage of glyco-curcuminoids to overcome these challenges. The curcumin analogs preserve the specific chemical skeleton of curcumin that is responsible for its biological efficacy while also enhancing its biological activity, solubility, and/or stability.

In the current study, we evaluated the ability of glyco-curcumin derivatives to bind to the membrane proteins ACE2 and RBD. We created surface-modified

ITO which served as the working electrode in our electrochemical setup for the EIS measurements. In our investigation, membrane proteins like ACE2 and RBD were immobilized on the PDA modified ITO to conduct electrochemical measurements. Using electrochemical impedance spectroscopy data (EIS) data, the binding constant was assessed.

References

1. Roco, M. C.; Bainbridge, W. S., Overview converging technologies for improving human performance: Nanotechnology, biotechnology, information technology, and cognitive science (NBIC). In *Converging technologies for improving human performance: Nanotechnology, biotechnology, information technology and cognitive science*, Springer: 2003; pp 1-27.
2. Ishikawa, M.; Biju, V., Chapter 2 - Luminescent Quantum Dots, Making Invisibles Visible in Bioimaging. In *Progress in Molecular Biology and Translational Science*, Villaverde, A., Ed. Academic Press: 2011; Vol. 104, pp 53-99.
3. Priyanka, P.; Kumar, D.; Yadav, A.; Yadav, K., Nanobiotechnology and its Application in Agriculture and Food Production. 2020; pp 105-134.
4. Fortina, P.; Kricka, L. J.; Surrey, S.; Grodzinski, P., Nanobiotechnology: the promise and reality of new approaches to molecular recognition. *Trends in biotechnology* **2005**, *23* (4), 168- 73.
5. Lowe, C. R., Nanobiotechnology: the fabrication and applications of chemical and biological nanostructures. *Current opinion in structural biology* **2000**, *10* (4), 428-34.
6. Bohr, M. T., Nanotechnology goals and challenges for electronic applications. *IEEE Transactions on Nanotechnology* **2002**, *1* (1), 56-62.
7. Saritha, G. N. G.; Anju, T.; Kumar, A., Nanotechnology - Big impact: How nanotechnology is changing the future of agriculture? *Journal of Agriculture and Food Research* **2022**, *10*, 100457.
8. Min, J.; Lee, T.; Oh, S.-M.; Kim, H.; Choi, J.-W., Electrochemical biomemory device consisting of recombinant protein molecules. *Biotechnology and Bioprocess Engineering* **2010**, *15*, 30-39.
9. Yagati, A. K.; Lee, T.; Min, J.; Choi, J.-W., A robust nanoscale biomemory device composed of recombinant azurin on hexagonally packed Au-nano array. *Biosensors and Bioelectronics* **2013**, *40* (1), 283-290.
10. Yoon, J.; Shin, M.; Lee, T.; Choi, J.-W., Highly sensitive biosensors based on biomolecules and functional nanomaterials depending on the types of nanomaterials: A perspective review. *Materials* **2020**, *13* (2), 299.
11. Zhang, A.; Lieber, C. M., Nano-bioelectronics. *Chemical reviews* **2016**, *116* (1), 215-257.
12. Kaur, K.; Thombre, R., Chapter 1 - Nanobiotechnology: methods, applications, and future prospects. In *Nanobiotechnology*, Ghosh, S.; Webster, T. J., Eds. Elsevier: 2021; pp 1-20.
13. Bhalla, P.; Singh, N., Generalized Drude scattering rate from the memory function formalism: an independent verification of the Sharapov-Carbotte result. *The European Physical Journal B* **2016**, *89*, 1-8.
14. Baryeh, K.; Takalkar, S.; Lund, M.; Liu, G., Introduction to medical biosensors for point of care applications. In *Medical biosensors for point of care (POC) applications*, Elsevier: 2017; pp 3-25.
15. Bhalla, N.; Jolly, P.; Formisano, N.; Estrela, P., Introduction to biosensors.

- Essays in biochemistry* **2016**, 60 (1), 1-8.
16. Heineman, W. R.; Jensen, W. B., Leland c. clark jr.(1918–2005). *Biosensors and Bioelectronics* **2006**, 21 (8), 1403-1404.
17. Malhotra, S.; Verma, A.; Tyagi, N.; Kumar, V., Biosensors: principle, types and applications. *Int. J. Adv. Res. Innov. Ideas Educ* **2017**, 3 (2), 3639-3644.
18. Malik, P.; Katyial, V.; Malik, V.; Asatkar, A.; Inwati, G.; Mukherjee, T. K., Nanobiosensors: concepts and variations. *International Scholarly Research Notices* **2013**, 2013.
19. Grieshaber, D.; MacKenzie, R.; Vörös, J.; Reimhult, E., Electrochemical biosensors-sensor principles and architectures. *Sensors* **2008**, 8 (3), 1400-1458.
20. Tothill, I. E. In *Biosensors for cancer markers diagnosis*, Seminars in cell & developmental biology, Elsevier: 2009; pp 55-62.
21. Bohunicky, B.; Mousa, S. A., Biosensors: the new wave in cancer diagnosis. *Nanotechnology, science and applications* **2010**, 1-10.
22. Gupta, G.; Jha, K.; Chaudhary, S., Biosensor Assays Types and Their Roles Toward Ligand-Receptor Interactions in Drug Discovery. *Assay and drug development technologies* **2023**, 21 (5), 190-201.
23. Hoffman, T. L.; Canziani, G.; Jia, L.; Rucker, J.; Doms, R. W., A biosensor assay for studying ligand-membrane receptor interactions: binding of antibodies and HIV-1 Env to chemokine receptors. *Proceedings of the National Academy of Sciences of the United States of America* **2000**, 97 (21), 11215-20.
24. Dwek, R. A., Glycobiology: toward understanding the function of sugars. *Chemical reviews* **1996**, 96 (2), 683-720.
25. Varki, A., Glycan-based interactions involving vertebrate sialic-acid-recognizing proteins. *Nature* **2007**, 446 (7139), 1023-1029.
26. Ratner, D. M.; Adams, E. W.; Disney, M. D.; Seeberger, P. H., Tools for glycomics: mapping interactions of carbohydrates in biological systems. *ChemBioChem* **2004**, 5 (10), 1375-1383.
27. Seeberger, P. H.; Werz, D. B., Automated synthesis of oligosaccharides as a basis for drug discovery. *Nature Reviews Drug Discovery* **2005**, 4 (9), 751-763.
28. Bard, A. J.; Abruna, H. D.; Chidsey, C. E.; Faulkner, L. R.; Feldberg, S. W.; Itaya, K.; Majda, M.; Melroy, O.; Murray, R. W., The electrode/electrolyte interface - a status report. *The Journal of Physical Chemistry* **1993**, 97 (28), 7147-7173.
29. Scaramuzzo, F. A.; Salvati, R.; Paci, B.; Generosi, A.; Rossi-Albertini, V.; Latini, A.; Barteri, M., Nanoscale in situ morphological study of proteins immobilized on gold thin films. *The journal of physical chemistry. B* **2009**, 113 (48), 15895-9.
30. Diaconescu, B.; Yang, T.; Berber, S.; Jazdyk, M.; Miller, G. P.; Tománek, D.; Pohl, K., Molecular Self-Assembly of Functionalized Fullerenes on a Metal Surface. *Physical Review Letters* **2009**, 102 (5), 056102.
31. De Luca, G.; Treossi, E.; Liscio, A.; Mativetsky, J. M.; Scolaro, L. M.; Palermo, V.; Samorì, P., Solvent vapour annealing of organic thin films: controlling the self-assembly of functional systems across multiple length scales. *Journal of Materials Chemistry* **2010**, 20 (13), 2493-2498.

32. Walczak, M. M.; Chung, C.; Stole, S. M.; Widrig, C. A.; Porter, M. D., Structure and interfacial properties of spontaneously adsorbed n-alkanethiolate monolayers on evaporated silver surfaces. *Journal of the American Chemical Society* **1991**, *113*, 2370-2378.
33. Biosensors. IntechOpen: Rijeka, 2011.
34. Miura, Y.; Kimura, S.; Kobayashi, S.; Imanishi, Y.; Umemura, J., Cation recognition by self-assembled monolayers of oriented helical peptides having a crown ether unit. *Peptide Science* **2000**, *55* (5), 391-398.
35. Gatto, E.; Stella, L.; Formaggio, F.; Toniolo, C.; Lorenzelli, L.; Venanzi, M., Electroconductive and photocurrent generation properties of self-assembled monolayers formed by functionalized, conformationally-constrained peptides on gold electrodes. *Journal of Peptide Science : an official publication of the European Peptide Society* **2008**, *14* (2), 184-91.
36. Koufaki, M.; Detsi, A.; Kiziridi, C., Multifunctional lipoic acid conjugates. *Current Medicinal Chemistry* **2009**, *16* (35), 4728-42.
37. Love, J. C.; Estroff, L. A.; Kriebel, J. K.; Nuzzo, R. G.; Whitesides, G. M., Self-assembled monolayers of thiolates on metals as a form of nanotechnology. *Chemical Reviews* **2005**, *105* (4), 1103-1170.
38. Vericat, C.; Vela, M.; Benitez, G.; Carro, P.; Salvarezza, R., Self-assembled monolayers of thiols and dithiols on gold: new challenges for a well-known system. *Chemical Society Reviews* **2010**, *39* (5), 1805-1834.
39. Sam, S.; Touahir, L.; Salvador Andres, J.; Allongue, P.; Chazalviel, J.-N.; Gouget-Laemmel, A.; Henry de Villeneuve, C.; Moraillon, A.; Ozanam, F.; Gabouze, N., Semiquantitative study of the EDC/NHS activation of acid terminal groups at modified porous silicon surfaces. *Langmuir* **2010**, *26* (2), 809-814.
40. Chen, Y.; Yang, Y.; Tu, Y., An electrochemical impedimetric immunosensor for ultrasensitive determination of ketamine hydrochloride. *Sensors and Actuators B: Chemical* **2013**, *183*, 150-156.
41. Sharma, R.; Deacon, S. E.; Nowak, D.; George, S. E.; Szymonik, M. P.; Tang, A. A. S.; Tomlinson, D. C.; Davies, A. G.; McPherson, M. J.; Wälti, C., Label-free electrochemical impedance biosensor to detect human interleukin-8 in serum with sub-pg/ml sensitivity. *Biosensors & Bioelectronics* **2016**, *80*, 607-613.
42. Xiao, S.-J.; Brunner, S.; Wieland, M., Reactions of Surface Amines with Heterobifunctional Cross-Linkers Bearing Both Succinimidyl Ester and Maleimide for Grafting Biomolecules. *The Journal of Physical Chemistry B* **2004**, *108* (42), 16508-16517.
43. Bart, J.; Tiggelaar, R.; Yang, M.; Schlautmann, S.; Zuilhof, H.; Gardeniers, H., Room-temperature intermediate layer bonding for microfluidic devices. *Lab on a chip* **2009**, *9*, 3481-8.
44. Hou, Y.-H.; Wang, J.-J.; Jiang, Y.-Z.; Lv, C.; Xia, L.; Hong, S.-L.; Lin, M.; Lin, Y.; Zhang, Z.-L.; Pang, D.-W., A colorimetric and electrochemical immunosensor for point-of-care detection of enterovirus 71. *Biosensors and Bioelectronics* **2018**, *99*, 186-192.
45. Saleem, W.; Salinas, C.; Watkins, B.; Garvey, G.; Sharma, A. C.; Ghosh, R., Antibody functionalized graphene biosensor for label-free electrochemical immunosensing of fibrinogen, an indicator of trauma induced coagulopathy. *Biosensors & Bioelectronics* **2016**, *86*, 522-529.

46. Lee, H.; Rho, J.; Messersmith, P. B., Facile Conjugation of Biomolecules onto Surfaces via Mussel Adhesive Protein Inspired Coatings. *Advanced materials (Deerfield Beach, Fla.)* **2009**, *21* (4), 431-434.
47. Lee, H.; Dellatore, S. M.; Miller, W. M.; Messersmith, P. B., Mussel-inspired surface chemistry for multifunctional coatings. *Science (New York, N.Y.)* **2007**, *318* (5849), 426-30.
48. Zhao, L.; Chen, D.; Hu, W., Patterning of Metal Films on Arbitrary Substrates by Using Polydopamine as a UV-Sensitive Catalytic Layer for Electroless Deposition. *Langmuir* **2016**, *32*(21), 5285-5290.
49. Sun, K.; Xie, Y.; Ye, D.; Zhao, Y.; Cui, Y.; Long, F.; Zhang, W.; Jiang, X., Mussel-inspired anchoring for patterning cells using polydopamine. *Langmuir* **2012**, *28* (4), 2131-6.
50. Hu, W.; He, G.; Zhang, H.; Wu, X.; Li, J.; Zhao, Z.; Qiao, Y.; Lu, Z.; Liu, Y.; Li, C. M., Polydopamine-functionalization of graphene oxide to enable dual signal amplification for sensitive surface plasmon resonance imaging detection of biomarker. *Analytical chemistry* **2014**, *86* (9), 4488-93.
51. Chen, D.; Zhao, L.; Hu, W., Protein immobilization and fluorescence quenching on polydopamine thin films. *Journal of colloid and interface science* **2016**, *477*, 123-30.
52. Zhang, Y.; Geng, X.; Ai, J.; Gao, Q.; Qi, H.; Zhang, C., Signal Amplification Detection of DNA using a Sensor Fabricated by One-step Covalent Immobilization of Amino-terminated Probe DNA onto the Polydopamine-modified Screen-printed Carbon Electrode. *Sensors and Actuators B: Chemical* **2015**, *221*.
53. Gui, Y.; Ji, B.; Yi, G.; Li, X.; Zhang, K.; Fu, Q., Polydopamine-Assisted Rapid One-Step Immobilization of L-Arginine in Capillary as Immobilized Chiral Ligands for Enantioseparation of Dansyl Amino Acids by Chiral Ligand Exchange Capillary Electrochromatography. *Molecules (Basel, Switzerland)* **2021**, *26* (6), 1800.
54. Polat, E. O.; Cetin, M. M.; Tabak, A. F.; Bilget Güven, E.; Uysal, B. Ö.; Arsan, T.; Kabbani, A.; Hamed, H.; Gül, S. B., Transducer Technologies for Biosensors and Their Wearable Applications. *Biosensors* **2022**, *12* (6), 385.
55. Bhattarai, J. K.; Neupane, D.; Nepal, B.; Mikhaylov, V.; Demchenko, A. V.; Stine, K. J., Preparation, modification, characterization, and biosensing application of nanoporous gold using electrochemical techniques. *Nanomaterials* **2018**, *8* (3), 171.
56. Collinson, M. M., Nanoporous gold electrodes and their applications in analytical chemistry. *International Scholarly Research Notices* **2013**, *2013*.
57. Daggumati, P.; Matharu, Z.; Wang, L.; Seker, E., Biofouling-resilient nanoporous gold electrodes for DNA sensing. *Analytical chemistry* **2015**, *87* (17), 8618-8622.
58. Saraf, S.; Neal, C. J.; Park, S.; Das, S.; Barkam, S.; Cho, H. J.; Seal, S., Electrochemical study of nanoporous gold revealing anti-biofouling properties. *Rsc Advances* **2015**, *5* (58), 46501-46508.
59. Quan, X.; Fischer, L. M.; Boisen, A.; Tenje, M., Development of nanoporous gold electrodes for electrochemical applications. *Microelectronic*

Engineering **2011**, 88 (8), 2379-2382.

60. Santoro, K.; Ricciardi, C., Biosensors. In *Encyclopedia of Food and Health*, Caballero, B.; Finglas, P. M.; Toldrá, F., Eds. Academic Press: Oxford, 2016; pp 430-436.
61. Idili, A.; Montón, H.; Medina-Sánchez, M.; Ibarlucea, B.; Cuniberti, G.; Schmidt, O. G.; Plaxco, K. W.; Parolo, C., Chapter Eleven - Continuous monitoring of molecular biomarkers in microfluidic devices. In *Progress in Molecular Biology and Translational Science*, Pandya, A.; Singh, V., Eds. Academic Press: 2022; Vol. 187, pp 295-333.
62. Höök, F.; Kasemo, B.; Nylander, T.; Fant, C.; Sott, K.; Elwing, H., Variations in coupled water, viscoelastic properties, and film thickness of a Mefp-1 protein film during adsorption and cross-linking: a quartz crystal microbalance with dissipation monitoring, ellipsometry, and surface plasmon resonance study. *Analytical chemistry* **2001**, 73 (24), 5796-5804.
63. Sauerbrey, G., Verwendung von Schwingquarzen zur Wägung dünner Schichten und zur Mikrowägung. *Zeitschrift für physik* **1959**, 155, 206-222.
64. Aydın, E. B.; Sezgintürk, M. K., Indium tin oxide (ITO): A promising material in biosensing technology. *TrAC Trends in Analytical Chemistry* **2017**, 97, 309-315.
65. Yang, L.; Li, Y., AFM and impedance spectroscopy characterization of the immobilization of antibodies on indium-tin oxide electrode through self-assembled monolayer of epoxysilane and their capture of Escherichia coli O157: H7. *Biosensors and Bioelectronics* **2005**, 20 (7), 1407-1416.
66. Lazanas, A. C.; Prodromidis, M. I., Electrochemical Impedance Spectroscopy—A Tutorial. *ACS Measurement Science Au* **2023**, 3 (3), 162-193.
67. Bahadır, E. B.; Sezgintürk, M. K., A review on impedimetric biosensors. *Artificial cells, nanomedicine, and biotechnology* **2016**, 44 (1), 248-262.
68. Benavente, J., Recent Advances in Multidisciplinary Applied Physics. **2005**.
69. Magar, H. S.; Hassan, R. Y. A.; Mulchandani, A., Electrochemical Impedance Spectroscopy (EIS): Principles, Construction, and Biosensing Applications. *Sensors (Basel, Switzerland)* **2021**, 21 (19).
70. Wang, S.; Zhang, J.; Gharbi, O.; Vivier, V.; Gao, M.; Orazem, M. E., Electrochemical impedance spectroscopy. *Nature Reviews Methods Primers* **2021**, 1 (1), 41.
71. Ha, L. D.; Park, K.; Chang, B.-Y.; Hwang, S., Implementation of second-generation fourier transform electrochemical impedance spectroscopy with commercial potentiostat and application to time-resolved electrochemical impedance spectroscopy. *Analytical chemistry* **2019**, 91 (22), 14208-14213.
72. Katz, E.; Willner, I., Probing biomolecular interactions at conductive and semiconductive surfaces by impedance spectroscopy: routes to impedimetric immunosensors, DNA-sensors, and enzyme biosensors. *Electroanalysis: An International Journal Devoted to Fundamental and Practical Aspects of Electroanalysis* **2003**, 15 (11), 913-947.
73. Anusha, T.; Bhavani, K. S.; Kumar, J. S.; Brahman, P. K.; Hassan, R. Y., Fabrication of electrochemical immunosensor based on GCN- β -CD/Au

- nanocomposite for the monitoring of vitamin D deficiency. *Bioelectrochemistry* **2022**, *143*, 107935.
74. Kim, D. C.; Kang, D. J., Molecular recognition and specific interactions for biosensing applications. *Sensors* **2008**, *8* (10), 6605-6641.
 75. Millner, P.; Caygill, R.; Conroy, D.; Shahidan, M., Biosensors for Medical Applications. Elsevier Amsterdam, The Netherlands:: 2012.
 76. Manickam, A.; Chevalier, A.; McDermott, M.; Ellington, A. D.; Hassibi, A., A CMOS electrochemical impedance spectroscopy (EIS) biosensor array. *IEEE Transactions on Biomedical Circuits and Systems* **2010**, *4* (6), 379-390.
 77. Osteryoung, J. G.; Schreiner, M. M., Recent advances in pulse voltammetry. *CRCCritical Reviews in Analytical Chemistry* **1988**, *19* (sup1), S1-S27.
 78. Barker, G. C.; Gardner, A. W., Forty years of square-wave polarography. *Analyst* **1992**, *117*(12), 1811-1828.
 79. Mirceski, V.; Skrzypek, S.; Stojanov, L., Square-wave voltammetry. *ChemTexts* **2018**, *4*.
 80. Mirceski, V.; Gulaboski, R.; Lovric, M.; Bogeski, I.; Kappl, R.; Hoth, M., Square-wave voltammetry: a review on the recent progress. *Electroanalysis* **2013**, *25* (11), 2411-2422.
 81. Osteryoung, J. G.; Osteryoung, R. A., Square wave voltammetry. *Analytical chemistry* **1985**, *57* (1), 101-110.
 82. Gulaboski, R.; Mirceski, V., Calculating of square-wave voltammograms—a practical on-line simulation platform. *Journal of Solid State Electrochemistry* **2023**.
 83. Chen, H.; Kätelhön, E.; Compton, R. G., Machine learning in fundamental electrochemistry: Recent advances and future opportunities. *Current Opinion in Electrochemistry* **2023**, 101214.
 84. Gulaboski, R.; Mirceski, V., Square-wave voltammetry of two-step diffusional electrode mechanism coupled with a reversible follow-up chemical reaction. *Journal of Solid State Electrochemistry* **2021**, *25* (12), 2893-2901.
 85. Mirceski, V.; Laborda, E.; Guziejewski, D.; Compton, R. G., New approach to electrode kinetic measurements in square-wave voltammetry: amplitude-based quasireversible maximum. *Analytical chemistry* **2013**, *85* (11), 5586-5594.
 86. Mirceski, V.; Stojanov, L.; Ogorevc, B., Step potential as a diagnostic tool in square-wave voltammetry of quasi-reversible electrochemical processes. *Electrochimica Acta* **2019**, *327*, 134997.
 87. Shahzad, A.; Köhler, G.; Knapp, M.; Gaubitzer, E.; Puchinger, M.; Edetsberger, M., Emerging applications of fluorescence spectroscopy in medical microbiology field. *Journal of translational medicine* **2009**, *7*, 99.
 88. Mocz, G.; Ross, J. A., Fluorescence techniques in analysis of protein-ligand interactions. *Methods in molecular biology (Clifton, N.J.)* **2013**, *1008*, 169-210.
 89. Rossi, A. M.; Taylor, C. W., Analysis of protein-ligand interactions by fluorescence polarization. *Nature protocols* **2011**, *6* (3), 365-87.
 90. Dillingham, M. S.; Tibbles, K. L.; Hunter, J. L.; Bell, J. C.; Kowalczykowski, S. C.; Webb, M. R., Fluorescent single-stranded DNA binding

- protein as a probe for sensitive, real-time assays of helicase activity. *Biophysical Journal* **2008**, *95* (7), 3330-3339.
91. Sridharan, R.; Zuber, J.; Connelly, S. M.; Mathew, E.; Dumont, M. E., Fluorescent approaches for understanding interactions of ligands with G protein coupled receptors. *Biochimica et Biophysica Acta (BBA) - Biomembranes* **2014**, *1838* (1, Part A), 15-33.
 92. Dube, D. H.; Bertozzi, C. R., Glycans in cancer and inflammation — potential for therapeutics and diagnostics. *Nature Reviews Drug Discovery* **2005**, *4* (6), 477-488.
 93. Thomas, D.; Rathinavel, A. K.; Radhakrishnan, P., Altered glycosylation in cancer: A promising target for biomarkers and therapeutics. *Biochimica et Biophysica Acta. Reviews on Cancer* **2021**, *1875* (1), 188464.
 94. Qiu, Y.; Patwa, T. H.; Xu, L.; Shedden, K.; Misek, D. E.; Tuck, M.; Jin, G.; Ruffin, M. T.; Turgeon, D. K.; Synal, S.; Bresalier, R.; Marcon, N.; Brenner, D. E.; Lubman, D. M., Plasmaglycoprotein profiling for colorectal cancer biomarker identification by lectin glycoarray and lectin blot. *J Proteome Res* **2008**, *7* (4), 1693-1703.
 95. Couchourel, D.; Aubry, I.; Delalandre, A.; Lavigne, M.; Martel-Pelletier, J.; Pelletier, J.P.; Lajeunesse, D., Altered mineralization of human osteoarthritic osteoblasts is attributable to abnormal type I collagen production. *Arthritis and Rheumatism* **2009**, *60* (5), 1438-50.
 96. Schinke, T.; Amendt, C.; Trindl, A.; Pöschke, O.; Müller-Esterl, W.; Jahnen-Dechent, W., The serum protein alpha2-HS glycoprotein/fetuin inhibits apatite formation in vitro and in mineralizing calvaria cells. A possible role in mineralization and calcium homeostasis. *The Journal of biological chemistry* **1996**, *271* (34), 20789-96.
 97. Brylka, L.; Jahnen-Dechent, W., The role of fetuin-A in physiological and pathological mineralization. *Calcified tissue international* **2013**, *93* (4), 355-64.
 98. Xiao, J.; Wang, X. R.; Hu, K. Z.; Li, M. Q.; Chen, J. W.; Ma, T.; Li, Z. C., Serum fetuin-A levels are inversely associated with clinical severity in patients with primary knee osteoarthritis. *Biomarkers : biochemical indicators of exposure, response, and susceptibility to chemicals* **2013**, *18* (1), 51-4.
 99. Akiba, U.; Anzai, J.-i., Recent Progress in Electrochemical Biosensors for Glycoproteins. *Sensors* **2016**, *16* (12), 2045.
 100. Raposo, C. D.; Canelas, A. B.; Barros, M. T., Human Lectins, Their Carbohydrate Affinities and Where to Find Them. *Biomolecules* **2021**, *11* (2).
 101. Wu, J.; Zhu, J.; Yin, H.; Buckanovich, R. J.; Lubman, D. M., Analysis of glycan variation on glycoproteins from serum by the reverse lectin-based ELISA assay. *J Proteome Res* **2014**, *13* (4), 2197-204.
 102. Blixt, O.; Head, S.; Mondala, T.; Scanlan, C.; Alvarez, R.; Bryan, M. C.; Fazio, F.; Calarese, D.; Stevens, J.; Razi, N.; Die, I.; Burton, D.; Wilson, I. A.; Cummings, R.; Huflejt, M.; Bovin, N.; Wong, C. H.; Paulson, J., *Printed covalent glycan array for ligand profiling of diverse glycan binding proteins*. 2004; p 1072-1072.
 103. Rüdiger, H.; Gabius, H. J., Plant lectins: occurrence, biochemistry,

- functions and applications. *Glycoconjugate journal* **2001**, *18* (8), 589-613.
104. Sondhi, P.; Neupane, D.; Bhattarai, J. K.; Demchenko, A. V.; Stine, K. J., Facile fabrication of hierarchically nanostructured gold electrode for bio-electrochemical applications. *Journal of electroanalytical chemistry (Lausanne, Switzerland)* **2022**, 924.
105. Sondhi, P.; Stine, K. J., Methods to Generate Structurally Hierarchical Architectures in Nanoporous Coinage Metals. *Coatings* **2021**, *11* (12), 1440.
106. Fischer, E.; Brossmer, R., Sialic acid-binding lectins: submolecular specificity and interaction with sialoglycoproteins and tumour cells. *Glycoconjugate journal* **1995**, *12* (5), 707-713.
107. Shibuya, N.; Goldstein, I. J.; Broekaert, W. F.; Nsimba-Lubaki, M.; Peeters, B.; Peumans, W. J., The elderberry (*Sambucus nigra* L.) bark lectin recognizes the Neu5Ac(α 2-6)Gal/GalNAc sequence. *The Journal of biological chemistry* **1987**, *262* (4), 1596-601.
108. Kaeothip, S.; Paranjape, G.; Terrill, S. E.; Bongat, A. F. G.; Udan, M. L. D.; Kamkhachorn, T.; Johnson, H. L.; Nichols, M. R.; Demchenko, A. V., Development of LPS antagonistic therapeutics: synthesis and evaluation of glucopyranoside-spacer-amino acid motifs. *RSC Advances* **2011**, *1* (1), 83-92.
109. Heine, H.; Rietschel, E. T.; Ulmer, A. J., The biology of endotoxin. *Molecular biotechnology* **2001**, *19* (3), 279-96.
110. Uchiyama, T.; Jacobs, D. M., Modulation of immune response by bacterial lipopolysaccharide (LPS): multifocal effects of LPS-induced suppression of the primary antibody response to a T-dependent antigen. *Journal of immunology (Baltimore, Md. : 1950)* **1978**, *121* (6), 2340-6.
111. Virzi, G. M.; Mattiotti, M.; de Cal, M.; Ronco, C.; Zanella, M.; De Rosa, S., Endotoxin in Sepsis: Methods for LPS Detection and the Use of Omics Techniques. *Diagnostics* **2023**, *13* (1), 79.
112. Slater, O.; Dhami, K. B.; Shrestha, G.; Kontoyianni, M.; Nichols, M. R.; Demchenko, A. V., Development of a Simple and Effective Lipid-A Antagonist Based on Computational Prediction. *ACS infectious diseases* **2022**, *8* (6), 1171-1178.
113. Zähringer, U.; Lindner, B.; Rietschel, E. T., Molecular structure of lipid A, the endotoxic center of bacterial lipopolysaccharides. *Advances in carbohydrate chemistry and biochemistry* **1994**, *50*, 211-76.
114. Sondhi, P.; Maruf, M. H. U.; Stine, K. J., Nanomaterials for Biosensing Lipopolysaccharide. *Biosensors* **2020**, *10* (1), 2.
115. Beveridge, T. J., Structures of gram-negative cell walls and their derived membrane vesicles. *Journal of bacteriology* **1999**, *181* (16), 4725-33.
116. Weiss, J.; Barker, J., Diverse pro-inflammatory endotoxin recognition systems of mammalian innate immunity. *F1000Research* **2018**, 7.
117. Jin, M. S.; Lee, J. O., Structures of the toll-like receptor family and its ligand complexes. *Immunity* **2008**, *29* (2), 182-91.
118. Cochet, F.; Peri, F., The Role of Carbohydrates in the Lipopolysaccharide (LPS)/Toll-Like Receptor 4 (TLR4) Signalling. *International journal of molecular sciences* **2017**, *18* (11).

119. Price, N. P.; Jeyaretnam, B.; Carlson, R. W.; Kadrmas, J. L.; Raetz, C. R.; Brozek, K. A., Lipid A biosynthesis in *Rhizobium leguminosarum*: role of a 2-keto-3-deoxyoctulosonate-activated 4' phosphatase. *Proceedings of the National Academy of Sciences of the United States of America* **1995**, *92* (16), 7352-6.
120. Peri, F.; Granucci, F.; Costa, B.; Zanoni, I.; Marinzi, C.; Nicotra, F., Inhibition of lipid astimulated activation of human dendritic cells and macrophages by amino and hydroxylamino monosaccharides. *Angewandte Chemie (International ed. in English)* **2007**, *46* (18), 3308-12.
121. Kowalczyk, P.; Madej, A.; Paprocki, D.; Szymczak, M.; Ostaszewski, R., Coumarin Derivatives as New Toxic Compounds to Selected K12, R1-R4 *E. coli* Strains. *Materials (Basel, Switzerland)* **2020**, *13* (11).
122. Kowalczyk, P.; Gawdzik, B.; Trzepizur, D.; Szymczak, M.; Skiba, G.; Raj, S.; Kramkowski, K.; Lizut, R.; Ostaszewski, R., δ -Lactones—A New Class of Compounds That Are Toxic to *E. coli* K12 and R2–R4 Strains. *Materials* **2021**, *14* (11), 2956.
123. Kamizela, A.; Gawdzik, B.; Urbaniak, M.; Lechowicz, Ł.; Białońska, A.; Kutniewska, S.E.; Gonciarz, W.; Chmiela, M., New γ -Halo- δ -lactones and δ -Hydroxy- γ -lactones with Strong Cytotoxic Activity. *Molecules (Basel, Switzerland)* **2019**, *24* (10).
124. Visintin, A.; Halmen, K. A.; Latz, E.; Monks, B. G.; Golenbock, D. T., Pharmacological inhibition of endotoxin responses is achieved by targeting the TLR4 coreceptor, MD-2. *Journal of immunology (Baltimore, Md. : 1950)* **2005**, *175* (10), 6465-72.
125. Alikiaii, B.; Bagherniya, M.; Askari, G.; Johnston, T. P.; Sahebkar, A., The role of phytochemicals in sepsis: A mechanistic and therapeutic perspective. *BioFactors (Oxford, England)* **2021**, *47* (1), 19-40.
126. Zhao, L.; Lee, J. Y.; Hwang, D. H., Inhibition of pattern recognition receptor-mediated inflammation by bioactive phytochemicals. *Nutrition reviews* **2011**, *69* (6), 310-20.
127. Peluso, M. R.; Miranda, C. L.; Hobbs, D. J.; Proteau, R. R.; Stevens, J. F., Xanthohumol and related prenylated flavonoids inhibit inflammatory cytokine production in LPS-activated THP-1 monocytes: structure-activity relationships and in silico binding to myeloid differentiation protein-2 (MD-2). *Planta medica* **2010**, *76* (14), 1536-43.
128. Roh, E.; Lee, H.-S.; Kwak, J.-A.; Hong, J. T.; Nam, S.-Y.; Jung, S.-H.; Lee, J. Y.; Kim, N. D.; Han, S.-B.; Kim, Y., MD-2 as the target of nonlipid chalcone in the inhibition of endotoxin LPS-induced TLR4 activity. *J Infect Dis* **2011**, *203* (7), 1012-1020.
129. Panaro, M. A.; Corrado, A.; Benameur, T.; Paolo, C. F.; Cici, D.; Porro, C., The Emerging Role of Curcumin in the Modulation of TLR-4 Signaling Pathway: Focus on Neuroprotective and Anti-Rheumatic Properties. *International journal of molecular sciences* **2020**, *21* (7).
130. Wang, Z.; Chen, G.; Chen, L.; Liu, X.; Fu, W.; Zhang, Y.; Li, C.; Liang, G.; Cai, Y., Insights into the binding mode of curcumin to MD-2: studies from molecular docking, molecular dynamics simulations and experimental

- assessments. *Molecular BioSystems* **2015**, *11* (7), 1933- 1938.
131. Cheung, K. L.; Khor, T. O.; Kong, A. N., Synergistic effect of combination of phenethyl isothiocyanate and sulforaphane or curcumin and sulforaphane in the inhibition of inflammation. *Pharmaceutical research* **2009**, *26* (1), 224-31.
132. Khurana, A. L.; Ho, C.-T., High Performance Liquid Chromatographic Analysis of Curcuminoids and Their Photo-oxidative Decomposition Compounds in Curcuma Longa L. *Journal of Liquid Chromatography & Related Technologies* **1988**, *11*, 2295-2304.
133. Vyas, A.; Dandawate, P.; Padhye, S.; Ahmad, A.; Sarkar, F., Perspectives on new synthetic curcumin analogs and their potential anticancer properties. *Current pharmaceutical design* **2013**, *19* (11), 2047-69.
134. Rodrigues, F. C.; Anil Kumar, N. V.; Thakur, G., Developments in the anticancer activity of structurally modified curcumin: An up-to-date review. *European journal of medicinal chemistry* **2019**, *177*, 76-104.
135. Aggarwal, S.; Ndinguri, M. W.; Solipuram, R.; Wakamatsu, N.; Hammer, R. P.; Ingram, D.; Hansel, W., [DLys(6)]-luteinizing hormone releasing hormone-curcumin conjugate inhibits pancreatic cancer cell growth in vitro and in vivo. *International journal of cancer* **2011**, *129* (7), 1611-23.
136. Ferrari, E.; Lazzari, S.; Marverti, G.; Pignedoli, F.; Spagnolo, F.; Saladini, M., Synthesis, cytotoxic and combined cDDP activity of new stable curcumin derivatives. *Bioorganic & medicinal chemistry* **2009**, *17* (8), 3043-52.
137. Wu, J. C.; Lai, C. S.; Badmaev, V.; Nagabhushanam, K.; Ho, C. T.; Pan, M. H., Tetrahydrocurcumin, a major metabolite of curcumin, induced autophagic cell death through coordinative modulation of PI3K/Akt-mTOR and MAPK signaling pathways in human leukemia HL-60 cells. *Molecular nutrition & food research* **2011**, *55* (11), 1646-54.
138. Kumar, P.; Kandi, S. K.; Manohar, S.; Mukhopadhyay, K.; Rawat, D. S., Monocarbonyl Curcuminoids with Improved Stability as Antibacterial Agents against Staphylococcus aureus and Their Mechanistic Studies. *ACS Omega* **2019**, *4* (1), 675-687.
139. Khan, M.; Adil, S. F.; Alkhatlan, H. Z.; Tahir, M. N.; Saif, S.; Khan, M.; Khan, S. T., COVID-19: A Global Challenge with Old History, Epidemiology and Progress So Far. *Molecules (Basel, Switzerland)* **2020**, *26* (1).
140. Nadeem, M. S.; Zamzami, M. A.; Choudhry, H.; Murtaza, B. N.; Kazmi, I.; Ahmad, H.; Shakoori, A. R., Origin, Potential Therapeutic Targets and Treatment for Coronavirus Disease (COVID-19). *Pathogens (Basel, Switzerland)* **2020**, *9* (4).
141. Han, P.; Li, L.; Liu, S.; Wang, Q.; Zhang, D.; Xu, Z.; Han, P.; Li, X.; Peng, Q.; Su, C.; Huang, B.; Li, D.; Zhang, R.; Tian, M.; Fu, L.; Gao, Y.; Zhao, X.; Liu, K.; Qi, J.; Gao, G. F.; Wang, P., Receptor binding and complex structures of human ACE2 to spike RBD from omicron and delta SARS-CoV-2. *Cell* **2022**, *185* (4), 630-640.e10.
142. Chauhan, G.; Madou, M. J.; Kalra, S.; Chopra, V.; Ghosh, D.; Martinez-Chapa, S. O., Nanotechnology for COVID-19: Therapeutics and Vaccine Research. *ACS nano* **2020**, *14* (7), 7760-7782.
143. Mehdipour, A. R.; Hummer, G., Dual nature of human ACE2

- glycosylation in binding to SARS-CoV-2 spike. *Proceedings of the National Academy of Sciences of the United States of America* **2021**, *118* (19).
144. Walls, A. C.; Park, Y. J.; Tortorici, M. A.; Wall, A.; McGuire, A. T.; Veesler, D., Structure, Function, and Antigenicity of the SARS-CoV-2 Spike Glycoprotein. *Cell* **2020**, *181*(2), 281-292.e6.
145. Li, F., Structure, Function, and Evolution of Coronavirus Spike Proteins. *Annual review of virology* **2016**, *3* (1), 237-261.
146. Yan, R.; Zhang, Y.; Li, Y.; Xia, L.; Guo, Y.; Zhou, Q., Structural basis for the recognition of SARS-CoV-2 by full-length human ACE2. *Science (New York, N.Y.)* **2020**, *367*(6485), 1444-1448.
147. Basile, V.; Ferrari, E.; Lazzari, S.; Belluti, S.; Pignedoli, F.; Imbriano, C., Curcumin derivatives: molecular basis of their anti-cancer activity. *Biochemical pharmacology* **2009**, *78*(10), 1305-15.
148. Sardi, J. C. O.; Polaquini, C. R.; Freires, I. A.; Galvão, L. C. C.; Lazarini, J. G.; Torrezan, G. S.; Regasini, L. O.; Rosalen, P. L., Antibacterial activity of diacetylcurcumin against *Staphylococcus aureus* results in decreased biofilm and cellular adhesion. *Journal of medical microbiology* **2017**, *66* (6), 816-824.
149. Chen, T. H.; Tsai, M. J.; Chang, C. S.; Xu, L.; Fu, Y. S.; Weng, C. F., The exploration of phytocompounds theoretically combats SARS-CoV-2 pandemic against virus entry, viral replication and immune evasion. *Journal of infection and public health* **2023**, *16* (1), 42-54.
150. Wang, Y. J.; Pan, M. H.; Cheng, A. L.; Lin, L. I.; Ho, Y. S.; Hsieh, C. Y.; Lin, J. K., Stability of curcumin in buffer solutions and characterization of its degradation products. *Journal of pharmaceutical and biomedical analysis* **1997**, *15* (12), 1867-76.
151. Yang, Y.; Wu, X.; Wei, Z.; Dou, Y.; Zhao, D.; Wang, T.; Bian, D.; Tong, B.; Xia, Y.; Xia, Y.; Dai, Y., Oral curcumin has anti-arthritic efficacy through somatostatin generation via cAMP/PKA and Ca²⁺/CaMKII signaling pathways in the small intestine. *Pharmacological research* **2015**, *95-96*, 71-81.

CHAPTER II: MATERIALS AND METHODS

This chapter will provide a comprehensive list of all the chemicals and reagents used to fabricate and surface-modify the major transduction components used in our work, including the NPG, hbNPG, ITO, and Au coated QCM sensor. A separate section has a list of all the proteins used in our research to examine their absorption capacity on electrodes or their interactions with pharmacological molecules, glycoproteins, etc. The methods section essentially outlines the step-by-step procedure required to build, change the surface of electrodes, prepare varying solutions, and the procedures to characterize the material employed in the study. Without adequate characterization, the study would not be complete, hence the instrumentation section will go overall of the analytical tools employed in this investigation.

2.1 *Materials:* Gold wire (0.2mm diameter, 99.99%) was obtained from Electron Microscopy Sciences (Fort Washington, PA). Alkaline phosphatase labeling kits were purchased from Dojindo Molecular Technologies Inc. (Rockville Maryland). Micro-square Spectrosil quartz fluorometer cell type 3-3.30-Q-3(nominal volume = 0.225 mL) was purchased with an adaptor (FCA3.30) from Starna Cells (Atascadero, CA). Unpolished float glass, 50 x 75 x 0.7 mm, SiO₂ passivated/IndiumTin Oxide coated both surfaces, R_s = 5-15 Ω were purchased from Delta technologies limited (partno. CD-50IN-S207).

Sodium chloride (NaCl), potassium dicyanoargentate (K[Ag(CN)₂]) (99.96%), potassiumdicyanoaurate (K[Au(CN)₂])(99.98%), potassium hexacyanoferrate (II) trihydrate, potassium hexacyanoferrate(III), ethanol (HPLC/spectrophotometric

grade), α -lipoic acid, sodium hydroxide (99.99%), 4-aminophenyl phosphate monosodium salt hydrate, acetonitrile (HPLC grade), N-(3-dimethylaminopropyl)-N'-ethylcarbodiimide hydrochloride (EDC) (>99%), glycine (99%), gold (III) chloride trihydrate, silver nitrate, dextran from *Leuconostoc mesenteroides* (average Mr = 60,000- 76,000), 11-mercaptoundecanoic acid (11-MUA), curcumin, DL- dithiothreitol (DTT), HCl, DMSO, acetic acid, potassium chloride (KCl), citric acid anhydrous, and TRIZMA base were purchased from Sigma–Aldrich (St. Louis, MO). Sodium carbonate (enzyme grade, >99%), sulfuric acid (certified ACS plus), nitric acid (trace metal grade), hydrogenperoxide (50%), N-hydroxysuccinimide (NHS, $\geq 97\%$), sulphuric acid, sodium bicarbonate (certified ACS), acetone, isopropyl alcohol, dopamine hydrochloride, (3-aminopropyl) triethoxysilane, (APTES), sodium citrate were all from Fisher Scientific (Pittsburg, PA). Sodium phosphate dibasic (Na_2HPO_4), potassium phosphate monobasic (KH_2PO_4), tribasic sodium citrate dihydrate, sodium acetate anhydrous, and glycine were purchased from Fluka. 6-Ferrocenyl-1- hexanethiol (FcSH) was procured from Dojindo Molecular Technologies, Inc. West Gude Dr. Suite 260, Rockville MD20850. Milli-Q water (18.2M Ω cm at 25°C) was prepared using a Simplicity UV system from Millipore Corporation, Boston, MA, USA.

Peroxidase from horseradish, fetuin from fetal calf serum (lyophilized powder), asialofetuin (type I) from fetal calf serum, bovine serum albumin (BSA) of $\geq 98\%$ purity, SARS- CoV-2 Receptor Binding Domain (SAE-1000-50 μg) and Angiotensin Converting Enzyme-2 (SAE0064-50 μg) were purchased from Sigma-Aldrich (St. Louis, MO). Sambucus Nigra from elderberry bark (SNA, EBL)

unconjugated lectin was obtained from Vector Laboratories. Lipid binding protein (LBP), Cluster of differentiation 14 (CD14), Recombinant human MD2-protein (50 μ g, unconjugated, derived from *E. coli*) were purchased from R&D systems. All chemicals, reagents, and proteins were used as received.

2.2 Instrumentation: The surface morphology, thickness, and the live quantitative colored images of the fabricated electrodes were obtained using ThermoFisher Scientific Apreo 2C scanning electron microscopy equipped with Color SEM technology. Thermogravimetric analysis to estimate the SAM surface coverage was done using a Q500 thermogravimetric analyzer (TA Instruments, DE, USA). The UV–vis spectra and adsorption of proteins onto NPG was studied using a Varian Cary 50 UV–Visible spectrophotometer. A Suprasil quartz spectrophotometer cuvette with a 10mm light path and volume capacity of 1.0 mL (model number 14-385-902C, Fischer Scientific, Pittsburgh, PA, USA) was used for all experiments. Electrodeposition and dealloying were carried out using an EG&G Princeton Applied Research 273A digital potentiostat/galvanostat and the PowerPULSE software. Cyclic voltammetry scans and reductive desorption studies were done using a VersaSTAT 4 potentiostat/galvanostat (Princeton Applied Research, AMETEK Scientific Instruments) and the VersaStudio software.

Square wave voltammetry (SWV) measurements were done using a VersaSTAT 4 potentiostat/galvanostat (Princeton Applied Research, AMETEK Scientific Instruments) and the VersaStudio software. A Beckman Coulter SA-3100 Gas Adsorption Surface Area and Pore Size Analyzer (Beckman Coulter, Inc.

California, USA), with a claimed resolution of $>0.01 \text{ m}^2 \text{ g}^{-1}$, was used to analyze surface area and pore size. The hb-NPG monolith samples were held in place using a typical BET sample holder (3cc RapiTube, model number 7215 006B, Beckman Coulter, Inc. California, USA). Annealing was done using a Barnstead Thermolyne 47900 digital lab furnace (model F47915). QCM-I Mini from MicroVacuum Ltd. (model: eQCM-I-Mini, S/N:43122) equipped with BioSense 3 software, Masterflex Ismatec peristaltic pump (digital 12 roller model), QCM-Ti/Au coated sensors were acquired from Gamry (14 mm in diameter, 5MHz fundamental frequency) were used for all the QCM experiments. Harrick PDC-3XG plasma cleaner/ sterilizer was used to clean and activate the surface of QCM sensors. The stability and solubility studies on glycocurcumin analogs were done using a Varian Cary 50 UV–Visible spectrophotometer. Fluorescence spectra were acquired using a Varian Cary Eclipse Fluorescence Spectrometer (Cary-50).

Harrick PDC-3XG plasma cleaner/ sterilizer was used to clean and activate the surface of ITO plates. The absorbance spectrum of gold nanoparticles in water was measured using a Varian Cary 50 UV–visible spectrophotometer. The surface modification on ITO plate (working electrode) was characterized using ThermoFisher Scientific Apreo 2C scanning electron microscopy. Electrochemical impedance spectroscopy analysis was carried out using a VersaSTAT 4 potentiostat/galvanostat (Princeton Applied Research, AMETEK Scientific Instruments) and the VersaStudio software.

2.3 Fabrication of electrodes

2.3a) Nanoporous gold coated gold wires: Solutions of 50 mM solutions of $\text{K}[\text{Ag}(\text{CN})_2]$ and $\text{K}[\text{Au}(\text{CN})_2]$ in 0.25 M Na_2CO_3 were prepared. The already prepared solutions of $\text{K}[\text{Ag}(\text{CN})_2]$ and $\text{K}[\text{Au}(\text{CN})_2]$ were combined in a volume of 3.5 mL and 1.5 mL, respectively, and then degassed with argon for 10 minutes to create the electrodeposition solution. Using a three-electrode configuration in a glass cell with an $\text{Ag}|\text{AgCl}$ (sat'd. KCl) reference electrode, a platinum wire counter-electrode, and 5 mL of salt solution, electrodeposition was carried out. The working electrode was made of a gold wire that was 5.0 mm long and 0.2 mm in diameter. The $\text{Au}:\text{Ag}$ alloy with a composition of $\text{Au}_{30}\text{Ag}_{70}$ (at.%) was produced by electrodeposition for a period of 10 min at a potential of -1.0 V (vs. $\text{Ag}|\text{AgCl}$ in KCl (sat'd)). The electrodeposited $\text{Au}+\text{Ag}$ alloy-coated gold wire underwent dealloying by being immersed in concentrated nitric acid for 17 hours, followed by a rinse with Milli-Q water and ethanol, giving rise to NPG electrode.¹

2.3b) Hierarchical bimodal nanoporous gold coated gold wires: The sequential use of electrochemical dealloying-annealing-chemical dealloying process was used to create a hierarchical bimodal nanoporous gold structure with two unique ranges of pore size. In 0.25 M Na_2CO_3 , 50 mM solutions of $\text{K}[\text{Ag}(\text{CN})_2]$ and $\text{K}[\text{Au}(\text{CN})_2]$ were created. The solution for electrodeposition was created by mixing 4.5 mL of $\text{K}[\text{Ag}(\text{CN})_2]$ solution with 0.5 mL of $\text{K}[\text{Au}(\text{CN})_2]$ solution, then degassing with argon for 10 minutes. A glass cell containing 5 mL of solution with a three-electrode configuration was used for the electrodeposition process. Ten minutes of

electrodeposition at a potential of -1.0 V (vs. Ag|AgCl in KCl (sat'd.)) produced an alloy of gold and silver with a composition of Au₁₀Ag₉₀ (at.%). Ten minutes of electrochemical dealloying were performed at a voltage of 0.6 V (vs. Ag|AgCl in KCl (sat'd.)) in 1N HNO₃. After the dealloying, the sample underwent a 3-hour annealing process at 600°C. The annealed gold wire was subjected to a second chemical dealloying process after cooling to room temperature, which involved soaking it in concentrated nitric acid for 17 hours before rinsing it with Milli-Q water and ethanol. Also, hierarchical structures were constructed of various alloy compositions, such as Au₁₅Ag₈₅, Au₂₀Ag₈₀, Au₂₅Ag₇₅, and Au₃₀Ag₇₀ (at.%), using a three-step method that involved alloying, partial dealloying, annealing, and chemical dealloying. A separate electrodeposition solution was utilized depending on the desired initial alloy composition. Au₁₅Ag₈₅, Au₂₀Ag₈₀, Au₂₅Ag₇₅, and Au₃₀Ag₇₀ needed the K[Ag(CN)₂] and K[Au(CN)₂] solutions to be combined in the amounts of (4.25 mL + 0.75 mL), (4 mL + 2 mL), (3.75 mL + 1.25 mL), and (3.5 mL + 1.5 mL), respectively.¹

2.3 c) Hierarchical bimodal nanoporous gold monolith: A monolith with hierarchical architecture and two different ranges of pore size was created using a soft template technique and dealloying. Stock solutions containing 50 mM AuCl₃ and 50 mM AgNO₃ were made in Milli-Q water. Dextran (2 g) was added to a Milli-Q water-based solution of Au₁₀:Ag₉₀ to produce a viscous, brown liquid. The metal ions were then totally reduced by leaving this combination at room temperature overnight.² The organic template then decomposed because of thermal treatment

during the subsequent 30-minute annealing of the composite at 600°C.

2.4 *Self-assembled monolayer preparation and analysis:* The electrodes were placed in 1 mM alkanethiol ethanolic solution (17h) to create SAMs of thiolated molecules. Before doing any studies, the generated SAMs on the gold surfaces were thoroughly cleaned with ethanol, water, and the appropriate solvent. Our biosensor studies used 11-MUA and lipoic acid SAMs. To calculate the number of molecules immobilized on the electrode during SAM formation, the electrode was subjected to reductive desorption in a 0.5 M NaOH solution while being gassed with argon for 30 minutes. In a three-electrode cell setup, CV scans were carried out in 5 mL of solution. A 20 mVs⁻¹ scan rate was used for the CV scan, which was conducted between 0 and -1.5 V (versus. Ag|AgCl).¹

2.5 *Activation and Surface modification of ITO glass:* A series of 10-minute ultrasonic cleaning sessions in acetone, ethanol, isopropyl alcohol, and DI water were used to clean the ITO-coated glass plates. ITO glass plates that had been thoroughly cleaned were then put in a plasma chamber and exposed to oxygen plasma for five minutes.³ After then, SAM of APTES was produced on clean, surface-activated ITO glass plates by immersing them in a 1 mM APTES solution (in ethanol) for two hours at room temperature. After three rinses with ethanol, the APTES molecules that were interacting non-specifically with the substrate's surface were removed. Finally, the APTES modified ITO plates were dried while flowing N₂. In the following stage of surface modification, AuNPs were synthesized using the Turkevich method, which comprises citrate reduction of HAuCl₄ in aqueous solution. In a 10 mL glass vial, 1 ml of 1 mM HAuCl₄ in 8 mL of water was heated

to a rolling boil while being aggressively agitated. The rapid addition of 1 ml of 38.8 mM sodium citrate to the solution's vortex after boiling caused the solution's hue to change from pale yellow to wine-red. The flame was turned off after 10 minutes of boiling, and 30 more minutes were spent stirring.⁴ The resulting solution of colloidal gold nanoparticles was applied to the APTES ITO glass plate for an hour to prepare AuNPs-APTES-ITO sensor. After that, AuNPs and dopamine (0.5 mg/mL) were incubated together in an oxidative environment (pH 8.5), which promoted the creation of the polydopamine layer. A freshly prepared 0.5 mg mL⁻¹ dopamine solution in Tris-buffer (10 mM, pH = 8.5) was applied to the AuNPs-APTES-glass slide for 30 min at room temperature. Following the slide's removal from the solution, drying with N₂ gas and rinsing with DI water. The final step of surface modification involved protein immobilization. The PDA-AuNPs-APTES-glass slide was exposed to membrane protein (ACE2 or RDB) solution (0.1 μM) for 24 hours. The response to immobilization on the ITO surface was assessed using EIS in terms of increase in R_{ct} value.

2.6 *Activation and Surface modification of Au-QCM sensor:* When employing the QCM sensors, adequate cleaning/activation is required to get consistent readings. In this study, the QCM sensor gold surface was cleaned with the use of piranha and ozone plasma. The piranha solution was made by combining concentrated sulfuric acid in a 3:1 ratio with a 30% hydrogen peroxide solution. For 5 minutes, each sensor was immersed in 1 mL of piranha solution. The sensor was then washed with ethanol and Milli-Q water. Then, oxygen plasma cleaning was carried out in the plasma generator for 5 minutes at a medium radio frequency

(RF) level. Nitrogen gas was utilized to dry the QCM sensor after cleaning.⁵⁻⁶ SAM of 11-MUA was immobilized on the sensor surface after the QCM sensor surface had been thoroughly cleaned. The pretreated sensors were thoroughly cleaned with ethanol before being used as a support for the SAM. The sensor was then immersed in 1 mL of a 1.0 mM 11-MUA solution for 17 hours at 4°C with Au-coated side of the crystal exposed to the solution. The SAM-coated Au sensors were then rinsed with ethanol to ensure the removal of physically absorbed 11-MUA molecules. The SAM surfaces were dried under N₂ gas. In order to change the terminal carboxylic group into an active NHS ester, the 11-MUA-modified sensors were next subjected to a 4-hour treatment with 5 mM EDC and 5 mM NHS in acetonitrile. The sensor was then rinsed with acetonitrile and PBS buffer, dried, then dropped cast with a protein solution prepared in phosphate buffered saline (PBS, 10 mM, pH 7.4) for 17 hours at 4 °C to evaluate the binding affinities of the immobilized protein with LPS antagonists using QCM. Extra protein molecules were removed by rinsing with PBS.⁷

2.7 Preparation of protein solutions: In separate preparations, solutions of the proteins fetuin, BSA, and HRP at concentrations of 1 mg/mL, 0.5 mg/mL, and 1 mg/mL in PBS buffer (0.01 M, pH 7.4) were prepared. Real-time monitoring of protein loading on the fabricated electrode was done by immersing it in 500 µL of the prepared solution placed in the low volume cuvette. Varying concentrations of fetuin and asialofetuin (from 0.2 µM to 5 µM) were prepared in PBS buffer (0.01M, pH 7.4) for carrying out kinetic ELLA experiment. The impact of interfering proteins using BSA as a model serum protein was also investigated. To the

incubation solution for the kinetic ELLA, 5 mg mL⁻¹ of BSA and 2 μM fetuin were added. For experiments to investigate the binding affinities of the immobilized protein with LPS antagonists using QCM, protein solutions of LBP and CD14 were prepared separately in PBS buffer (0.01 M, pH 7.4) and stored at 4 °C. For carrying out EIS binding affinity experiments, 0.1 μM of protein (ACE2 or RBD) was prepared in PBS buffer and immobilized on the surface-modified ITO plate. A solution of recombinant MD2 protein was prepared using PBS buffer (0.01 M, pH 7.4). Through dilutions from the stock solution, a protein solution containing 50 nM was produced and used for fluorescence intensity measurement.

2.8 *Solution depletion technique to study protein loading onto fabricated electrodes:*

A UV-Vis spectrophotometer-based kinetic absorption analysis was carried out to assess the loading of protein molecules onto NPG and hb-NPG surfaces. The proteins fetuin, BSA, and HRP were prepared separately as solutions in PBS buffer (0.01 M, pH 7.4) at concentrations of 1 mg mL⁻¹, 0.5 mg mL⁻¹, and 1 mg mL⁻¹, respectively. One fabricated electrode was placed in the cuvette, which also contained 500 μL of the prepared solution. Before the protein solution was introduced, a baseline recording was made using only PBS buffer. At a wavelength of 280 nm, loading was continuously monitored for 120 minutes.¹ The Beer-Lambert equation, $A_{280} = \epsilon (280) \times C \times L$, was used to calculate the concentration of the protein solutions in which, A_{280} is the absorbance at 280 nm measured with a UV spectrophotometer, C is the concentration in M, L is the path length in cm, and ϵ_{280} is the protein's extinction coefficient at 280 nm measured in units of M⁻¹ cm⁻¹. The proposed equation was used to determine the ϵ_{280} values of proteins as the

weighted sum of the ϵ_{280} values of Trp, Tyr, and Cys: $\epsilon_{280} (\text{M}^{-1} \text{cm}^{-1}) = \text{no. of tryptophan } 5500 + \text{no. of tyrosine } 1490 + \text{no. of cysteine } 125$.⁸ $\epsilon_{280} (\text{BSA}) = 42,925 \text{ M}^{-1} \text{cm}^{-1}$, $\epsilon_{280} (\text{Fet}) = 19,840 \text{ M}^{-1} \text{cm}^{-1}$, and $\epsilon_{280} (\text{HRP}) = 25,250 \text{ M}^{-1} \text{cm}^{-1}$ were the values. After preparation, the protein solutions were used right away. First, we need to figure out the protein's molar extinction coefficient. The Lambert-Beer rule was then applied to the absorbance at time $t=0$ min to determine the initial number of molecules. Using the same formula, the number of molecules at time t was determined. By deducting the number of molecules present at the relevant time from the initial number present at $t = 0$ min, we determine the number of protein molecules that have entered the electrode structure and likely been immobilized. The desorption of proteins from NPG and hb-NPG electrodes was also examined by suspending the electrodes in PBS buffer (0.01 M, pH 7.4) after they had been submerged in the protein solutions for two hours. After 24 and 48 hours of incubation, desorbed proteins were quantified using UV absorbance.

2.9 *Investigation of the electron transfer in 6-ferrocenyl-1-hexanethiol SAMs on NPG and hb-NPG:* By dipping the three electrodes—bare gold wire, NPG, and hb-NPG—in a 1 mM ethanolic solution of 6-ferrocenyl-1-hexanethiol (FcC_6SH) for 18 hours at room temperature, SAM formation was accomplished. The electrodes were rinsed with ethanol after monolayer development. In the presence of 0.1 M NaClO_4 supporting electrolyte that had been deoxygenated for at least 15 minutes, CV of all the modified electrodes were taken in the range of 0-0.8 V potential.

2.10 *Electrochemical detection of glucose and the effect of interferents:* Working electrodes used for CV and chronoamperometry included bare gold, NPG, and hb-

NPG. Before usage, ethanol and water were used to clean the electrodes. The working electrodes were utilized to detect glucose. At a scan rate of 50 mV s^{-1} , the CV was conducted in 10 mM glucose in 0.1 M NaOH from -0.8 to 0.8 V, and the current response was recorded. For each of the three electrodes, the response was compared. With the aid of chronoamperometry, the real-time electrocatalytic activity for glucose oxidation on a bare gold electrode, NPG, and hb-NPG at potentials of -0.39 V, -0.02 V, and 0.57 V, respectively (vs. Ag|AgCl, sat'd KCl), was determined. The procedure for detecting glucose involved adding 50 μL of 10 mM glucose incrementally to 4 mL of 0.1 M NaOH while continuously stirring the mixture at 300 rpm.

The non-enzymatic sensor was evaluated in PBS buffer (pH 7.4) containing interfering species that have concentrations 30 times lower than those of glucose. Ascorbic acid (50 μL of 2 mM), lactose (50 μL of 2 mM), sodium chloride (50 μL of 2 mM), and sucrose (50 μL of 2 mM) were used to assess the selectivity of the glucose sensor in the presence of these common interfering species. In 0.1 M NaOH, the current response of the sensor to successive injections of glucose with the interferents was investigated.

2.11 *Stability analysis of curcumin analog solutions:* Using a UV-vis spectrophotometer, the absorbance spectra (200 to 800 nm) were collected at a regular time interval of 5 min for up to 2 hours to assess the stability of curcumin and curcuminoids. For this, a 25 μM solution of the analyte was prepared in a solvent system containing 1% DMSO and PBS (pH of 7.4, 10 mM sodium phosphate, 150 mM NaCl). The chemical stability of deacetylated glucosyl/galactosyl

curcuminoids in aqueous media with a pH range of (4-9) was examined using the aforementioned method. Different buffers were utilized to achieve the desired pH range, ranging from tris buffer (0.01M, pH 8.5) and glycine buffer (0.1M, pH 9) in the alkaline range to citrate buffer (0.1M, pH4), acetate buffer (0.1M, pH 5), and PBS (0.1M, pH 6.4) in the acidic range and PBS (0.01M, pH7.4) in the neutral range. To mirror the cytoplasmic environment, the stability of curcumin and curcuminoids was also tested in a reducing condition. By adding 10 μ M DTT in the solvent system made up of 1% DMSO and PBS (pH 7.4), the reducing state was kept in place. Recordings of absorbance spectra were made after repeating the experiment. The following formula was used to determine how much curcumin and curcuminoids degraded:

$$\% \text{ Degradation} = 100 (A_0 - A_t) / A_0$$

Where A_t denotes the absorbance at the wavelength of maximal absorbance at time t , and A_0 is the initial absorbance at this wavelength.

2.12 *Solubility analysis of curcumin analog solutions:* Curcumin and curcuminoids were examined for solubility in PBS (pH 7.4, 10 mM sodium phosphate, 150 mM NaCl). In a centrifuge tube with 1 mL of PBS, excessive curcumin was added. The mixture was shaken all night long. The following day, after performing high-speed centrifugation at 15,000 rpm for 10 min, the supernatant was collected to check the absorbance using a UV-vis spectrophotometer. The analog's calibration curve was then fitted with the absorbance value to calculate the concentration, which was then used to calculate the solubility in mg/L.

2.13 *Preparation and immobilization of lectin-enzyme conjugate:* The pre-activated alkaline phosphatase (NH_2 reactive ALP) was used to produce $50 \mu\text{g mL}^{-1}$ of the SNA-ALP conjugate in accordance with the instructions provided in the Dojindo labeling kit. Briefly, $300 \mu\text{g}$ of SNA was put to the microcentrifuge filter provided in the kit, washed twice with $100 \mu\text{L}$ of washing buffer, and then $30 \mu\text{L}$ of ALP dissolved in reaction buffer were added to the tube. The tube was then incubated at 37°C for two hours. After being fully mixed, the SNA-ALP conjugate was added to the tube and kept there at -20°C until needed. The created stock solution was diluted to the required concentration for additional experiments using PBS. After conjugate preparation, for 4 hours, electrodes coated with lipoic acid SAMs were immersed in a mixture of EDC (5 mM) and NHS (5 mM) in acetonitrile. To study enzyme kinetics in the presence and absence of glycoproteins, the electrodes were rinsed with acetonitrile, dried, and then rinsed twice with phosphate buffered saline (PBS, 10 mM , $\text{pH } 7.4$). They were then immersed in the SNA-ALP conjugate solution (containing $50 \mu\text{g}$ of conjugate), in PBS buffer ($100 \mu\text{L}$) of $\text{pH } 7.4$, for 17 hours, and then rinsed with PBS buffer.⁹

2.14 *Michaelis-Menten kinetics of the SNA-ALP conjugates on electrodes:* The activity of the SNA-ALP conjugate on electrode surfaces was investigated to determine whether the lipoic acid SAM modified electrodes were suitable for conjugate immobilization. The SWV differential currents were monitored as the substrate concentration was changed to better understand the kinetics of ALP on the electrode surface. We changed the concentration of the substrate, p-APP, between 0.01 and 1.0 mM to examine the response. The SNA-ALP conjugate modified electrodes were exposed to these substrate concentrations for 5 minutes

each in order to produce the greatest differential current. The peak difference current, as determined at the peak potential, is the difference between the maximum value of current and a background difference current.⁹

2.15 Electrochemical enzyme-linked kinetic lectin assay: The electrodes modified with SNA-ALP were employed as a substrate for the binding of different concentrations (from 0.2 mM to 5 mM) of glycoprotein fetuin diluted in PBS buffer (10 mM, pH 7.4) for the kinetic immunoassay. Modified electrodes were incubated for two hours in the glycoprotein fetuin solution prepared in PBS buffer (pH 7.4, 10 mM). The electrodes were next removed from the incubation solution, rinsed, and placed in 3 mL of glycine buffer (pH 9.0, 100 mM). The substrate, p-aminophenyl phosphate (p-APP), was introduced using a micropipette into the stirred solution with the SNA- ALP conjugate modified electrodes before the potential scan was conducted. Prior to running the potential scan, the substrate was given five minutes to react. To get acceptable peak currents in SWV scans, 1 mM of p-APP was employed as the working substrate concentration. The square wave voltammetric measuring parameters were adjusted. 50 mV, 0.2 sec, and 2 mV, respectively, were chosen as the optimal values for pulse width, pulse height, and step height. The potential ranged from 0.1 V to 0.2 V and was scanned at a rate of 5.0 mV/sec. The absolute value of the difference between the greatest peak currents $|I \text{ (before incubation)} - I \text{ (after incubation)}|$ was plotted vs. the glycoprotein concentration to produce the response plots. A similar investigation was carried out utilizing the glycoprotein asialofetuin to study the specificity of the conjugate towards the glycoprotein of interest.

2.16 Characterization of surface-modified sensors:

2.16a) Imaging the microstructure and morphology of the material (SEM/EDS):

SEM was used to analyze the surface morphology of the manufactured electrodes and sensors. To determine the thickness of the electrode, it was positioned vertically on the SEM stage. EDS was used for elemental analysis with a voltage of 15 kV and current of 1.6 nA. Using the gold oxide stripping method, the electrochemical surface area was calculated by scanning in 0.5 M H₂SO₄ at 100 mV/s from -0.2 V to 1.6 V and back to -0.2 V (vs. Ag|AgCl). Using the reported conversion factor of 450 $\mu\text{C cm}^{-2}$,¹⁰ the charge under the oxide reduction peak was integrated to measure the electrodes' electrochemically active surface area.

2.16b) Thermal (TGA): The SAM-modified electrodes were air-dried, rinsed with ethanol and water, placed in a platinum weighing pan, and heated inside the thermogravimetric analyzer from room temperature to 600 °C or higher at a ramping rate of 20 °C min⁻¹. Nitrogen was employed as the carrier gas and was passed at a rate of 40 mL min⁻¹. N₂ gas was allowed to pass through the sample for 5–10 minutes before the temperature ramp began. The analysis produced the initial mass, mass losses, and weight change percentage. Based on the net mass loss and the electrochemical surface area estimated using the gold oxide stripping method, the surface coverage of the molecules on the manufactured electrode was calculated.

2.16c) Mechanical (AFM): Due to the technique's sensitivity to height differences, the coating must be placed on top of exceptionally flat surfaces. In our study, gold coating on top of the quartz crystals is not flat, but because it is just a few nanometers rough, the AFM may be used to scan the modified surface. The molecular-level characterization of organic thin films is made possible by AFM.

On a (3 μm x 3 μm) area, the topographic image and roughness profile were evaluated. On the surface profile depicted in the software, a line was drawn to depict the average surface roughness (R_{rms}) of the sensors at each level of surface modification.¹¹ Peak Force Tapping mode was used to take pictures with ScanAsyst Air tips, and measurements were obtained in ambient conditions.

2.16d) Optical (contact angle measurement): The contact angles of the Au-QCM sensors were measured using a home-built apparatus after each modification stage. Following the surface modification on the Au-QCM sensors, 10 μL of Milli-Q water was dropped before the measurement was taken. The contact angle was used to gauge the hydrophilic/hydrophobic characteristics of the sensor surfaces as well as surface energy.¹² ImageJ was used in conjunction with contact angle plugins, much as the work cited by Lamour and colleagues.¹³

2.16e) Surface chemical characterization (XPS): Using Smartsoft as the controller software and Multipak V9 as the analysis application, the chemical composition of the adsorbed species on the modified Au-QCM sensor was assessed using XPS on a PHI 5000 VersaProbe II. Monochromated Al K α as X-ray source was employed. The X-ray was 90 degrees away from the analyser. When the tests were conducted at a stage tilt of 45 degrees, the analyzer axis was approximately 54.7 degrees away from the axis of the sample. XPS was used to evaluate the various signals generated by the surface alteration processes. By measuring the signals generated by the sensor modification phases, the relative abundance of the atoms present on the surface was discovered.¹⁴ The study was performed by Dr. Huafang Li at the institute of material science and engineering at Washington University in Saint Louis.

2.17 *Evaluation of binding affinities:* The binding affinities of membrane proteins with other small molecules were investigated using various analytical techniques. In our investigation, EIS has been used to comprehend the binding affinity of ACE2 and RBD with curcumin analogs. In a three- electrode electrochemical cell, a modified working electrode (membrane protein/Au NPs/APTES), Ag/AgCl as the reference electrode, and Pt wire as the auxiliary electrode were used. With a pH of 7.4, a concentration of 5 mM $[\text{Fe}(\text{CN})_6]^{3-}/[\text{Fe}(\text{CN})_6]^{4-}$, an AC voltage of 10 mV, a DC potential of 0.2 V, and a scan rate of 50 mV/s, EIS was performed in the frequency range of 1 Hz to 100 kHz. EIS data was represented by Nyquist plot. A "Nyquist Plot" is created when the imaginary part (Z_{imag}) is plotted on the Y-axis and the real part (Z_{real}) is plotted on the X-axis. The Z_{imag} is negative, whereas each point on the Nyquist plot represents an impedance value at a certain frequency point. Low frequency impedance is applied to the right side of the plot along the X-axis, whilst higher frequency impedances are applied to the left. The Randles equivalent circuits simplify the Warburg resistance (Z_w), charge transfer resistance (R_{ct}), resistance of solution (R_s), and double layer capacitance at the electrode surface (C_{dl}). By fitting the values in the circuit, practical data was acquired. The electrical circuit simulation was fit, and the surface properties were assessed.¹⁵

In the current investigation, fluorescence measurements were used to assess the MD2 protein's binding affinity for curcumin and its analogues. Prior to performing fluorescence intensity measurements, solutions of glycocurcumin derivatives with protein MD2 were prepared. A recombinant MD2 protein solution was created using PBS buffer (0.01 M, pH 7.4). Through dilutions from the stock solution, a

protein solution with a 50 nM concentration was produced. For doses ranging from 0.3 to 30 μM , PBS buffer dilutions were used to create stock solutions of the curcumin analogs. Along with 25 μL of protein solution, the curcumin analog (5 μL of one of the stock solutions ranging from 0.3 to 30 μM) was introduced to the fluorometer cell. The capacity volume was increased to 500 μL by adding, 470 μL of PBS buffer. Each measurement was performed at 25°C in a 3 mm quartz cell. The slit width used for excitation and emission was 20 nm. Fluorescence titrations were carried out at an excitation wavelength specific to the analog in order to measure the increase in curcumin fluorescence after coming into contact with the protein. In a nutshell, 0.05 M MD-2 was used to titrate curcumin at doses ranging from 0.3 μM to 30 μM . In order to make sure that the protein and analog would interact, the curcumin analogs and rh-MD-2 protein solution were incubated for 15 minutes. Curcumin's fluorescence in the presence of MD-2 was subtracted from curcumin's fluorescence on its own. SigmaPlot 12.0 was used to fit the gathered data using nonlinear regression in order to determine the K_D of curcumin using the equation below:

$$Y = B_{\max} * X / K_d + X$$

The technique of QCM is based on molecule recognition, in which the selective binding may result in changes to mass loading and interfacial properties that are recognized by a corresponding shift in oscillation frequency. Receptor-ligand interactions can be examined in real-time using this method.¹⁶ Using the following equation, Sauerbrey theorized the relationship between the frequency shift and the mass change on the QCM's surface.

$$\Delta f = -\frac{2f_0^2 \Delta m}{A\sqrt{\rho_q \mu_q}} = -C_f \cdot \Delta m$$

Here, the negative sign shows that as the additional mass on the surface of QCM grows, the resonance frequency lowers. The fundamental frequency of the QCM is f_0 , the density of the quartz crystal is ρ_q ($=2.648 \text{ g/cm}^3$), the shear modulus of the AT-cut quartz crystal is μ_q ($=2.947 \times 10^{11} \text{ g/cm} \cdot \text{s}^2$), the effective vibration area is A , and the Sauerbrey mass sensitivity is C_f . The extra mass that is adhered to the QCM's surface and the accompanying frequency shift are denoted by the letters Δm and Δf , respectively. It is important to note that when the additional mass layer is stiff, evenly distributed, and of small mass, the Sauerbrey equation is satisfied. The link between electrical impulses and mass information can be quantified using the Sauerbrey equation, providing the theoretical framework for the use of a QCM as a mass sensor.¹⁷

Using QCM, we have attempted to quantify the binding interactions of CD14 and LBP with LPS antagonists. The QCM chamber and the biosens3 program were used to set up each protein-immobilized sensor for the experiment. Using a 12-roller peristaltic pump in continuous flow mode, PBS buffer was pushed at a flow rate of $0.5 \mu\text{L}/\text{min}$ to create a stable baseline. Following the establishment of a stable baseline using PBS buffer, the sensor was subjected to injections of LPS antagonists at a variety of concentrations diluted in running buffer, through the inlet pipe.¹⁸

References

1. Sondhi, P.; Neupane, D.; Bhattarai, J. K.; Demchenko, A. V.; Stine, K. J., Facile fabrication of hierarchically nanostructured gold electrode for bio-electrochemical applications. *Journal of Electroanalytical Chemistry* **2022**, *924*, 116865.
2. Walsh, D.; Arcelli, L.; Ikoma, T.; Tanaka, J.; Mann, S., Dextran templating for the synthesis of metallic and metal oxide sponges. *Nature materials* **2003**, *2* (6), 386-90.
3. Mishra, S. K.; Srivastava, A. K.; Kumar, D.; Biradar, A. M.; Rajesh, Microstructural and electrochemical impedance characterization of bio-functionalized ultrafine ZnS nanocrystals– reduced graphene oxide hybrid for immunosensor applications. *Nanoscale* **2013**, *5* (21), 10494- 10503.
4. Huang, H.; Yang, X., Chitosan mediated assembly of gold nanoparticles multilayer. *Colloids and Surfaces A: Physicochemical and Engineering Aspects* **2003**, *226*, 77-86.
5. Easley, A.; Ma, T.; Eneh, C.; Yun, J.; Ratul, M. K.; Lutkenhaus, J., A practical guide to quartz crystal microbalance with dissipation monitoring of thin polymer films. *Journal of Polymer Science* **2021**, *60*.
6. Tlili, A.; Abdelghani, A.; Hleli, S.; Maaref, M. A., Electrical Characterization of a ThiolSAM on Gold as a First Step for the Fabrication of Immunosensors based on a Quartz Crystal Microbalance. *Sensors* **2004**, *4* (6), 105-114.
7. Thanh Ngo, V. K.; Nguyen, D. G.; Uyen Nguyen, H. P.; Man Tran, V.; My Nguyen, T.K.; Phat Huynh, T.; Vinh Lam, Q.; Dat Huynh, T.; Lien Truong, T. N., Quartz crystal microbalance (QCM) as biosensor for the detecting of Escherichia coli O157:H7. *Advances in Natural Sciences: Nanoscience and Nanotechnology* **2014**, *5* (4), 045004.
8. Pace, C. N.; Vajdos, F.; Fee, L.; Grimsley, G.; Gray, T., How to measure and predict the molar absorption coefficient of a protein. *Protein science : a publication of the Protein Society* **1995**, *4* (11), 2411-23.
9. Pandey, B.; Bhattarai, J. K.; Pornsuriyasak, P.; Fujikawa, K.; Catania, R.; Demchenko, A. V.; Stine, K. J., Square-wave voltammetry assays for glycoproteins on nanoporous gold. *Journal of electroanalytical chemistry (Lausanne, Switzerland)* **2014**, *717-718*, 47-60.
10. Evans, U.; Colavita, P. E.; Doescher, M. S.; Schiza, M.; Myrick, M. L., Construction and Characterization of a Nanowell Electrode Array. *Nano Letters* **2002**, *2* (6), 641-645.
11. Hruška, M.; More-Chevalier, J.; Fitl, P.; Novotný, M.; Hruška, P.; Prokop, D.; Pokorný, P.; Kejzlar, J.; Gadenne, V.; Patrone, L.; Vřnata, M.; Lančok, J., Surface Enhancement Using Black Coatings for Sensor Applications. *Nanomaterials* **2022**, *12* (23), 4297.
12. Matsumoto, T.; Tashiro, Y.; Komasa, S.; Miyake, A.; Komasa, Y.; Okazaki, J., Effects of Surface Modification on Adsorption Behavior of Cell and Protein on Titanium Surface by Using Quartz Crystal Microbalance System. *Materials (Basel)*

Switzerland **2020**, *14* (1).

13. Lamour, G.; Hamraoui, A.; Buvailo, A.; Xing, Y.; Keuleyan, S.; Prakash, V.; Eftekhari- Bafrooei, A.; Borguet, E., Contact Angle Measurements Using a Simplified Experimental Setup. *Journal of Chemical Education* **2010**, *87* (12), 1403-1407.

14. Miyake, A.; Komasa, S.; Hashimoto, Y.; Komasa, Y.; Okazaki, J., Adsorption of Saliva Related Protein on Denture Materials: An X-Ray Photoelectron Spectroscopy and Quartz Crystal Microbalance Study. *Advances in Materials Science and Engineering* **2016**, *2016*, 5478326.

15. Magar, H. S.; Hassan, R. Y. A.; Mulchandani, A., Electrochemical Impedance Spectroscopy (EIS): Principles, Construction, and Biosensing Applications. *Sensors (Basel, Switzerland)* **2021**, *21* (19).

16. Zhang, Q.; Huang, Y.; Zhao, R.; Liu, G.; Chen, Y., Determining binding sites of drugs on human serum albumin using FIA-QCM. *Biosensors & bioelectronics* **2008**, *24* (1), 48-54.

17. Huang, X.; Chen, Q.; Pan, W.; Yao, Y., Advances in the Mass Sensitivity Distribution of Quartz Crystal Microbalances: A Review. *Sensors (Basel, Switzerland)* **2022**, *22* (14).

18. Maglio, O.; Costanzo, S.; Cercola, R.; Zambrano, G.; Mauro, M.; Battaglia, R.; Ferrini, G.; Nastri, F.; Pavone, V.; Lombardi, A., A Quartz Crystal Microbalance Immunosensor for Stem Cell Selection and Extraction. *Sensors* **2017**, *17* (12), 2747.

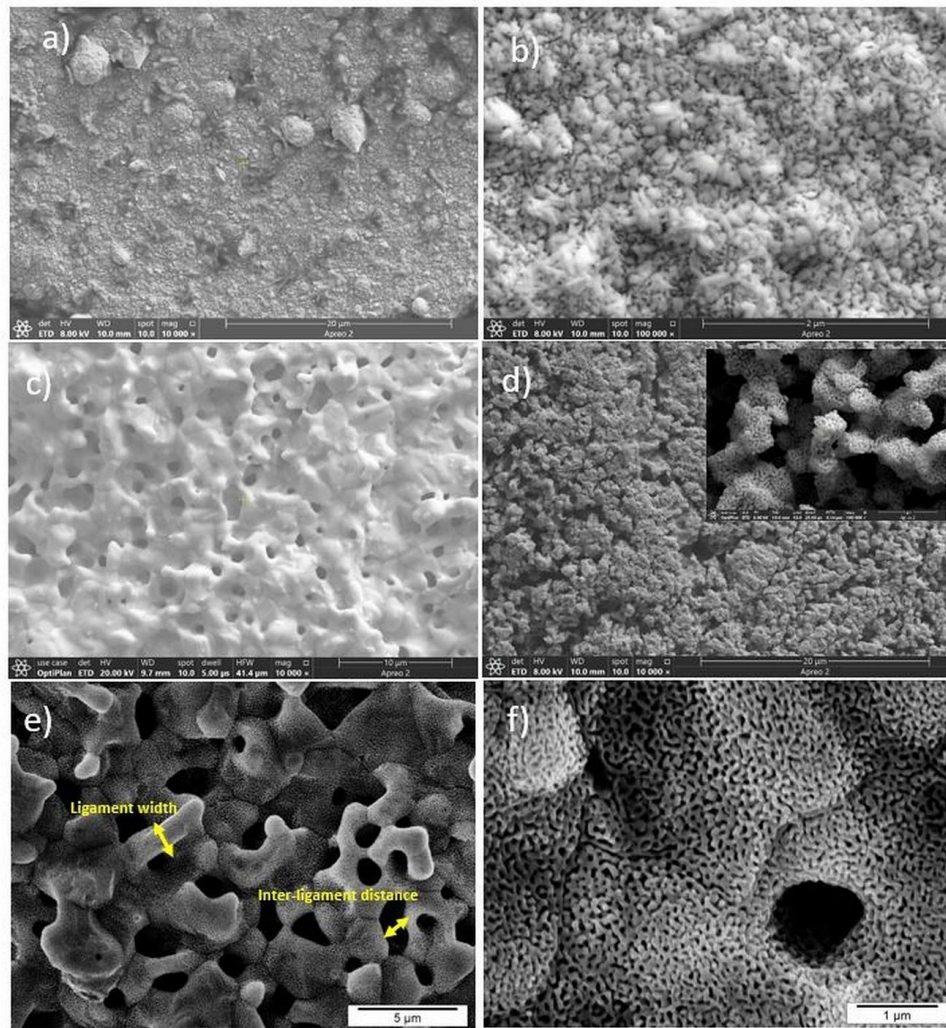
CHAPTER III: METHODS TO GENERATE HIERARCHICAL BIMODAL NANOPOROUS GOLD ELECTRODE AND ITS APPLICATION (RESULTS AND DISCUSSION)

3A. FABRICATION OF HIERARCHICAL BIMODAL NANOPOROUS GOLD FOR STUDYING GLYCOPROTEIN-LECTIN INTERACTION BY AN ELECTROCHEMICAL BIOSENSOR

The pore volume and ligament size adjustments are of utmost significance for our prepared electrodes. In comparison to conventional NPG, the bimodal pore shape has demonstrated better electrocatalytic activity and sensitivity towards glucose oxidation. In this study, we fabricated a bimodal structure with changing Au/Ag ratios and focused on the characterization of the electrode based on surface morphology, surface coverage, and loading capacity.

3.1 *Characterization of nanoporous gold and hierarchical bimodal nanoporous gold electrode prepared by varying the ratio of the Au-Ag alloy:* SEM was used for structural characterization, while EDX was used for composition analysis following the first and second dealloying steps. Around the gold wire, electrodeposition produced a shell-like shape. Using the side view images from the SEM and manually measuring the thickness using the scale bar, it was determined that the thickness of the hb-NPG surrounding the gold wire is approximately 3 μm . NPG has demonstrated an open, linked network of ligaments and pores following chemical dealloying. Out of all the compositions, hb-NPG made from $\text{Au}_{10}\text{Ag}_{90}$ (at.%) was comprised of upper and lower hierarchy without cracks in the structure, as seen in the SEM images of various alloy compositions. Here, larger pores are indicated by an upper hierarchy, whilst smaller pores are shown by a lower hierarchy. Figure 3.1 displays the SEM pictures of the top and side views of the

exterior of hb-NPG coated gold wire made from alloys with different Au: Ag ratios. According to EDX study, there was a noticeable quantity of silver left over after the initial dealloying, as shown in Figure 3.2, and it ranged from 80 to 85 atomic%. Silver (red color) and gold (yellow color) are displayed at each stage of the fabrication of hb-NPG, and the color images show the changes in elemental composition.



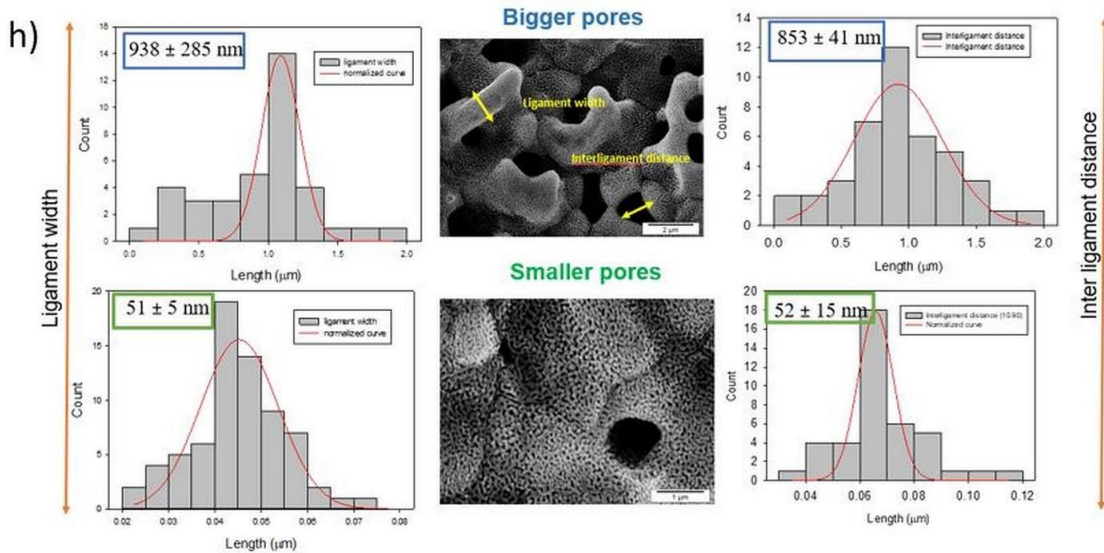
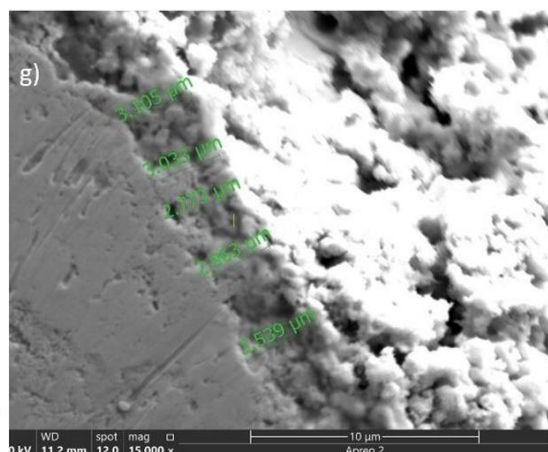
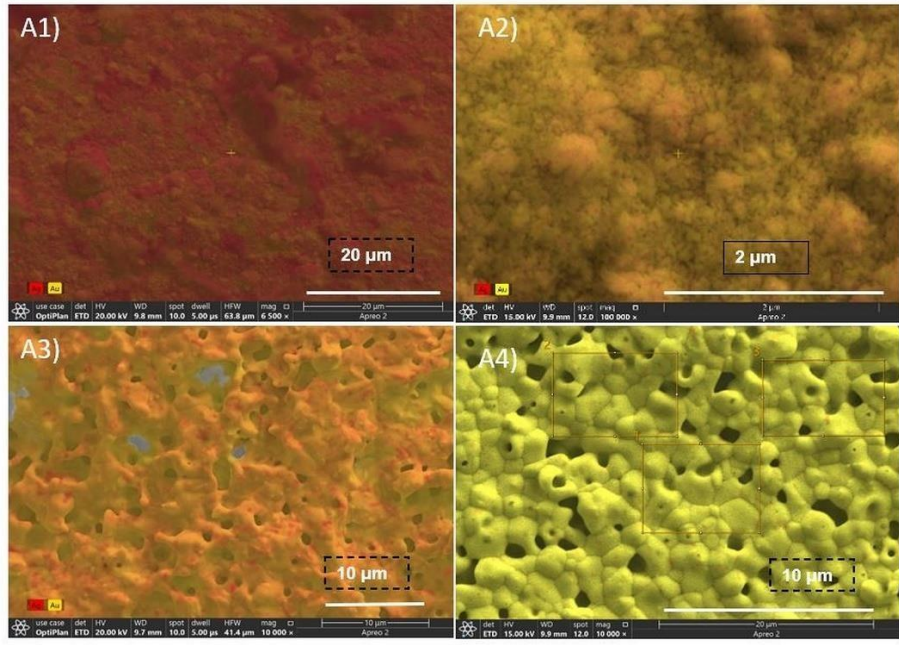


Figure 3.1. SEM images of a) 10:90 (Au: Ag) alloy prepared by applying -1.0 V (vs. Ag/AgCl, KCl saturated) for 10 min on gold wire, b) morphology after electrochemical dealloying, c) pore-coarsening seen after annealing, d) Larger pores seen after chemical dealloying in concentrated nitric acid, e) and f) are showing the ligament width and interligament distance in upper and lower hierarchy respectively. The thickness of the hierarchical structure deposited on gold wire is shown in (g), (h) Histograms showing the ligament width and interligament distance in upper and lower hierarchy respectively.



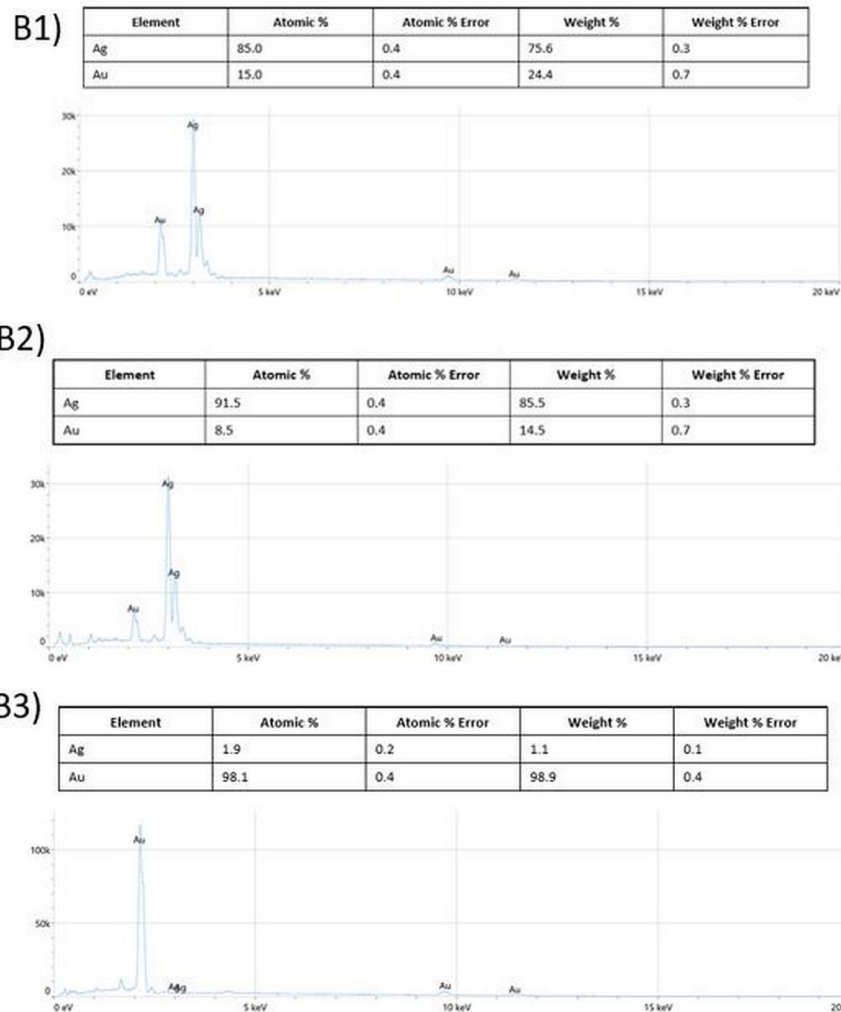


Figure 3.2. A) Color SEM of the A1) Au₁₀:Ag₉₀ alloy, A2) electrochemically dealloyed structure, A3) annealed structure, and a4) hierarchical nanoporous structure after the final step of chemical dealloying B) EDX spectrum showing the elemental composition of the B1) alloy, B2) electrochemically dealloyed structure, and B3) hierarchical bimodal nanoporous gold structure

The Apreo 2 instrument's ability to assign different colors to different elements is a useful feature of color SEM. Using ImageJ software, the electrode of interest for future study, made from Au₁₀Ag₉₀ (at.%), was further studied to identify structural parameters including ligament width and inter-ligament distance, which

are shown in Tables 1 and 2. Investigated were the impacts of the alloy composition on the nanoporous structure's microstructures. It was observed that the ligament's size increased from 819 ± 71 to 1031 ± 272 nm when the silver content increased. During dealloying, the structure begins to coarsen; the rate at which this occurs may depend on the alloy composition, the amount of residual silver, the temperature, or the electrolyte.

Table 2 displays the ligament width and interligament distance distributions for the bimodal $\text{Au}_{10}\text{Ag}_{90}$ alloy structure. According to calculations, the ligament width in the upper and lower hierarchies was 938 ± 285 nm and 51 ± 5 nm, respectively. The interligament distance, which was found to be 853 ± 41 nm and 52 ± 15 nm for the upper and lower hierarchical features, respectively, was comparable to their ligament width.

Table 1. Distribution of ligament width and inter-ligament distance of varying alloy compositions. The evaluation was done after completion of the multistep synthesis involving electrochemical dealloying, annealing, and chemical dealloying.

Alloy composition (Au:Ag)	Mean pore size (nm)	
	Ligament width (nm)	Inter-ligament distance (nm)
30:70	819 ± 71	52 ± 7
25:75	940 ± 269	50 ± 3
20:80	1031 ± 272	62 ± 11

Table 2. Distribution of ligament width and inter-ligament distance for the hierarchical bimodal structure where alloy composition was $\text{Au}_{10}:\text{Ag}_{90}$. The evaluation was done after completion of the multistep synthesis involving electrochemical dealloying, annealing, and chemical dealloying.

Hierarchy level	Ligament width (nm)	Inter-ligament distance (nm)
Upper	938 ± 285	853 ± 41
Lower	51 ± 5	52 ± 15

3.2 Surface area measurement and roughness factor analysis: The roughness factor of all the fabricated electrodes, which is the ratio of electrochemical surface area (ECSA) to the geometrical surface area, was determined using CV with a value of $450 \mu\text{C cm}^{-1}$ for the reduction of a single layer of gold oxide¹, where the charge under the oxide reduction peak was integrated to estimate the ECSA. Figure 3.3 depicts the effects of different alloy compositions as well as the significance of the three-step fabrication method. Figure 3.3a displays the CV curves for hb-NPG electrodes made from Au: Ag alloys with various compositions. The area under the peaks for gold oxidation and reduction for the hb-NPG electrodes dramatically increases when the initial electrodeposited alloy's silver concentration rises, which raises the roughness factor. Figure 3.3b also compares the chemically dealloyed NPG (10:90) with the multistep-fabricated hb-NPG (10:90), demonstrating the critical impact of two-step dealloying and annealing in raising the ECSA in comparison to chemical dealloying. The CV depicted in Figure 3.3c was taken after electrochemical dealloying and annealing. The CV demonstrates the presence of Ag and Au on the electrode surface upon annealing. Compared to pure silver (0.4 V), the alloy's silver begins to oxidize at a more positive potential of 0.52 V. The oxidation of Au, on the other hand, occurs at a potential of about 0.8 V, while the oxidation peak for pure gold is observed at 0.96 V. The bimetallic composition was verified by the observed Au and Ag reduction peak during annealing. The absence

of the gold peak before annealing may be caused by the silver coating that covers the gold. Because Ag's atomic percentage was larger in the alloy than Au's, Ag had a higher peak intensity. The peak at 0.6 V was related to the oxidation of Ag_2O to AgO , whereas the peak at 0.38 V in both cases was caused by the production of Ag_2O layers.

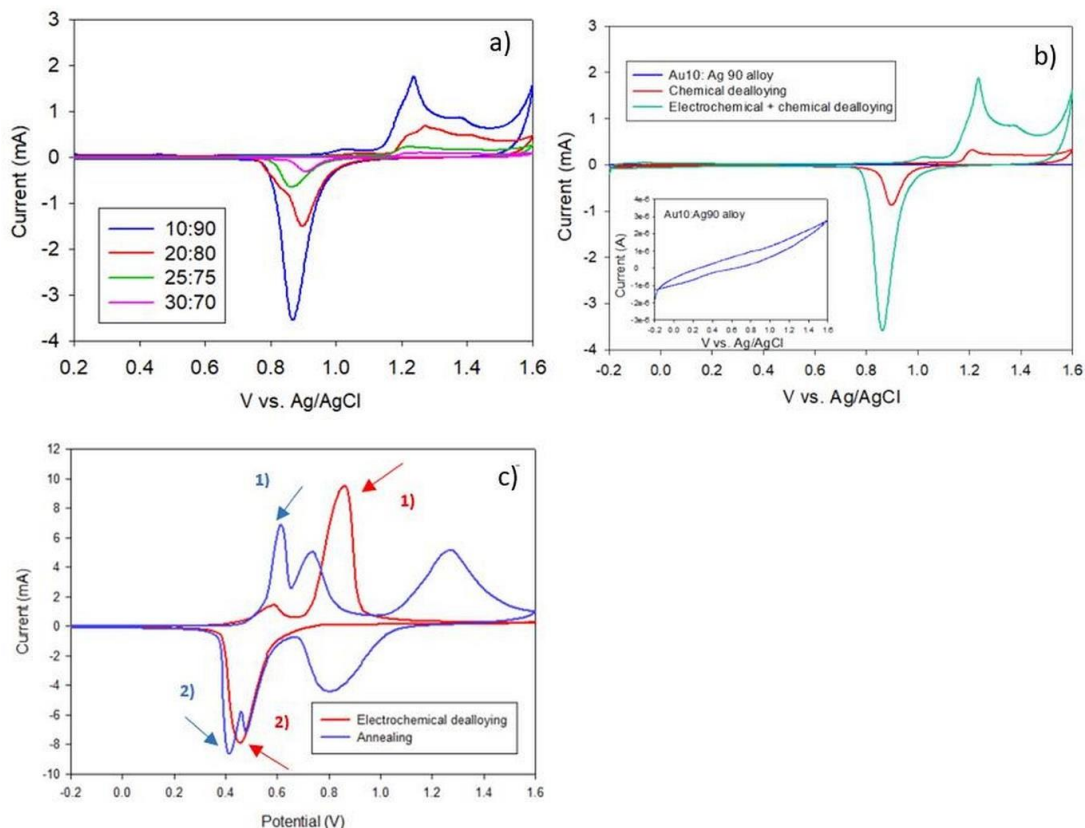


Figure 3.3. Cyclic voltammograms showing a) the comparison of electrochemically active surface area for the porous structure formed from different Au: Ag atomic percentages of the alloy. The varying composition of the starting alloy was $\text{Au}_{10}:\text{Ag}_{90}$, $\text{Au}_{20}:\text{Ag}_{80}$, $\text{Au}_{25}:\text{Ag}_{75}$ and $\text{Au}_{30}:\text{Ag}_{70}$ b) $\text{Au}_{10}:\text{Ag}_{90}$ alloy, chemically dealloyed structure formed after immersing in nitric acid, and finally the enhancement of peak current when electrochemical and chemical dealloying is used

in combination (c) the oxidation and reduction peaks after electrochemical dealloying are shown in red where the peak at 1) denotes the oxidation of Au. The oxidation and reduction peaks after annealing are shown in blue where the peak at 1) is associated with the oxidation of Ag_2O to AgO . The peak at 2) in both cases is due to the reduction to Ag_2O layers.

ECSA for hb-NPG was found to be 7.64 cm^2 . The average ECSA of NPG ($\text{Au}_{30}\text{Ag}_{70}$) (at.%) reported by our lab earlier was 12.5 cm^2 and was based on oxide stripping tests using substrates with the same size gold wire. The surface roughness factor calculation and the ECSA values for all the electrodes that were manufactured are listed in Table 3.

Table 3. Calculation of the roughness factor (R_f) and electrochemically active surface area (ECSA) of the final structure formed from varying Au:Ag alloy composition. The charge under the reduction peak seen in CV was evaluated for all the different compositions. The 10:90 composition formed the hb-NPG structure with the highest roughness factor.

Composition	Charge (mC) under reduction peak	Mean	Standard dev	ECSA/ cm^2	R_f
10:90	3.51	3.44	0.07	7.64	231.5
	3.44				
	3.37				
20:80	1.82	1.82	0.11	4.04	122.4
	1.93				
	1.7				
25:75	1.07	1.02	0.28	2.26	68.5
	0.97				
	0.54				
30:70	0.13	0.20	0.14	0.45	13.6
	0.11				
	0.37				

3.3 Determination of surface coverage of lipoic acid molecules on NPG and hb-NPG using thermogravimetric analysis and reductive desorption: In the current investigation, we employed the TGA method to quantify the molecules loaded onto hb-NPG and NPG, which in turn allowed us to estimate the surface coverage of the molecules while accounting for the electrodes' electrochemical surface area. We scanned up to 600 °C while pyrolytically decomposing the air-dried SAM modified NPG and hb-NPG electrodes in an inert environment. Lipoic acid molecules are anticipated to totally break down at this temperature. The modified electrodes were tested using TGA, and it was discovered that NPG lost 0.05% of its weight and hb-NPG lost 0.1% of its weight throughout the temperature scan. The loading of 0.266 g cm⁻² of LA self-assembled onto the NPG surface, is equivalent to 1.3 x 10⁻⁹ mol cm⁻² (12.5 cm² electrochemical surface area), and 0.788 g cm⁻² of LA loaded onto the hb-NPG surface is equivalent to 3.8 x 10⁻⁹ mol cm⁻² (7.64 cm² electrochemical surface area), and were responsible for the mass losses. Figure 3.4 and Table 4 show the TGA thermograms of LA loading on both electrodes (temperature ramped at 20 °C min⁻¹) as well as data on reductive desorption. The higher coverage of LA molecules per unit area on hb-NPG than on NPG could be due to the better accessibility deeper into the material afforded by the larger pores.

The reductive desorption approach was used to estimate the surface coverage. Around -0.9 V, a reduction peak connected with the Au-S bond in the SAM was seen. This peak resulted from the lipoic acid's reductive desorption from the gold surface. Utilizing the charge under the reductive desorption peak and the electrode surface area discovered by oxide stripping tests, the number of lipoic acid

molecules was estimated. On hb-NPG and NPG, respectively, the average surface coverage of lipoic acid SAMs was determined to be $3.42 \times 10^{-10} \text{ mol cm}^{-2}$ and $2.09 \times 10^{-10} \text{ mol cm}^{-2}$, respectively. According to surface coverage data from TGA, more molecules are present in an electrode's region per unit of surface area than is typically the case. This shows that molecules from places inside electrodes that cannot be reached by electrochemical desorption may be contributing to mass loss. On top of those attached to Au surfaces, lipoic acid molecules may also be physisorbed in the interior. Prior research using commercially available gold plates (6.0 mm x 6.0 mm x 0.25 mm) revealed a surface coverage of 1.31×10^{18} molecules m^{-2} (equal to $2.18 \times 10^{-10} \text{ mol cm}^{-2}$). Theoretically, based on the unit cell dimensions of LA (a= 11.744, b= 9.895, c= 9.246), it is predicted that a fully ordered coverage of LA molecules on a gold surface would lie between 3.45×10^{18} and 4.40×10^{18} molecules m^{-2} . Per unit cell, this translates to four LA molecules. Among the surface coverages of LA on flat gold surfaces that have been reported are those of $3.0 \times 10^{-10} \text{ mol cm}^{-2}$ (1.81×10^{18} molecules m^{-2}), $3.50 \times 10^{-10} \text{ mol cm}^{-2}$ (2.11×10^{18} molecules m^{-2}), and $2.42 \times 10^{-10} \text{ mol cm}^{-2}$ (1.46×10^{18} molecules m^{-2}).

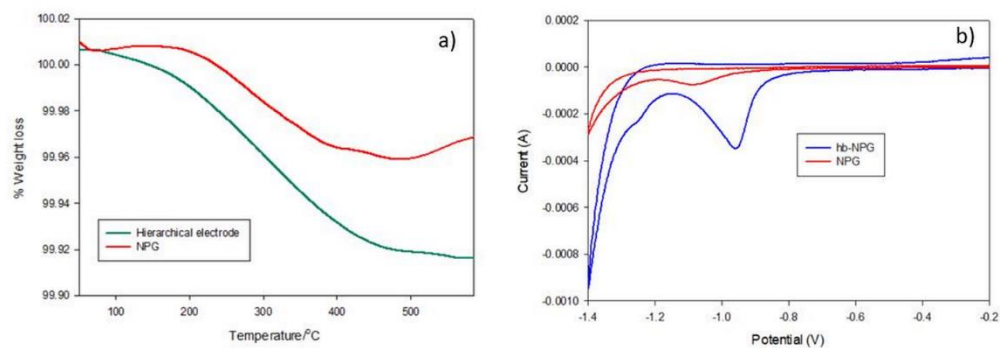


Figure 3.4. A) TGA thermograms of lipoic acid loading on NPG and hb-NPG from room temperature to 600 °C at a ramping rate of 20 °C min⁻¹. B) Reductive desorption of lipoic acid immobilized on NPG and hb-NPG carried out in 0.5 M NaOH solution, performed between 0 and -1.5 V at a scan rate of 20 mV s⁻¹.

Table 4. TGA and reductive desorption data showing surface coverage for Lipoic acid SAMs on NPG and hb-NPG. The data presented is compared with previously reported values.

Method	Substrate	Surface coverage for LA SAMs (mol cm ⁻²)		
		Wt. change (%)	Mass loss (µg)	Surface coverage LA mol /cm ²
Reductive desorption	NPG			2.09 x 10 ⁻¹⁰
	hb-NPG			3.42 x 10 ⁻¹⁰
TGA analysis	NPG	0.05	3.3 ± 0.7	1.3 x 10 ⁻⁹
	hb-NPG	0.1	6.02 ± 0.03	3.8 x 10 ⁻⁹

3.4 Adsorption of proteins with varying structures onto NPG and hb-NPG:

The adsorption of three selected proteins onto NPG and hb-NPG was examined and compared to evaluate differences in the capability of these two nanomaterials as supports for hosting proteins. Applications of enzymes adsorbed inside NPG have been extensive and subject of reviews. Additionally, other hosted

inside NPG materials have been used to develop biosensors. The absorption of proteins from solution onto NPG electrodes has attracted tremendous amounts of attention, primarily due to the great interest in the development of biosensor devices.¹⁶⁹⁻¹⁷¹ Hierarchical bimodal nanoporous gold (hb-NPG) presents a new opportunity as a support for a range of applications due to the high loading capacity. The influence of surface morphology, pore size, and pore volume play a pivotal role in the study of absorption kinetics of proteins and glycoproteins.¹⁷² Synthesis of an electrode with a bimodal pore size distribution is highly promising to achieve high capacity loading of proteins as their diffusion deeper into the material should be enabled. This suggests that the rational design of a hierarchical bimodal pore size distribution in the hb-NPG electrode and the optimization of meso- and macropores maximized the protein loading.¹⁷³

Due to its use in various bioanalytical applications and diagnostic kits, horseradish peroxidase (HRP) is one of the enzymes of the plant peroxidase superfamily that has received the greatest research attention. The protein's glycosylation modification adds roughly 9.4 kDa to the HRP's 44 kDa molecular weight. The protein structure is sustained by four disulfide bonds and two calcium-binding sites, according to the X-ray findings. The pH range of 6 to 8 is where HRP exhibits its highest activity, and its isoelectric point (pI) is 9. The pH of PBS, which was used for the loading experiment is 7.4, which is lower than the pI of HRP and can electrostatically bind with the negatively charged gold electrode surface. On or near its surface, HRP has 8 cysteine, 4 methionine, and 6 lysine residues. The

multipoint attachment of HRP on the electrode's surface has been made easier by the sulfur-containing amino acid residues (cysteine and methionine) and the -NH₂-containing amino acid residues (lysine). Additionally, the macropores found in hb-NPG may be responsible for the improved accessibility of the enzyme to the inner surface.

The 48.4 kDa serum glycoprotein fetuin, which is an important component of bone formation and human metabolic processes, was chosen as the second candidate in our loading experiment. It is an acidic glycoprotein with a lot of sialic acid, which contributes to its net negative charge at physiological pH in multiple aspartate/glutamate-rich regions as well as the terminal residues. Its isoelectric point is approximately 5, similar to albumin. When exposed to a metallic surface, the aqueous solution of fetuin partially adsorbs as a result of the dynamic interplay of electrostatic, van der Waals, and hydration interactions. This protein is useful for creating biosensors for glycoproteins and is of interest for future applications of hb-NPG as a glycoprotein sensor.

BSA, a protein with a higher molecular weight (66.4 kDa), accounts for roughly 10% of the total whey proteins in milk. The structural characteristics of BSA have made it suitable for applications involving medication delivery. The preferential binding of BSA to negatively charged surfaces has been linked to the 60 lysine groups that are present on its surface and can interact electrostatically with negatively charged surfaces. BSA's isoelectric point is 4.6, making it negatively charged at pH 7.4. There are two probable methods for explaining the adsorption of BSA on the electrode surface: "end-on" binding and "side-on"

binding, where end-on contact results in a larger surface coverage of BSA on the electrode surface.

Figure 3.5 shows graphically a study of real-time protein loading. Due to the strong electrostatic contact between the protein and the metal surface, more HRP molecules were observed to be immobilized on the electrode during the loading experiment than fetuin or BSA. For BSA and fetuin, the immobilization was higher for hb-NPG than NPG (Table 5). The dimensions of BSA are reported to be 14 nm x 4 nm x 4 nm, indicating a surface footprint for each protein molecule as small as 16 nm² or as large as 64 nm², corresponding to coverages of 6.25 x 10¹² molecules cm⁻² and 2.5 x 10¹³ molecules cm⁻², respectively. Our observed estimations of 2.0 x 10¹² molecules cm⁻² and 2.85 x 10¹² molecules cm⁻² on NPG and hb-NPG are accurate and indicate a very substantial level of BSA protein coverage within NPG and hb-NPG. The dimensions of HRP are reported to be 4.0 nm x 6.7 nm x 11.7 nm. This indicates that each protein molecule may have a surface footprint as small as 27 nm² or as large as 78 nm², which corresponds to coverages of 3.7 x 10¹² molecules cm⁻² and 1.07 x 10¹³ molecules cm⁻², respectively, and assumes complete coverage on a flat surface. Our observed estimations of 9.48 x 10¹² molecules cm⁻² and 7.0 x 10¹² molecules cm⁻² on NPG and hb-NPG, respectively, are plausible and reflect a very substantial extent of protein coverage of HRP within NPG and hb-NPG perhaps enhanced by electrostatic interactions. Our measured estimations for the amount of fetuin immobilized on NPG and hb-NPG, respectively, of 8.63 x 10¹² and 9.33 x 10¹² molecules cm⁻², are reasonable and also indicate a very significant degree of fetuin

coverage within NPG and hb-NPG.

After 48 hours of incubation in the buffer ($V = 1$ mL), the desorption process of integrated proteins under the same conditions showed that the proteins did not desorb out into the buffer. It is widely known that proteins cling to gold surfaces through Au-NH₂ interactions with accessible cysteines in the protein structure or with lysines on the protein surface. The internal gold surfaces appear to be highly physisorbed with these proteins.

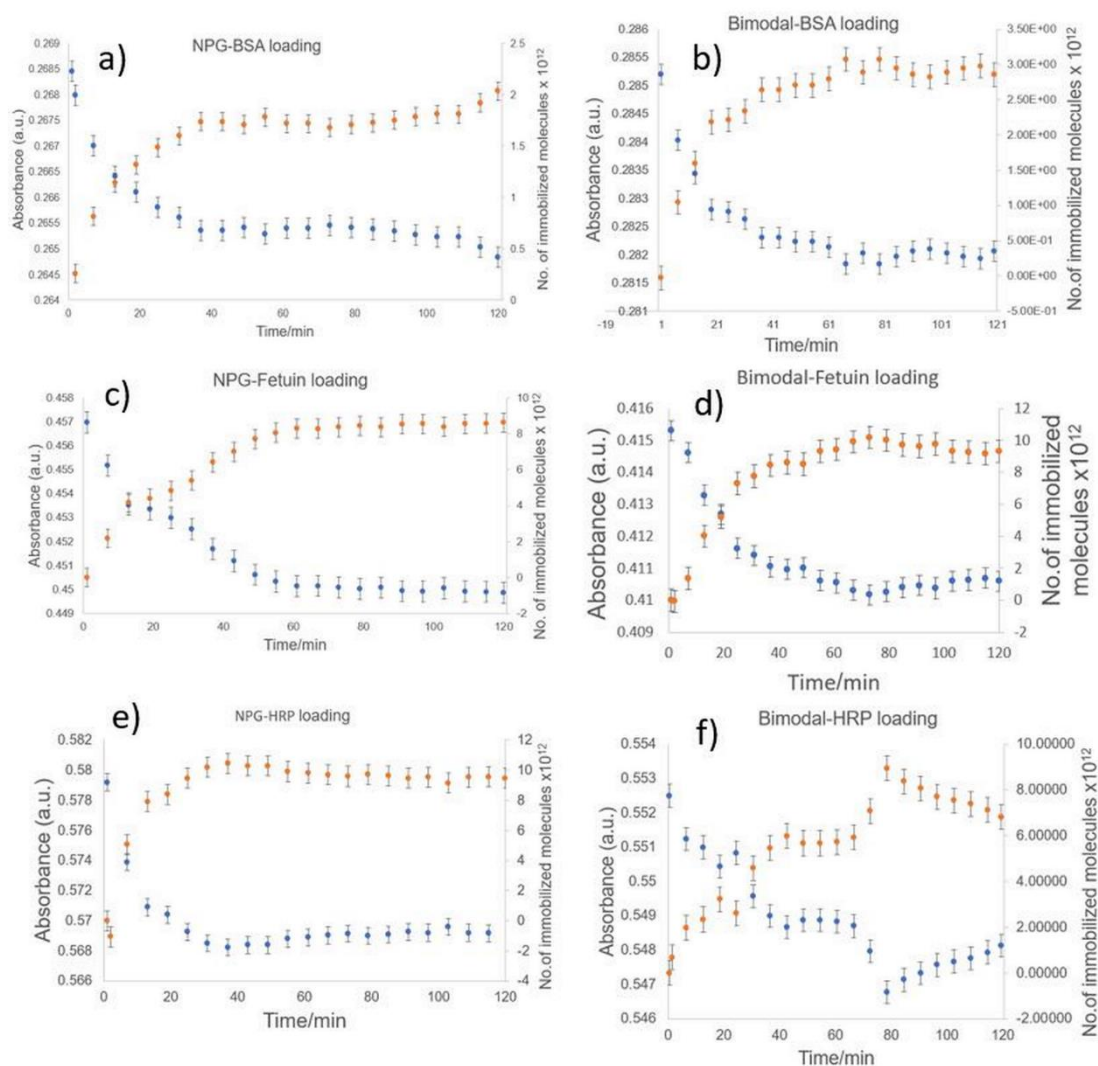


Figure 3.5. Real-time protein loading study using UV-vis spectrophotometer

showing the change in absorbance and the average number of immobilized BSA, Fetuin and HRP molecules on NPG and hb-NPG electrodes. BSA, Fetuin, and HRP loading on NPG is shown in (a), (c), and (e) respectively. The loading of same proteins on hb-NPG is shown in (b), (d), and (f) respectively. Each graph depicted is an average of three measurements. Data depicted as an average (N=3).

Table 5. Number of immobilized protein molecules on NPG and hb-NPG. Data depicted as average (3 measurements)

Proteins used in the study (Molar extinction coefficient.M ⁻¹ cm ⁻¹)	No. of molecules immobilized/cm ² on NPG	No. of molecules immobilized/cm ² on hb- NPG
BSA	2.03 x 10 ¹²	2.85 x 10 ¹²
HRP	9.48 x 10 ¹²	7 x 10 ¹²
Fetuin	8.63 x 10 ¹²	9.33 x 10 ¹²

3.5 Quantitative analysis of the SAMs of ferrocene 1-hexanethiol

Figure 3.6 shows CV data for FcC₆SH ferrocene moieties immobilized on the Au, NPG, and hb-NPG electrodes as self-assembled monolayers. Sharp oxidation and reduction peaks can be visible on voltammograms taken on bare gold wire and an NPG electrode, whereas broad peaks can be seen on hb-NPG. Voltammogram form was discovered to be independent of scan rate from 0-0.8 V. The characteristics showing the stability of the monolayer to electrochemical cycling are not altered by repeated scanning. Monolayer heterogeneity causes the peak to broaden, and it appears that hb-NPG offers a more heterogeneous environment for SAM production. Because of the interaction between ferrocene sites or the high surface coverage that causes site inhomogeneity, the monolayer

experiences lateral repulsive interaction, leading to a broader peak. The creation of a tightly packed monolayer, where anions screen repulsive interactions between ferrocenium cations, is suggested by the narrow width of the redox peak. The fact that there is such a minor difference between the anodic and cathodic peaks indicates that the adsorbed species on the electrodes underwent a redox reaction. The terminal ferrocene group of the monolayer undergoes both oxidation and reduction as seen in the cyclic voltammograms, which exhibit a pair of redox peaks in the potential range between +300 and +400 mV. The charge of the oxidation peak was used to estimate the amount of 6-ferrocenyl-1-hexanethiol.

The charge associated with the cathodic voltammetric peak has been integrated to calculate the surface coverage of the redox-active surface group using the formula $\Gamma = Q_{cv}/nFA_{ECSA}$, where Q is the faradaic charge, $n = 1$ is the number of electrons involved in the redox process for the F_c/F_{c+} redox couple, F is the Faraday constant, and A_{ECSA} is the electrode's electrochemical surface area.

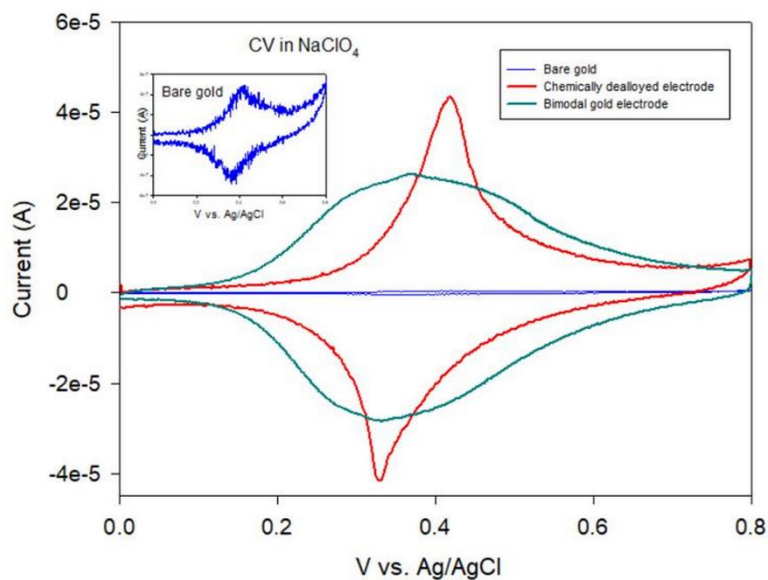


Figure 3.6. Cyclic voltammograms of SAMs of 6-ferrocenyl-1-hexanethiol with unmodified bare gold wire, chemically dealloyed electrode, and hb-NPG (solution composition reported) (NaClO_4 , 0.1M; scan rate = 50 mV s^{-1}). Increasing the concentration of the electrolyte to 0.5M has little variation on the shape of the curve.

According to theory, ferrocene alkanethiol can cover a maximum surface area of $4.5 \times 10^{-10} \text{ mol cm}^{-2}$ on Au (111). NPG and hb-NPG electrodes have been found to have high surface coverage of 5.47×10^{-9} and $30.1 \times 10^{-10} \text{ mol cm}^{-2}$, respectively. This may be explained by additional physisorbed molecules, lateral electron transport, or electrostatic interactions between redox groups.

Along with other voltammetric parameters, the values for FWHM for the monolayers produced on NPG and hb-NPG are presented in Table 6. When the monolayer displays a perfect electrochemical response, the theoretical value of FWHM for a one-electron process is 90.6 mV. The differing responses from the monolayers on the various electrodes indicate that the monolayers created on hb-NPG have repulsive interactions ($\text{FWHM} > 90.6$), whereas the monolayers formed on NPG have attractive interactions ($\text{FWHM} 90.6 \text{ mV}$). We observed that the FWHM values for the bare gold wire, NPG, and hb-NPG were 9.1, 39, and 160 mV. It has been found that the local habitats of the electroactive species anchored on surfaces with varying microstructures might be non-uniform due to various forces such as electrostatic interactions, strong dipole–dipole interactions, or high mobility. When there are such lateral interactions, molecules that are experiencing repulsive interactions have wider peaks, whereas molecules that are experiencing

attractive interactions have narrower peaks. The change in orientation of the ferrocene thiol species on the same substrate, but with different morphological properties, is what causes the kind of interaction. The monolayer's lateral contacts or a neighbor-attractive surface activity effect are demonstrated by the redox peak's narrowness. A densely packed layer where anions create attractive forces between ferricenium cations is characterized by the limited breadth of the redox peak of ferrocene hexanethiol SAMs in NPG. In contrast, the redox peak of ferrocene hexanethiol SAMs in hb-NPG is broader and less sharp. A widened voltammetric peak indicates kinetic inhomogeneity within the surface ferrocene population, which could be the result of repulsive interactions between ferrocene units or monolayer heterogeneity brought on by the presence of upper and lower hierarchical architectures on the electrode surface. The average of the anodic and cathodic potentials was used to calculate the redox potential E^0 , and the fact that there is only a few mV of difference between the peaks shows that the electron transfer happens quickly and reversibly.

Table 6. Voltammetric parameters and surface coverage (per geometric area) values. Data depicted as average (3 measurements) \pm std dev.

Electrode	Charge/ μC	Surface coverage /nmol cm^{-2}	$E^0=(E_c+E_a)/2$ (mV)	FWHM/mV	$I_c/\mu\text{A}$	$I_a/\mu\text{A}$
Bare gold	1.1 ± 0.03	0.35	347.0	9.1	-3.46	4.6
Chemically dealloyed	16.9 ± 0.7	5.47	354.5	39.14	-25.89	37.07
hb-NPG	92.9 ± 5.5	30.1	326.1	160	27.14	29.56

3.6. Electrochemical detection of Glucose:

To determine the electrodes' catalytic efficiency, CVs for bare gold, NPG, and hb-

NPG were measured in both the presence and absence of 10 mM glucose. According to Figure 3.7, the oxidation peak current was observed at -0.39 V for bare gold, -0.02 V for NPG, and 0.57 V for hb-NPG. Peak currents for bare gold, NPG, and hb-NPG were determined to be 30, 400, and 1000 μA , respectively. Hb-NPG produced more than a two-fold increase in current compared to bare gold and NPG, demonstrating the electrode's increased sensitivity. More active sites are produced by the dual-sized pores and significantly greater roughness in hb-NPG, further demonstrating the electrode's enhanced catalytic activity. The characteristics observed in the NPG CV in the absence of glucose are identical to those previously reported in 0.1 M NaOH and likewise to those observed on cooled bead gold electrodes in 0.1 M NaOH solution. By oxidizing the water adlayer, an adsorbed layer of hydroxide is formed. Then, during the anodic scan, a surface layer of $\text{Au}(\text{OH})_3$ is formed, which is later reduced back to Au during the cathodic scan. The CV for hb-NPG in the absence of glucose has a reduction peak that is comparable to that of NPG, but it also has additional features in the anodic scan that could point to the presence of various exposed gold crystalline faces and perhaps a trace amount of residual silver.

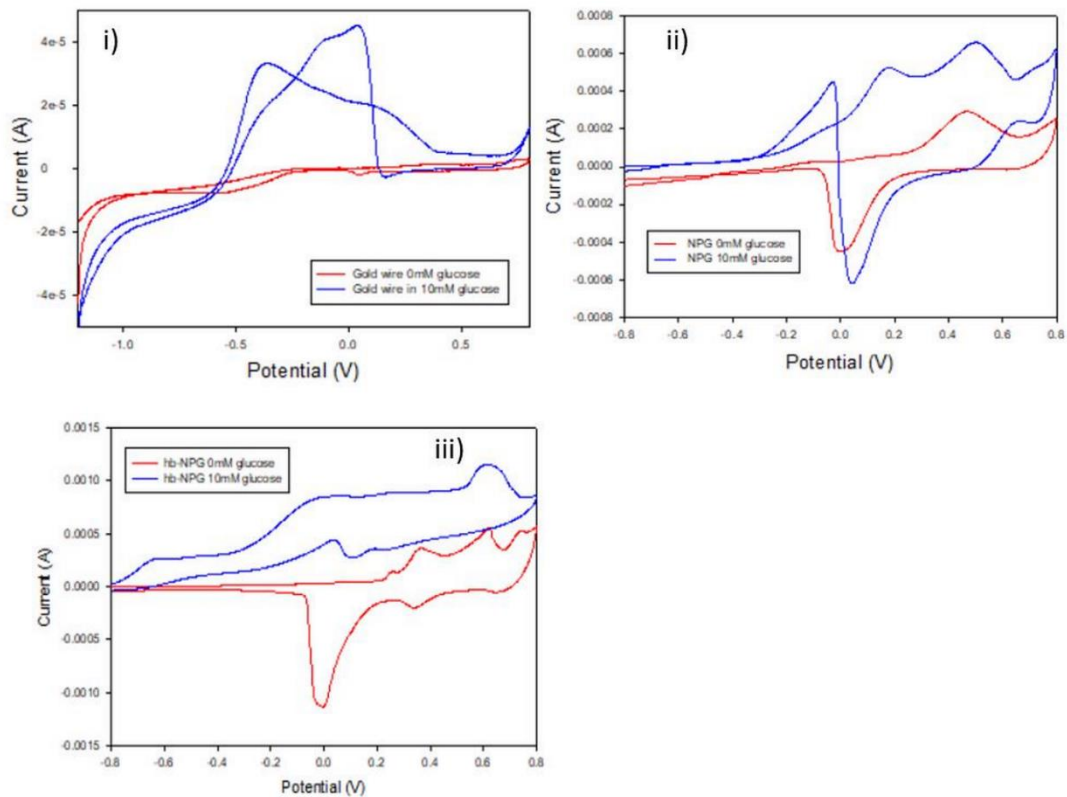


Figure 3.7. CVs of (i) bare gold, (ii) NPG and (iii) hb-NPG recorded in N_2 saturated NaOH solution with 10 mM glucose.

Utilizing the chronoamperometric method at an applied constant voltage derived from the CV of the appropriate electrode, the electrocatalytic response of various quantities of glucose on NPG and hb-NPG was assessed in real-time. Figure 3.8 illustrates the rapid current increment that was seen as the glucose concentration rose from 10 mM to 50 mM. The current response seen in NPG reached saturation at glucose concentrations greater than 50 mM. This could be as a result of the intermediates generated during the process adhering to the NPG electrode's active sites, which prevented the diffusion of incoming glucose molecules. As opposed to this, at 90 mM in hb-NPG, the current still did not saturate. Diffusion-controlled behavior is shown by the current response to changing glucose concentration, which showed a linear connection with a correlation coefficient of $r^2 = 0.93$.

Previous studies on the effectiveness of glucose sensors based on gold nanostructures have demonstrated that the high sensitivity of the nanoporous gold electrode is due to its surface area, which promotes the electro-oxidation of glucose.

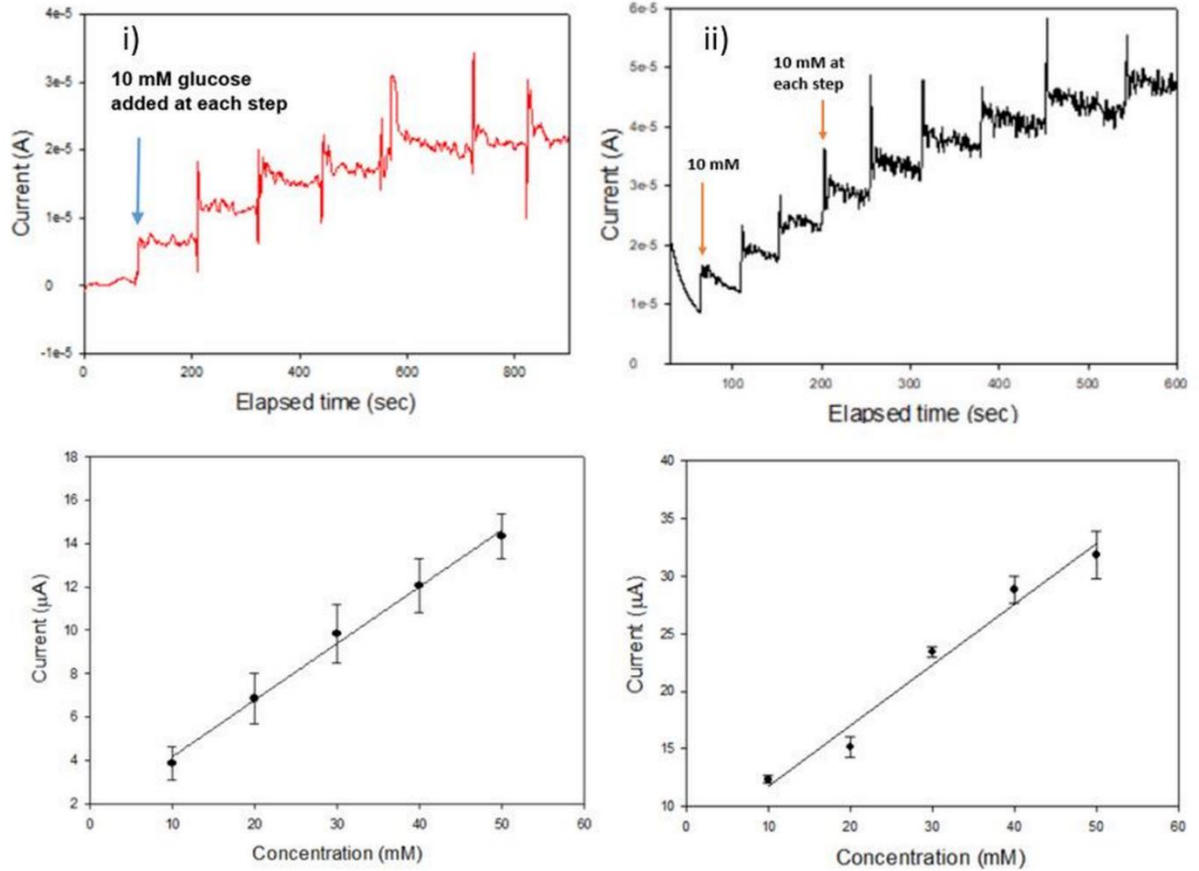


Figure 3.8. The chronoamperometric curve of (i) NPG and (ii) hb-NPG towards glucose with successive addition in 0.1M NaOH at the working potential of 0.02 V and 0.57 V, respectively. The calibration curve of the NPG and hb-NPG glucose sensor is shown below each of the figures.

The sensitivity was determined using the slope of the current versus concentration plot. In the current study, it was discovered to be $15.97 \mu\text{A mM}^{-1} \text{cm}^{-2}$ for hb-NPG against $6.53 \mu\text{A mM}^{-1} \text{cm}^{-2}$ for NPG, showing a better sensitivity for the hb-NPG

electrode. Hb-NPG is a promising electrode for electrochemical sensing applications because of its greater sensitivity and low detection limit. Evidently, a better current response results from the hierarchical architecture's exposure of numerous active Au-OH sites, which are known to be the active site for glucose oxidation in basic solution. In the presence of other competing species, the electrode's reaction to glucose was selective. As illustrated in Figure 3.9, the amperometric response for the selectivity of the hb-NPG sensor electrodes was tested by adding 10 mM glucose followed by 2 mM of interferents. It was determined that the hb-NPG-based sensor electrode was extremely selective, demonstrating negligible response for other species in the mixture under these circumstances after comparing the current response to glucose with several typical interferents. It has been suggested that the oxidation of glucose on NPG is kinetically controlled, but the oxidation of the interferents is controlled by diffusion, and that the magnitude of the current owing to the oxidation of glucose grows dramatically with surface area, whilst the magnitude from the interferents does not. Some of the interferents might also undergo oxidation at the higher potential required to detect the glucose reaction on hb-NPG.

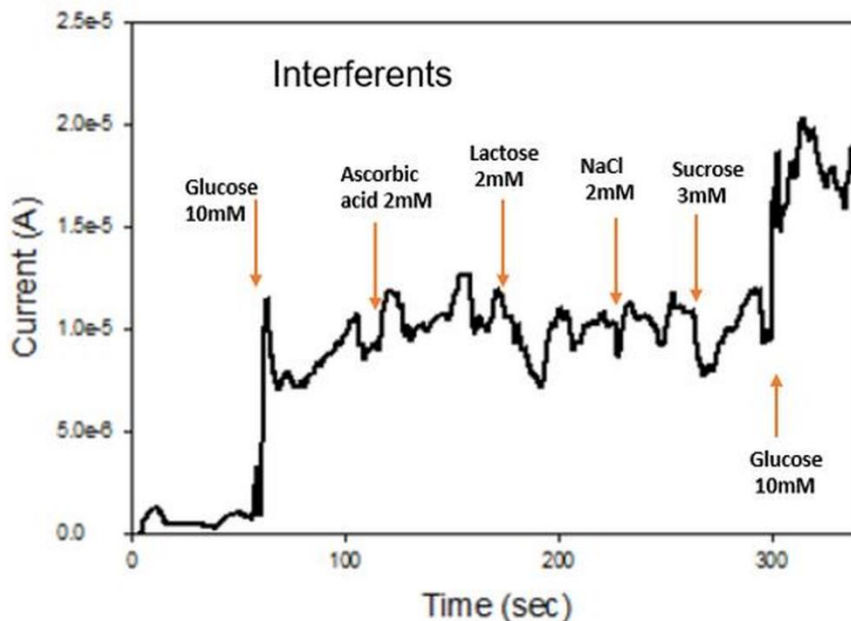


Figure 3.9. The current response of the fabricated hb-NPG glucose sensor in the presence of common interferents

Conclusion and future perspectives

We have presented a simple procedure of hierarchically structuring porous gold nanostructures consisting of dual-sized pores, higher active electrochemical surface area, and high roughness factor by employing a multistep process involving electrochemical dealloying-annealing-chemical dealloying. We have shown how the variation in process parameters can alter the morphology and the electrochemical performance of the electrode. It was seen that the resulting hierarchical nanoporous gold electrode possessed macro and mesopores giving rise to higher loading capacity as compared to a nanoporous gold electrode when made with Au: Ag (10:90) and annealed at 600°C for 3h.

The hierarchical electrode possessed curved interconnected ligaments with a ligament width of 938 ± 285 nm for the upper hierarchy dominated by highly active

low-coordinated atoms. The enhanced ligament width of hb-NPG is an excellent platform for catalytic reactions. The presence of an additional lower hierarchical ligament width of 51 ± 5 nm imparts a large specific surface area for functionalization. By transitioning from dealloying a binary alloy of Au-Ag to a dual-level hierarchy in hb-NPG, we are creating material for applications requiring fast access to larger molecules and their fast detection as seen in catalysis and sensing. A significant increase in the roughness factor from 13.6 to 231.5 was seen when going from Au₃₀:Ag₇₀ to Au₁₀:Ag₉₀ alloy composition. The higher surface roughness of hb-NPG as compared to NPG gives rise to greater electrochemical activity. This work lays a solid foundation for the design of high-performance electrochemical biosensors. The advantages of the hierarchical design of an electrode in biosensor applications stem from the high surface area and easy modification of the surface.

The hierarchical structure of the electrodes with a high surface area has an impact on the protein loading. In our study, we found that hb-NPG with dual hierarchical features enables higher loading capacity than the conventional NPG. The hierarchical architecture allows proteins to penetrate through their interconnected macropores and the lower hierarchical features lay a base for protein binding and communication with the substrate. Protein loading in an electrode is determined by the type of the material and its morphology. NPG and hb-NPG are both gold-based but the number of immobilized proteins is higher in hb-NPG due to the presence of macropores and mesoporosity which accelerates the binding of most proteins by physical/electrostatic interactions. The effect of morphological features in the

bimodal electrode has been seen to affect the shapes of CVs of ferrocene thiol SAMs. Non-ideal behavior in the form of peak broadening is observed in the case of hb-NPG. The electrochemical response of redox-active SAMs measured using CV has major a contribution coming from its electronic and supramolecular arrangement on the substrate.

The hierarchical electrode fabricated in our study has shown the great potential of monitoring human health via tracking signals from biological fluids. The hb-NPG electrode demonstrated a higher sensitivity of $15.97 \mu\text{A mM}^{-1} \text{cm}^{-2}$ for glucose detection compared to the traditional NPG ($6.53 \mu\text{A mM}^{-1} \text{cm}^{-2}$). The dual-sized porosity in hb-NPG provides a large surface area and easy penetration of the glucose molecules facilitating their oxidation.

Although the materials with hierarchical architecture have realized great progress, there are still some challenges. For commercialization, there is a need to develop novel preparation strategies involving fewer steps and lower costs. The electrochemical performance of cathode and anode materials can be enhanced in the future by logically bringing together the strengths of compatible materials with novel architectonics. Studies focusing on solving the issue of large-scale production and deep investigation of the in-situ formation mechanism of the hierarchical structures will be interesting to work in the future.

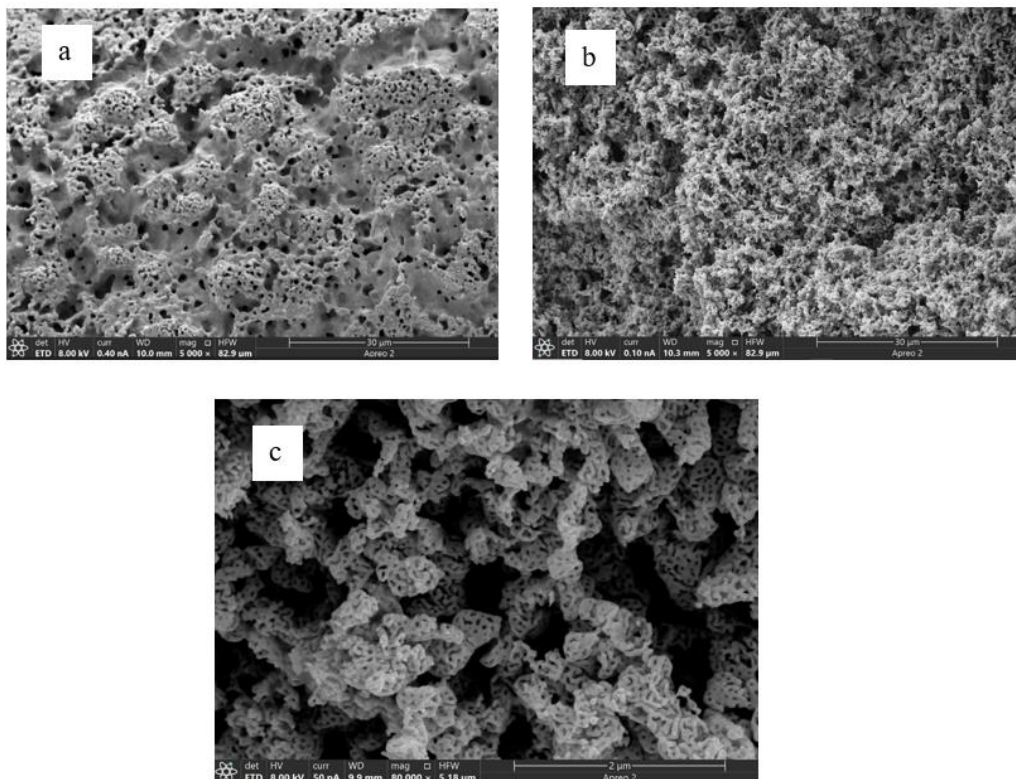
3B. ENGINEERING HIERARCHICALLY NANOPOROUS GOLD MONOLITH USING TEMPLATING APPROACH

Enhancing mass transfer and growing the active surface area are opposing processes in porous materials. Structural hierarchy could resolve this dilemma by generating continuous channels with varying length scales. However, it is relatively difficult to create porous metallic materials with discrete hierarchical layers. Here, a straightforward method combining chemical dealloying and soft templating is described for creating a hierarchical nanoporous gold (hb-NPG) monolith with bimodal hierarchy. The current process has a lot of potential for creating more hierarchically porous metals with enhanced structural and functional properties.⁷

3.7 The hierarchical bimodal pore structure characterization of hb-NPG monolith

Larger pores in the structure improve mass transmission whereas smaller pores increase surface area, making multimodal porosity, or hierarchical porous materials, of importance. Despite major advancements in the production of multimodal porous ceramics and metal oxides, hierarchical porous noble metal materials cannot currently be produced synthetically. This is despite the fact that porous noble metal materials have been extensively used in catalytic, electrochemical, and purifying processes.⁸ In our study hierarchically porous noble metal materials were produced by combining the templating and dealloying processes.⁹ At each stage of the preparation procedure, SEM and composition analyses were performed to understand the morphology, porosity structure, and function of the residual silver. It has been noted that the increase in porosity was associated with the increase in compaction of the sponge-like framework brought on by the coarsening of the connected silver particles, development of the sintering

necks, and shrinkage of the empty spaces.¹⁰ The organic template was thermally destroyed and a complete silver-gold monolith was left behind after heating the mixture of gold, silver, and dextran to 600°C (Figure 3.10 a). SEM micrographs (Figure 3.10 b, 3.10 c) have verified the existence of the hierarchical porous structure, which comprises of numerous micro/mesopores and related macropores. The bimodal porous architecture, in which silver was dissolved with concentrated HNO₃, was found to be uniformly distributed throughout the 3D gold nanostructured monolith, creating voids in the framework. Only 1-2 atomic % of silver remained after chemical dealloying with strong nitric acid, which is significantly less than the alloy's initial composition, as shown in (Figure 3.10 d), according to an EDS study.



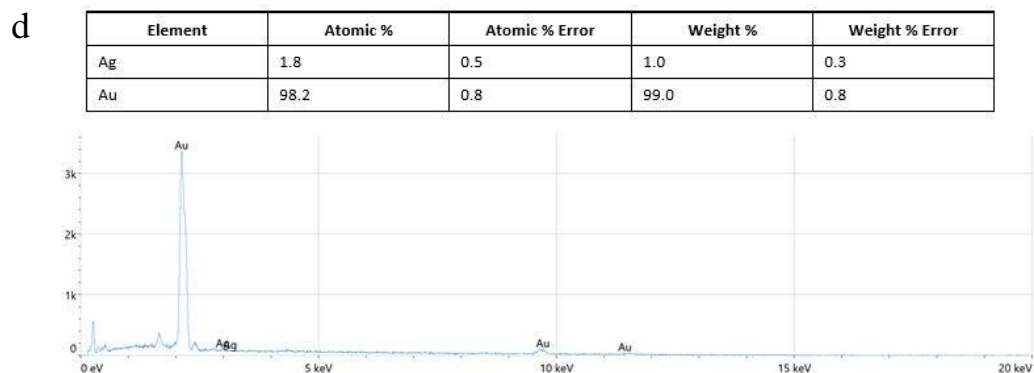


Figure 3.10. SEM images of a) gold-silver monolith after being annealed at 600°C showing porecoarsening b) pores of upper hierarchy, c) pores of lower hierarchy after chemical dealloying, and d) EDS data after chemical dealloying in concentrated nitric acid.

The resulting hierarchical nanoporous gold sponge contained pores of upper hierarchy that measured $0.359 \pm 0.143 \mu\text{m}$ and an open framework comprised of metallic gold strands that were connected and had discrete crystallites (Figure 3.11a). The distributions of pore size for the lower hierarchy were found to be $42.5 \pm 14.8 \text{ nm}$, respectively (Figure 3.11 b). In order to create the hierarchical nanoporous gold sponges, the viscous dextran matrix had to be broken down and transformed into a carbon foam that contained metallic particles. Upon gradually removing the carbon by heating to higher temperatures, the foam was compressed, and the metallic particles fused to make an open framework sponge. This sponge was then treated to chemical dealloying to produce the hierarchical powder.

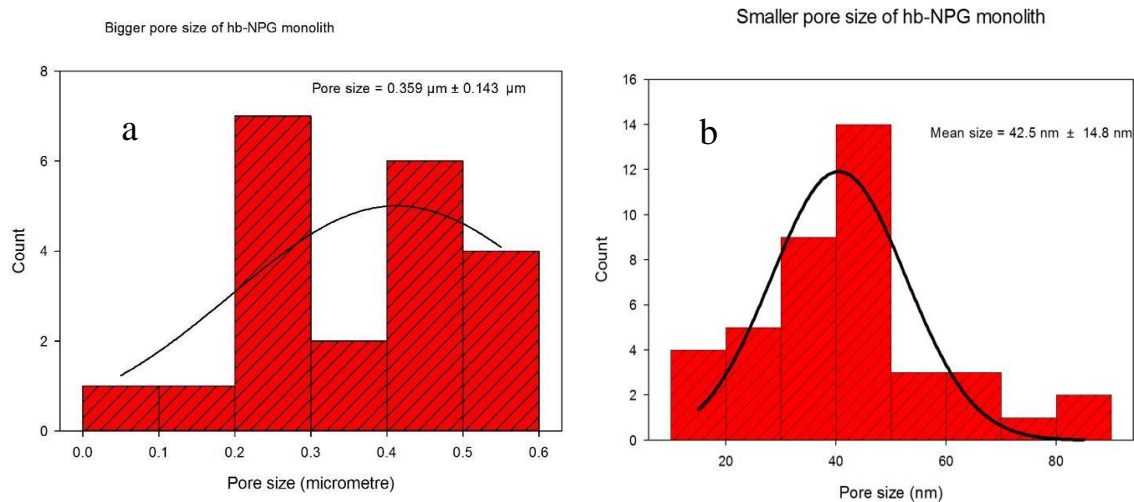


Figure 3.11. Pore size distribution in hierarchical bimodal nanoporous gold monolith, representing a) upper hierarchical pore size distribution and b) lower hierarchical pore size distribution.

3.8 BET analysis

The examination of the specific surface area and pore size distribution involved nitrogen adsorption-desorption. The monolith (alloy) has a surface area of $0.311 \text{ m}^2 \text{ g}^{-1}$, and the pore volume was 0.0019 mL/g (as seen in Figure 3.12). It was hypothesized that mesopores, increasing the surface area and active sites, were present in these folds on the skeleton surface of the monolith. When dealloying was completed, the monoliths displayed a noticeably greater surface area of $1.50 \text{ m}^2 \text{ g}^{-1}$ (pore volume, 0.0259 mL/g). Additionally, as compared to before the dealloying operation, the pore size distribution broadened. The manufactured monolith showed a highly porous surface area and a hierarchically porous structure that not only offered fluids passageways, but also additional active sites and space to encourage interaction between the analyte and solution.¹¹

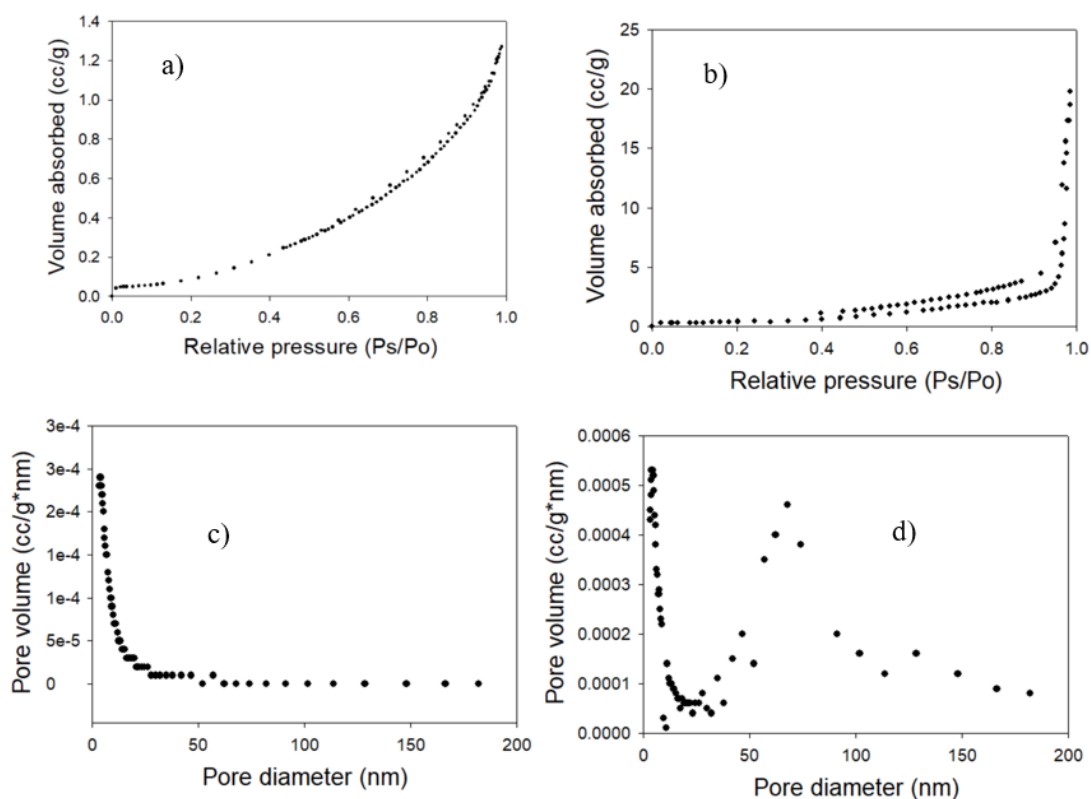


Figure 3.12. BET isotherm (N_2 gas) of a) annealed and b) hbNPG. BJH pore size distribution is shown for c) annealed and d) hbNPG.

3.9 TGA analysis

TGA can be used to quantitatively measure the change or rate of change in a material's weight as a function of temperature or time. In the current study, we analyzed the amount of lipoic acid molecules loaded onto the hb-NPG monolith and annealed monolith using TGA in order to quantify the surface coverage of the molecules being immobilized while taking into account the distinct surface areas of the monoliths. On the air-dried modified material, we performed pyrolytic breakdown while scanning up to 800 °C in an inert environment. At this temperature, it was anticipated that lipoic acid molecules would completely

pyrolize.¹²

The thermal stability and loading capacity of the monolithic material (both with and without lipoic acid) were examined using TGA. As the temperature rose from 20 to 600 °C in the lipoic acid loaded dealloyed sample where the hierarchical bimodal porous structure was developed, a considerable weight loss occurred. The beginning temperature of weight loss during the TGA on the lipoic acid loaded sample started from 200°C until 400 °C due to the creation of bimodal pores in the monolith.

It was found that the sample with lipoic acid immobilized on hb-NPG monolith had lost 6.5 % of its original weight throughout the temperature scan. The average mass loss for the hb- NPG monolith was determined to be 2.13×10^{-4} g (initial average sample weight was 3.29 mg). This mass loss amounted to 0.01032×10^{-4} moles (molecular weight of LA is 206.33 g/mol) of self-assembled LA on the sample surface, equivalent to 0.01 moles or 6.21×10^{17} molecules (2.06×10^{-4} mol/cm² or 1.24×10^{16} molecules/cm²). The TGA thermograms of hb-NPG monolith with and without LA loading are shown in Figure 3.13 (temperature raised at 20 °C min⁻¹).

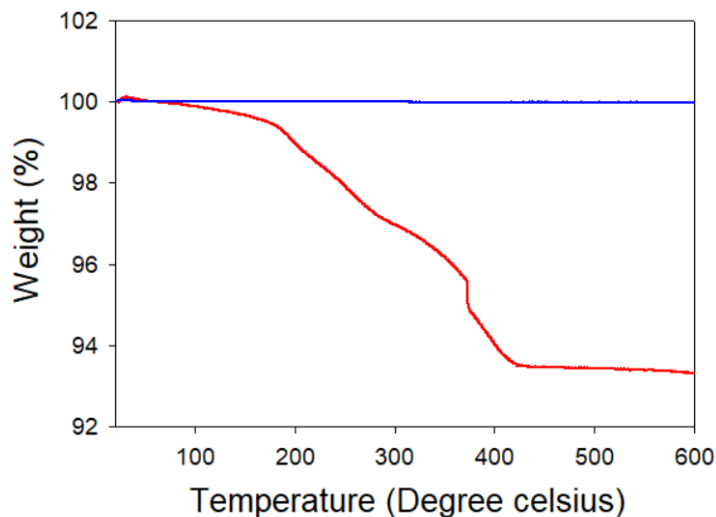


Figure 3.13. Thermogravimetric curve of hb-NPG (blue) and hb-NPG with lipoic acid (red)

Conclusion and future perspectives

This study focused on the fabrication of a hb-NPG monolith with bimodal pores ($0.359 \pm 0.143 \mu\text{m}$ and $42.5 \pm 14.8 \text{ nm}$) created using a mix of alloying, annealing, and soft templating techniques. Using BET, the prepared monolith's specific surface area was assessed, and was found to be $1.50 \text{ m}^2 \text{ g}^{-1}$. According to TGA, the monolith's hierarchy increases its loading capacity. Furthermore, our findings show how dextran may be used as a framework-generating agent to create a bicontinuous gold monolith with uniform hierarchical pore morphology throughout a variety of length scales without the need for additional support materials. An open framework template is created when the dextran matrix expands during annealing, and a hierarchical pore structure is created when the dextran matrix is subsequently chemically dealloyed. Even though we have concentrated on gold monoliths in our study, we anticipate that this approach will easily lead to

a variety of technologically significant materials with hierarchical bicontinuous architecture and be useful in a number of emerging applications, including energy systems, sensors, and tissue engineering.

3C. COMPARATIVE STUDY OF ELECTROCHEMICAL RECOGNITION OF GLYCOPROTEIN BIOMARKERS USING LECTIN MODIFIED NPG AND HB-NPG

The lectin's binding affinity for the glycoprotein immobilized is determined by the differences in ligand display at substrate's surface (hb-NPG and NPG surfaces in our study). The analyte molecules' access to ligands might be constrained by the tiny NPG pores. Larger holes in hb-NPG make it simpler for molecules to be transported. In this study, the bimodal pore structure has proven to have better responsiveness to fetuin binding than traditional NPG.

3.10 *Analysis of the surface morphology of the fabricated electrodes*

The structural characterization of manufactured electrodes was carried out using SEM. The NPG is shown in the top view in Figure 3.14 a. Following chemical dealloying, NPG exhibits the anticipated open, connected network of ligaments and pores. The average interligament distance was determined to be 36.4 ± 10 nm, while the average ligament breadth was found to be 48.1 ± 14 nm. SEM imaging revealed that the hb-NPG synthesized from Au₁₀Ag₉₀ (at.%) contained upper and lower hierarchical structures. Here, larger pores indicate an upward hierarchy whereas smaller pores indicate a lower hierarchy. Figure 3.14.b shows the top view of the outside of the gold wire coated with hb-NPG.

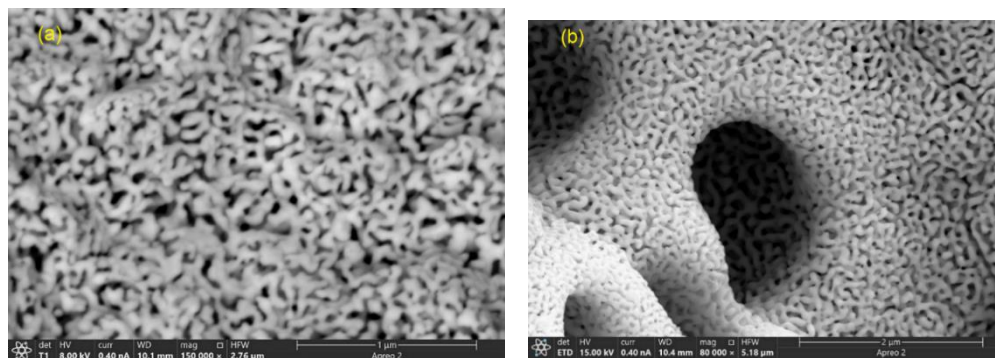


Figure 3.14. SEM images (top-view) of two different types of electrodes (a) nanoporous gold prepared (at 150 kX magnification) using 30:70 (Au:Ag) alloy deposition by providing -1.0 V (vs. Ag/AgCl, KCl saturated) for 10 min on gold wire and subsequently immersing in concentrated nitric acid for chemical dealloying to generate a porous architecture and, (b) hierarchical bimodal nanoporous gold (at 80 kX magnification) prepared using a multistep alloying-partial dealloying-annealing-chemical dealloying strategy to generate dual sized pores.

3.11 *Lectin-enzyme conjugate activity detected by square-wave voltammetry*

By producing lipoic acid SAMs on both electrode's surfaces and immobilizing the SNA-ALP conjugate onto the EDC/NHS activated SAMs, it was feasible to compare NPG covered gold wire and hb-NPG covered gold wire for potential usage in electrochemical ELLA. In order to conduct SWV investigations, these modified electrodes were immersed in 1 mM p-APP in glycine buffer (pH 9.0, 100 mM) for 5 minutes before the SWV sweep was recorded. Following the interaction with the substrate (p-APP), Figure 3.15 shows the SWVs of both electrodes (NPG and hb-NPG, respectively), with the presence of the lectin-enzyme combination. The

SWVs of the electrodes treated with the SNA-ALP conjugate modified electrodes exhibit peak difference current after being incubated with 1 mM p-APP, as can be shown. Following incubation with 1 mM p-APP, the modified hb-NPG displays a sizable peak difference current (36.9 μA), whereas the modified NPG's SWV displays a lesser peak difference current (29.1 μA). This research reveals that the hb-NPG coated Au wire electrode is more sensitive than the NPG electrode for use in an electrochemical experiment using an immobilized enzyme-lectin combination. Only when the enzyme and substrate interact to form the product does the peak difference current appear.

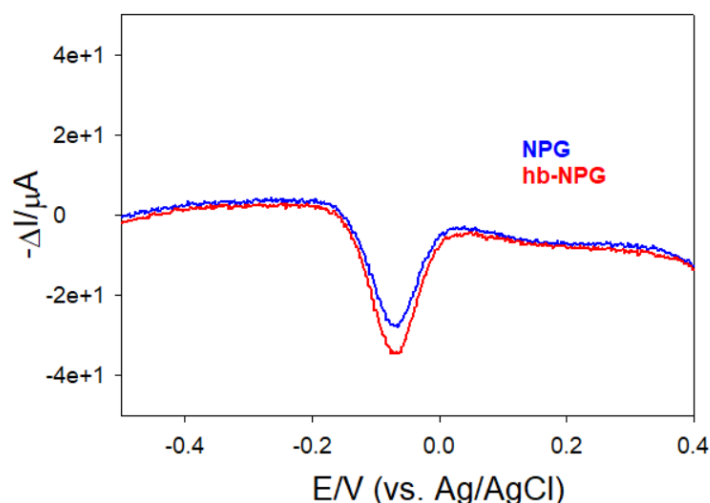


Figure 3.15. Square-wave voltammograms of SNA-ALP conjugate immobilized on lipoic acid modified a) NPG and b) Hb-NPG. SWV were recorded with 1 mM p-APP in glycine buffer (pH 9, 100 mM) after 5 min incubation with the substrate p-APP. To conduct SWV (vs. the Ag|AgCl reference electrode), the following parameters were used: 50 mV for the pulse height, 0.2 sec for the pulse width, 2 mV for the step height, and 5.0 mV sec^{-1} for the scan rate.

3.12 Evaluation of the Michaelis-Menten constant K_m for NPG and hb-NPG electrodes

Significant variations can be seen when comparing measurements of enzyme kinetics in free solution to those for immobilized enzyme reactions. In porous materials, the reaction rate of the enzyme can be influenced by a variety of variables, including the accessibility of the substrate in the local microenvironment of the enzyme, partitioning and mass transfer constraints, and others.¹³ It was demonstrated that free alkaline phosphatase had a K_m value of $56 \pm 5 \mu\text{M}$ in pH 9.0 TRIS buffer solution using p-APP as the substrate.¹⁴ In our previous research, we discovered that the measured value of K_m increased from $40 \mu\text{M}$ to $210 \mu\text{M}$ when the IgG antibody was conjugated to the ALP enzyme itself in solution. Immobilization with EDC/NHS activated lipoic acid monolayers using IgG-ALP conjugates, where the monoclonal IgG binds free prostate specific antigen (fPSA), was observed to result in an increase in K_m from $210 \mu\text{M}$ to $300 \mu\text{M}$ with UV-visible detection of the p-nitrophenyl phosphate product at 410 nm .¹⁵

Individual SWV are displayed in Figures 3.16 a and 3.16 c throughout a substrate concentration range of 0.01 mM to 1.0 mM . The SWV sweeps showed a distinct p-aminophenol oxidation peak in this concentration range. The ALP activity's byproduct, p-AP, is converted to p-quinoneimine on NPG and hb-NPG at a potential of roughly -0.1 V (vs. Ag|AgCl). Porous surfaces have greater electroactivity than relatively flat gold surfaces. Nanostructure, which establishes the oxidation potential based on surface flaws, curvature, and roughness, is a prerequisite for catalytic activity. According to Michaelis-Menten kinetic behavior, when the

substrate concentration grew, the peak difference current also increased and demonstrated a tendency toward saturation before plateauing, as seen in Figures 3.16 b and 3.16 d. The peak differential current of the SWV measurement is related to the initial reaction rate and, subsequently, to the reaction kinetics. The K_m value was established by fitting the data to the Michaelis-Menten equation. The conjugate of SNA-ALP on NPG in this experiment shows the K_m value to be $185 \pm 1.87 \mu\text{M}$. After the conjugate was immobilized on hb-NPG, the K_m value rose to $728 \pm 1.2 \mu\text{M}$. These findings were significant because the majority of enzyme electrodes function near K_m values. A lower K_m value for NPG indicates that less substrate is required for the enzyme to saturate or reach its maximum velocity. The increased K_m of hb-NPG clearly indicates that more substrate is needed for the enzyme to reach its optimum activity.¹⁶

The increase in K_m value in the case of hb-NPG over NPG can be attributed to several variables, including the well-known effect of enzyme immobilization. The enzyme affinity can change if the enzyme's structure is altered during immobilization on the electrode's heterogeneous surface. Another factor is the diffusion restriction brought on by the hierarchically porous structure, where the substrate must diffuse via the pores in order to reach the enzyme. When compared to standard NPG, the bimodal pore structure offers more pathways for substrate entry and allows for changes in substrate concentration to reach deeper inside the electrode. The increased K_m found for hb-NPG is consistent with the idea that deeper substrate diffusion into hb-NPG than NPG should require a higher substrate concentration to reach half of the highest reported enzyme activity. The time it takes

for substrate and product diffusion into and out of the electrode's structure might be quite important because of the hierarchical porosity in the electrode's structure.¹⁷

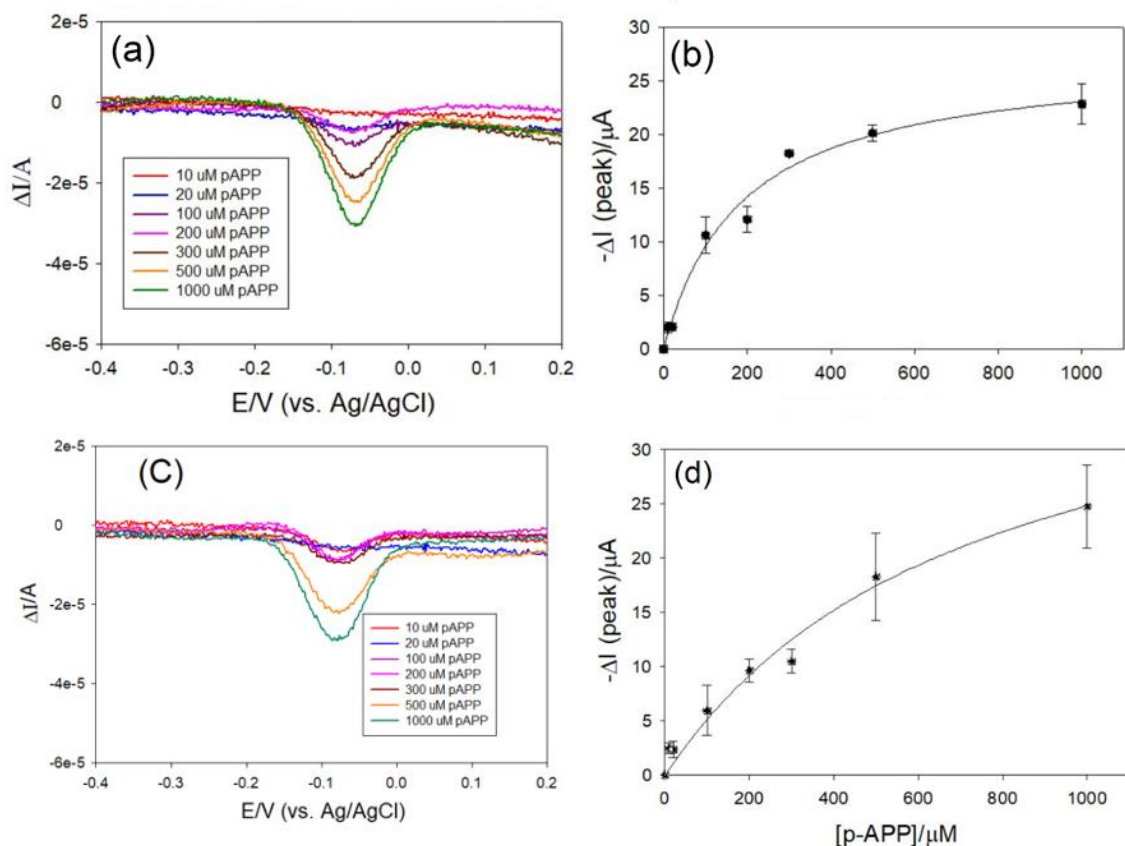


Figure 3.16. SWV for lipoic acid SAMs that have SNA-alkaline phosphatase conjugate immobilized on (a) NPG and (c) hb-NPG. After two minutes of incubation, SWV was tested for p-APP concentrations in a pH 9.0 glycine buffer (100 mM). SWV was measured using an Ag|AgCl reference electrode, a pulse height of 50 mV, a pulse width of 0.2 seconds, a step height of 2 mV, and a scan rate of 5.0 mV sec^{-1} .

The difference current peak heights from SWV scans of the SNA-ALP conjugate immobilized on lipoic acid SAMs on b) NPG and d) hb-NPG were used to fit the Michaelis-Menten equation. The standard errors of the three measurements are

displayed in the error bars.

3.13 Kinetic enzyme-linked lectinsorbent assay on NPG and hb-NPG electrodes

The kinetic enzyme-linked lectinsorbent assay is, in theory, based on the difference in the rate of the enzyme reaction of ALP conjugated to SNA before and after glycoprotein binding to the SNA. The proximity of a large glycoprotein molecule linked to a lectin prevents the p-APP substrate from binding to ALP sterically. Due to the glycoprotein binding that prevents substrate from reaching the active site, the initial rate of enzyme-catalyzed oxidation of p-APP to the oxidizable p-aminophenol product will be slower. It has been postulated that the square wave voltammogram's peak difference current is inversely related to the rate of the enzyme reaction. The difference between the SWV peak difference current before and after incubation with glycoprotein serves as the response variable for the assay. The concentration of p-APP at 1 mM, which is close to the K_m value at hb-NPG, was used for our measurements since lesser concentrations did not produce current peaks of significant amplitude in the SWV scans. For the kinetic glycoprotein assay, the incubation period for conjugate and glycoproteins is crucial. The incubation period of two hours was selected to ensure that peak current saturation had been attained.

In our study, we found that when glycoprotein attaches to SNA-ALP complex, access of the p-APP to the enzyme active site is hindered and a decrease in reaction velocity was revealed (Figure 3.17 a and 3.17 c). Figures 3.17 b and 3.17 d depict the fetuin binding isotherms to the immobilized SNA-ALP conjugate on NPG and hb-NPG. As was expected, a decrease in enzymatic activity accompanied the rise in

glycoprotein content; this is demonstrated by the rising difference in peak difference current. When compared to NPG, SNA has a stronger affinity for binding fetuin to hb-NPG, with K_d values of $0.23 \pm 0.02 \mu\text{M}$ and $0.83 \pm 0.13 \mu\text{M}$, respectively.

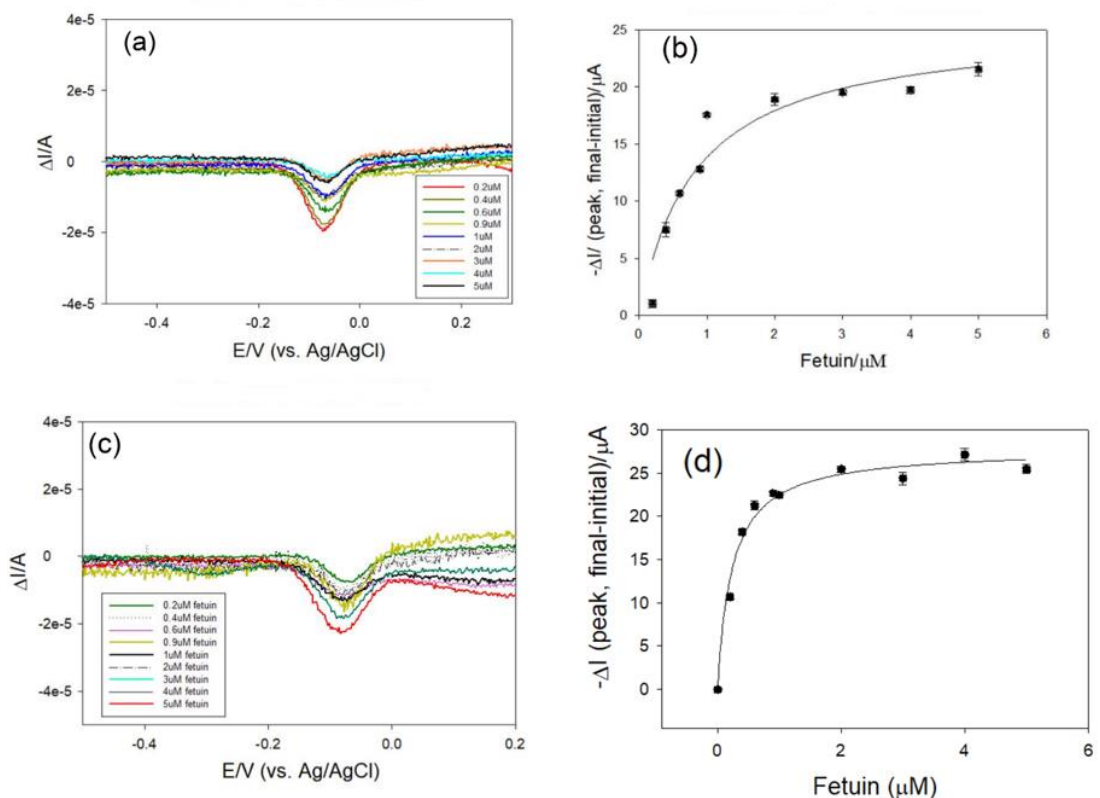


Figure 3.17. Voltammograms recorded after binding of SNA – ALP conjugate to varying concentrations of fetuin immobilized on (a) NPG and (c) hb-NPG by covalent conjugation to lipoic acid SAMs. Different concentrations of fetuin were incubated for 2 hours (in PBS, pH 7.4, 10 mM with 1 mM) with SNA-ALP conjugate immobilized on lipoic acid modified electrodes. To perform SWV, a pH 9.0 glycine buffer (100 mM) with a pulse height of 50 mV, a pulse width of 0.2 sec, a step height of 2 mV, and a scan rate of 5.0 mV sec^{-1} were used.

The kinetic ELLA response for (b) NPG and (d) hb-NPG is shown. The difference in SWV peak difference current before and after incubation was plotted to obtain

the response plot. The error bars show the standard deviation across three measurements.

Another glycoprotein known as asialofetuin was also looked at for the kinetic assay, but the protein did not produce any discernible change in the peak current, which we presume is because the protein has a markedly reduced binding affinity for SNA (Figures 3.18 a and 3.18 b). On hb-NPG and NPG, SNA has demonstrated a poor affinity for binding asialofetuin, with K_d values of $0.53 \pm 0.06 \mu\text{M}$ and $1.08 \pm 0.24 \mu\text{M}$, respectively. SNA mostly attaches to sialic acid coupled to terminal galactose in a 2-6 and, to a lesser extent, a 2-3 linkage. Mono-, bi-, and triantennary glycans with a 2:1 ratio of $\alpha 2 \rightarrow 3$ - and $\alpha 2 \rightarrow 6$ -linked sialic acid residues can be found in fetuin. The proteins fetuin and asialofetuin have identical sequences and three N-linked glycosylation sites. In contrast, fetuin has an average of 11 mol of sialic acid per mol of protein, whereas asialofetuin does not, which results in decreased SNA binding.¹⁸⁻¹⁹ Weaker secondary forces may be the cause of non-specific binding of SNA with asialofetuin.

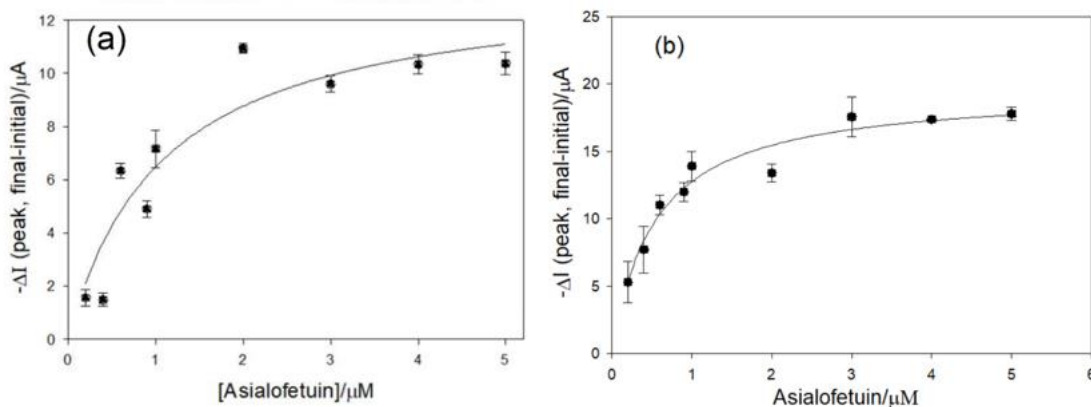


Figure 3.18. (a) NPG and (b) hb-NPG kinetic ELLA response. The difference in SWV peak difference current before and after incubation was plotted to obtain the response plot. Different concentrations of asialofetuin were incubated for 2 hours (in PBS, pH 7.4, 10 mM with 1 mM) with SNA-ALP conjugate immobilized on lipoic acid modified electrodes. To perform SWV, a pH 9.0 glycine buffer (100 mM) with a pulse height of 50 mV, a pulse width of 0.2 sec, a step height of 2 mV, and a scan rate of 5.0 mV sec⁻¹ were used. The error bars show the standard deviation across three measurements.

3.14 Effect of BSA on ELLA

In the study, the effect of interfering protein was investigated using BSA as a model serum protein. The incubation solution for the kinetic ELLA contained 2 mM fetuin and 5 mg mL⁻¹ of BSA. The addition of 5 mg mL⁻¹ BSA had no impact on the difference in peak current. Therefore, the binding of glycoprotein to SNA and the associated lower enzymatic reaction rate are to blame for the dropping peak current observed. When 5 mg mL⁻¹ BSA was used in place of glycoprotein in the kinetic test as a control experiment, there was no difference in the signal (Figure 3.19).

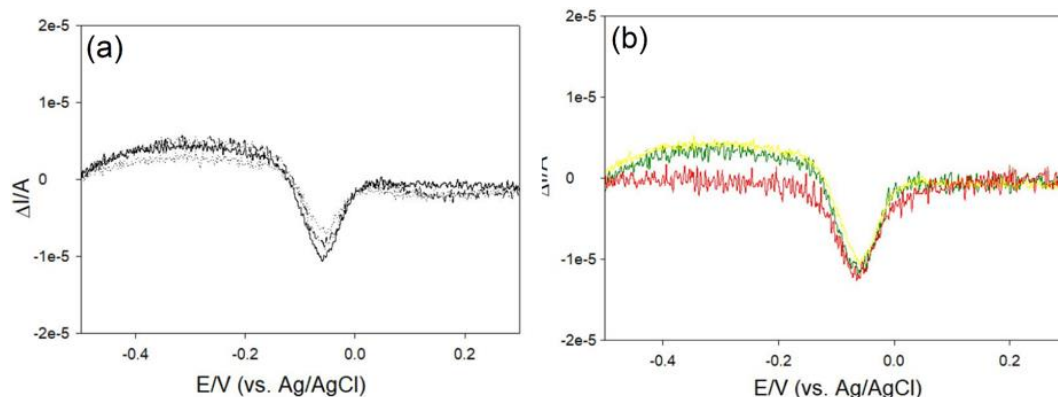


Figure 3.19. Effect of BSA on hb-NPG kinetic ELLA assay. SWV measurements were carried out a) before and b) after the addition of BSA (5 mg mL^{-1}) in the incubation solution containing fetuin $2 \mu\text{M}$ dissolved in PBS, pH 7.4, 10 mM. SWV was carried out in pH 9.0 glycine buffer (100 mM) with pulse heights of 50 mV, pulse widths of 0.2 sec, step heights of 2 mV, and scan rates of 5.0 mV sec^{-1} .

Conclusion and future perspectives

Through this study, we demonstrate how hb-NPG can be used as a lectin immobilized support to detect glycoproteins. The creation and implementation of devices based on this architecture for use in the diagnosis of important glycoproteins can be facilitated by having a basic understanding of the structure of hb-NPG. Hb-NPG is undoubtedly more sensitive than previously employed NPG from the perspective of binding characteristics. The structural architecture of hb-NPG comprising of a bimodal porous structure, is advantageous. The preparation of its monolithic form for targeting biologically significant glycoproteins acting as biomarkers and receptors in disease signaling pathways can be challenging but is a promising future development for hb-NPG, with significantly improved affinity for a wide range of practical applications. Additionally, the incorporation of additional cutting-edge materials (such metal-organic frameworks, quantum dots, and zeolites) would significantly increase the utility of hierarchically porous gold materials for the sensitive and precise detection of glycoprotein and other biomarkers.

References

1. Evans, U.; Colavita, P. E.; Doescher, M. S.; Schiza, M.; Myrick, M. L., Construction and Characterization of a Nanowell Electrode Array. *Nano Letters* **2002**, 2 (6), 641-645.
2. Shalev, G.; Landman, G.; Amit, I.; Rosenwaks, Y.; Levy, I., Specific and label-free femtomolar biomarker detection with an electrostatically formed nanowire biosensor. *NPG Asia Materials* **2013**, 5 (3), 1-7.
3. Damborský, P.; Švitel, J.; Katrlík, J., Optical biosensors. *Essays Biochem* **2016**, 60 (1), 91-100.
4. Song, M.; Lin, X.; Peng, Z.; Xu, S.; Jin, L.; Zheng, X.; Luo, H., Materials and Methods of Biosensor Interfaces With Stability. *Frontiers in Materials* **2021**, 7 (438), 1-11.
5. Tan, Y. H.; Schallom, J. R.; Ganesh, N. V.; Fujikawa, K.; Demchenko, A. V.; Stine, K. J., Characterization of protein immobilization on nanoporous gold using atomic force microscopy and scanning electron microscopy. *Nanoscale* **2011**, 3 (8), 3395-3407.
6. Tokudome, Y.; Fukui, M.; Tarutani, N.; Nishimura, S.; Prevot, V.; Forano, C.; Poologasundarampillai, G.; Lee, P. D.; Takahashi, M., High-Density Protein Loading on Hierarchically Porous Layered Double Hydroxide Composites with a Rational Mesostructure. *Langmuir* **2016**, 32 (35), 8826-8833.
7. Shi, Y.; Zhang, Y.; Yu, B.; Yin, K.; Qin, J.; Zhang, Z., Porous gold with three-level structural hierarchy. *iScience* **2022**, 25 (10), 105113.
8. Bond, G. C.; Thompson, D. T., Gold-catalysed oxidation of carbon monoxide. *Gold Bulletin* **2000**, 33 (2), 41-50.
9. Brezesinski, K.; Wang, J.; Haetge, J.; Reitz, C.; Steinmueller, S. O.; Tolbert, S. H.; Smarsly, B. M.; Dunn, B.; Brezesinski, T., Pseudocapacitive Contributions to Charge Storage in Highly Ordered Mesoporous Group V Transition Metal Oxides with Iso-Oriented Layered Nanocrystalline Domains. *Journal of the American Chemical Society* **2010**, 132 (20), 6982-6990.
10. Walsh, D.; Arcelli, L.; Ikoma, T.; Tanaka, J.; Mann, S., Dextran templating for the synthesis of metallic and metal oxide sponges. *Nature materials* **2003**, 2 (6), 386-90.
11. Wang, Y.; Zhang, L.; Asoh, T. A.; Uyama, H., Facile Preparation of Hierarchically Porous Monolith with Optical Activity Based on Helical Substituted Polyacetylene via One-Step Synthesis for Enantioselective Crystallization. *ACS applied materials & interfaces* **2021**, 13 (40), 48020-48029.
12. Sondhi, P.; Neupane, D.; Bhattarai, J. K.; Demchenko, A. V.; Stine, K. J., Facile fabrication of hierarchically nanostructured gold electrode for bio-electrochemical applications. *Journal of electroanalytical chemistry (Lausanne, Switzerland)* **2022**, 924.
13. Neira, H. D.; Herr, A. E., Kinetic Analysis of Enzymes Immobilized in Porous Film Arrays. *Analytical chemistry* **2017**, 89 (19), 10311-10320.
14. Thompson, R. Q.; Barone, G. C., 3rd; Halsall, H. B.; Heineman, W. R.,

- Comparison of methods for following alkaline phosphatase catalysis: spectrophotometric versus amperometric detection. *Analytical biochemistry* **1991**, *192* (1), 90-5.
15. Shulga, O. V.; Zhou, D.; Demchenko, A. V.; Stine, K. J., Detection of free prostatespecific antigen (fPSA) on a nanoporous gold platform. *Analyst* **2008**, *133* (3), 319-322.
16. Robinson, P. K., Enzymes: principles and biotechnological applications. *Essays in biochemistry* **2015**, *59*, 1-41.
17. Goldhahn, C.; Taut, J. A.; Schubert, M.; Burgert, I.; Chanana, M., Enzyme immobilization inside the porous wood structure: a natural scaffold for continuous-flow biocatalysis. *RSC Advances* **2020**, *10* (35), 20608-20619.
18. Du, W.; Dai, M.; Li, Z.; Boons, G. J.; Peeters, B.; van Kuppeveld, F. J. M.; de Vries, E.; de Haan, C. A. M., Substrate Binding by the Second Sialic Acid-Binding Site of Influenza A Virus N1 Neuraminidase Contributes to Enzymatic Activity. *Journal of virology* **2018**, *92* (20).
19. Shipman, J. T.; Nguyen, H. T.; Desaire, H., So You Discovered a Potential Glycan-Based Biomarker; Now What? We Developed a High-Throughput Method for Quantitative Clinical Glycan Biomarker Validation. *ACS omega* **2020**, *5* (12), 6270-6276.

CHAPTER IV: EVALUATING THE BINDING AFFINITY OF LPS ANTAGONISTS AND CURCUMIN ANALOGS TO PROTEIN RECEPTORS INVOLVED IN SEPSIS

4A. QUARTZ CRYSTAL MICROBALANCE AS A SENSITIVE TECHNIQUE FOR REAL- TIME ANALYSIS OF THE BINDING AFFINITY OF LPS ANTAGONISTS TO PROTEIN RECEPTORS

Sepsis is a life-threatening condition characterized by bacterial infection with a strong inflammatory response and is a serious health problem throughout the globe with mortality rates of 40-60%. Bacterial endotoxin or LPS are amphiphilic macromolecules occupying a large portion of the outer membrane of the Gram-negative bacteria and contribute significantly to the structural integrity. The three regions of LPS are lipid A, the core oligosaccharide domain, and O-antigen with repetitive sugar units. The toxic activity is generated from the polyacylated glucosamine disaccharide in lipid A. The event wherein lipid A interacts with the macrophages is of utmost importance because that will eventually lead to a series of chemical reactions activating the immune system and releasing the proinflammatory molecules leading to systemic toxicity. LPS interacts with the macrophage receptor protein, cluster of differentiation 14 (CD14), via its Lipid A moiety. The LPS-binding protein (LBP) is another important factor in the pathogenesis of sepsis through LBP-LPS complexation. Therefore, it is crucial to understand how LPS interacts with proteins when creating efficient anti-sepsis therapeutics. A tremendous amount of potential has been seen in techniques that prevent the binding interactions between an endotoxin and a host. Because of this, it is heavily thought that LPS antagonists could be effective weapons to manage the condition of sepsis. The primary objective of our study is to design a sensitive

platform to gather quantitative data on the binding affinity of membrane proteins with LPS antagonists. Using a surface-modified quartz crystal microbalance (QCM) sensor, we have investigated the binding affinities of LPS antagonists with proteins including LBP and CD14 in this work.

A sensitive technique for measuring mass change occurring at or near surfaces, or inside thin films, is the Quartz Crystal Microbalance with Dissipation Monitoring (QCM-D). Extremely minute chemical, mechanical, and electrical changes occurring on the sensor surface can be detected by QCM-D and converted into electrical signals that can be examined to analyze dynamic processes. Since interactions of medical devices with the physiological environment are mediated by surface features, surface topography and chemical composition are of utmost significance in biomedical applications.¹ This work is based on the modification of a sensor surface in order to examine protein-drug interactions in the study of sepsis. Based on the findings of our experiments, LPS antagonists may be employed as a therapeutic agent to treat diseases brought on by LPS.

4.1 Characterization of surface modified QCM sensors using contact angle measurement

According to the protein adsorption principle, the wettability of a material's surface plays a crucial role in the adsorption of proteins. One common technique for determining a material's wettability is to measure the water contact angle.² Figure 4.1 displays the contact angles and a cross-sectional image of a water droplet on the bare, 11-MUA modified, and protein immobilized QCM sensors. It was discovered that the contact angles for the bare, 11-MUA modified, and protein immobilized QCM sensors, respectively, were 75.4°, 66.5°, and 43.9°. After SAM

formation and protein immobilization, the clean Au surface's contact angle of 75.4° was reduced to 66.5° and 43.9° , respectively. The observation demonstrates clearly that the addition of 11- MUA to the Au sensor surface results in the introduction of polar head groups (-COOH) and increases the surface's hydrophilicity relative to bare Au. The presence of -COOH groups on the surface is the cause for lower contact angles of carboxylic acid-terminated monolayers than the bare gold surface.³ The Au@NHS surface exhibits an increase in contact angle to 67.8° compared to the Au@MUA surface, which denotes an increase in the surface's hydrophobicity as a result of the synthesis of succinimide ester intermediate.⁴ The presence of polar hydrophilic biological molecules such as proteins tends to increase the hydrophilicity of the sensor surface. Further decrease in the contact angle from Au@NHS to Au@protein provides more evidence that proteins were successfully immobilized on the QCM electrode surface.⁵

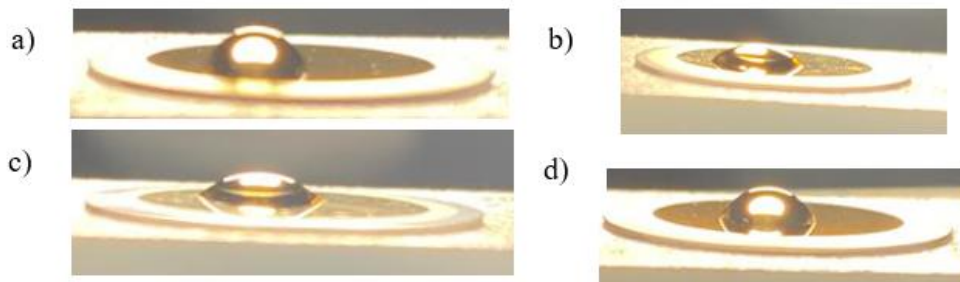


Figure 4.1: Surface contact angles of the unmodified a) QCM sensor, b) 11-MUA modified, c) EDC/NHS treated, and d) protein immobilized QCM sensor.

4.2 Characterization of surface modified QCM sensors using AFM

Figure. 4.2 displays AFM images showcasing the 3D topography of the bare gold substrate, the 11-MUA monolayer and the protein layer with their respective

sectional profile across $(3 \times 3) \mu\text{m}^2$ area. It was determined that the bare gold substrate's surface root mean square (rms) roughness was a 1.40 nm. The rms roughness was discovered to be 1.83 nm and 1.78 nm and 2.1 nm for SAM treated and protein modified (CD14 and LBP respectively) surfaces, respectively indicating a smooth and homogeneous surface before and after the surface modification. The roughness increased due to the immobilization of bumpy proteins. On the surfaces of Au@MUA and Au@protein, different nanostructures were seen, which would indicate that successful modification occurred during these steps. This is further substantiated by the Z bar variation (equivalent to height), which changed from 10.7 nm for the bare gold substrate to 7.4 nm for the 11-MUA monolayer and 7.8 nm for CD14 and 9.6 nm for the LBP protein monolayer, respectively.⁶⁻⁷ A conformational shift in the SAM layer on the bare gold surface could be indicated by the decline in rms roughness.⁸ Comparing Au@protein to Au and Au@MUA surfaces, an extremely rough sectional view was observed, demonstrating that the protein molecules are physisorbed on the Au surface following EDC/NHS activation. The negatively charged -COOH groups that interact electrostatically with the positively charged amino acids found in LBP and CD14 can be the cause of the physisorbed and inhomogeneous attachment of proteins.⁴

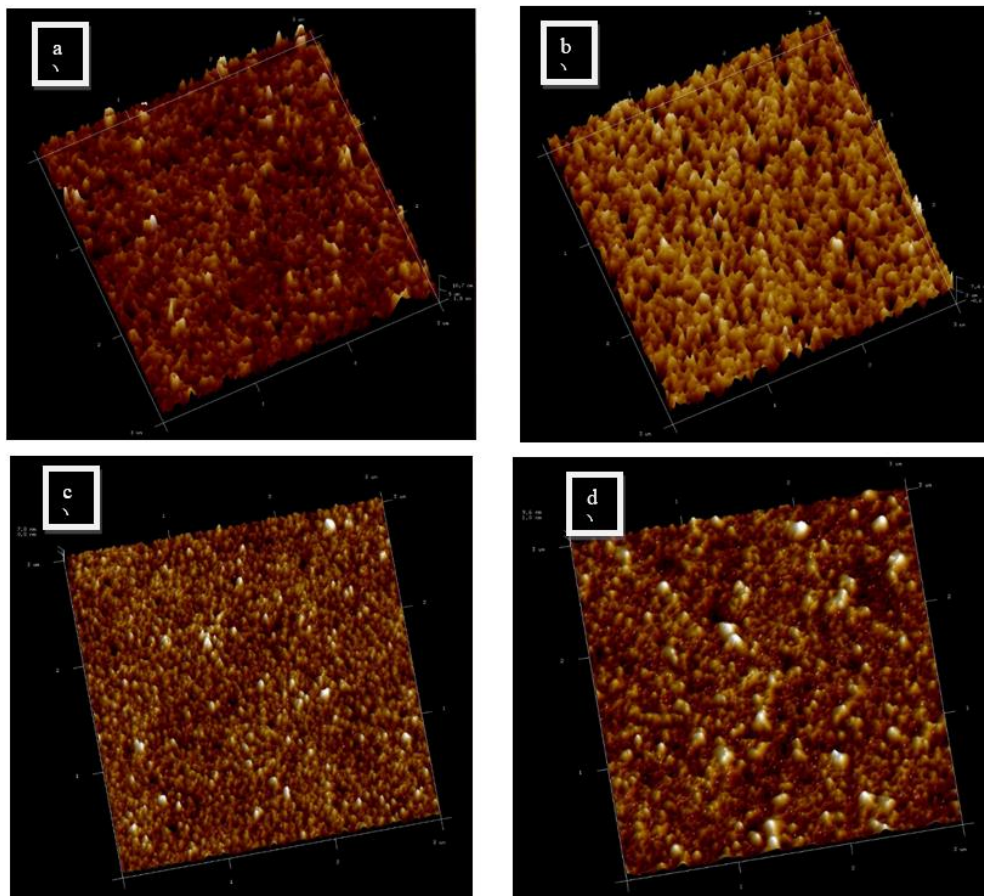


Figure 4.2: AFM micrographs of a) unmodified QCM sensor, b) 11-MUA modified, c) CD14 immobilized, and d) LBP modified QCM sensor.

4.3 Characterization of surface modified QCM sensors using XPS

Using XPS, the successful surface modification steps were verified, and the chemical makeup of the coating on the QCM sensors was examined. In the subsequent stages of the modification process, the XPS spectra at regions of carbon (C 1s), nitrogen (N 1s), oxygen (O 1s), sulfur (S 2p), and gold (Au 4f) are compared in Figure 4.3. A change in the chemical environment at the surface is suggested by differences in the XPS spectra for each modification stage, especially following

protein conjugation. At 282.5 eV, a C-C, C-H peak was observed. Carbon contamination, which is frequently seen in samples exposed to the atmosphere, is what is responsible for the carbon peak in bare gold sensors. Because of the S-C bond and the exposed groups O-C=O (288 eV) present in the 11-MUA, the displacement of the C-C peak to a higher binding energy (BE) in Figure 4.3a indicates that SAM was successfully formed. After EDC/NHS treatment and CD14 immobilization, a wider peak with a bump to a higher BE was seen, indicating an increase in the concentration of carbon-related novel species connected to amine and amide groups emanating from the immobilized protein.⁹

In Figure 4.3b, a large peak was observed near 530 eV for the bare gold sensor. There is a small shift to lower BE as a result of surface modification. An increase in the electron density (reduction in BE) of the photoelectrons of oxygen originating from the carboxylic acid of 11-MUA and $-\text{SO}_3$ from sulfo-NHS is what is responsible for this chemical shift. When there is protein on the surface, the oxygen peak is stronger. Since protein is the source of the majority of the electrons that reach the detector, the peak has less broadening than bare gold.^{2,9}

In Figure 4.3c, after protein immobilization, a strong signal at 398 eV that corresponded to the adsorbed protein's N1s core-level spectra was seen. The near-400 eV N 1s photoelectron peaks observed are typical of nitrogen in an organic matrix.⁴

In Figure 4.3d, the presence of the Au 4f peak, which is typical of atomic Au, was indicated by the bare Au-QCM sensors. The Au-QCM sensor in this study displayed

similar BEs of Au4f7/2 (83.0eV) and Au4f5/2 (85.7 eV), which are indicative of metallic Au. When protein covers the gold surface, attenuation of the gold surface is seen, which reduces the signal. Due to the effects of electronegativity, the spectra of Au 4f undergoes a chemical shift to reduce the binding energy. A red shift in the position of the BE peak results from the doping element's lower electronegativity than the base element, an increase in the electron density all around it, and a drop in binding energy. The S 2p spectra in Figure 4.3e exhibits a peak at about 161 eV that deviates from 164–165 eV and indicates the establishment of a S–Au bond.⁹

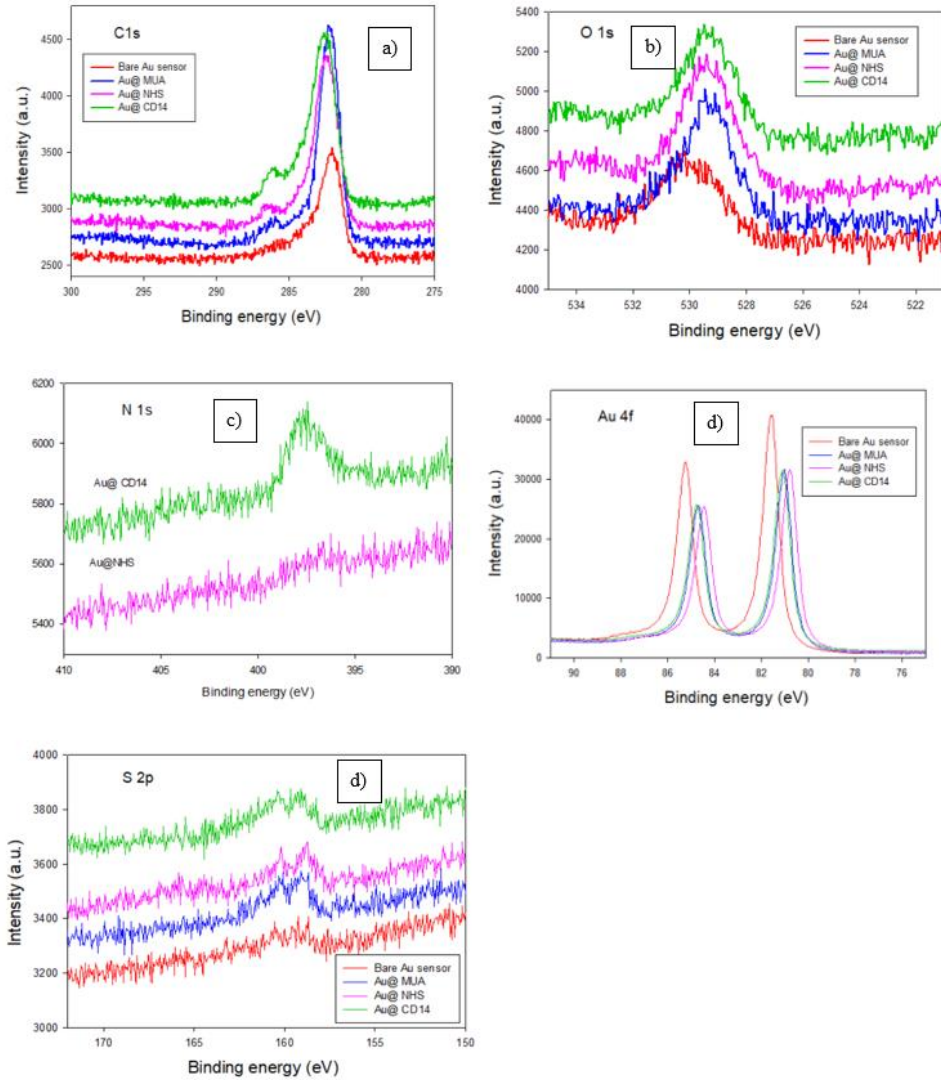


Figure 4.3: XPS analysis of QCM sensor after each stage of surface modification.

XPS spectra for a) C1s, b) O1s, c) N1s, d) Au4f, and e) S2p

4.4 Binding affinities of LPS antagonists with CD14 and LBP

The binding was monitored in real-time and the binding affinity of protein receptors such as CD14 and LBP for LPS antagonists are shown in Figure 4.4. Figure

4.4a and 4.4c show a typical sensorgram of fundamental frequency variation profiles after subsequent injection of the LPS antagonist (c10 lactone) over CD14 and LBP respectively. A remarkable drop in the frequency is observed after introducing varying concentrations of antagonists. As is well known, the decrease in frequency correspond to the increase in mass density.¹⁰ By employing a ligand binding curve to fit the frequency variation values with concentration variation, the dissociation constants for C10 with CD14 ($K_d = 0.47 \pm 0.16 \mu\text{M}$) and LBP ($K_d = 0.66 \pm 0.26 \mu\text{M}$) were determined as seen in Figure 4.4b and 4.4d.

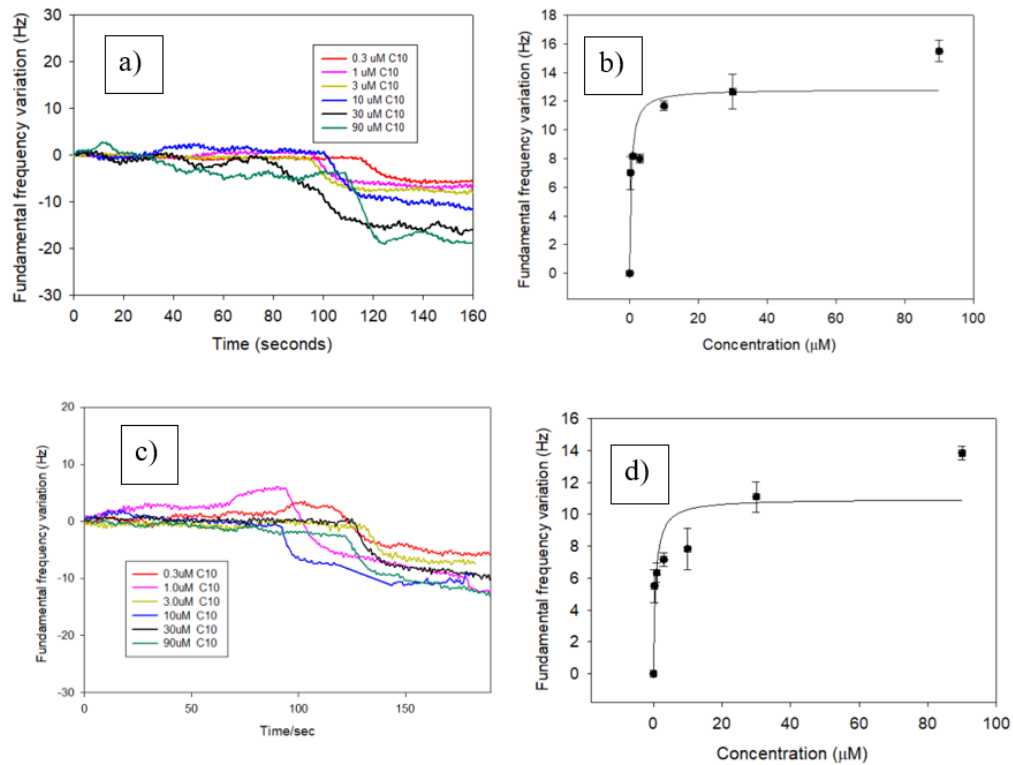


Figure 4.4 QCM data illustrating fundamental frequency variation derived from LPS antagonist deposition onto a protein-immobilized Au-coated quartz crystal. The QCM profiles made using (a) CD14 and (c) LBP together with C10 lactone

are displayed. Ligand binding curves showing the frequency variation with concentration of the antagonist are shown in (b) and (d) to evaluate the binding affinity of C10 with CD14 and LBP respectively.

Figure 4.5 shows the binding affinity of protein receptors like CD14 and LBP for AM12 based on real-time binding monitoring. A typical sensorgram fundamental frequency variation profile is shown in Figures 4.5a and 4.5c following the AM12's subsequent addition/binding over CD14 and LBP, respectively. The dissociation constants for AM12 with CD14 ($K_d = 1.23 \pm 0.27 \mu\text{M}$) and LBP ($K_d = 0.005 \pm 0.002 \mu\text{M}$) were calculated using a ligand binding curve to suit the frequency variation values with concentration variation, as shown in Figures 4.5b and 4.5d.

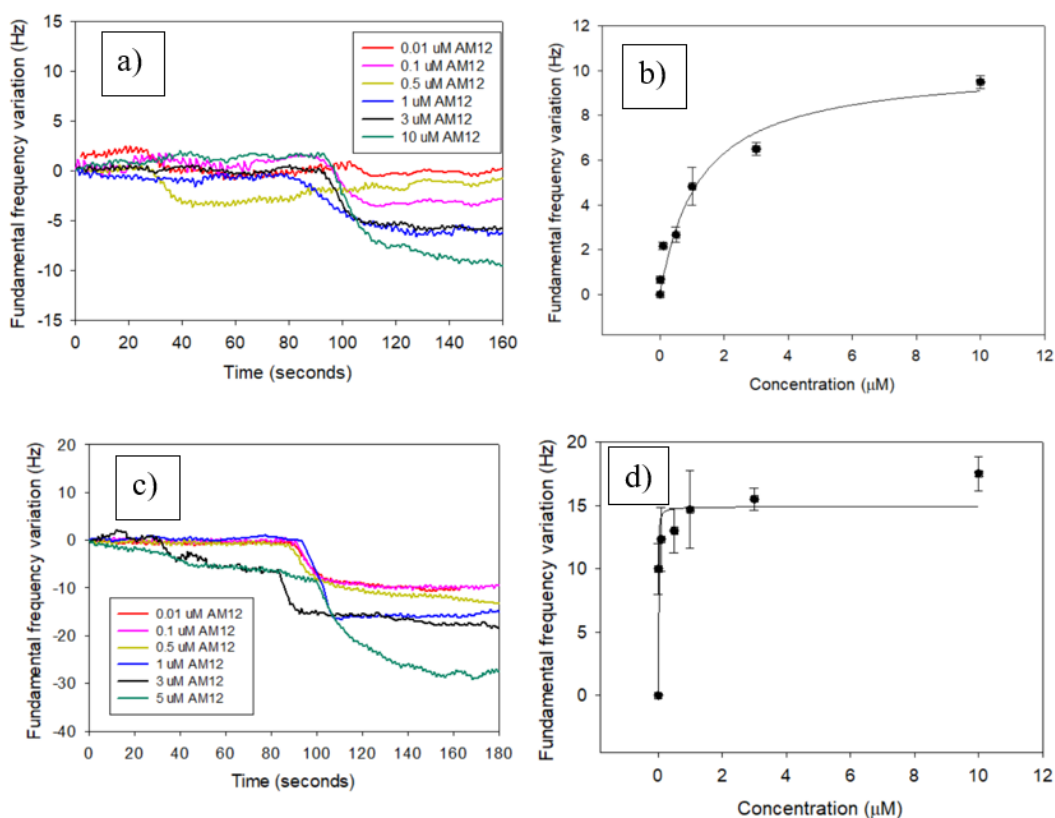


Figure 4.5 QCM data illustrating fundamental frequency variation derived from AM12 onto a protein-immobilized Au-coated quartz crystal. The QCM profiles

made using (a) CD14 and (c) LBP together with AM12 are displayed. Ligand binding curves showing the frequency variation with concentration of the antagonist are shown in (b) and (d) to evaluate the binding affinity of AM12 with CD14 and LBP respectively.

The lack of response from the null-control protein BSA and its inability to affect how LPS antagonists interacted with it (Figure 4.6) confirmed the specificity of the binding event on the sensor chip surface.¹¹

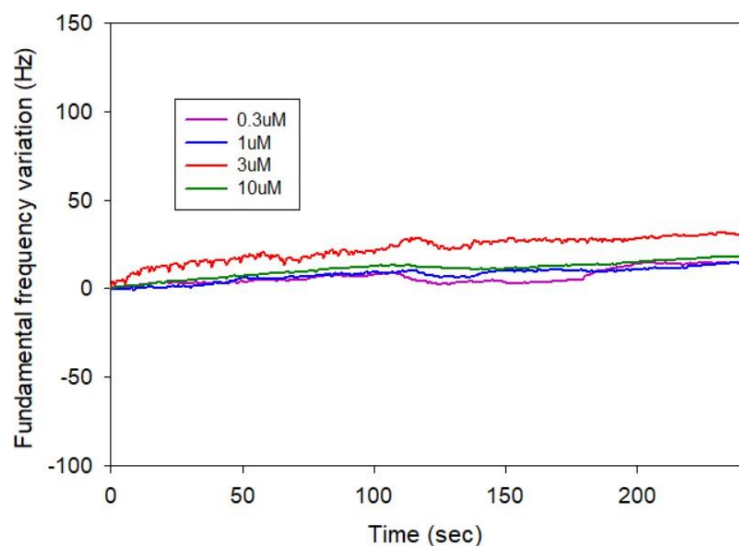


Figure 4.6 QCM sensorgram showing the fundamental frequency variation vs time when varying concentrations of BSA was added on the modified Au-coated quartz crystal.

Conclusion and future perspectives

A surface-sensitive method for examining how proteins interact with other small molecules has been employed in our study. The sensitivity of the method has

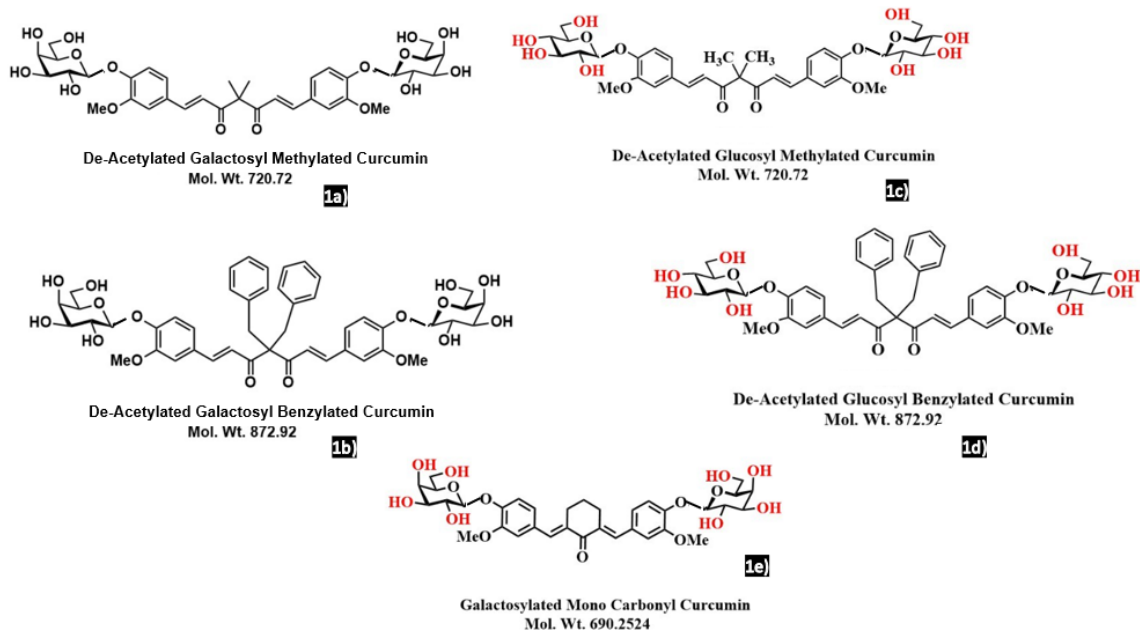
made it a popular approach in research on cytotoxicity, drug transport, and lipid self-assembly. It also allows for in situ monitoring of interaction phenomena.¹² Here, QCM-D has been successfully applied to examine structurally heterogeneous LPS antagonists with proteins such as CD14 and LBP.

This study developed a QCM biosensor for real-time analysis of the binding kinetics of protein-LPS antagonist interactions based on protein receptor modified gold surfaces. The sensor surface was prepared through an extremely simple incubation process where 11-MUA was used to prepare a SAM onto the gold sensor chip surface, with the protein immobilizing covalently onto the chip surface through EDC/NHS chemistry. Excellent specificity, a crucial characteristic for a trustworthy real-time evaluation of the binding kinetics, was demonstrated by the fabricated sensorchip.

Dissociation constants (K_d) were calculated for LPS antagonists based on oscillation frequency data for quartz crystal resonators. The K_d values were consistent with those obtained by other methods. The binding affinity of CD14 to C10 lactone was greater than that of AM12-CD14. However, the binding affinity of LBP to AM12 was much more pronounced as compared to the lactone. Based on the results obtained in our study, we hypothesize that water soluble LPS antagonists, such as those used in our study, may be potential ligands for endotoxin binding due to their strong binding ability with the protein receptors, LBP and CD14. The 4-O-sulfated derivative of AM12 was used as a control in the experiment. The compound did not show binding with either of the protein receptors.

4B. EXPLORING THE POTENTIAL ROLE OF GLYCO-CURCUMIN ANALOGS AS MD-2 INHIBITORS IN THE INHIBITION OF RESPONSE TOWARDS LPS

Curcumin has been shown to be useful in treating sepsis in numerous investigations. To improve the stability and water solubility of the curcumin core, we changed the curcumin's structure by attaching carbohydrates to the aromatic moiety and adding alkyl/aryl groups to the active methylene carbon. Despite its therapeutic benefits, its activity is constrained by poor solubility and stability. The binding affinities of different curcumin analogs (LPS antagonists) to the membrane protein MD-2 have been determined. In this study, we show that the library of curcumin analogs which are stable and soluble in addition to determining their binding affinities using fluorescence measurements to show the potential role of the curcumin analogs as drugs for MD-2 targeting. The structural alteration has greatly increased the stability and solubility of these analogs. Five water-soluble curcuminoids (shown in scheme 1) with LPS antagonist activity have been synthesized. Together, these investigations demonstrated the potential of the new MD-2 selective inhibitor gluco-benzylcurcuminoid as a sepsis treatment option.



Scheme 1. Water-soluble curcuminoids with LPS antagonist activity

4.5 Curcumin and Curcuminoids Chemical Stability Analysis by UV-Visible

Absorption Spectra

It is understood that curcumin dissolves in water when the acidic phenol group undergoes deprotonation to create phenolate ions in an aqueous environment with an alkaline pH. At neutral and alkaline pH values, the molecule is swiftly degraded into vanillin, ferulic acid, and other compounds. Under pH 7, curcumin is stable, but when pH levels drop, the dissociation equilibrium shifts in favor of the neutral form, which has a very limited solubility in water. At acidic pH levels, this reaction results in a considerable shift in the UV-vis absorbance spectrum of curcumin. However, at neutral pH and room temperature, it is practically insoluble.¹³ Physiological buffer conditions were used for the experiment, and after 30 minutes the absorbance of curcumin at the peak absorbance wavelength of 425 nm declines to 50% of its initial value. On the other hand, the studied curcuminoids' absorbance did not considerably decrease. They retained nearly constant absorbance even after two hours of incubation. Figure 4.7 displays the absorbance spectra of curcumin and curcuminoids in PBS buffer (pH 7.4). The percentage degradation of each analog during the course of two hours in PBS buffer (0.01 M, pH=7.4) is shown in Table 4.1. Additionally, it was assessed how different pH levels affected the stability of glucosyl benzylated curcumin (which exhibits the strongest binding to MD-2) (Figure 4.8). The stability of the curcumin derivatives was greatly improved, and they did not degrade within the 2-hour window.

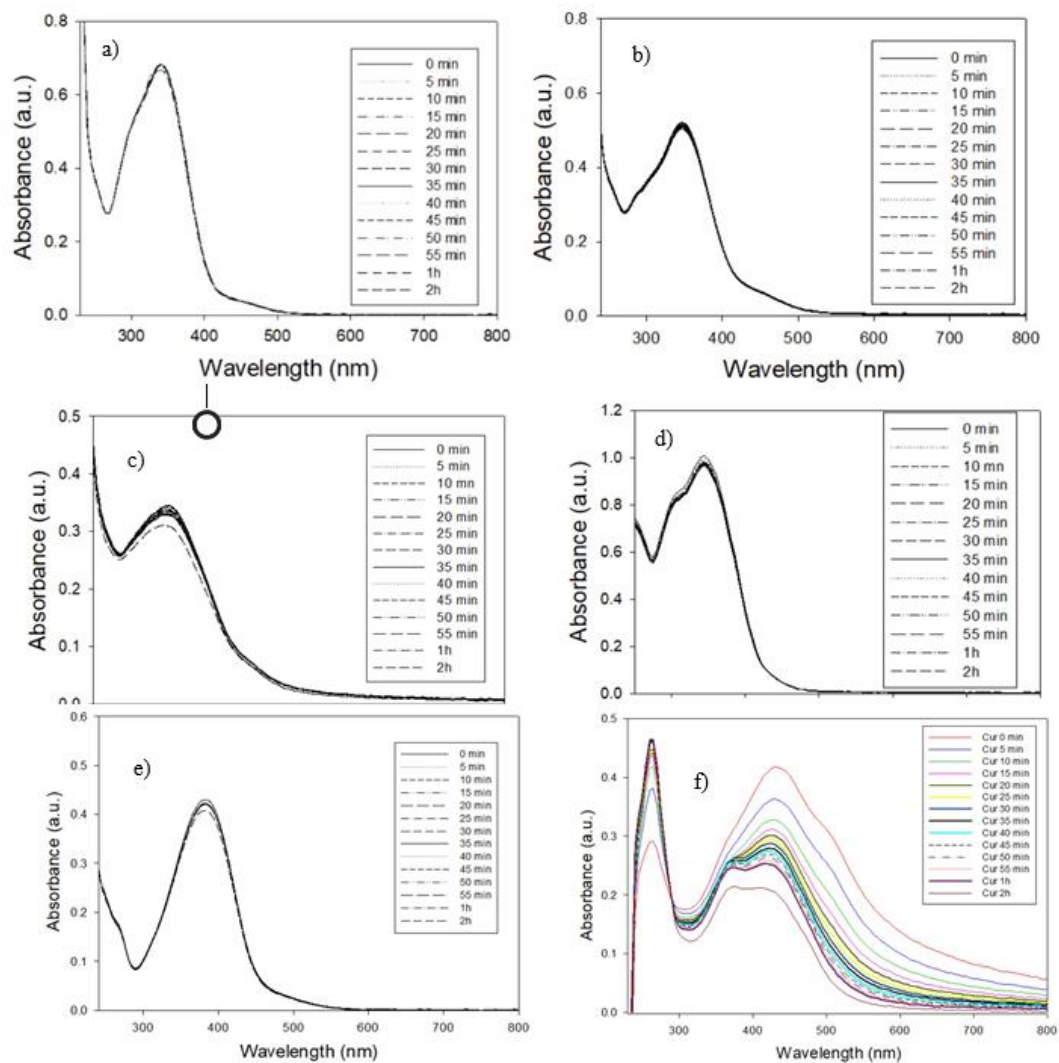


Figure 4.7: UV- visible absorption spectra of curcumin and glycocurcuminoids in PBS buffer (pH 7.4) a) deacetylated-galactosylated methylated curcumin b) deacetylated-glucosyl methylated curcumin c) deacetylated-glucosyl benzylated curcumin d) deacetylated-galactosylated benzylated curcumin e) deacetylated-galactosyl monocarbonyl curcumin f) curcumin

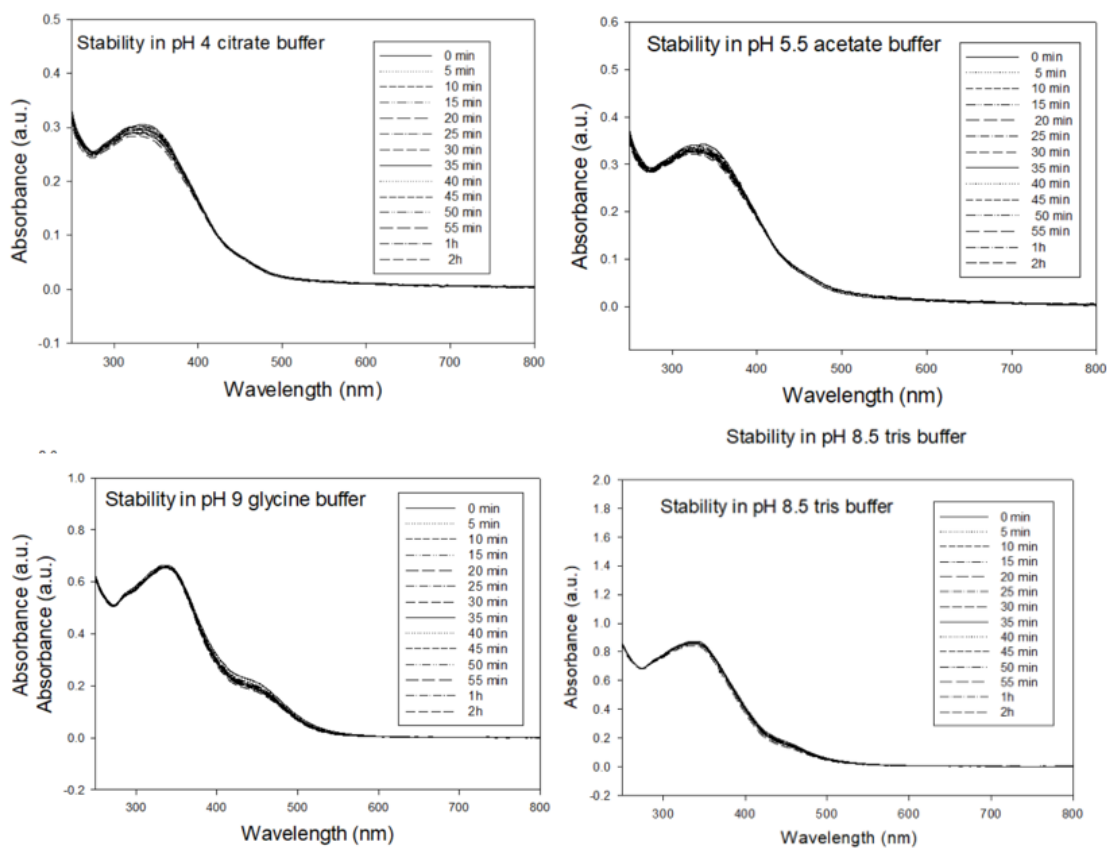


Figure 4.8: UV-visible absorption spectra showing the impact of varying pH on the stability of deacetylated glucosyl benzylated curcumin.

Table 4.1: Degradation (%) of curcumin and curcuminoid during a period of 2h in PBS buffer (pH 7.4)

Curcuminoids tested	Degradation (%) \pm SD
Curcumin	$52 \pm 0.1\%$
Deacetylated-glucosyl methylated curcumin	$3.3 \pm 1.6\%$
Deacetylated-glucosyl benzylated curcumin	$6.5 \pm 1.3\%$
Galactosylated monocarbonyl curcumin	$5 \pm 0.2\%$
Deacetylated-galactosylated methylated curcumin	$2.3 \pm 0.52\%$
Deacetylated-galactosylated benzylated curcumin	$5.4 \pm 1.8\%$

4.6 Solubility analysis of curcumin and curcuminoids

Curcumin has been discovered to have poor aqueous solubility. Due to the absence of any polar groups in the molecule and the stretch of the conjugated (heptadiene) backbone, curcumin is completely hydrophobic at neutral pH, making it water-insoluble substance. Contrarily, our curcuminoids have improved aqueous solubility as a result of the attachment of hydrophilic sugarunits to the two aromatic rings. The solubility of the curcuminoids generated in the current investigation is shown in Table 4.2. The supernatant was gathered to create the combined UV-visible spectra of curcumin and curcuminoids as shown in Figure 4.9 after an overnight stirring of a dispersion of the curcuminoids to create a saturated solution of the compounds to be evaluated.

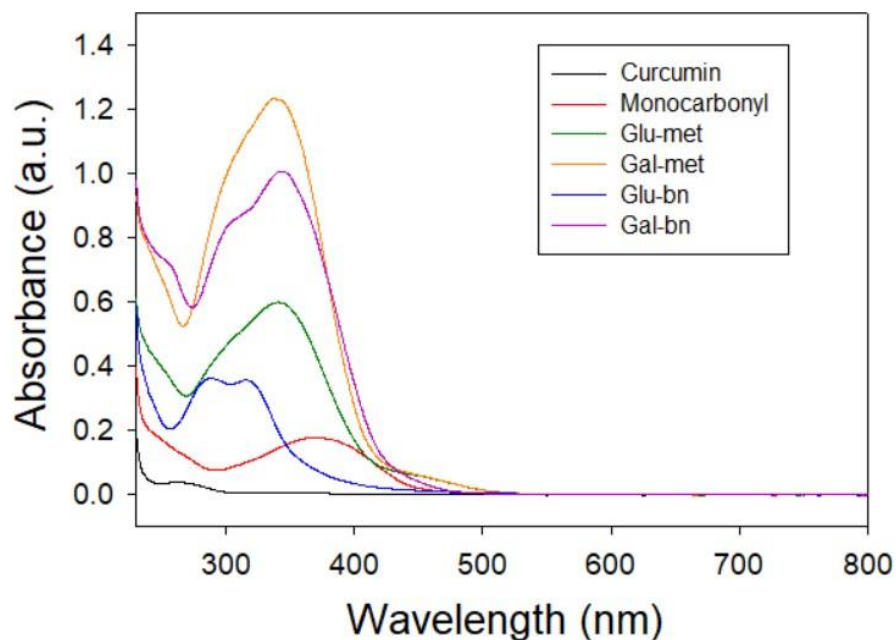


Figure 4.9: UV-visible spectra of the supernatant collected after 24h from the saturated solutions of curcumin and curcuminoid formulations prepared in PBS

buffer (pH 7.4)

Table 4.2: Solubility of curcumin and curcuminoid in PBS buffer (pH 7.4)

Curcuminoids tested	Molecular weight (g/mol)	Molar extinction coefficient ($M^{-1} cm^{-1}$)	Solubility ($mg L^{-1}$)
Curcumin	368.38	27,200	0.0002
Deacetylated-glucosyl methylated curcumin	718	32,400	0.018
Deacetylated-glucosyl benzylated curcumin	870	32,800	0.010
Galactosylated monocarbonyl curcumin	690	63,600	0.003
Deacetylated-galactosylated methylated curcumin	718	30,934	0.039
Deacetylated-galactosylated benzylated curcumin	870	22,934	0.044

The calibration plot for deacetylated glucosyl benzylated curcumin can be seen in Figure 4.10. The data show that the curcumin has a solubility of 0.0002 mg/L, whereas the deacetylated curcumin derivatives show solubilities that are two orders of magnitudes higher. The solubility seems to be a factor of the sugar substituents with the galactosyl-substituted curcumin somewhat more soluble than the glucosylated ones, irrespective of the methyl substituent.

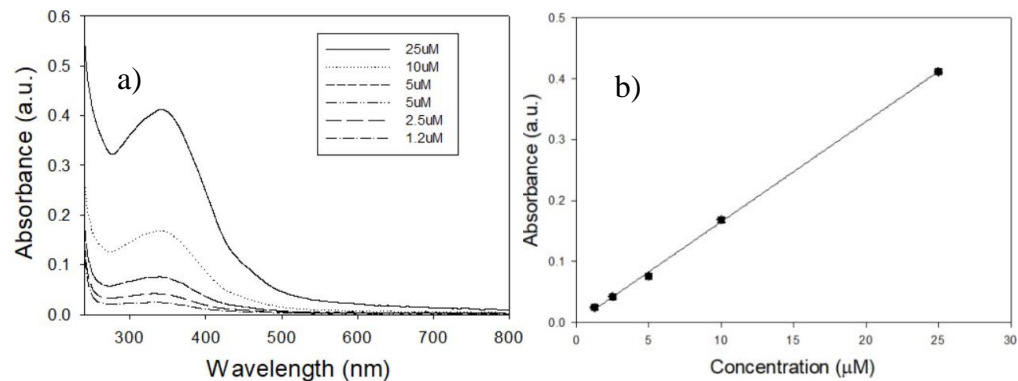


Figure 4.10 (a) UV-visible absorption spectrum of varying concentrations of deacetylated glucosylbenzylated curcumin and (b) Calibration plot of deacetylated glucosyl benzylated curcumin showing a linear plot with slope as 0.0164. Similar calibration plots were made with other analogs to evaluate the slope which was used to calculate and molar extinction coefficient for solubility calculations.

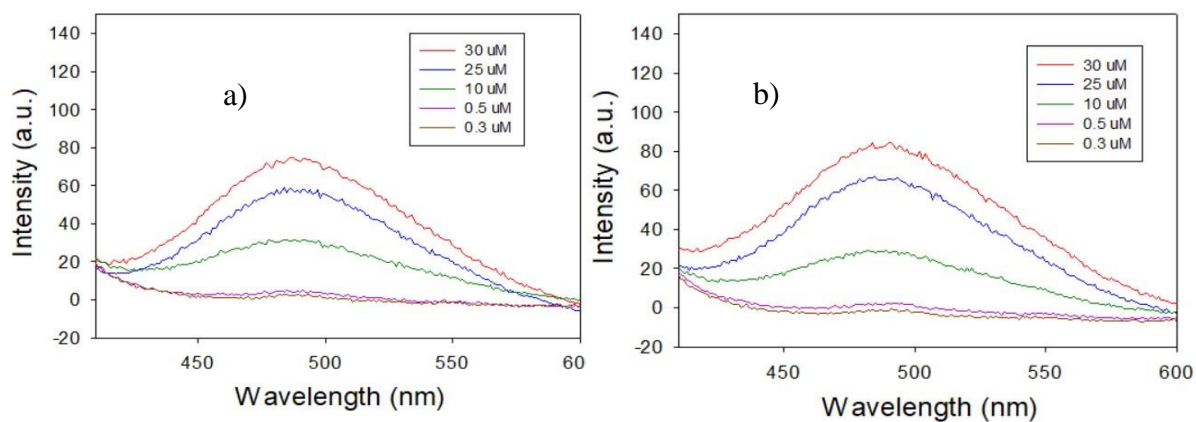
4.7 The binding affinities of Curcuminoids to MD-2 receptor

Curcumin is a planar molecule that fluoresces more when it interacts to hydrophobic protein binding sites or is present in nonpolar environments like organic solvents. Adding MD-2 has been seen to significantly increase curcumin's fluorescence in the past.¹⁴ A little blue shift in the absorbance maximum has been used to show the interaction between the molecules in solution and the adhesion of curcumin into the nonpolar pocket of MD-2 protein.¹⁴ Additionally, it has been found that the important residues Arg-90 and Tyr-102 of the MD-2 protein play a significant role in stabilizing the curcumin-MD-2 complexes by forming two essential hydrogen bonds.¹⁵ From this angle, experimental techniques were used to look into the basic structural mechanisms of curcumin binding to the MD-2 protein. They were able to ascertain curcumin's high affinity and K_d value of 379 μM for the MD-2 protein by using SPR experiments to measure the substance's binding affinity.

¹⁵ The useful design guidance provided by this work has assisted the creation of more potent MD-2 inhibitors as potential anti-inflammatory medicines. Chalcone, a naturally occurring compound, has the potential to be used as an MD-2 inhibitor. Wu et al. previously produced and tested several chalcone derivatives as anti-inflammatory drugs in LPS-stimulated macrophages and mice models. The (E)-2,3-dimethoxy-4'-methoxychalcone (L6H21), one of these synthetic chalcones, has shown exceptional anti-inflammatory efficacy. While fitting into the hydrophobic portion of the MD-2 pocket via hydrogen bonding, compound L6H21 competitively removes LPS from MD-2. The evaluation of L6H21's binding to MD-2 protein using SPR studies revealed that L6H21 binds to MD-2 protein with a high affinity and a low K_D value of 33.3 μM .¹⁶ Monocarbonyl analogs of curcumin without the β -diketone moiety are designed and produced in an effort to boost the chemical stability of curcumin, and they have demonstrated improved chemical stability. The 1-ethyl-3,5-bis(3,4,5-trimethoxybenzylidene) piperidin-4-one (L48H37) analog of curcumin stood out among the group for its great chemical stability and potent anti-inflammatory properties. Additionally, L48H37 directly binds the rhMD2 protein with a very high affinity (K_D value = 11.3 μM) and in a dose-dependent way. This study has shown that the L48H37's interaction with MD2 significantly changed the way that LPS bound to rhMD2, indicating that the two molecules' binding sites overlap in the MD2 pocket.¹⁷ One study found that the main alkaloid in tobacco, nicotine, and its metabolite, cotinine, both quenched the intrinsic fluorescence of MD2 upon binding. Surface plasmon resonance (SPR) was used to verify that nicotine and cotinine are recognized by MD2. The K_D values for

nicotine's and cotinine's interactions with MD2 were $23.1 \pm 1.2 \mu\text{M}$ and $14.1 \pm 1.8 \mu\text{M}$, respectively.¹⁸ Another study used the fluorescence titration method to demonstrate the potent binding affinity of curcumin to soluble MD2 and evaluated the curcumin-induced fluorescence rise and the dampening of MD-2's intrinsic protein fluorescence. When curcumin was added to MD-2 solution, fluorescence emission spectra demonstrated a rise in fluorescence intensity. According to the fit of fluorescence intensity, K_D was $0.37 \mu\text{M} \pm 0.12 \mu\text{M}$.¹⁹ We investigated the direct interaction between glyco-curcumin analogs and the recombinant human (rh MD-2) protein using fluorescence spectroscopy. As can be observed in Figure 4.11, combining the two led to a concentration-dependent increase in the fluorescence generated by the analog-rh-MD-2 interaction, demonstrating a powerful binding of analogs to the hydrophobic pocket of MD-2. The ligand binding plots of each curcumin analog with the MD-2 protein are displayed in Figure 4.12. The glucose-benzyl analog displayed the greatest binding of all the analogs, according to testing results (Table 4.3). The robust interaction of the glucose-bn analog with MD-2 has been explained using the molecular docking model that was previously used to predict the binding mechanism of curcumin with MD2. The strong contact may be the result of several hydrogen bonds that can form between sugar units, carbonyl oxygen, and the residues Arg-90, Glu-92, and Tyr-102 of MD-2. Stereochemistry, which is crucial for pharmaceutical development, determines how drugs work. When compared to a mixture of enantiomers, single-enantiomer formulations of various therapies can offer higher selectivity for their biological targets, enhanced therapeutic indices, and/or better pharmacokinetics.²⁰ Because they have a stronger

affinity for the protein MD-2 than analogs with galactose units in the side chain, our research revealed that analogs with glucose units in the aryl side chains can more effectively inhibit LPS binding. The three dihedral angles (ϕ , ω , ψ) specify the conformations of carbohydrates.²¹ Flexibility at these angles opens for a wide range of conformational possibilities, which have an impact on overall shape and identification. Due to stereoelectronic effects, some sugar conformations are more frequent than others. Galactose and glucose, which are epimeric at the C4 position, have been observed to occupy different sites at the receptor proteins due to sterics, solvent interactions, and stereoelectronic effects.²² Ile52, Phe76, Phe119, and Phe121 residues in the MD-2 binding pocket have been demonstrated to engage in hydrophobic interactions with benzyl groups in the molecule. Curcumin analogs with the benzyl portion may interact with MD-2 more strongly than analogs with methyl groups because the hydrophobic groups are buried in the lipid-binding pocket of MD-2 as a result of the pi stacking interaction.²¹



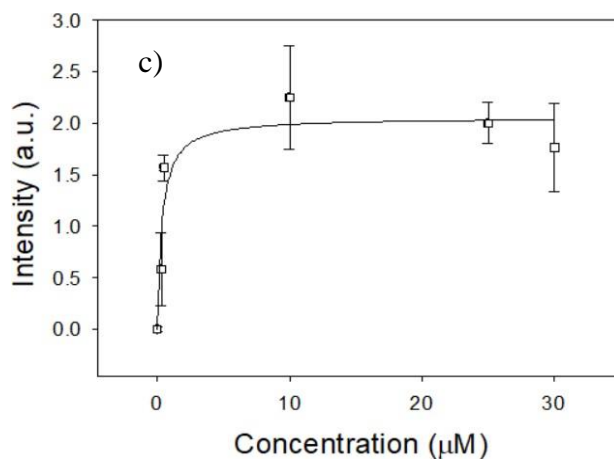


Figure 4.11: MD-2 interacts with deacetylated glucosyl benzylated curcumin in solution (excitation at 370 nm and emission at 490 nm, slit width at 20). The fluorescence emission of only glucosyl benzylated curcumin analog in PBS buffer is shown in (a). When MD-2 (50 nM) is added to a curcumin solution (25 μ M), the curcumin fluorescence emission (b) increases. The value of K_d of $0.34 \pm 0.39 \mu$ M is found from the data fit shown in (c)

Table 4.3: Comparing the dissociation constants for glyco-curcuminoids used in this work.

Compound interacting with MD-2 protein	Experimental model utilized	Dissociation constant (K_D)/ μM	Reference
L6H21	1:1 Langmuir binding model	33.3	16
L48H37	1:1 Langmuir binding model	11.3	17
Nicotine and Cotinine	SPR experiment	23.1± 1.2 and 14.1± 1.8	18
Curcumin	Intrinsic protein fluorescence and curcumin fluorescence	0.14± 0.04 and 0.37± 0.12	19
Deacetylated-glucosyl methylated curcumin	Fluorescence measurement model	5.93 ± 0.7	present study
Deacetylated-glucosyl benzylated curcumin		0.34 ± 0.39	
Galactosylated monocarbonyl curcumin		1.61 ± 0.55	
Deacetylated-galactosylated methylated curcumin		9.94 ± 0.53	
Deacetylated-galactosylated benzylated curcumin		3.76 ± 1.0	

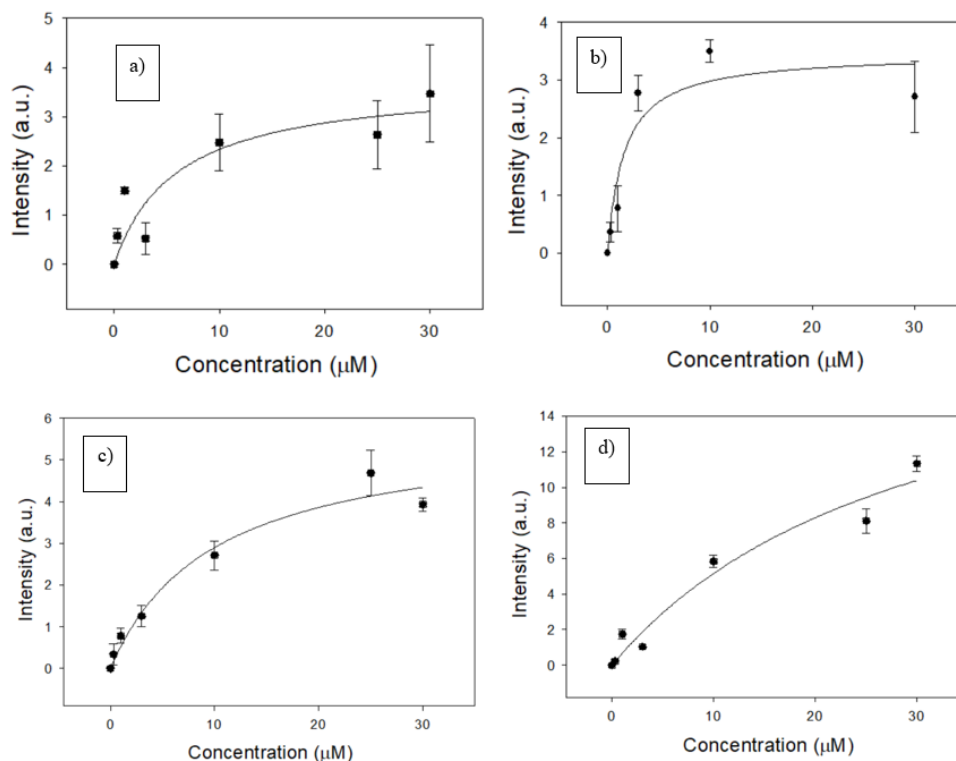


Figure 4.12: Ligand binding plots with MD-2 for (a) deacetylated glucosyl methylated curcumin (b) deacetylated galactosyl monocarbonyl curcumin (c) deacetylated galactosyl methylated curcumin (d) deacetylated galactosyl benzylated curcumin.

Conclusion and future perspectives

In our investigation, various structurally modified curcumin analogs were effectively synthesized, and they had improved solubility and stability. Notably, the produced analogs also exhibit strong binding to the MD-2 protein, as determined by fluorescence assays. It was discovered that the gluco-benzyl analog has the best binding affinity to the MD-2 protein, making it a possible contender for usage as a

therapeutic drug in the future. The goal of this study is to specifically highlight the increased binding affinity of curcumin analogs with membrane protein MD-2, where the analogs may interfere at various points/times during the infection caused by gram-negative bacteria, significantly advancing a new adjuvant therapy for the treatment of sepsis.

To fully understand curcumin's impact and potential mechanisms of action in humans, additional research is required to determine how it controls and neutralizes inflammatory and antioxidant compounds as well as protects tissues throughout the pathophysiology of sepsis and its complications. The variety of pathophysiological reactions brought on by sepsis emphasize the necessity for a treatment approach that combines many medications. Even when employed in high quantities, curcumin is a naturally occurring substance that is well tolerated by people. But there are a few questions to be pondered for future work in this arena: 1) Does curcumin protect host cells from sepsis infection? 2) Does the use of curcumin reduce the release of inflammatory mediators? 3) Can curcumin help the body to return to its equilibrium?

References

1. Tonda-Turo, C.; Carmagnola, I.; Ciardelli, G., Quartz Crystal Microbalance With Dissipation Monitoring: A Powerful Method to Predict the in vivo Behavior of Bioengineered Surfaces. *Frontiers in Bioengineering and Biotechnology* **2018**, *6*.
2. Miyake, A.; Komasa, S.; Hashimoto, Y.; Komasa, Y.; Okazaki, J., Adsorption of Saliva Related Protein on Denture Materials: An X-Ray Photoelectron Spectroscopy and Quartz Crystal Microbalance Study. *Advances in Materials Science and Engineering* **2016**, *2016*, 5478326.
3. Aylaz, G.; Andaç, M., Affinity Recognition Based Gravimetric Nanosensor for Equilin Detection. *Chemosensors* **2022**, *10* (5), 172.
4. Kamra, T.; Chaudhary, S.; Xu, C.; Montelius, L.; Schnadt, J.; Ye, L., Covalent immobilization of molecularly imprinted polymer nanoparticles on a gold surface using carbodiimide coupling for chemical sensing. *Journal of Colloid and Interface Science* **2016**, *461*, 1-8.
5. Jandas, P. J.; Luo, J.; Quan, A.; Li, C.; Fu, C.; Fu, Y. Q., Graphene oxide-Au nanoparticle coated quartz crystal microbalance biosensor for the real time analysis of carcinoembryonic antigen. *RSC Advances* **2020**, *10* (7), 4118-4128.
6. Radmacher, M.; Fritz, M.; Cleveland, J. P.; Walters, D. A.; Hansma, P. K., Imaging adhesion forces and elasticity of lysozyme adsorbed on mica with the atomic force microscope. *Langmuir* **1994**, *10* (10), 3809-3814.
7. Li, L.; Chen, S.; Oh, S.; Jiang, S., In situ single-molecule detection of Antibody–Antigen binding by tapping-mode atomic force microscopy. *Analytical chemistry* **2002**, *74* (23), 6017- 6022.
8. Yoshimoto, K.; Nishio, M.; Sugasawa, H.; Nagasaki, Y., Direct Observation of Adsorption-Induced Inactivation of Antibody Fragments Surrounded by Mixed-PEG Layer on a Gold Surface. *Journal of the American Chemical Society* **2010**, *132* (23), 7982-7989.
9. Torres-González, L.; Díaz-Ayala, R.; Vega-Olivencia, C. A.; López-Garriga, J., Characterization of Recombinant His-Tag Protein Immobilized onto Functionalized Gold Nanoparticles. *Sensors (Basel)* **2018**, *18* (12).
10. Iturri, J.; García-Fernandez, L.; Reuning, U.; García, A. J.; Campo, A. d.; Salierno, M. J., Synchronized cell attachment triggered by photo-activatable adhesive ligands allows QCM- based detection of early integrin binding. *Scientific reports* **2015**, *5* (1), 9533.
11. Wu, C.; Li, X.; Song, S.; Pei, Y.; Guo, L.; Pei, Z., QCM Biosensor Based on Polydopamine Surface for Real-Time Analysis of the Binding Kinetics of Protein-Protein Interactions. *Polymers* **2017**, *9* (10), 482.
12. Yousefi, N.; Tufenkji, N., Probing the Interaction between Nanoparticles and Lipid Membranes by Quartz Crystal Microbalance with Dissipation Monitoring. *Frontiers in Chemistry* **2016**, *4*.
13. Jagannathan, R.; Abraham, P. M.; Poddar, P., Temperature-Dependent Spectroscopic Evidences of Curcumin in Aqueous Medium: A Mechanistic Study of Its Solubility and Stability. *The Journal of Physical Chemistry B* **2012**, *116* (50), 14533-14540.

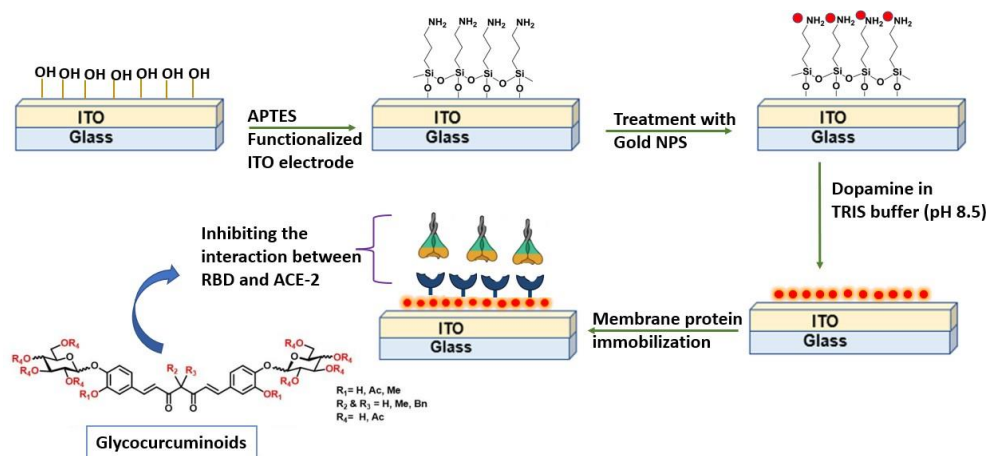
14. Gradisar, H.; Keber, M. M.; Pristovsek, P.; Jerala, R., MD-2 as the target of curcumin in the inhibition of response to LPS. *Journal of leukocyte biology* **2007**, *82* (4), 968-74.
15. Wang, Z.; Chen, G.; Chen, L.; Liu, X.; Fu, W.; Zhang, Y.; Li, C.; Liang, G.; Cai, Y., Insights into the binding mode of curcumin to MD-2: studies from molecular docking, molecular dynamics simulations and experimental assessments. *Molecular BioSystems* **2015**, *11* (7), 1933-1938.
16. Wang, Y.; Shan, X.; Chen, G.; Jiang, L.; Wang, Z.; Fang, Q.; Liu, X.; Wang, J.; Zhang, Y.; Wu, W.; Liang, G., MD-2 as the target of a novel small molecule, L6H21, in the attenuation of LPS-induced inflammatory response and sepsis. *Br J Pharmacol* **2015**, *172* (17), 4391-405.
17. Wang, Y.; Shan, X.; Dai, Y.; Jiang, L.; Chen, G.; Zhang, Y.; Wang, Z.; Dong, L.; Wu, J.; Guo, G.; Liang, G., Curcumin Analog L48H37 Prevents Lipopolysaccharide-Induced TLR4 Signaling Pathway Activation and Sepsis via Targeting MD2. *The Journal of pharmacology and experimental therapeutics* **2015**, *353* (3), 539-50.
18. Li, H.; Peng, Y.; Lin, C.; Zhang, X.; Zhang, T.; Wang, Y.; Li, Y.; Wu, S.; Wang, H.; Hutchinson, M. R.; Watkins, L. R.; Wang, X., Nicotine and its metabolite cotinine target MD2 and inhibit TLR4 signaling. *Innovation (Cambridge (Mass.))* **2021**, *2* (2), 100111.
19. Gradisar, H.; Keber, M. M.; Pristovsek, P.; Jerala, R., MD-2 as the target of curcumin in the inhibition of response to LPS. *J Leukoc Biol* **2007**, *82* (4), 968-74.
20. McConathy, J.; Owens, M. J., Stereochemistry in Drug Action. *Primary care companion to the Journal of clinical psychiatry* **2003**, *5* (2), 70-73.
21. Zhang, X.; Peng, Y.; Grace, P. M.; Metcalf, M. D.; Kwilasz, A. J.; Wang, Y.; Zhang, T.; Wu, S.; Selfridge, B. R.; Portoghese, P. S.; Rice, K. C.; Watkins, L. R.; Hutchinson, M. R.; Wang, X., Stereochemistry and innate immune recognition: (+)-norbinaltorphimine targets myeloid differentiation protein 2 and inhibits toll-like receptor 4 signaling. *FASEB journal : official publication of the Federation of American Societies for Experimental Biology* **2019**, *33* (8), 9577-9587.
22. McMahon, C. M.; Isabella, C. R.; Windsor, I. W.; Kosma, P.; Raines, R. T.; Kiessling, L.L., Stereoelectronic Effects Impact Glycan Recognition. *Journal of the American Chemical Society* **2020**, *142* (5), 2386-2395.

CHAPTER V: EVALUATING THE BINDING AFFINITY OF CURCUMIN ANALOGS TOWARDS PROTEIN RECEPTORS INVOLVED IN COVID-19

5. INVESTIGATION OF THE POTENTIAL INHIBITORY EFFECT OF GLYCOCURCUMINOIDS AGAINST THE BINDING OF SPIKE PROTEIN AND MEMBRANE RECEPTOR ACE2: POTENTIAL NEW TREATMENT OPTION FOR SARS- COV-2

The SARS-CoV-2 virus strain has been implicated in an alarmingly high number of fatalities globally. The virus has a robust airborne transmission pattern. Angiotensin-converting enzyme 2 (ACE2) is bound by the receptor-binding domain (RBD) of the spike glycoprotein (S protein), facilitating host entrance. Curcumin and its synthetically modified derivatives may exhibit inhibition through interfering with the binding of the RBD and ACE2. The COVID-19 pandemic, which resulted in more than 766 million illnesses and 6.9 million fatalities worldwide, is currently in remission, but there are still no universally effective treatments or vaccines to halt the disease's spread.

Here, we have developed an easy-to-use platform based on an ITO-coated glass plate with a surface modification for measuring the binding affinities of glyco-curcuminoids with the membrane proteins ACE2 and RBD (as shown in Schematic 2). Using electrochemical impedance spectroscopy data (EIS) data, the binding constant was assessed. The investigation's findings on the role of glyco-curcuminoids in inhibiting the binding of the RBD of spike protein with the ACE2 receptor will allow for the development of a new SARS-CoV-2 therapy option.



Schematic 2. The surface modification steps performed on ITO glass.

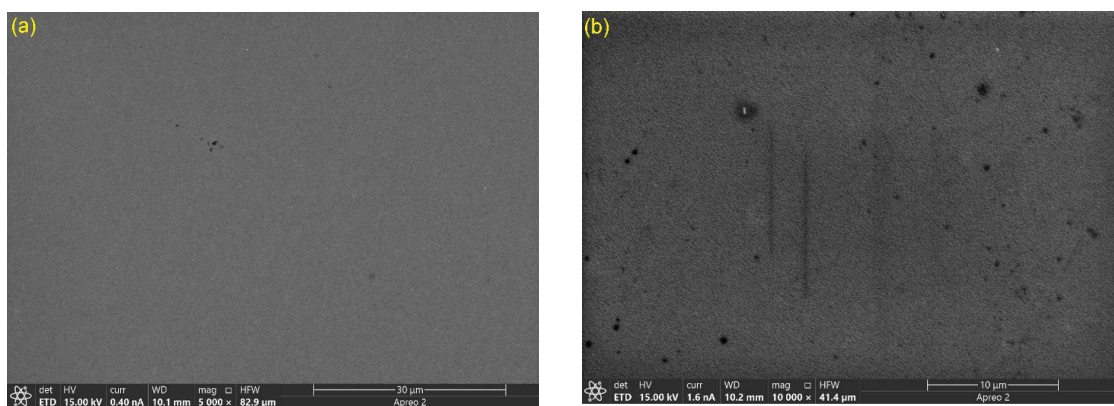
5.1 Topography and elemental composition of the surface-modified working electrode using SEM-EDS analysis

The surface morphologies of the bare ITO electrode and the ITO electrode with surface modifications were described using SEM (Figure 5.1). The elemental makeup and surface morphology of the ITO deposited glass were determined using EDS in conjunction with SEM. On the glass surface, the SEM micrograph (Figure 5.1a) shows a continuous, void-free ITO layer and a homogenous microstructure.¹ The surface features did not change after thin layer deposition using APTES (Figure 5.1b).

In order to create AuNPs-APTES-glass (Figures 5.1c), the pre-synthesised AuNPs were electrostatically drawn to the APTES-modified ITO glass. After that, a thin layer of PDA was applied to this modified surface via spontaneous oxidative polymerization of dopamine in an alkaline solution (Figure 5.1d). After being coated with PDA film, the AuNPs-APTES-glass surface still has perfectly preserved well-adsorbed AuNPs with good monodispersity and uniform surface

distribution without substantial aggregation.

EDS examination showed that the elemental composition of the surface had changed (Figure 5.1e). Peaks for silicon (11.9 at%), carbon (4.3 at%), oxygen (58.3 at%), and nitrogen (5.2 at%) were seen in the elemental analysis, demonstrating the efficacy of the APTES modification of the ITO surface. Depending on the functionality of the amine coupling agent, the quantity of amino groups on the ITO surface will vary. Due to the hydroxyl groups on the ITO changed to siloxane linkages by bonding to APTES, there are more hydrogen bond interactions between the modified ITO.² By using EDS analysis, which revealed the presence of discrete Au peaks, the as-prepared AuNPs were confirmed. The clear peaks for the gold in the EDS spectra, close to 2.4 keV, confirmed that AuNPs had been successfully prepared.³ The EDS analysis is displayed in Figure 5.1f.



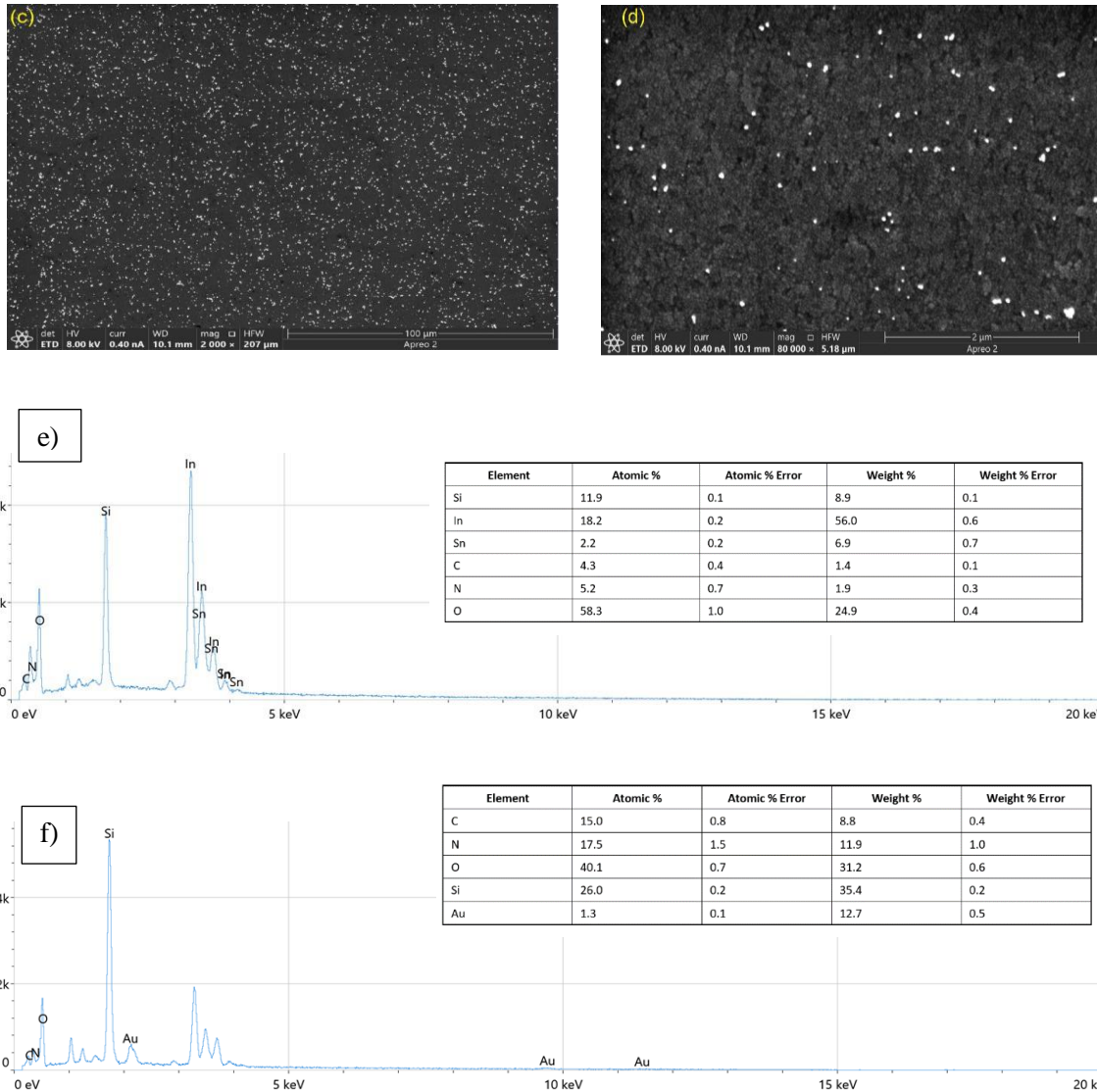


Figure 5.1. SEM images of (a) clean ITO glass at the magnification of 5kX, (b) APTES modified ITO coated glass (magnification 10kX), (c) AuNPS/APTES/ITO modified surface (at 2kX magnification), and (d) PDA (30 min polymerization)/AuNPs/APTES/ITO (at 80kX magnification). EDS analysis for APTES modified ITO glass is shown in e) and f) is showing the EDS spectrum of AuNPS/APTES/ITO modified surface.

5.2 Gold nanoparticle's colloidal solution- characterization using UV-vis spectroscopy

Figure 5.2 shows the UV-vis absorbance spectrum for the gold colloid produced by the Turkevich process. It was discovered that AuNPs's localized surface plasmon resonance allows its absorption peak to be discernible at 528 nm. The AuNPs exhibited a quasi-spherical shape and had an average size of roughly 15-20 nm.⁴

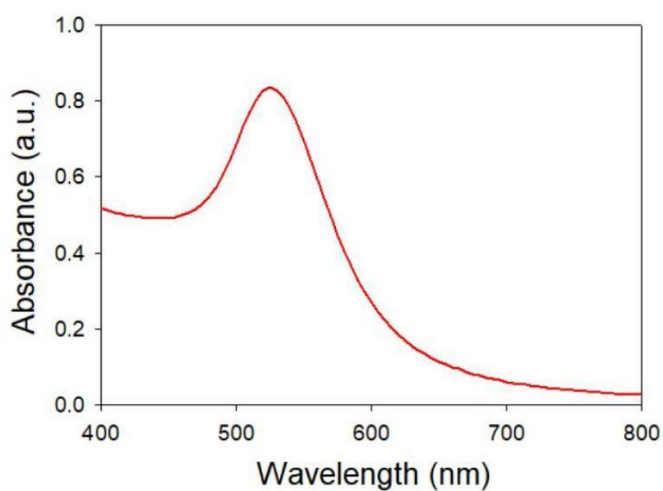


Figure 5.2. UV-Visible absorption spectrum of AuNPs, collected in milli-Q water, showing a strong absorbance peak observed at 525 nm.

5.3 Step-wise modification of the working electrode using electrochemical impedance spectroscopy (EIS)

For investigating an electrode with surface modification, EIS is a useful technique. EIS integrates the analysis of materials' capacitive and resistive properties based on the perturbation of an equilibrium system by a small amplitude sinusoidal excitation signal. To replicate electrochemical changes at the electrode/electrolyte contact, the traditional Randles electronic equivalent circuit commonly uses the following four components: In order to assess the surface properties of the modified electrode, measurements of the Warburg impedance, Z_d , the charge transfer resistance, R_{ct} , the ohmic resistance of the electrolyte solution, R_s , and the interfacial double layer capacitance (C_{dl}) between an electrode and a solution were made. Compared to other impedance components, R_{ct} values usually experience greater changes. In an impedance spectrum depicted as a Nyquist plot, charge-transfer resistance (R_{ct}) is equal to the semicircle diameter. The R_{ct} is connected to the charge transfer kinetics of the redox probe at the electrode contact. Therefore, it was decided that changes in the R_{ct} value were a good signal for identifying the interfacial properties of the created bioelectrode across all surface modification steps.⁵ Each stage of surface modification is represented by the electrode's Nyquist plot in Figure 5.3. The fact that the APTES-modified ITO electrode (17.24 Ω) has a lower R_{ct} value than the clean, bare ITO electrode (104.25 Ω) shows that there is little resistance to electronic transport at the electrode solution interface after the

creation of an APTES SAM. Because the anionic probe $[\text{Fe}(\text{CN})_6]^{3-/4-}$ has a strong affinity for the polycationic layer, the concentration of the probe increases as the amino groups of APTES are protonated (NH_3^+) in neutral aqueous solution.⁶ After the covalent bonding of the AuNPs to the silane layer, R_{ct} quickly increases to (83.98Ω) due to the charge repellent behavior of the negatively charged AuNPs citrate groups at pH 7.4 towards the anionic probe at the electrode/solution interface.⁷ Depending on the period of deposition and the thickness of the PDA layer generated following the production of the AuNPs, the R_{ct} (112.1Ω) has somewhat risen.⁸

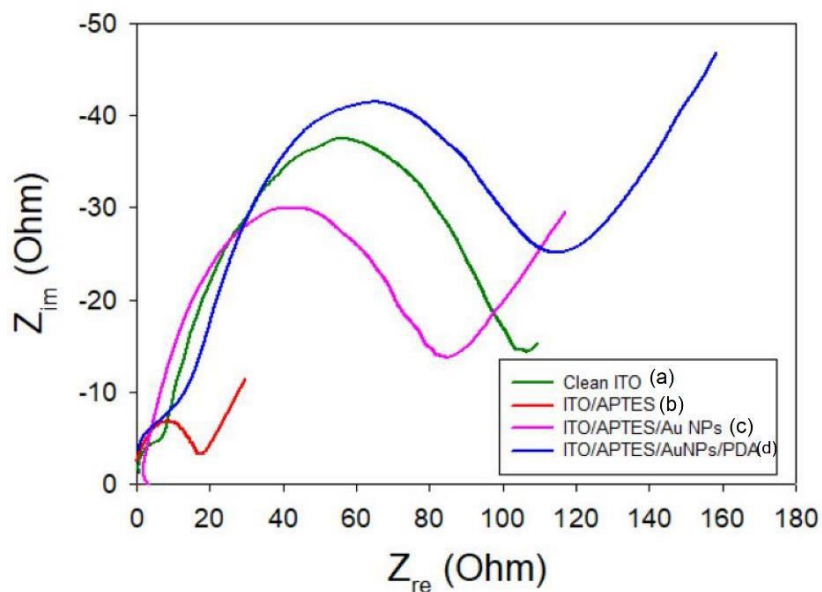


Figure 5.3. Nyquist plots for (a) clean bare ITO (b) APTES/ITO (c) AuNPs/APTES/ITO and (d) PDA/AuNPs/APTES/ITO, acquired in a PBS solution containing 5 mM $[\text{Fe}(\text{CN})_6]^{3-}/[\text{Fe}(\text{CN})_6]^{4-}$ in the frequency range from 1 Hz to 100 kHz at an AC voltage of 10 mV and a scan rate of 50 mV/s.

5.4 Optimization of analysis parameters

It is essential to measure protein concentrations, analyze the kinetics of protein-protein interactions (k_a , k_d , and K_D), and screen small molecule fragment libraries when looking for new therapeutics. If the experimental settings, analysis, and protein immobilization are properly optimized, the results will be meaningful. By assessing protein solution concentration and incubation duration, we have looked into the proper membrane protein immobilization level on the modified working electrode.⁹ A range of concentrations between 0.01 and 0.6 μM were looked at for this. The target was additionally produced in low-salt buffer at a pH just below its pI value in order to achieve a balance between creating enough charge to attract the target to the modified electrode and maintaining as much unprotonated lysine as is practical.¹⁰ The S1 subunit's capacity to bind the SARS-CoV-2 virus to human ACE2 depends critically on RBD. The computed value of hACE2's theoretical isoelectric point (pI) is 5.36. The calculated pI ranges for the RBD/His are 7.36-9.88 (8.91), the S1/His are 7.30-8.37 (7.80), and the determined pI for the RBD/Fc (fragment of human IgG) is 8.55. Different variants exhibit a range of isoelectric points, charges, and transmissibility at pH 7. As an illustration, the Alpha variation has a charge of 3.9 and a pI of 8.27, but the Beta variant has a charge of 4.9 and a pI of 8.42. The dynamics of the protein have been seen to be impacted by pH changes.¹¹⁻

5.5 Electrochemical impedance response of the modified electrode (with ACE2 and RBD) towards varying concentrations of glyco-curcuminoids

Figures 5.4 and 5.5 demonstrate the EIS responses of the ACE2 and the RBD modified electrodes, respectively, in response to the addition of various glyco-curcuminoids concentrations. Figures 5.4 and 5.5 show that a considerable change in the R_{ct} value results from the diameter of the semicircle section of the Nyquist plot (a measurement of electron transfer rate) increasing dramatically with an increase in glyco-curcuminoids concentrations. Because of the higher binding of the glyco-curcuminoid to the receptor protein (ACE2 or RBD), an elevated R_{ct} value was seen at the modified electrode. When glyco-curcuminoids bind to the membrane protein that has been surface-immobilized, access for the redox pair is severely constrained. As the Faradaic reaction of a redox pair becomes more and more constrained, the electron transfer resistance increases and the capacitance decreases. The glyco-curcumin-protein complex alters electrical capacitance and interferes with ion transport as a layer. Both factors have a significant effect on the electrochemical impedance of electrodes. The binding affinities of the glyco-curcuminoids for the receptor proteins were determined by building a ligand binding curve of concentration against R_{ct} value for each analog. As a result, the dissociation constant (K_d) was calculated using the newly constructed ligand binding curve.¹³⁻¹⁴ The binding affinities of curcuminoid (1d) were much higher than those of the other four curcumin analogs, measuring $7.65 \pm 1.48 \mu\text{M}$ and $4.09 \pm 0.9 \mu\text{M}$, respectively, for the receptor proteins ACE2 and RBD.

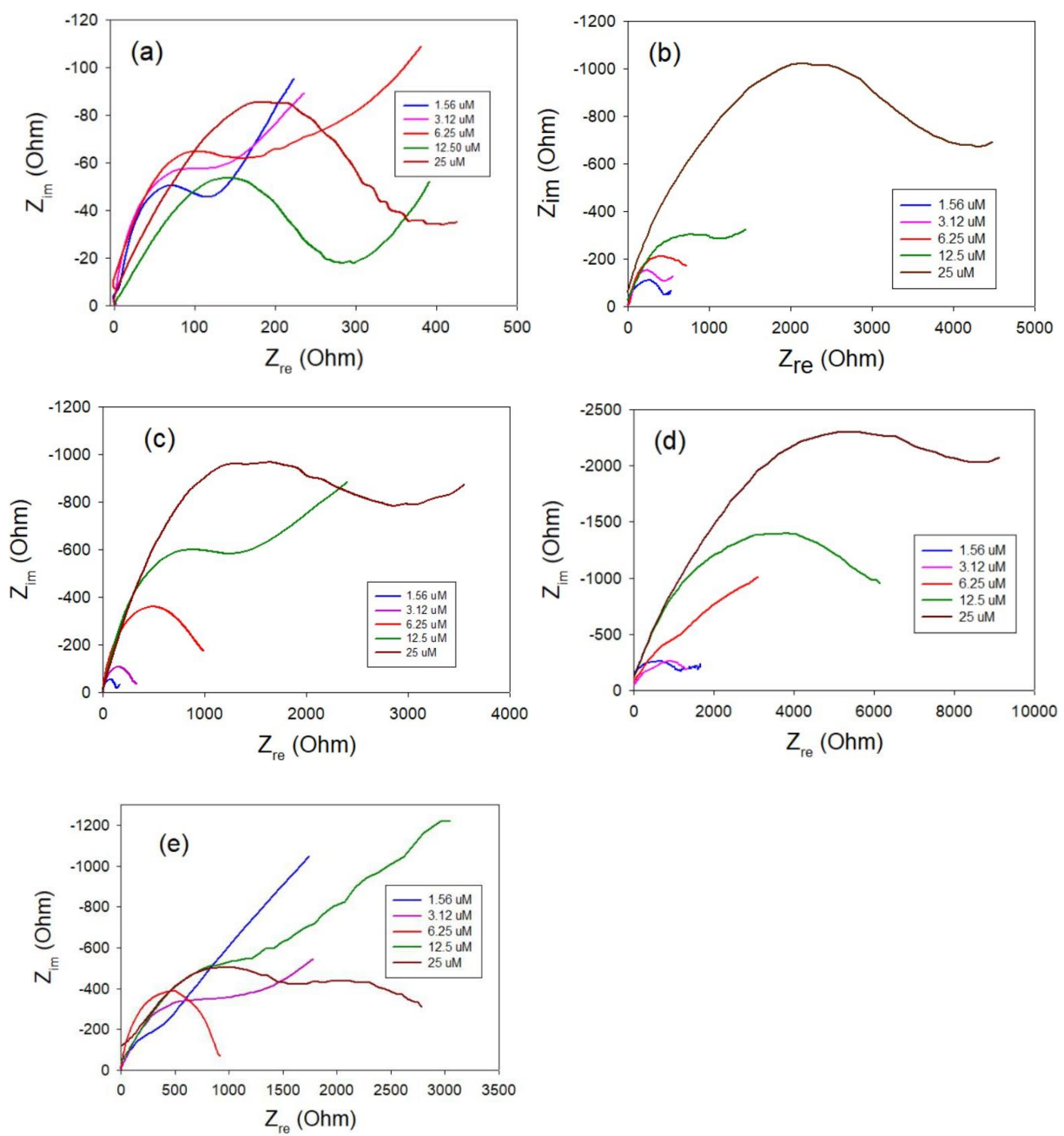


Figure 5.4. Nyquist plots of different concentrations (1.56 μM , 3.12 μM , 6.25 μM , 12.5 μM , and 25 μM) of curcumin analogs on the ACE2 (0.1 μM) modified ITO surface in the frequency range from 1 Hz to 100 kHz at an AC voltage of 10 mV and a scan rate of 50 mV/s. (a) glucosylated benzylated curcumin, (b) glucosylated methylated curcumin, (c) galactosylated monocarbonyl curcumin, (d) galactosylated-methylated curcumin, and (e) galactosylated-benzylated curcumin.

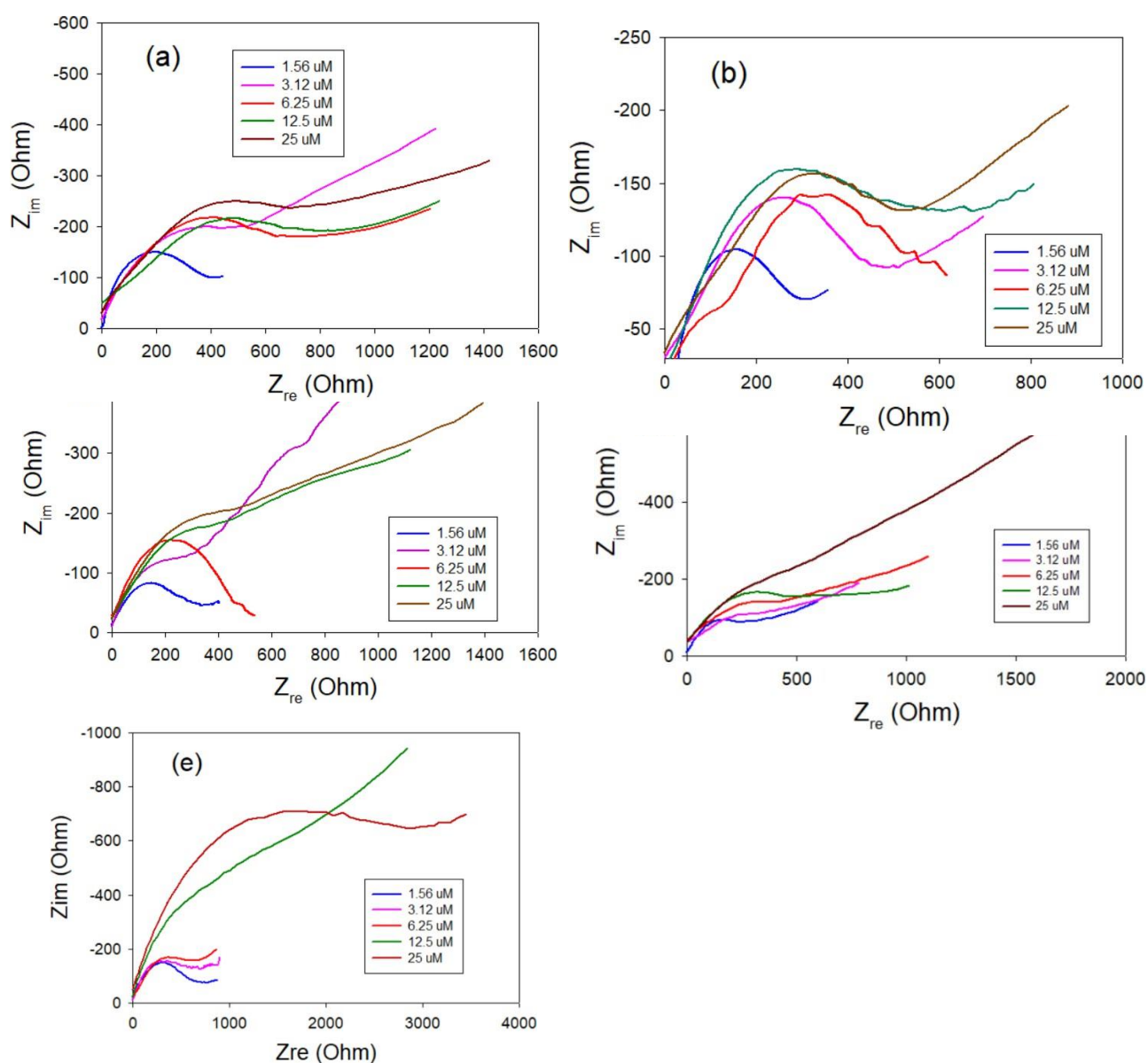
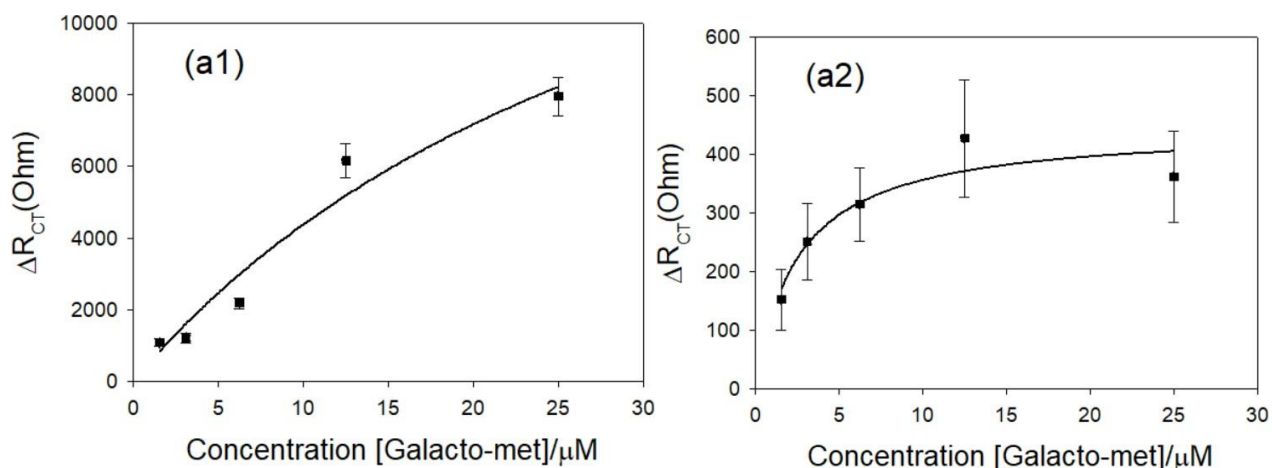
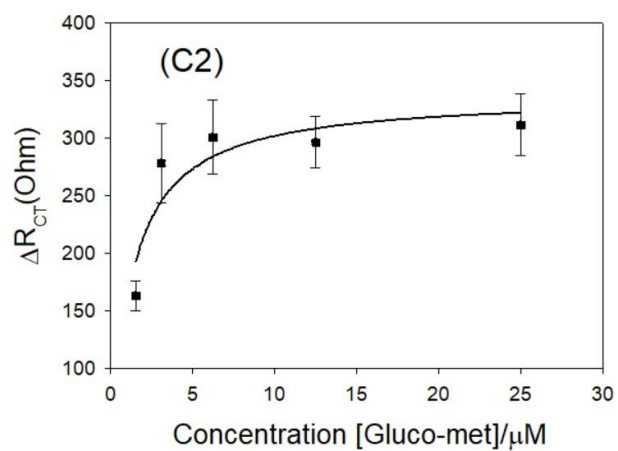
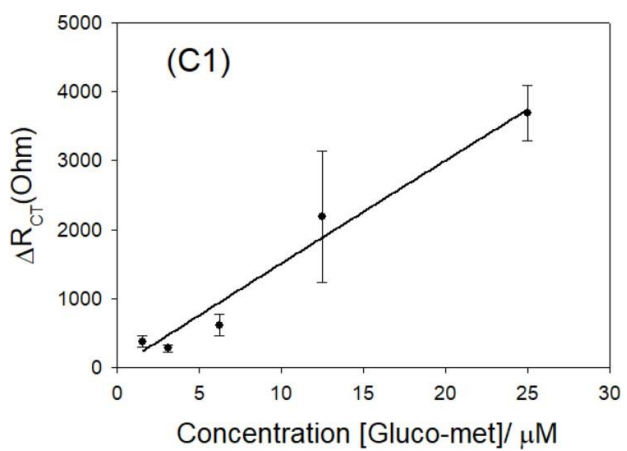
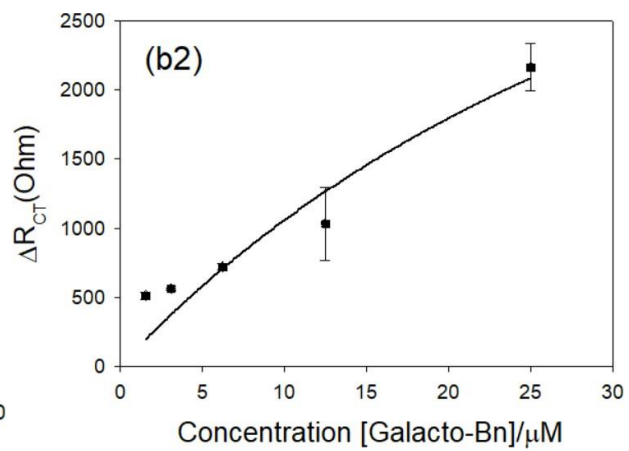
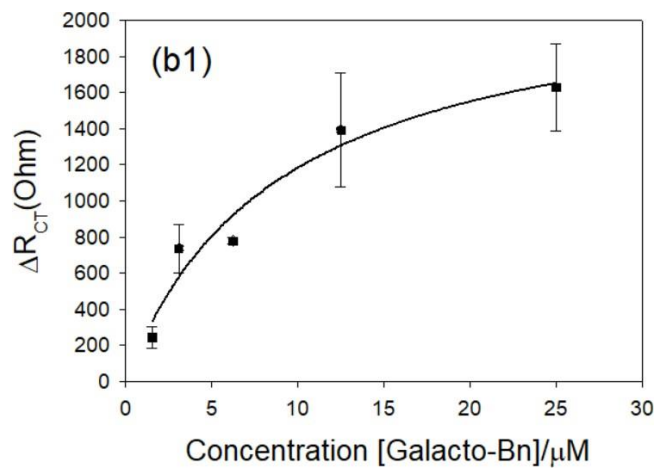


Figure 5.5. Nyquist plots of different concentrations (1.56 μM , 3.12 μM , 6.25 μM , 12.5 μM , and 25 μM) of curcumin analogs on the RBD (0.1 μM) modified ITO surface in the frequency range from 1 Hz to 100 kHz at an AC voltage of 10 mV and a scan rate of 50 mV/s. (a) glucosylated benzylated curcumin, (b) glucosylated methylated curcumin, (c) galactosylated monocarbonyl curcumin, (d) galactosylated-methylated curcumin, and (e) galactosylated-benzylated curcumin.

Figure 5.6 displays the glyco-curcuminoids' ligand binding plots with ACE2 and RBD. In an experiment without protein on the modified ITO, glyco-curcuminoids were employed as a control. The generated EIS curves are shown in Figure 5.7. The non-specific increase in R_{ct} was seen when protein was not immobilized, although the reaction was not as strong as the measurement-related increase in R_{ct} with immobilized protein.





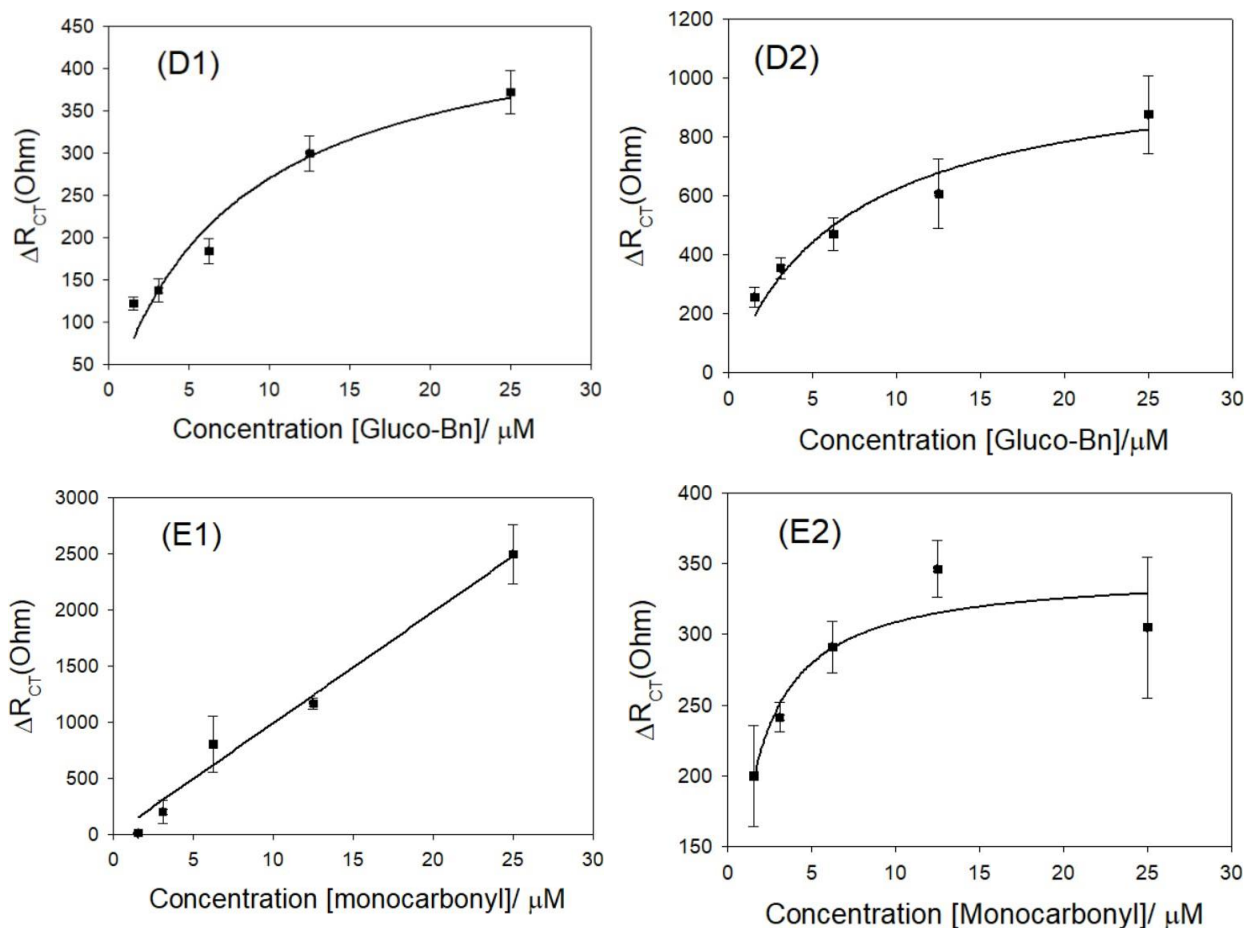


Figure 5.6. Ligand binding plots of glyco-curcuminoids with ACE2 (a1 to e1) and RBD (a2 to e2) where, (a) galactosylated-methylated curcumin, (b) galactosylated-benzylated curcumin, (c) glucosylated methylated curcumin, (d) glucosylated benzylated curcumin, and (e) galactosylated monocarboxyl curcumin

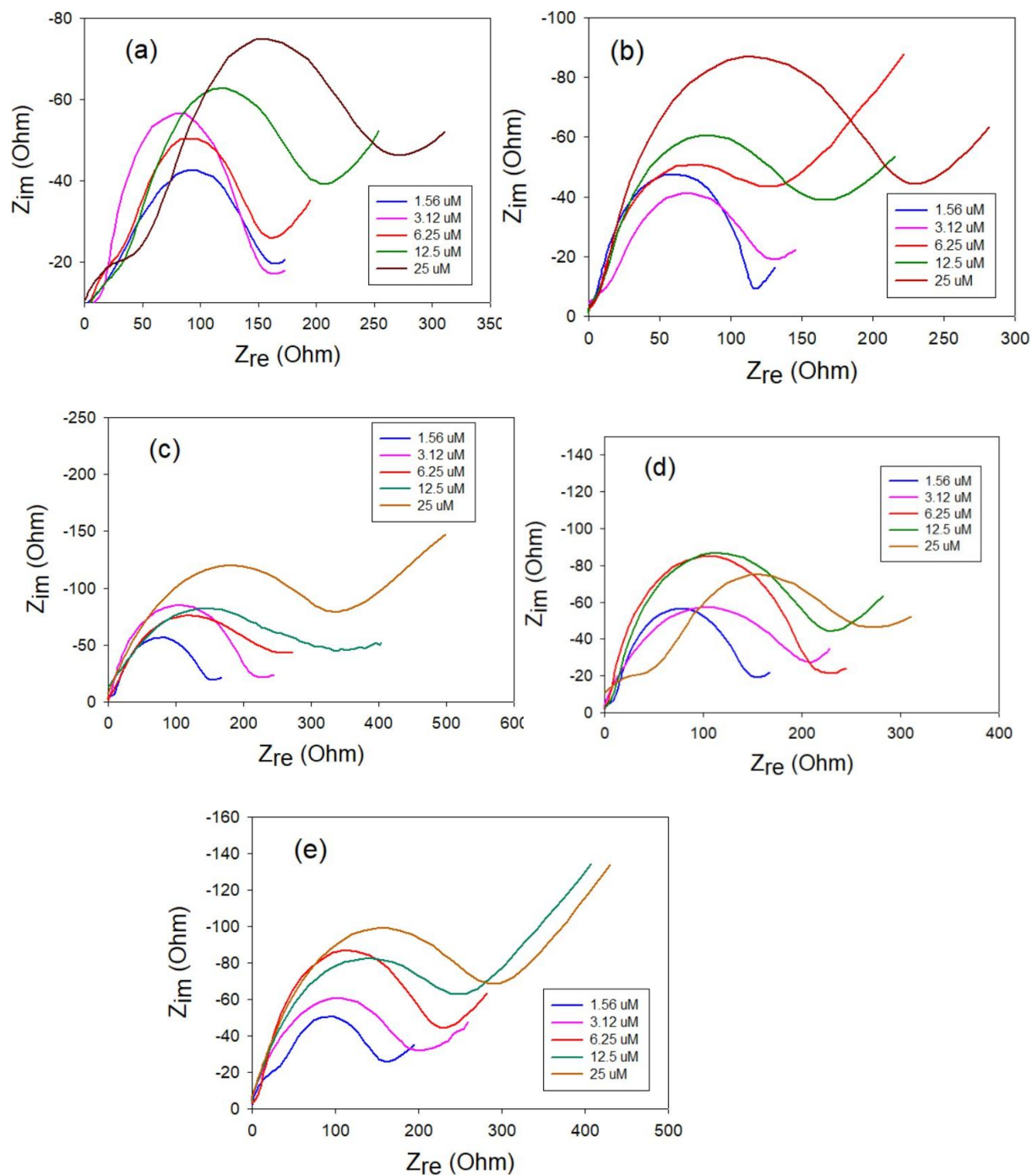


Figure 5.7. Blank test of glycoconjugated curcuminoids on the modified ITO (without RBD or ACE2) where, (a) galactosylated-methylated curcumin, (b) galactosylated-benzylated curcumin, (c) glucosylated methylated curcumin, (d) glucosylated

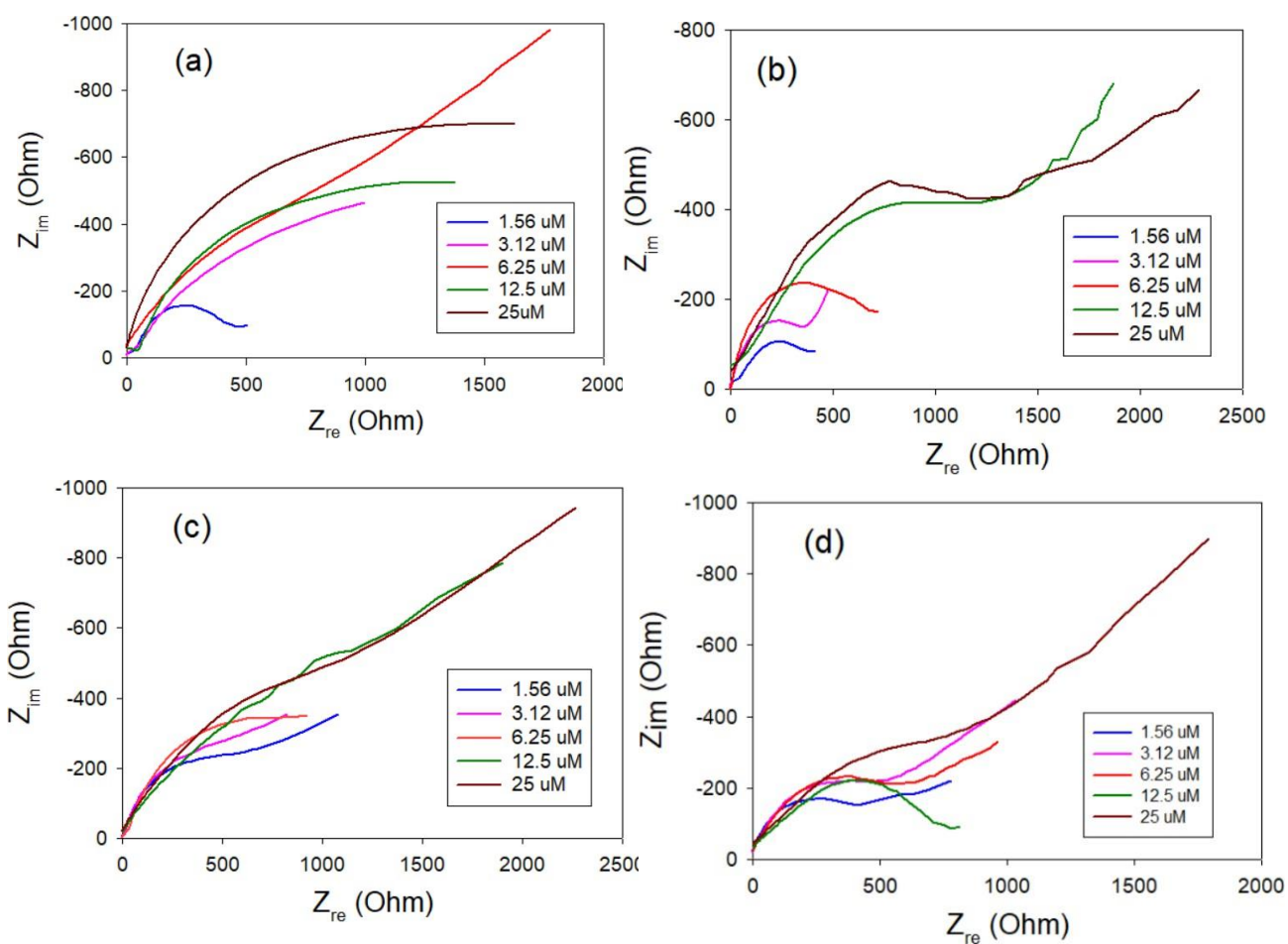
benzylated curcumin, and (e) galactosylated monocarbonyl curcumin

5.6 Understanding how ACE-2, RBD, and glyco-curcuminoids work in conjunction to cause binding

We used RBD and glyco-curcumin analogs in solution along with the immobilized ACE2 protein on the sensor surface to examine the mechanism of action of curcumin analogs. Curcuminoid (1d) binds strongly to both ACE2 and RBD, according to concentration-response tests of binding to membrane proteins, and the K_d value drops even lower ($2.4 \pm 0.51 \mu\text{M}$), which may point to the creation of a tunnel connecting ACE2, RBD, and the curcumin analog.¹⁵ Table 5.1 compiles the data on the binding affinities of all glyco-curcuminoids with ACE2 and RBD. The interaction between two partners during the binding equilibrium is reflected by the dissociation constant, which gauges their affinities. A lower K_d value denotes a stronger engagement.¹⁶ Curcuminoids (1d) and (1b) have been shown to bind with ACE2 more effectively than the other glyco-curcuminoids. Curcuminoids (1a), (1c), (1d), and (1e) all demonstrate strong binding with RBD; galacto-bn, however, could not demonstrate satisfactory findings. Curcuminoid (1d) demonstrated stronger binding when all the components were present when compared to its binding to both membrane proteins independently. Figures 5.8 demonstrate the EIS responses of Nyquist plots of different concentrations of curcumin analogs with RBD (0.1 μM) on the ACE2 (0.1 μM) modified ITO surface.

Table 5.1. Binding affinity data of glyco-curcuminoids with membrane proteins-ACE2 and RBD

Curcumin analog used	K_d with ACE2/ μ M	K_d with RBD/ μ M	K_d when all components are together (RBD-curcumin analog-ACE2)/ μ M
Galacto-met (1a)	31.9 ± 11.4	2.09 ± 0.51	1.69 ± 0.27
Galacto-Bn (1b)	7.85 ± 2.1	28.76 ± 14.4	6.15 ± 1.15
Gluko-met (1c)	111.9 ± 13.6	1.32 ± 0.24	9.15 ± 1.75
Gluko-Bn (1d)	7.65 ± 1.48	4.09 ± 0.9	2.4 ± 0.51
Monocarbonyl (1e)	86.3 ± 51.4	1.27 ± 0.15	1.6 ± 0.23



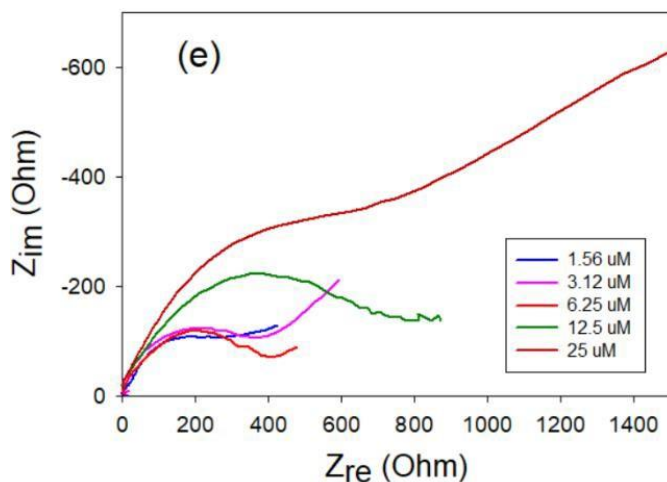


Figure 5.8 Nyquist plots of different concentrations (1.56 μ M, 3.12 μ M, 6.25 μ M, 12.5 μ M, and 25 μ M) of curcumin analogs with RBD (0.1 μ M) on the ACE2 (0.1 μ M) modified ITO surface in the frequency range from 1 Hz to 100 kHz at an AC voltage of 10 mV and a scan rate of 50 mV/s. (a) glucosylated benzylated curcumin, (b) glucosylated methylated curcumin, (c) galactosylated monocarbonyl curcumin, (d) galactosylated-methylated curcumin, and (e) galactosylated- benzylated curcumin.

Conclusion and Future perspective

Following the coronavirus outbreak, research is being done to better understand the mechanisms by which antiviral phytochemicals work. The potential antiviral activities of numerous medicinal plants and their compounds have been investigated. Additionally, the bioactive compounds isolated from these medicinal plants have immune-boosting qualities that give a thorough strategy to treat a range of illnesses. The phytochemicals derived from plants can be a significant potential source of therapy to treat various viral infections, including the infection caused by mutating coronavirus strains, as a result of the ongoing

evolution of various viruses leading to increased resistance against the current drug therapy.¹⁷ Through this work, we aim to highlight the innovatively designed glyco-curcuminoids that can be employed to combat the difficult COVID-19 strains. With methyl, benzyl, and monocarbonyl groups attached to the methylene carbon of curcumin and sugar units in the side chain, five structurally distinct glyco-curcuminoids were synthesized. The ability of the produced glyco-curcuminoids to bind to ACE2 and RBD, two important membrane proteins involved in the spread of the Covid infection, was tested using EIS technique. In contrast to the benzylated curcuminoid, which had a strong interaction with RBD only when glucose was present in the side chain, the analog with the methyl group had robust interaction with RBD regardless of the sugar unit linked to the side chain. The analog that contains both glucose and benzyl show stronger RBD and ACE2 interaction. On the other hand, galactosylated monocarbonyl analog only interacts strongly with RBD. The dissociation constant decreases when all three components (glyco-curcuminoids, RBD, and ACE2) are present together in the assay, which may indicate the onset of an association between curcuminoid and the two membrane proteins.

The EIS binding results of these curcumin analogs indicate significant potential for their usage as viral inhibitors; nevertheless, much effort needs to be done to identify the best protocols, dosages, and formulations for their commercial application as preventative supplements. Research needs to move forward in the area of creating drugs against COVID-19 from phytochemicals. Additionally, in order to fully utilize glyco-curcuminoids, future research into their

pharmacologic and pharmacokinetic mechanisms of action on the structure and functionality of new coronaviruses is required.

References

1. Hemasiri, B. W. N. H.; Kim, J.-K.; Lee, J.-M., Fabrication of highly conductive graphene/ITO transparent bi-film through CVD and organic additives-free sol-gel techniques. *Scientific Reports* **2017**, *7* (1), 17868.
2. Jeshuran, R.; Xavier, J. R., Electrochemical and Mechanical Studies of Epoxy Coatings Containing Eco-Friendly Nanocomposite Consisting of Silane Functionalized Clay–Epoxy on Mild Steel. *Journal of Bio- and Tribo-Corrosion* **2020**, *6*, 126.
3. Li, J.; Tian, B.; Li, T.; Dai, S.; Weng, Y.; Lu, J.; Xu, X.; Jin, Y.; Pang, R.; Hua, Y., Biosynthesis of Au, Ag and Au-Ag bimetallic nanoparticles using protein extracts of *Deinococcus radiodurans* and evaluation of their cytotoxicity. *International journal of nanomedicine* **2018**, *13*, 1411-1424.
4. Feng, T.; Ding, L.; Chen, L.; Di, J., Deposition of gold nanoparticles upon bare and indium tin oxide film coated glass based on annealing process. *Journal of Experimental Nanoscience* **2019**, *14* (1), 13-22.
5. Amouzadeh Tabrizi, M.; Acedo, P., An Electrochemical Impedance Spectroscopy-Based Aptasensor for the Determination of SARS-CoV-2-RBD Using a Carbon Nanofiber-Gold Nanocomposite Modified Screen-Printed Electrode. *Biosensors* **2022**, *12* (3).
6. Sun, L.; Li, W.; Wang, M.; Ding, W.; Ji, Y., Development of An Electrochemical Impedance Immunosensor for Myoglobin Determination. *International Journal of Electrochemical Science* **2017**, *12* (7), 6170-6179.
7. Mishra, S. K.; Srivastava, A. K.; Kumar, D.; Rajesh, Bio-functionalized Pt nanoparticles based electrochemical impedance immunosensor for human cardiac myoglobin. *RSC Advances* **2014**, *4* (41), 21267-21276.
8. Zhang, W.; Tang, Y.; Liu, J.; Ma, Y.; Jiang, L.; Huang, W.; Huo, F.-w.; Tian, D., An electrochemical sensor for detecting triglyceride based on biomimetic polydopamine and gold nanocomposite. *Journal of Materials Chemistry B* **2014**, *2* (48), 8490-8495.
9. Hilbert, M., Towards Understanding Protein Immobilization Rules Through Site-Specific Covalent Immobilization of T4 Lysozyme. **2021**.
10. Krebs, F.; Scheller, C.; Grove-Heike, K.; Pohl, L.; Wätzig, H., Isoelectric point determination by imaged CIEF of commercially available SARS-CoV-2 proteins and the hACE2 receptor. *Electrophoresis* **2021**, *42* (6), 687-692.
11. Aksenova, A. Y.; Likhachev, I. V.; Grishin, S. Y.; Galzitskaya, O. V., The Increased Amyloidogenicity of Spike RBD and pH-Dependent Binding to ACE2 May Contribute to the Transmissibility and Pathogenic Properties of SARS-CoV-2 Omicron as Suggested by In Silico Study. *International Journal of Molecular Sciences* **2022**, *23* (21), 13502.
12. Campbell, F.; Archer, B.; Laurensen-Schafer, H.; Jinnai, Y.; Konings, F.; Batra, N.; Pavlin, B.; Vandemaele, K.; Van Kerkhove, M. D.; Jombart, T.; Morgan, O.; le Polain de Waroux, O., Increased transmissibility and global spread of SARS-CoV-2 variants of concern as at June 2021. *Euro surveillance : bulletin Europeen sur les maladies transmissibles = European*

communicable disease bulletin **2021**, 26 (24).

13. You, X.-H.; Liu, Y.; Li, Y.-Y.; Zhao, B.; Yang, Y.; Weerasooriya, R.; Chen, X., Sensitive detection of SARS-CoV-2 spike protein based on electrochemical impedance spectroscopy of Fe₃O₄@SiO₂-Au/GCE biosensor. *Advanced Sensor and Energy Materials* **2023**, 2 (3), 100067.

14. Wang, L.; Wu, Y.; Yao, S.; Ge, H.; Zhu, Y.; Chen, K.; Chen, W. Z.; Zhang, Y.; Zhu, W.; Wang, H. Y.; Guo, Y.; Ma, P. X.; Ren, P. X.; Zhang, X. L.; Li, H. Q.; Ali, M. A.; Xu, W. Q.; Jiang, H. L.; Zhang, L. K.; Zhu, L. L.; Ye, Y.; Shang, W. J.; Bai, F., Discovery of potential small molecular SARS-CoV-2 entry blockers targeting the spike protein. *Acta pharmacologica Sinica* **2022**, 43 (4), 788-796.

15. Chuang, S. T.; Buchwald, P., Broad-Spectrum Small-Molecule Inhibitors of the SARS-CoV-2 Spike-ACE2 Protein-Protein Interaction from a Chemical Space of Privileged Protein Binders. *Pharmaceuticals (Basel, Switzerland)* **2022**, 15 (9).

16. Eble, J. A., Titration ELISA as a Method to Determine the Dissociation Constant of Receptor Ligand Interaction. *Journal of visualized experiments : JoVE* **2018**, (132).

17. Chaturvedi, P., Antiviral medicinal plants of India as a potential tool against COVID-19: A review with ethno scientific evidence. *Journal of Medicinal Herbs and Ethnomedicine* **2023**, 9, 1-17.

CHAPTER VI PRELIMINARY WORK

6.1 *GUVs to study the interaction of LPS analogs with cell membrane*

The cell membrane forms a dynamic and flexible barrier with high complexity in composition and shape, separating the living cell from the external environment. The interaction and diffusion of molecules with the cell membrane depend on the overall membrane composition, underlying cytoskeleton¹, surrounding medium, and membrane shape. Also, in *in vivo* experiments the presence of a high variety of lipids and proteins, and the continuous reorganization offered by cellular processes makes the study difficult.² Therefore, investigation of an interaction phenomenon in a complex and dynamic membrane poses a challenge as the event might be influenced by certain unknown processes. Therefore, we thought to reduce the complexity of the cellular membrane by creating a membrane model system with controlled composition to study the binding of our LPS analogs with the basic lipid membrane under well-defined conditions.

Giant Unilamellar Vesicles (GUVs) consisting of lipid bilayers with diameters of $> 10 \mu\text{m}$, mimicking the size to that of eukaryotic cells have been used in our study. The large size of GUVs enabled us to observe them with optical microscopy.³⁻⁴ Shape changes in a single GUV can be induced by peptides, proteins, and small molecules. It has been seen that lipopolysaccharide (LPS) can insert from the solution into the preformed lipid GUVs and cause shape changes and vesicle fission.⁵

The outer membrane of Gram-negative bacteria is majorly composed of LPSs which are critical for the defense of Gram-negative bacterial cells against macromolecules, hydrophobic compounds, and other chemical agents.

They are important to maintain the structural integrity of Gram-negative bacterial cell membrane however, LPSs act as pyrogenic endotoxins in normal animal immune systems generating massive inflammatory responses.⁶ In this work, we focused on investigating the interaction of LPS antagonists with the biomimetic system wherein we are observing the concentration-dependent changes in the GUVs.⁷ We expect that the model developed here will be useful for microscopically characterizing the interactions of LPS analogs (potential new drug candidates against sepsis) of different chain lengths and varying concentrations with the lipid membrane of GUVs.

6.1a) Giant Unilamellar Vesicles (GUVs) electroformation procedure: Assembling the chamber

Giant Unilamellar Vesicles (GUVs) were generated using the technique of electroformation using sinusoidal potential waves applied between the conductive sides of indium tin oxide (ITO) coated glass electrodes. For electroformation, we used DMPC dissolved in chloroform (2 μ M) along with NBD-C₆-HPC (0.5 mol%) transferred and spread on the clean conductive side of the ITO slides using a Hamilton syringe (volume added was roughly 20 μ L). Lipid coated ITO slide was dried for 5 min under an N₂ stream. Afterwards, the electroformation chamber was created by placing the conductive side of ITO slides facing each other along with a silicon gasket in the middle having a copper tape on top, contacting the conductive side of the slide. The chamber was clamped with two binder clips from the sides. Subsequently, the chamber was filled with 300 mM sucrose (avoiding air bubbles). Once the chamber is ready, it is then connected to the function generator via BNC (Bayonet Neill

Concelman) cables with alligator clips clamping to the copper tape that is protruding from the chamber.⁸

6.1b) Electroformation

A programmable function generator (Agilent 33120A) has been used to modulate peak-to-peak voltage (V_{PP}) and frequency at room temperature. A two-phase program has been used in our study wherein the Sine wave with frequency 10 Hz was used for 60 min followed by another cycle of 60 min with the frequency of 2 Hz keeping the V_{PP} at 2.2 V constant throughout the experiment.⁹⁻¹⁰

6.1 c) Harvesting GUVs and preparing the imaging chamber

After the electroformation program has run to completion, the sucrose solution containing GUVs was extracted slowly from the chamber with the help of a syringe. At this stage an imaging set up is created using slide wells attached onto a glass slide. In order to immobilize GUVs in the wells, 0.6% w/v agarose gel has been used wherein GUVs get caged inside the pockets of the gel meshwork and their motion was restricted GUVs-agarose gel was then placed in wells using pipette tips cut to a larger diameter to avoid shearing of GUVs while pipetting.¹¹ GUVs were imaged using confocal microscope (ZEISS LSM 900). Images were acquired using a 20x objective using the excitation at 488 nm.

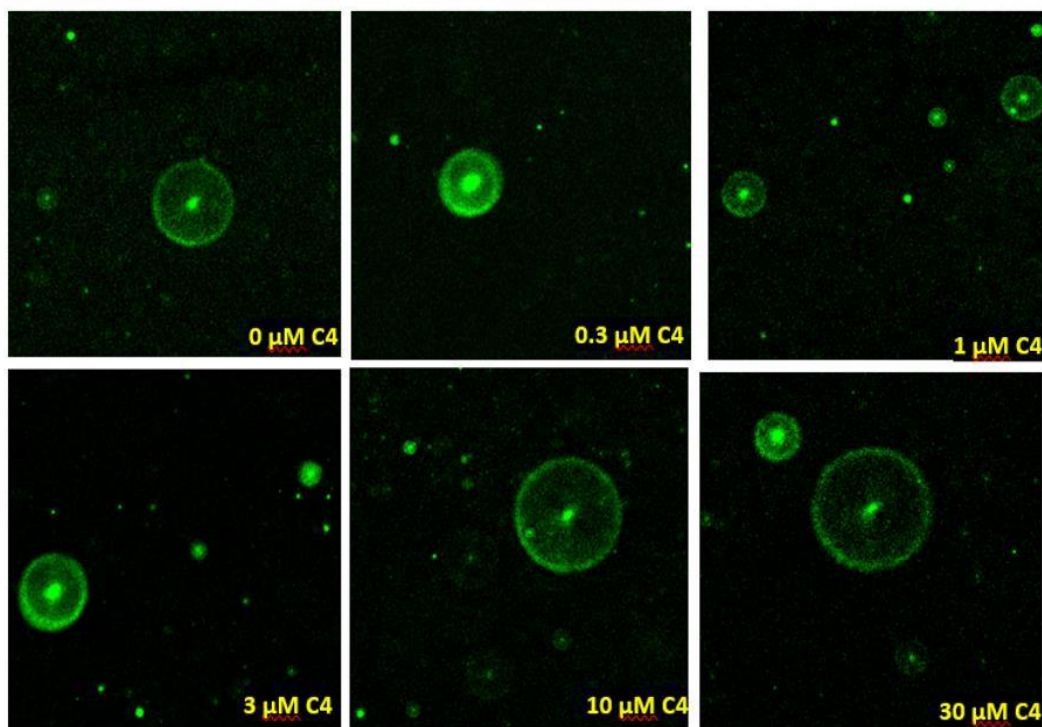
6.1 d) LPS analogs of varying chain lengths incubation with GUVs

The synthesized analogs with varying chain lengths have differing degrees of LPS antagonistic activity. Their activity is evaluated by incubating GUVs with increasing concentrations of the analogs. A concentrated working stock

solution was prepared using DMSO. The stock solution was further diluted in DMSO to generate a concentration range. The final series of concentrations were prepared by diluting the stock solutions in PBS keeping DMSO at 1%. The slide wells in the imaging chamber were then filled with 100 μL of the varying concentrations of the analog. After that 50 μL of the GUV solution was gently added to each of the slide wells. The mixture was incubated at room temperature for about an hour to allow the interaction of analogs to GUV membrane. Imaging was done after an hour of incubation using confocal microscope. Figure 6.1 shows the interaction of LPS antagonists of varying chain lengths (C4 to C12), LPS, and AM12 with the synthesized GUVs.

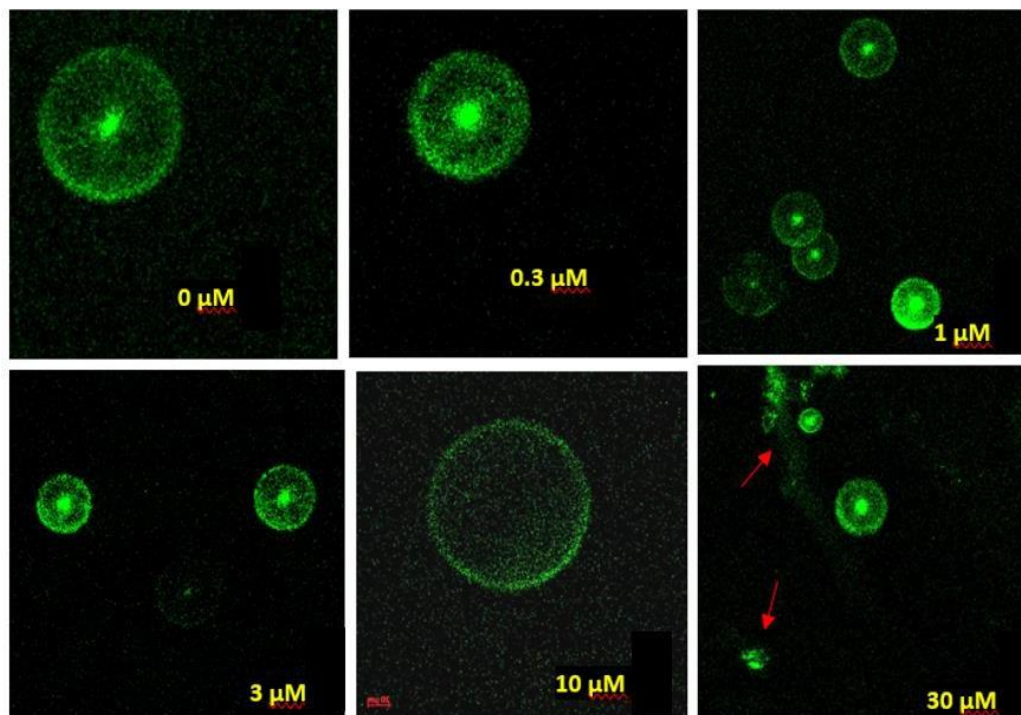
(A) LPS antagonists ranging from C4 to C12 carbon chain interacting with GUVs

(a) C4 lactone LPS analog incubation with GUV



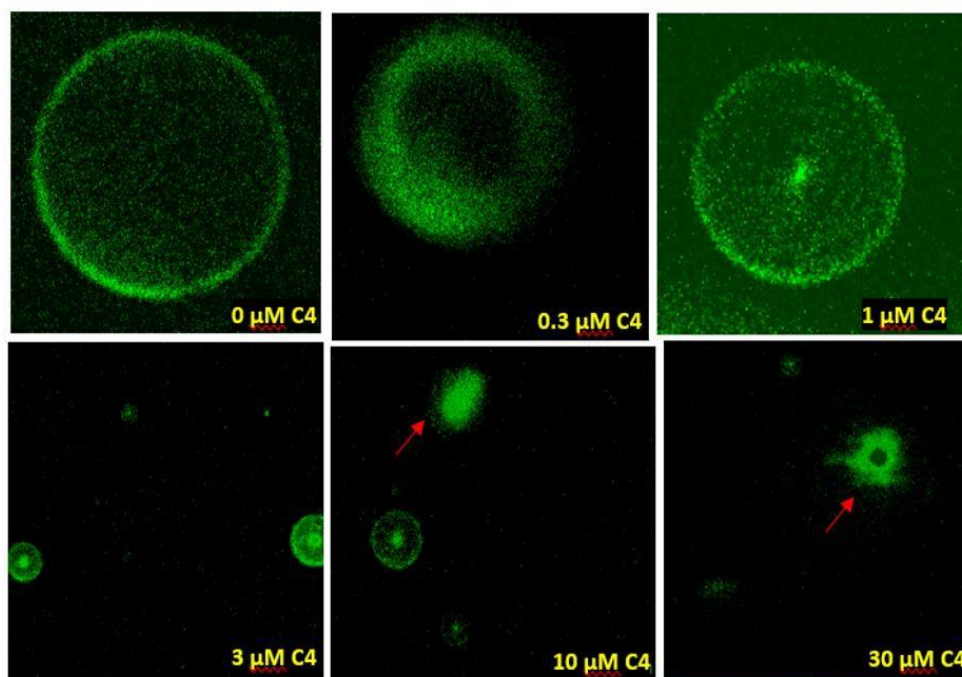
The GUV bilayer was unaffected by the presence of C4 lactone at various concentration ranges.

(b) C6 lactone LPS analog incubation with GUV



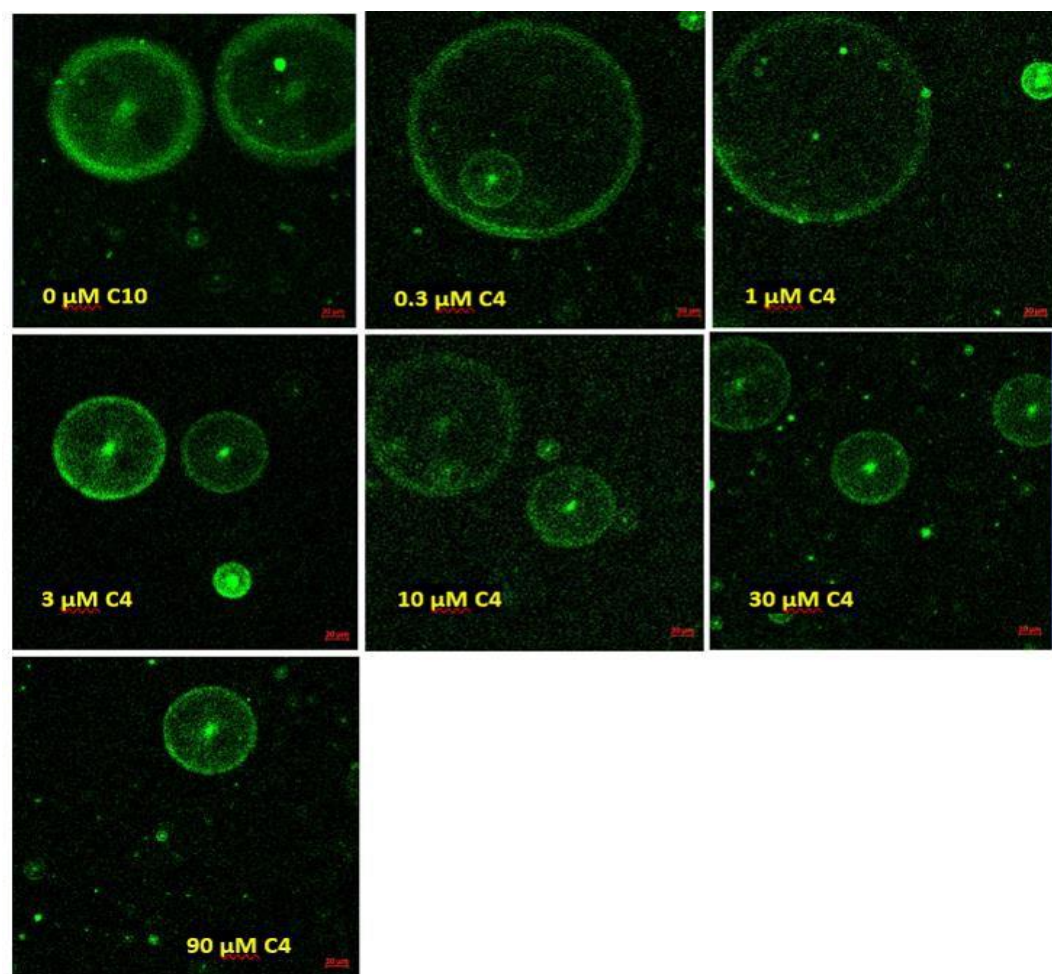
Subjecting GUVs to varying concentration of C6 lactone has shown non-toxic behavior. The GUV bilayer was unaffected by the presence of C6 lactone up to 10 μM . However, at higher concentrations we observed membrane inhomogeneities and artifacts in the lipid membrane in a small population of GUVs. These results reveal that direct interaction of C6 lactone to lipid bilayers at concentrations higher than 10 μM could perturb the lipid organization.¹²

(c) C8 lactone LPS analog incubation with GUV



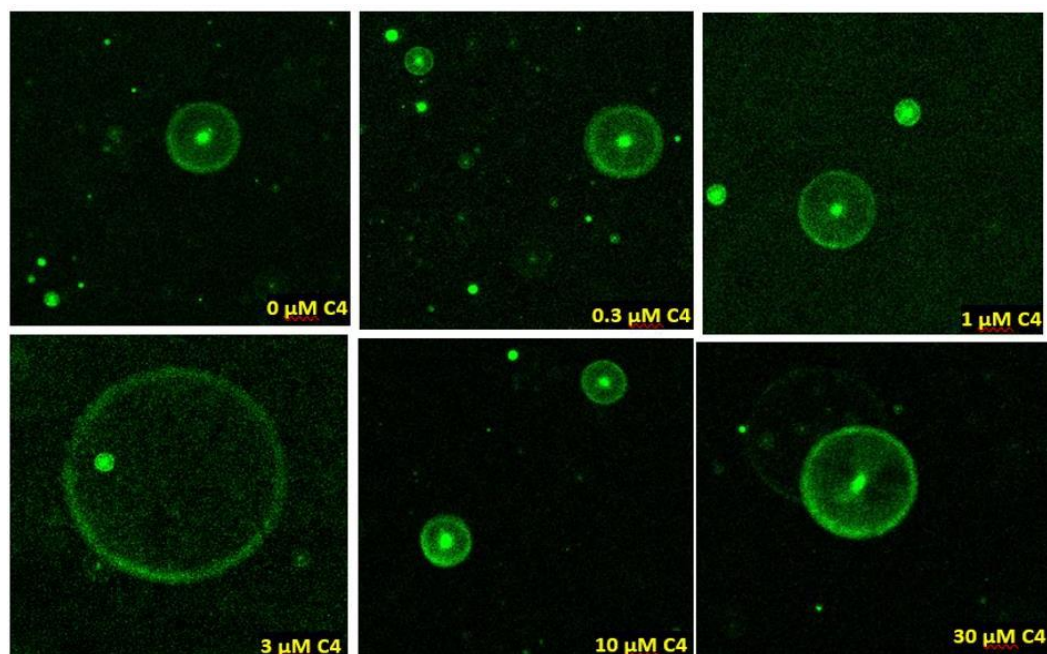
When the chain length was increased from C6 to C8, GUVs showed slightly different behavior when the lactone interacted directly to its bilayer. The GUV bilayer was unaffected by the presence of C8 lactone up to 3 μM . However, at higher concentrations of 10 and 30 μM we observed a decrease of vesicle size together with a shape deformation. These results reveal that direct interaction of C8 lactone to lipid bilayers at concentrations higher than 3 μM . could be toxic.

(d) C10 lactone LPS analog incubation with GUV



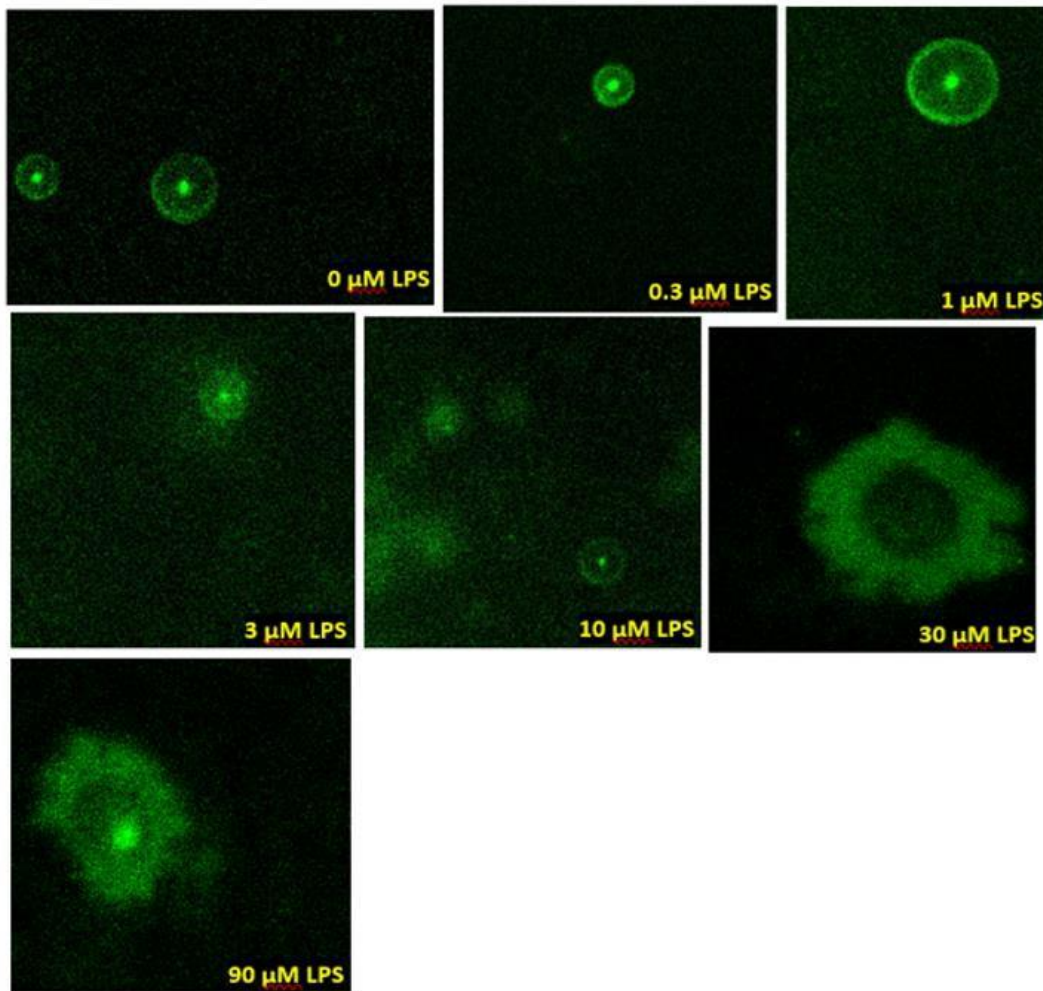
The LPS analog with 10 carbon units when incubated with GUVs, we observed that most GUVs were spherical without any shape deformation and possessed a clean membrane even at higher concentrations.¹³ So far, C10 lactone has given the best result in terms of non-toxic nature when interacted directly with GUVs membrane.

(e) C12 lactone LPS analog incubation with GUV



The GUV bilayer was unaffected by the presence of C12 lactone at various concentration ranges.

(B) LPS (E. coli O127:B8) incubation with GUV



When the concentration reached 3 μM and above, we did see a shape deformation in several of the GUVs. These findings suggest that at concentrations more than 3 μM, LPS could be harmful when it directly interacts with lipid bilayers.

(C) AM12 incubation with GUV

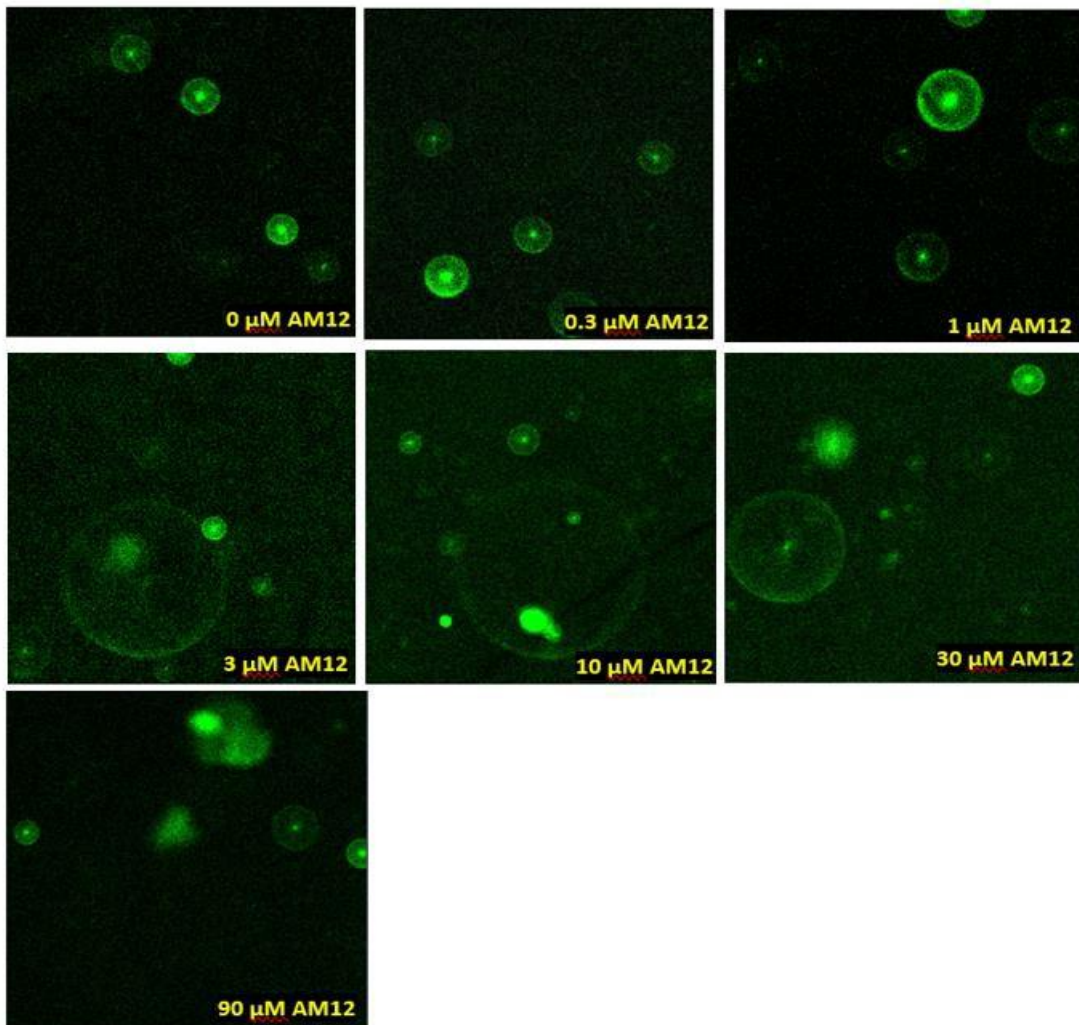


Figure 6.1. Interaction of (A) LPS antagonists of varying chain lengths (a) C4, (b) C6, (c) C8, (d) C10, (e) C12, (B) LPS, and (C) AM12 with GUVs.

6.2 *Formation of supported lipid bilayer*

The vesicles were prepared using a mini extruder. The size was analyzed using the DLS technique (Fig. 6.2a). 10 μ L of the solution was drop cast over the freshly cleaved mica. The topography was analyzed using the tapping mode in AFM (Fig. 6.2b) after fully drying the sample. Patches of lipid bilayer were seen which fused to form a bilayer over which small vesicles remain attached. The bilayer formation was tried on the QCM sensor as well (Fig. 6.2c).¹⁴ There is a two-phase behavior where in the first phase the frequency decreases depending on the substrate which indicates adsorption of substantial amount of non-ruptured vesicles. The final shift in the frequency corresponds to the formation of an adsorbed vesicle layer. Gold substrates are intractable to vesicle fusion and the fusion process will be induced on alkanethiol SAM decorated gold wherein alkanethiols act as hydrophobic monolayer substrates for the bilayer formation.¹⁵⁻¹⁶

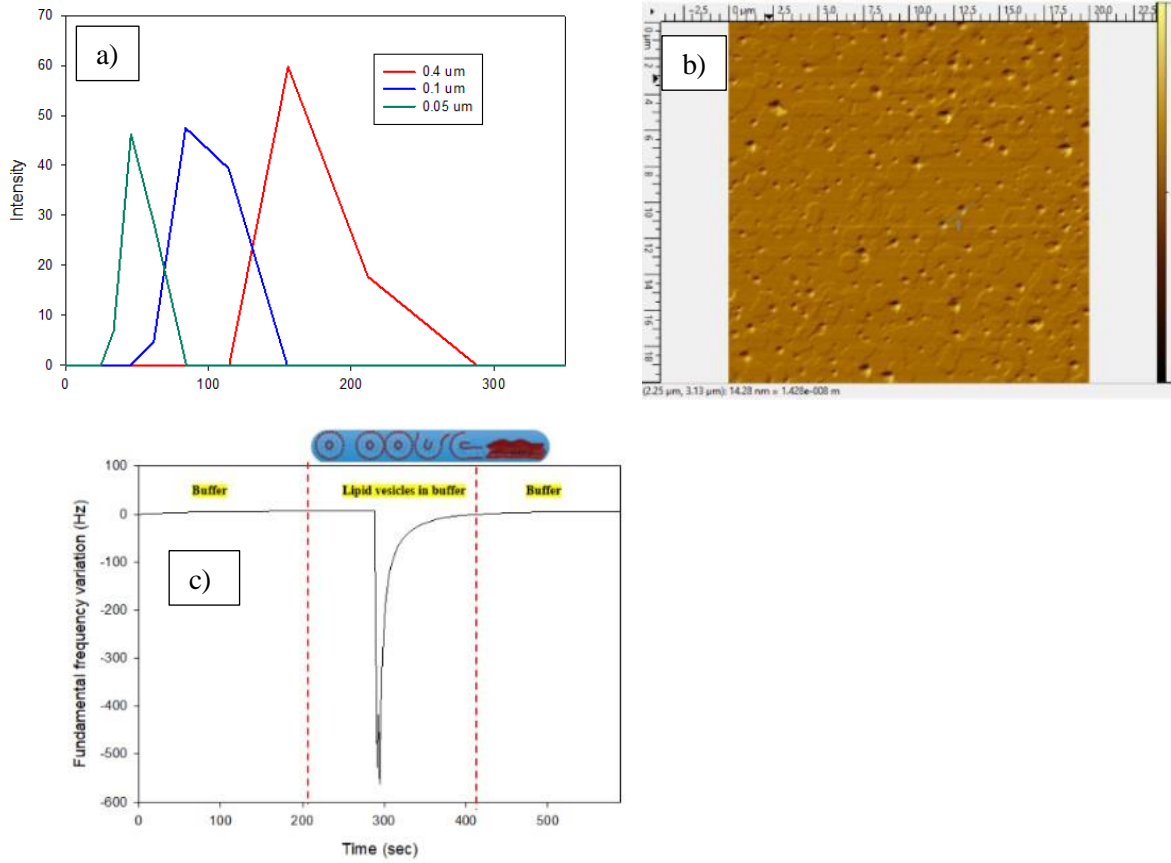


Fig 6.2. a) DLS analysis of lipid vesicles with filters of varying pore size b) AFM image after vesicle fusion c) QCM-D analysis of vesicle fusion

AFM was used to see the structural reorganization of the lipid bilayer after adding LPS. Planar lipid bilayer was exposed to LPS (0.4 mM) in PBS buffer and after rinsing holes were seen. The number of holes and subtle changes in the membrane curvature was seen to depend on the LPS concentration and incubation time as seen in Fig.6.3.

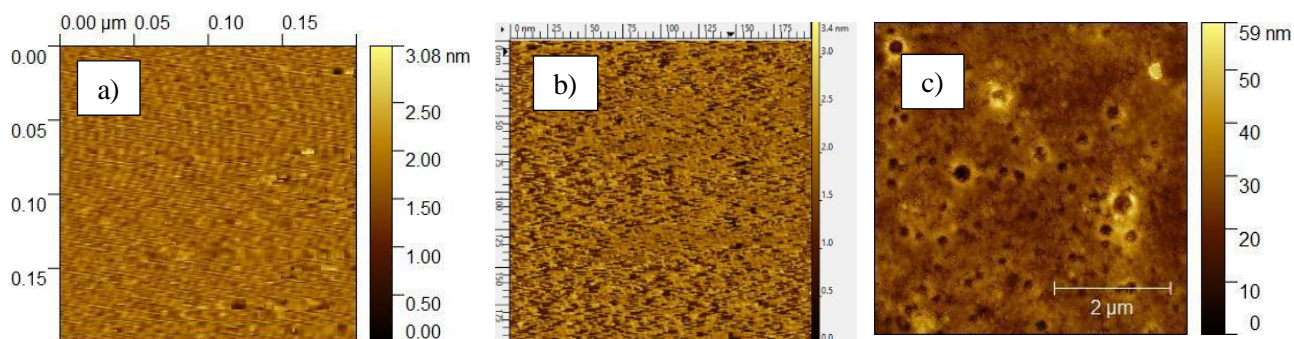


Figure 6.3. a) freshly cleaved mica surface b) 1,2-Dipalmitoyl-sn-glycero-3-phosphoethanolamine (DPPE) monolayer formation c) after incubation with LPS

6.3 *Evaluating the Effectiveness of β -Cyclodextrin as a Surface Modification to Nanoporous Gold in the Electrochemical Detection of Acetaminophen*

Acetaminophen is part of a class of pollutants referred to as endocrine disruptors. Acetaminophen is frequently used as an over-the-counter pain reliever, and these days, it can be found more frequently in natural water environments. Although its concentrations are typically between ppt and ppm, acetaminophen can change into a number of intermediates depending on the surrounding environment. It is extremely difficult to monitor, detect, and suggest appropriate treatment solutions due to the complexity of acetaminophen breakdown products and intermediates. In excess, these

pollutants can result in growth defects and cancers in humans and wildlife. Efforts to limit their harmful effects require precise detection. Current methods of detecting acetaminophen require specialized equipment that may not be efficient in all situations. Electrochemical sensing may instead allow accurate in-field detection. The concentration of such a chemical is determined based on the voltammetric peaks recorded analytically at a conductive electrode. One promising electrode for sensing is NPG. Its high surface area supports sensing because it allows for greater contact with target molecules. Thus, this project aimed to fabricate NPG wire electrode, and using this, characterize the activity of acetaminophen in regard to electrochemical sensing. To increase performance of the base electrode, surface modifications can be applied. One of these is thiolated β -cyclodextrin. Past studies have shown that it attaches to the surface of the gold via thiol group. The resulting cup-like structure has also been shown to effectively incorporate acetaminophen due to the polar hydroxyl groups. For surface modification, NPG was immersed in a 0.1mM β -cyclodextrin solution. Figure 6.4 shows the structure of thiolated β -cyclodextrin used in the study for surface modification of NPG surface.

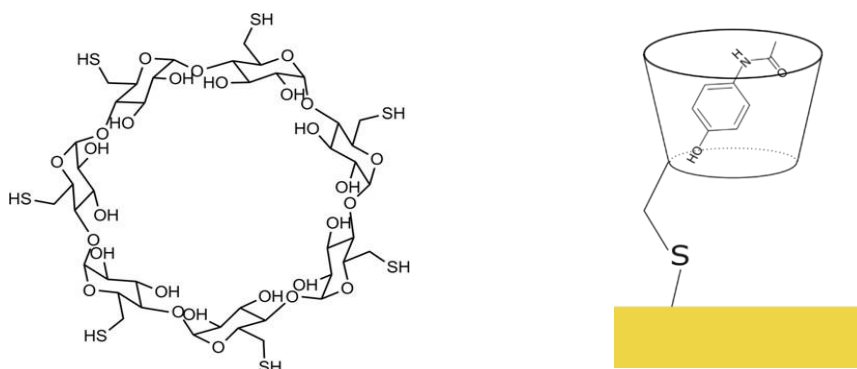


Figure 6.4 Structure of thiolated β -cyclodextrin and its attachment on the electrode's surface

Finally, CV was used to characterize the peak current and voltages. The graph showing a comparison between the typical cyclic voltammetry scans for modified and unmodified NPG is shown in Figure 6.5. For both electrodes, the anodic (forward scan) mean peak location was at $0.37\text{V} \pm 0.01$. The cathodic peak was obscured or absent. This suggests that the chemical oxidation was likely semi-irreversible. Qualitatively, the modified NPG peak was typically more defined and isolated than the peak for bare NPG. The process was repeated for various acetaminophen concentrations ($10\ \mu\text{M}$, $50\ \mu\text{M}$, and $100\ \mu\text{M}$). The graph of concentration vs. peak current (Figure 6.6) was analyzed to determine the sensitivity and selectivity of the electrode system. An electrochemical oxidation process was found to have occurred at 0.37V , like previous values. In this study, no significant trend between concentration and current was found for bare NPG, possibly due to saturation of the electrode at lower concentrations. Upon application of the β -cyclodextrin surface modification, the positive linear of the calibration curve was enhanced (Figure 6.7). The electrochemical peak became sharper and more distinct.

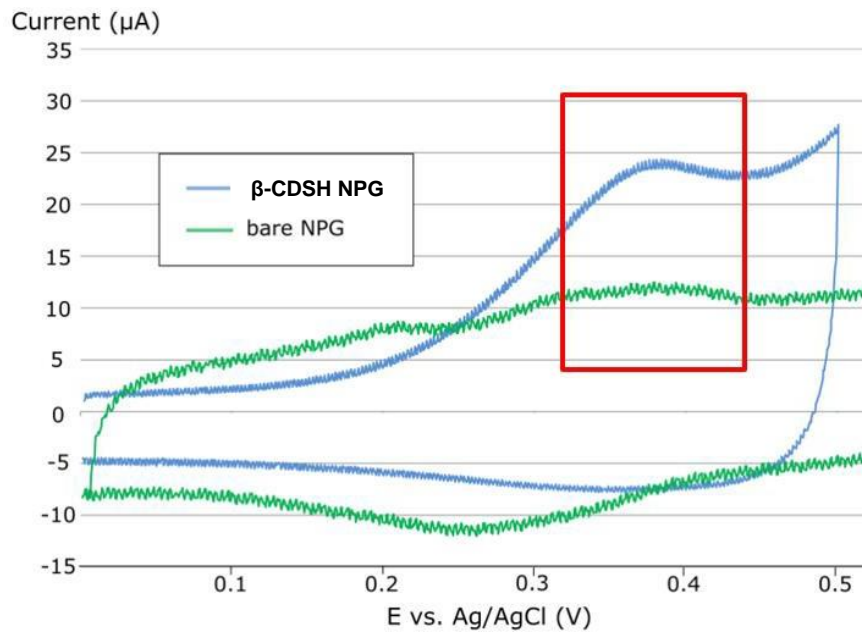


Figure 6.5 Comparison of typical cyclic voltammetry scans of 100 μM acetaminophen on bare and modified NPG

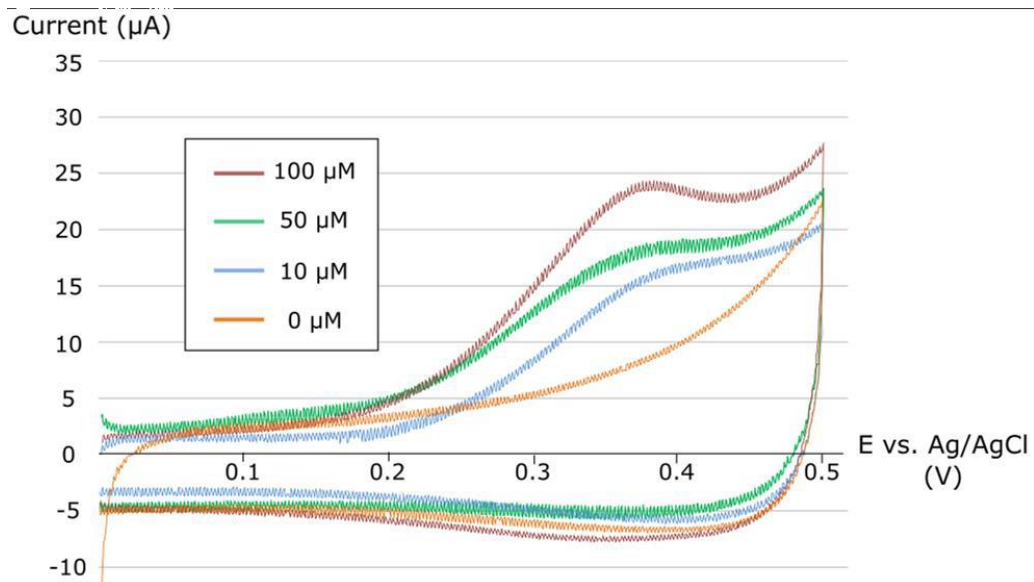


Figure 6.6 Cyclic voltammety scans at selected acetaminophen concentrations on modified NPG electrode

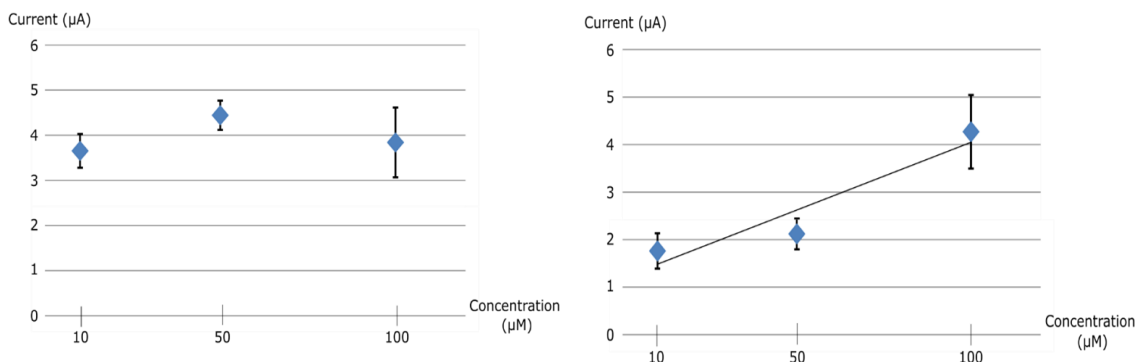


Figure 6.7 Comparison of peak current and concentration trend in (a) unmodified and (b) modified NPG

The results of the study will ultimately advance the electrochemical sensing of water and soil pollutants by determining the efficacy of nanoporous gold modified by β -cyclodextrin. Modified NPG holds promise for incorporation into rapid testing devices to monitor acetaminophen medically and in the environment. In addition, based on similar chemical concepts, β -CDSH could be a potential research interest to improve electrochemical sensing efficacy for other ubiquitous chemicals in the world around us.

References

1. Mueller, V.; Ringemann, C.; Honigsmann, A.; Schwarzmann, G.; Medda, R.; Leutenegger, M.; Polyakova, S.; Belov, V.; Hell, S.; Eggeling, C., STED nanoscopy reveals molecular details of cholesterol-and cytoskeleton-modulated lipid interactions in living cells. *Biophysical journal* **2011**, *101* (7), 1651-1660.
2. Stein, H.; Spindler, S.; Bonakdar, N.; Wang, C.; Sandoghdar, V., Production of Isolated Giant Unilamellar Vesicles under High Salt Concentrations. *Frontiers in Physiology* **2017**, *8*, 1- 16.
3. Wieprecht, T.; Apostolov, O.; Beyermann, M.; Seelig, J., Membrane binding and pore formation of the antibacterial peptide PGLa: thermodynamic and mechanistic aspects. *Biochemistry* **2000**, *39* (2), 442-452.
4. Alam, J. M.; Kobayashi, T.; Yamazaki, M., The Single-Giant Unilamellar Vesicle Method Reveals Lysenin-Induced Pore Formation in Lipid Membranes Containing Sphingomyelin. *Biochemistry* **2012**, *51* (25), 5160-5172.
5. Alam, J. M.; Yamazaki, M., Spontaneous insertion of lipopolysaccharide into lipid membranes from aqueous solution. *Chemistry and physics of lipids* **2011**, *164* (2), 166-174.
6. Alexander, C.; Rietschel, E. T., Invited review: bacterial lipopolysaccharides and innate immunity. *Journal of endotoxin research* **2001**, *7* (3), 167-202.
7. Kubiak, J.; Brewer, J.; Hansen, S.; Bagatolli, L. A., Lipid lateral organization on giant unilamellar vesicles containing lipopolysaccharides. *Biophysical journal* **2011**, *100* (4), 978-986.
8. Schmid, E. M.; Richmond, D. L.; Fletcher, D. A., Reconstitution of proteins on electroformed giant unilamellar vesicles. *Methods in cell biology* **2015**, *128*, 319-338.
9. Bhatia, T.; Husen, P.; Brewer, J.; Bagatolli, L. A.; Hansen, P. L.; Ipsen, J. H.; Mouritsen, O. G., Preparing giant unilamellar vesicles (GUVs) of complex lipid mixtures on demand: Mixing small unilamellar vesicles of compositionally heterogeneous mixtures. *Biochimica et Biophysica Acta (BBA) - Biomembranes* **2015**, *1848* (12), 3175-3180.
10. Morales-Pennington, N. F.; Wu, J.; Farkas, E. R.; Goh, S. L.; Konyakhina, T. M.; Zheng, J. Y.; Webb, W. W.; Feigenson, G. W., GUV preparation and imaging: Minimizing artifacts. *Biochimica et Biophysica Acta (BBA) - Biomembranes* **2010**, *1798* (7), 1324-1332.
11. Lira, R. B.; Steinkühler, J.; Knorr, R. L.; Dimova, R.; Riske, K. A., Posing for a picture: vesicle immobilization in agarose gel. *Scientific Reports* **2016**, *6* (1), 1-12.
12. Teissier, E.; Zandomenighi, G.; Loquet, A.; Lavillette, D.; Lavergne, J.-P.; Montserret, R.; Cosset, F.-L.; Böckmann, A.; Meier, B. H.; Penin, F.; Pécheur, E.-I., Mechanism of Inhibition of Enveloped Virus Membrane Fusion by the Antiviral Drug Arbidol. *PLOS ONE* **2011**, *6* (1), e15874.
13. Van de Cauter, L.; Fanalista, F.; van Buren, L.; De Franceschi, N.; Godino, E.; Bouw, S.; Danelon, C.; Dekker, C.; Koenderink, G. H.; Ganzinger, K. A., Optimized cDICE for Efficient Reconstitution of

Biological Systems in Giant Unilamellar Vesicles. *ACS Synthetic Biology* **2021**, *10* (7), 1690-1702.

14. Lind, T. K.; Cárdenas, M.; Wacklin, H. P., Formation of Supported Lipid Bilayers by Vesicle Fusion: Effect of Deposition Temperature. *Langmuir* **2014**, *30* (25), 7259-7263.

15. Richter, R. P.; Brisson, A. R., Following the Formation of Supported Lipid Bilayers on Mica: A Study Combining AFM, QCM-D, and Ellipsometry. *Biophys J* **2005**, *88* (5), 3422-3433.

16. Plant, A. L., Self-assembled phospholipid/alkanethiol biomimetic bilayers on gold. *Langmuir* **1993**, *9* (11), 2764-2767

